7. VALIDATION

Model validation for the *EBS Radionuclide Transport Abstraction* was performed in accordance with LP-2.29Q-BSC, *Planning for Science Activities*, and LP-SIII.10Q-BSC, *Models*, and follows the validation guidelines in the *Technical Work Plan for: Near-Field Environment and Transport: Engineered Barrier System: Radionuclide Transport Abstraction Model Report Integration* (BSC 2005 [DIRS 173617]).

LP-SIII.10Q-BSC, *Models*, requires that TSPA-LA model components be validated for their intended purpose and stated limitations, and to the level of confidence required by the relative importance of the component to the potential performance of the repository system. Three levels of model validation are defined in LP-2.29Q-BSC, *Planning for Science Activities*, Attachment 3, with the level of validation increasing with an increasing level of model importance ranging from low to moderate to high. Models whose variation could lead to a potentially large effect on the estimate of mean annual dose (e.g., a change greater than 1 mrem yr^{-1}) should receive a high or Level III model validation. Models whose variation could lead to moderate effect on the estimate of mean annual dose (less than 1 mrem yr^{-1}, but greater than 0.1 mrem yr^{-1}) should receive Level II model validation. Level I validation is sufficient for models of less importance to the estimate of mean annual dose.

The levels of confidence required for the models of the *EBS RT Abstraction*, as stated in Section 2.2.2 of the TWP, are given as follows.

The required level of confidence for the EBS flow model is Level I. The required level of confidence for the EBS transport model is Level II. The required level of confidence for radionuclide transport from the waste package to the drift wall through the invert is Level I (also specified in Table 1 of LP-2.29Q-BSC, *Planning for Science Activities*). The EBS-UZ interface model of the *EBS RT Abstraction* provides input to the unsaturated zone radionuclide transport model as described in *Particle Tracking Model and Abstraction of Transport Processes* (BSC 2004 [DIRS 170041]). The appropriate level of confidence identified for unsaturated zone radionuclide transport is Level II. Therefore, Level II also represents appropriate level of confidence for the EBS-UZ interface model of the *EBS RT Abstraction*.

Confidence Building During Model Development to Establish Scientific Basis and Accuracy for Intended Use

For Level I validation, Section 2.2.3 of the TWP (BSC 2005 [DIRS 173617]) cites Attachment 3 of LP-2.29Q-BSC as guidance for documenting a discussion of decisions and activities for confidence building during model development. Additionally, the development of the model will be documented in accordance with the requirements of Section 5.3.2(b) of LP-SIII.10Q-BSC. The development of the *EBS RT Abstraction* model has been conducted according to these requirements and the requisite criteria have been met as discussed below:

1. *Selection of input parameters and/or input data, and a discussion of how the selection process builds confidence in the model [LP-SIII.10Q-BSC 5.3.2(b) (1) and LP-2.29Q-BSC Attachment 3 Level I (a)].*

The inputs to the *EBS RT Abstraction* have been obtained from appropriate sources as described in Section 4.1. All the data are qualified project data developed by or for the Yucca Mountain Project. Tables 4.1-1 through 4.1-20 describe the input parameters, the values of the parameters and the source of the information. Inputs were selected because they are expected to represent conditions at the repository and therefore build confidence in the model. Thus, this requirement can be considered satisfied.

2. *Description of calibration activities, initial boundary condition runs, run convergences, simulation conditions set up to span the range of intended use and avoid inconsistent outputs, and a discussion of how the activity or activities build confidence in the model. Inclusion of a discussion of impacts of any non-convergence runs [(LP-SIII.10Q-BSC 5.3.2(b)(2) and LP-2.29Q-BSC Attachment 3 Level I (e)].*

   A detailed discussion of the computational implementation of the *EBS RT Abstraction* is described in Section 6.5.3. The discretization and development of the computational cell network of the sub-model domains is described in Section 6.5.3.5. Section 6.5.3.6 provides special emphasis and discussion of the EBS-UZ boundary condition. Simulation conditions account for both seepage or no seepage boundary conditions and the flux splitting algorithm accounts for the eight key flow pathways in the engineered barrier system. Discussion about non-convergence runs is not relevant for this model report. Thus, this requirement can also be considered satisfied.

3. *Discussion of the impacts of uncertainties to the model results including how the model results represent the range of possible outcomes consistent with important uncertainties [(LP-SIII.10Q-BSC 5.3.2(b)(3) and LP-2.29Q-BSC Attachment 3 Level 1 (d) and (f)].*

   Data uncertainty is addressed in Section 6 and parameter uncertainties are summarized in Table 6.5-6. In particular, corrosion rates of carbon and stainless steels are listed as model input with ranges and distributions determined from the data in Table 4.1-1. Sorption coefficient distribution ranges are summarized in Table 4.1-15 and sampling correlations are given in Table 4.1-16. Table 4.1-8 provides uncertainty for unsaturated zone parameters. The breached drip shield experimental test data in Tables 4.1-2 through 4.1-6 and Figure 4.1-1 are evaluated in Section 6.5.1, resulting in uncertain model input parameters listed in Table 6.5-6 (Flux_Split_DS_Uncert and Flux_Split_WP_Uncert).

   Model uncertainty is addressed through the evaluation of alternative conceptual models. In considering alternative conceptual models for radionuclide release rates and solubility limits (Sections 6.4. and 6.6), the EBS radionuclide transport abstraction uses models and analyses that are sensitive to the processes modeled for both natural and engineering systems.

   Conceptual model uncertainties are defined and documented, and effects on conclusions regarding performance are assessed. The fundamental relationships, e.g., mass balance and flow equations, upon which the *EBS RT Abstraction* is based, are well-established with a long history of use in the scientific community and as such are not subject to significant uncertainty. In addition, the alternative conceptual models have been screened out (Section 6.4), thereby increasing confidence in the selected conceptual

model. Other sources of uncertainty involve modeling choices (e.g., assumptions, geometry) that, because of their conservative nature, effectively bound uncertainty. Therefore this requirement can be considered satisfied.

4. *Formulation of defensible assumptions and simplifications [LP-2.29Q-BSC Attachment 3 Level I (b)].*

   A discussion of assumptions is provided in Section 5. The conceptual model for *EBS RT Abstraction* are documented in Section 6.3.1 and the simplifications necessary for implementation based on EBS design details and failure mechanisms are presented in Sections 6.3.3 and 6.3.4. Thus, this requirement can also be considered satisfied.

5. *Consistency with physical principles, such as conservation of mass, energy, and momentum [LP-2.29Q-BSC Attachment 3 Level I (c)].*

   Consistency with physical principles is demonstrated by the development of the mass balance mathematical formulations in Section 6.5.1. Thus, this requirement can also be considered satisfied.

Confidence Building After Model Development to Support the Scientific Basis of the Model

Level II validation includes the above Level I criteria and a single post development model validation method described in Paragraph 5.3.2c of LP-SIII.10Q-BSC, *Models*, consistent with a model of moderate importance to mean annual dose.

To build further confidence in the *EBS RT Abstraction*, an independent model validation technical review was conducted as specified by the TWP (BSC 2005 [DIRS 173617], Sections 2.2.3 and 2.2.4) for the EBS flow model, the EBS transport model, and the EBS-UZ interface model. This approach is based on requirements of LP-SIII.10Q-BSC, Section 5.3.2 c), where independent technical review is listed as an appropriate method for model validation. Validation is achieved if the review determines that the questions/criteria for this model, listed in Section 2.2.4 of the TWP, are met. Qualifications of and review tasks to be completed by the independent technical reviewer are described in Section 2.2.4 of the TWP. The model validation criteria are described as follows (BSC 2005 [DIRS 173617], Section 2.2.4).

EBS Flow Model Validation Criteria

Criteria that the validation of the EBS flow model is met are as follows. Each shall be confirmed by the independent model validation technical reviewer.

a) The approach and algorithms described in the document and provided to the TSPA capture all known flow pathways into and from EBS components.

b) Modeling assumptions are clearly defined, discussed, and justified as appropriate for the intended use of the model.

c) Uncertainties in parameters, processes, and assumptions are sufficiently described, and impacts of these uncertainties discussed.

d) The overall technical credibility of the approach, including assumptions, parameters, equations, and the TSPA implementation, are sufficient for the model's intended use.

EBS Transport Model Validation Criteria

Criteria that the validation of the EBS transport model is met are as follows. Each shall be confirmed by the independent model validation technical reviewer.

a) The approach and algorithms described in the document and provided to TSPA address all known modes of radionuclide transport within and from the EBS components.

b) Modeling assumptions are clearly defined, discussed, and justified as appropriate for the intended use of the model.

c) Uncertainties in parameters, processes, and assumptions are sufficiently described, and impacts of these uncertainties discussed.

d) The overall technical credibility of the approach, including assumptions, parameters, equations, and the TSPA implementation, are sufficient for the model's intended use.

EBS-UZ Interface Model Validation Criteria

The criterion that the validation of the EBS-UZ interface model is met shall consist of concurrence by an independent technical reviewer that the invert fracture-matrix partitioning results obtained using this model compare favorably with the fracture-matrix partitioning cumulative distribution function obtained using a discrete fracture model described in the *Drift-Scale Radionuclide Transport* model (BSC 2004 [DIRS 170040]). Results of the comparison shall show qualitative agreement between the two methods. The report shall document equivalent trends and correlations between input parameter variation and predicted results, identification of differences between the model results, and a discussion of the reasons and potential significance of these differences, and shall also demonstrate that the EBS-UZ interface model provided to TSPA does not underestimate radionuclide transport from the EBS to the UZ.

The results of the independent model validation technical review for the flow and transport models demonstrate that the appropriate criteria from above have been met, and are presented in Section 7.2.3. The results of the EBS-UZ interface model review demonstrate that the appropriate criteria listed above have been met, and are presented in Section 7.3.2.

The validation guidelines in the TWP (BSC 2005 [DIRS 173617]) also state that the Subject Matter Expert (author) may elect, as deemed appropriate, to provide additional validation in the form of:

- Corroboration of model results with data previously acquired from laboratory experiments or other relevant observations
- Corroboration of model results with results of alternative models

- Corroboration with information published in refereed journals or literature.

In addition to the independent model validation technical review, the post development model validation for the EBS-UZ interface model, as delineated in the TWP, includes corroboration by comparison to an alternative mathematical model developed for a closely comparable description of the relevant EBS-UZ features. This validation approach is consistent with Paragraph 5.3.2(c)(2) of LP-SIII.10Q-BSC, *Models*, which lists corroboration of results with alternative mathematical models as one of the validation methods for Level II validation. This comparison is documented in Section 7.3.1.

Additional validation of the flux splitting portion of the flow model was performed through corroboration of model results of experimental data. The results of that validation exercise are presented in Section 7.1.1.

Additional validation of the in-package diffusion portion of the transport model was performed through corroboration with alternative models. The results of that validation exercise are presented below in Section 7.2.

7.1 EBS FLOW MODEL

The EBS flow is modeled as a one-dimensional, steady advective flow through the components of the EBS. The sources of flow to the model include a seepage flux from the roof of the drift, condensation on the walls of the drift above the drift shield, and an imbibition flux from the unsaturated zone into the crushed tuff invert. The output of the flow model includes an advective flux from the invert into the unsaturated zone.

The conceptual model divides the EBS components into three domains: waste form, waste package corrosion products, and the invert. Flow and transport in these domains are treated separately. The output of the waste form domain feeds into the corrosion products domain. The output of the corrosion products domain in turn feeds the invert.

The flow through the EBS may occur along eight pathways: (1) total dripping flux (seepage inflow from the crown of the drift plus any condensation that may occur on the walls of the drift above the drift shield), (2) flux through the drip shield, (3) diversion around the drip shield, (4) flux through the waste package, (5) diversion around the waste package, (6) total flux into the invert, (7) imbibition flux from the unsaturated zone matrix to the invert, and (8) flux from the invert to the unsaturated zone fractures.

The magnitude of seepage fluid passing through the drip shield and the waste package is accounted for using the flux splitting submodel. This submodel determines how much water flows through the drip shield or waste package and how much is diverted around these components. Below is the validation of the submodel and validation criteria for both the drip shield and waste package applications. Further discussions relevant to the validation of the flow model can be found in Sections 5, 6.3.2, 6.3.3, 6.5.1.1.1, 6.5.1.1.2, and 6.5.1.1.3.

7.1.1 Flux Splitting Submodel

The EBS flux splitting submodel, which is part of the *EBS RT Abstraction* flow model, determines the fraction of total dripping flux that will flow through the drip shield and/or waste package. This submodel is directly related to the waste isolation attribute (i.e., the limited release of radionuclides from engineered barriers). The amount of water flowing through engineered barriers, when combined with radionuclide solubility limits and diffusive transport, defines the mass flux of radionuclides that is mobilized for transport through the EBS to the unsaturated zone.

Level I validation is appropriate for the flux splitting submodel, because it is part of the process for radionuclide transport from waste package to the drift wall through the invert (see Section 7 above). In addition, the flux splitting submodel has the following features:

- The submodel is not extrapolated over large distances, spaces or time.
- The submodel has large uncertainties because of the chaotic nature of the flow of droplets or rivulets on corroded, roughened surfaces.
- Sensitivity analyses in the prioritization report *Risk Information to Support Prioritization of Performance Assessment Models* (BSC 2003 [DIRS 168796], Sections 3.3.6 through 3.3.11) show that the flux splitting abstraction will not have a large impact on dose in the first 10,000 years.
- The flux splitting submodel plays a minor role in TSPA-LA. In the nominal scenario class, neither the drip shield nor the waste package fails due to general corrosion within the 10,000-year regulatory period (BSC 2004 [DIRS 169996], Section 7.2); if the TSPA-LA model is run to compute the peak dose, which occurs beyond the 10,000-year regulatory period, then the flux splitting model will be used in the nominal scenario class. When the drip shield does fail (beyond the 10,000-year regulatory period in the nominal scenario class), it is modeled as failing completely in a single time step (BSC 2004 [DIRS 169996], Section 6.3). The early waste package failure modeling case is part of the nominal scenario class, where the drip shield does not fail within the 10,000-year regulatory period; thus, the flux splitting submodel is not used. In the igneous scenario class, neither the drip shield nor the waste package survives an igneous intrusion, so the flux splitting submodel is not used. Stress corrosion cracking of the drip shield occurs in the seismic scenario class, but since no advective flux is allowed through the cracks, the flux splitting submodel is not used. Thus, the flux splitting submodel is actually applied only in the seismic scenario class when seismic damage occurs to the waste package from fault displacement leading to fractional failure of the waste package.

This flux splitting submodel is validated through comparison to experimental data. A work plan entitled *Test Plan for: Atlas Breached Waste Package Test and Drip Shield Experiments* (BSC 2002 [DIRS 158193]) defines the experiments used for validation of this flux splitting submodel.

The flux splitting submodel is applied to two components of the EBS–the drip shield and the waste package–and is validated for each. Validation is achieved through comparison of the models developed in this document (based in part on the qualified experimental data) to other qualified data collected during associated testing. This comparison is limited because the validation experiments are based on flow measurements from a single fixed source for dripping, whereas the abstraction is based on randomly located drips relative to multiple patches on the drip shield. In this situation, the appropriate criterion for model validation is that the ranges of predictions of the abstraction, based on smooth drip shield mock-up surface data, overlap the ranges of experimental measurements made on the rough drip shield mock-up surface. This criterion is appropriate because of the large spread of the experimental data.

The rough drip shield surface experiments replicate the smooth drip shield surface experiments and constitute a consistent set of data that can be compared with and serve as validation for the smooth drip shield surface data. The rough surface would be expected to yield results (specifically, the flux splitting uncertainty factors) that differ from those obtained for the smooth surface. However, because the only difference in the experiments is the surface texture, the trends in the data and the values obtained for the uncertainty factors should be similar, which validates the flux splitting submodel.

Experimental data used to develop the flux splitting submodel include the splash radius, the rivulet spread distance or angle, and the fraction of dripping flux that flowed into breaches. For the drip shield and waste package flux splitting submodels, data from smooth drip shield experiments were used (DTNs: MO0207EBSATBWP.022 [DIRS 163400]; MO0207EBSATBWP.023 [DIRS 163402]; MO0207EBSATBWP.024 [DIRS 163401]; MO0207EBSATBWP.025 [DIRS 163403]). For validation of the models, data from the rough drip shield experiments are used (DTNs: MO0207EBSATBWP.021 [DIRS 163399]; MO0208EBSATBWP.027 [DIRS 163404]; MO0208EBSATBWP.028 [DIRS 163405]). Each of the types of data used is discussed below, first for the drip shield submodel validation and then for the waste package flux splitting submodel validation.

7.1.1.1 Drip Shield Flux Splitting Submodel

Splash radius data for dripping onto the crown of the rough drip shield surface are listed in Table 7.1-1. The data are analyzed in the Microsoft Excel spreadsheet: Flux Splitting Validation, Worksheet: Splash Rad vs Number, which is documented in Appendix E. As shown in Figure 7.1-1, the splash radius tends to increase as the number of drips increases. The inner cluster radius is of interest because it is used to define the effective length of the drip shield in developing the flux splitting submodel (see Section 6.5.1.1.2). While the data do not indicate that a maximum splash radius was achieved, it stands to reason that a maximum must exist, simply because the distance a splashed droplet can travel is finite, limited by the kinetic energy of a falling drop. The uncertain parameter in the drip shield flux splitting submodel, f'_{DS}, was based on the maximum splash distance observed for the inner cluster of droplets on a smooth drip shield, 48 cm (see Section 6.5.1.1.2.4 for a discussion of the development of f'_{DS} based on the 48-cm maximum inner cluster splash radius). For the rough drip shield tests, the maximum inner cluster splash radius for dripping onto the crown was again 48 cm. Another approach is to use the splash radius at which rivulets begin to flow from coalesced droplets. In Splash Radius

Test #1, rivulet flow began after 143 drips; in Test #2, after 145 drips; and in Test #3, after 133 drips (DTN: MO0207EBSATBWP.021 [DIRS 163399]), for an average of 140 drips. Using the Microsoft Excel Trendline application (least squares fitting routine) for the inner cluster data in Figure 7.1-1, the splash radius when rivulets began to flow was 31 cm. The minimum splash radius was about 3.5 cm for more than 20 drips (see Table 7.1-1). The range of uncertainty is bounded using the extreme values of splash radius (3.5 – 48 cm). Since the value of splash radius at which rivulets begin to flow (31 cm) is between those extremes, an estimate of uncertainty based on that value will not affect the estimated bounds on uncertainty.

The flux splitting submodel also depends on the rivulet spread angle. These data are analyzed in the Microsoft Excel spreadsheet: Flux Splitting Validation, Worksheet: Rough DS, which is documented in Appendix E. For the smooth drip shield, the spread angle from crown drip locations ranged from 8.9° to 17.3° (± one standard deviation from the mean of 13.2°; see Section 6.5.1.1.2.4). For drip locations on the crown, the rough drip shield surface had a mean rivulet spread angle of 7.3°, with a range of 0° to 14.4° (± one standard deviation from the mean). Rivulet spread data for the rough surface are shown in Table 7.1-2. In Table 7.1-4, the spread angle calculation results are shown.

The amount of water dripped onto the crown and water flow into breaches on the rough drip shield surface are listed in Table 7.1-3. The fraction of the dripping flux that flowed into the pertinent breach, f_{expt}, is shown along with the rivulet spread angle for each particular test in Table 7.1-4.

Table 7.1-1. Atlas Breached Drip Shield Experiments on Rough Drip Shield Surface – Dripping on Crown – Splash Radius Tests

No. Drips	Splash Radius (cm)		Comments
	Left	Right	
Splash Radius Test #1			
10	2.0	2.0	Measured inner cluster (bulk)
10	15.0	25.5	Measured outer fringe
21	5.0	4.0	Measured inner cluster (bulk)
21	15.0	42.5	Measured outer fringe
60	18.0	22.0	Measured inner cluster (bulk)
60	72.5	75.5	Measured outer fringe
143	35.0	48.0	Measured inner cluster (bulk)
143	54.0	82.5	Measured outer fringe
203	35.0	48.0	Measured inner cluster (bulk)
203	79.5	106.5	Measured outer fringe
Splash Radius Test #2			
21	3.5	4.0	Measured inner cluster (bulk)
21	37.5	7.0	Measured outer fringe
82	10.5	19.0	Measured inner cluster (bulk)
82	63.0	32.0	Measured outer fringe
149	31.5	30.0	Measured inner cluster (bulk)
207	45.0	40.0	Measured inner cluster (bulk)
Splash Radius Test #3			
30	7.5	9.0	Measured inner cluster (bulk)
82	19.0	17.5	Measured inner cluster (bulk)
137	28.0	27.5	Measured inner cluster (bulk)
205	29.0	28.0	Measured inner cluster (bulk)

DTN: MO0207EBSATBWP.021 [DIRS 163399].

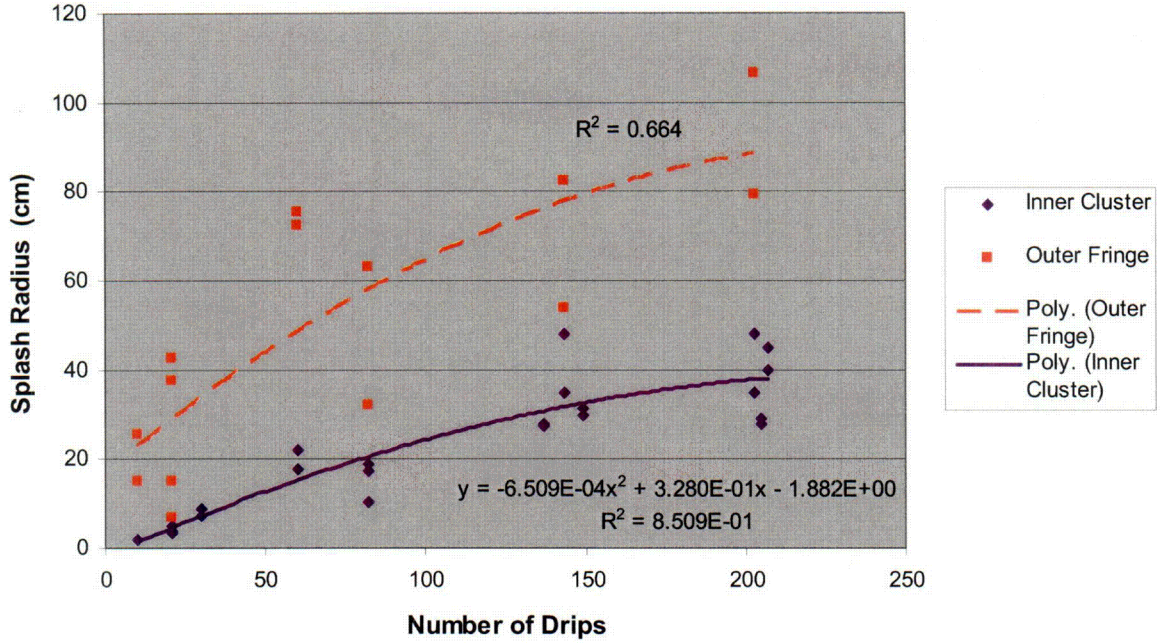

Figure 7.1-1. Splash Radius Dependence on Number of Drips for Rough Drip Shield Tests

Table 7.1-2. Atlas Breached Drip Shield Experiments on Rough Drip Shield Surface – Dripping on Crown – Rivulet Spread Data – 33° from Crown

Drip Location	Left (cm)	Right (cm)	Relevant Patch
Multiple Patch Tests (DTN: MO0208EBSATBWP.027 [DIRS 163404])			
81 cm left of drip shield center	32.5	17.5	4
27 cm left of drip shield center	21.5	18.0	4
27 cm right of drip shield center	10.0	10.0	5
27 cm right of drip shield center	1.0	0	5
81 cm right of drip shield center	17.0	34.0	5
Bounding Flow Rate Tests (DTN: MO0208EBSATBWP.028 [DIRS 163405])			
54 cm left of drip shield center (High Flow Rate)	2	0	4
27 cm left of drip shield center (High Flow Rate)	15	15	4
27 cm right of drip shield center (High Flow Rate)	6	6	5
27 cm right of drip shield center (Low Flow Rate)	50.0	16.0	5
27 cm right of drip shield center (Low Flow Rate)	—	1.0	5
27 cm left of drip shield center (Low Flow Rate)	25.5	12.0	4
54 cm left of drip shield center (Low Flow Rate)	0	0	4

Table 7.1-3. Atlas Breached Drip Shield Experiments on Rough Drip Shield Surface – Dripping on Crown – Flow into Breaches

Drip Location	Drip Location Relative to:		Water Input (g)	Water Collected in:	
	Breach B4 (cm)	Breach B5 (cm)		Breach B4 (g)	Breach B5 (g)
Multiple Patch Tests (DTN: MO0208EBSATBWP.027 [DIRS 163404])					
81 cm left of drip shield center	-27	-135	292.35	0.27	0.00
27 cm left of drip shield center	27	-81	288.45	5.27	0.00
27 cm right of drip shield center	81	-27	291.62	0.00	0.08
27 cm right of drip shield center	81	-27	294.13	0.00	0.27
81 cm right of drip shield center	135	27	290.10	0.00	1.01
Bounding Flow Rate Tests (DTN: MO0208EBSATBWP.028 [DIRS 163405])					
54 cm left of drip shield center (High Flow Rate)	0	-108	330.74	193.87	0.00
27 cm left of drip shield center (High Flow Rate)	27	-81	328.65	0.63	0.00
27 cm right of drip shield center (High Flow Rate)	81	-27	306.65	0.00	0.35
27 cm right of drip shield center (Low Flow Rate)	81	-27	545.14	0.00	11.11
27 cm right of drip shield center (Low Flow Rate)	81	-27	70.80	0.00	0.00
27 cm left of drip shield center (Low Flow Rate)	27	-81	113.32	1.36	0.00
54 cm left of drip shield center (Low Flow Rate)	0	-108	118.10	0.00	0.00

Table 7.1-4. Atlas Breached Drip Shield Experiments on Rough Drip Shield Surface – Dripping on Crown – Fraction of Dripping That Flowed into Breaches and Rivulet Spread Angle

Drip Location	Breach Collecting Flow	f_{expt}	Spread Angle (degree)	
			Left	Right
81 cm left of drip shield center	4	0.0018	13.4	7.3
27 cm left of drip shield center	4	0.0365	9.0	7.5
27 cm right of drip shield center	5	0.0005	6.6	6.6
27 cm right of drip shield center	5	0.0018	0	0.7
81 cm right of drip shield center	5	0.0070	11.2	21.6
54 cm left of drip shield center (High Flow Rate)	4	1.1723	0.8	0
27 cm left of drip shield center (High Flow Rate)	4	0.0038	6.3	6.3
27 cm right of drip shield center (High Flow Rate)	5	0.0023	4.0	4.0
27 cm right of drip shield center (Low Flow Rate)	5	0.0408	30.2	10.5
27 cm right of drip shield center (Low Flow Rate)	5	0.0110	—	0.7

Table 7.1-4. Atlas Breached Drip Shield Experiments on Rough Drip Shield Surface – Dripping on Crown – Fraction of Dripping That Flowed into Breaches and Rivulet Spread Angle (Continued)

Drip Location	Breach Collecting Flow	f_{expt}	Spread Angle (degree)	
			Left	Right
27 cm left of drip shield center (Low Flow Rate)	4	0.0240	10.6	5.0
54 cm left of drip shield center (Low Flow Rate)	4	0.0	0	0
Mean	—	0.108	7.25	
Standard Deviation	—	0.335	7.18	
Median	—	0.005	6.29	

Source: Microsoft Excel spreadsheet: Flux Splitting Validation, Worksheet: Rough DS, documented in Appendix E.

NOTES: — = no measurement.
Mean, standard deviation, and median for spread angle are for all (left and right) measurements.

Following the approach used in Section 6.5.1.1.2.4, the "inner cluster" splash diameter is used for the effective length of the drip shield in the validation of the flux splitting algorithm, which is given by Equations 6.3.2.4-4 and 6.3.2.4-6 (or 6.5.1.1.2-35). The form of the equation is:

$$F = \frac{N_b \ell}{L_{DS}}\left(1 + \frac{\tan\alpha}{2}\right) f_{VD}, \qquad \text{(Eq. 7.1.1.1-1)}$$

where F is the fraction of dripping flux that flows through breaches, ℓ is one-half the width of a breach or patch, L_{DS} is the effective length of the drip shield (i.e., the length over which dripping or splattering occurs), α is the rivulet spread angle, and f_{VD} is the uncertainty factor for the drip shield developed for validation, corresponding to the drip shield uncertainty factor, f_{DS}. For the validation tests, the number of breaches, N_b, is one.

The splash diameter is used for the effective length, L_{DS}. As shown in Table 7.1-1, the "inner cluster" splash radius on the rough drip shield surface ranged from 3.5 cm to 48 cm (for more than 20 drops), giving a range for L_{DS} of 7 cm to 96 cm. The spread angle ranged (one standard deviation from the mean) from zero to 14.4°. For a drip shield patch width of 27 cm, $\ell =$ 13.5 cm. Then, as shown in Table 7.1-5, $F / f_{VD} = \frac{N_b \ell}{L_{DS}}\left(1 + \frac{\tan\alpha}{2}\right)$ ranges from 0.141 to 2.17.

Table 7.1-5. Range of Estimates for F/f_{VD}

L_{DS} (cm)	Drip Shield F/f_{VD}	
	$\alpha = 0°$	$\alpha = 14.4°$
7	1.93	2.17
96	0.141	0.158

The fraction of dripping flux, f_{expt}, that entered breaches in 12 rough drip shield experiments ranged from zero to 1.17, with a mean of 0.108 and a median of 0.0054. The wide range of uncertainty and randomness in the experiments is demonstrated in two of the tests having the same drip location (54 cm to the left of the drip shield center). The high drip rate test yielded the highest flow into a breach with a negligible spread, which is the expected result. What appears to be an unphysical result for this test, $f_{expt} = 1.17$, is obtained from the assumption that half of the dripping flux onto the crown flows down each side of the drip shield. This was evidently not the case in this particular test, since more than half of the dripping flux flowed into the breach. However, since there are no data available to determine what fraction of the dripping flux flowed down the side with the breach, the procedure for calculating f_{expt} is followed without limiting the values that are obtained (e.g., by limiting f_{expt} to a maximum of 1.0). The low drip rate test at the same drip location, which had zero rivulet spread, unexpectedly resulted in no flow into the breach. Statistics for f_{expt} are compared in Table 7.1-6 between the smooth drip shield surface experimental results (Table 6.5-2) and the rough surface results discussed in this section.

Table 7.1-6. Comparison of f_{expt} Statistics for Smooth and Rough Drip Shield Surfaces

Experiments	Mean f_{expt}	Minimum f_{expt}	Maximum f_{expt}	Median f_{expt}
Drip Shield (Smooth Surface)	0.111	0.013	0.275	0.049
Drip Shield Validation (Rough Surface)	0.108	0.0	1.17	0.0054

The rough surface experimental results are now used to calibrate the drip shield flux splitting submodel that is developed for validation purposes, yielding the uncertainty factor f_{VD}:

$$f_{VD} = \frac{f_{expt}}{\frac{\ell}{L_{DS}}\left(1+\frac{\tan\alpha}{2}\right)}. \qquad \text{(Eq. 7.1.1.1-2)}$$

f_{VD} is at a minimum using the minimum value for L_{DS} (7 cm) and the maximum value for α (14.4°), resulting in $f_{VD} = 0.46 f_{expt}$. The maximum for f_{VD} is obtained using the maximum value for L_{DS} (96 cm) and the minimum value for α (0°), resulting in $f_{VD} = 7.1 f_{expt}$. Using the mean value for f_{expt} (0.108) results in a range for f_{VD} of 0.050 to 0.77. The drip shield flux splitting algorithm developed in Section 6.5.1.1.2.4 produced the corresponding factor f_{DS} ranging from about 0.36 to 0.73. These factors (f_{VD} and f_{DS}) actually represent the estimates of the upper bound on the uncertainty, since a lower bound is necessarily zero (i.e., no flow through a breach). Using the actual measured range of f_{expt} (0.0 to 1.17) instead of the mean increases the range estimated for f_{VD} to 0.0 to (7.1)(1.17) = 8.3. The corresponding range for f_{DS}, using the measured range of f_{expt} (0.013 to 0.275) (Table 6.5-2) for the smooth surface tests instead of the mean (0.111), is 0.013/0.31 = 0.041 (for $L_{DS} = 50\,\text{cm}$, $\alpha = 17.3°$) to 0.275/0.152 = 1.8 (for $L_{DS} = 96\,\text{cm}$, $\alpha = 8.9°$). Thus, using the extreme values of f_{expt} for estimating f_{DS} and f_{VD}, the

upper bound on f_{VD} actually spans the uncertainty in the upper bound estimate of f_{DS}, as summarized in Table 7.1-7.

Table 7.1-7. Summary of f_{DS} and f_{VD} Values

	Based on Mean f_{expt}		Based on Minimum f_{expt}	Based on Maximum f_{expt}
	Minimum	Maximum	Minimum	Maximum
f_{DS}	0.36	0.73	0.041	1.8
f_{VD}	0.050	0.77	0	8.3

Based on mean values for the experimentally measured fraction of the dripping flux that flows through a breach, the rough drip shield surface factor shows that less of the dripping flux will flow through a breach, compared with the smooth surface results used to develop the drip shield flux splitting submodel. The rough surface data validate the drip shield submodel by confirming an estimate of the upper bound on the uncertainty of 0.77, based on mean values for f_{expt}. The range on the estimate for f_{VD} is also about 0.7, which is comparable (about a factor of 2) to the uncertainty in f_{DS}. While the upper bound on the uncertainty factor is about the same for both the smooth and rough surfaces (0.73 vs. 0.77), the lower bound is much higher for the smooth surface (0.36 vs. 0.05). A random sampling from these ranges will give a mean value of about 0.54 for the smooth surface versus about 0.42 for the rough surface. So the smooth surface range will, on average, overestimate the flux through the drip shield compared to the rough surface range. Both the smooth surface and the rough surface results include a wide range of variability that is incorporated in the sampled uncertainty parameter f_{DS} for the drip shield flux splitting submodel. The rough drip shield surface data provide confirmation that the drip shield submodel will generally overestimate the flux through that barrier.

A final comparison is made between f'_{DS}, which lumps the uncertainty in the rivulet spread angle into f_{DS}, and a corresponding parameter for the rough drip shield surface, f'_{VD}, is derived, where

$$f'_{VD} = \left(1 + \frac{\tan\alpha}{2}\right) f_{VD}. \qquad \text{(Eq. 7.1.1.1-3)}$$

Since α ranges from 0° to 14.4°, applying the maximum value for α will result in the range for f'_{VD} of 0 to 0.87, based on the mean value of f_{expt} (0.108) that gives a range of 0.050 to 0.77 for f_{VD}. For comparison, f'_{DS} was estimated to range from 0 to 0.85. The nearly-identical ranges for f'_{DS} and f'_{VD} validate the drip shield flux splitting submodel.

7.1.1.2 Waste Package Flux Splitting Submodel

Whereas the drip shield flux splitting submodel is based on data from dripping on the crown of the smooth drip shield mock-up surface, the waste package flux splitting submodel is based on data from off-crown drip locations on the smooth drip shield mock-up surface. Off-crown drip

locations are used because the steeper slope on the mock-up surface at those locations simulates more closely the higher radius of curvature of the waste package compared with the drip shield (Section 6.5.1.1.3). Additionally, the drop distance to drip locations that are off the crown was greater than for drips on the crown (2.17 m to the crown, 2.22 m to the 16.5° line, and 2.31 m to the 33° line; BSC 2003 [DIRS 163406], p. 6), which more closely mimics the greater drop distance from the drift to the waste package compared with the drip shield surface. Consistent with the validation of the drip shield flux splitting submodel, the validation of the waste package flux splitting submodel is based on data from the rough drip shield mock-up surface, but for off-crown drip locations, to be consistent with the waste package flux splitting submodel. Using off-crown drip location data for the rough waste package surface (Table 7.1-8), the rivulet spread angle was found to depend strongly on the drip rate. These data are analyzed in the Microsoft Excel spreadsheet: Flux Splitting Validation, Worksheet: Rough off crown WP model, which is documented in Appendix E. The high drip rate resulted in an average spread angle of 27.1°; the nominal drip rate had a mean spread angle of 20.6°; and the low drip rate had a mean spread angle of 3.1°. However, to be consistent with the development of the spread angle for the waste package submodel, and to incorporate the real possibility of widely varying drip rates, all 50 data points are combined. The mean spread angle for the rough waste package surface with off-crown drip locations is therefore 9.4°, with a range (± one standard deviation of 9.6°) of 0° to 19.0°.

In the off-crown splash radius tests #4 and #5 (Table 7.1-9) (Microsoft Excel spreadsheet: Flux Splitting Validation, Worksheet: Splash Radius, which is documented in Appendix E), the drip location was 33° and 16.5° off the crown. The mean splash radius was 8.9 cm, with a measured range of 3.0 cm to 15.0 cm. This gives an effective waste package length of about 6 cm to 30 cm for the tests.

Table 7.1-8. Atlas Breached Waste Package Experiments on Rough Mock-Up Surface – Dripping off Crown – Rivulet Spread Data

Drip Location on Mock-Up	Spread at 33°		Spread at Transition		Relevant Patch
	Left (cm)	Right (cm)	Left (cm)	Right (cm)	
Multiple Patch Tests (DTN: MO0208EBSATBWP.027 [DIRS 163404])					
81 cm right of center, 16.5°	—[a]	—	—	—	5
27 cm right of center, 16.5°	8	12	6	8	5
27 cm left of center, 16.5°	21	19	12	13	4
81 cm left of center, 16.5°	16	22	14	12	4
81 cm right of center, 33°	—	—	2	2	5
27 cm right of center, 33°	—	—	3	1	5
27 cm left of center, 33°	—	—	2	1	4
81 cm left of center, 33°	—	—	3	4	4
Bounding Flow Rate Tests (DTN: MO0208EBSATBWP.028 [DIRS 163405])					
54 cm left of center, 33° (Low Flow Rate)	—	—	—	—	4
54 cm left of center, 33° (High Flow Rate)	—	—	—	—	4
27 cm left of center, 33° (High Flow Rate)	6[b]	9[b]	8	14	4
27 cm right of center, 33° (High Flow Rate)	5[b]	3[b]	12	11	5
27 cm right of center, 33° (Low Flow Rate)	—	—	2.5	2.5	5
27 cm right of center, 16.5° (High Flow Rate)	16	15	17	10	5

Table 7.1-8. Atlas Breached Waste Package Experiments on Rough Mock-Up Surface – Dripping off Crown – Rivulet Spread Data (Continued)

Drip Location on Mock-Up	Spread at 33°		Spread at Transition		Relevant Patch
27 cm left of center, 16.5° (High Flow Rate)	26	32	13	34	4
54 cm left of center, 16.5° (High Flow Rate)	25	20	26	19	4
54 cm left of center, 16.5° (Low Flow Rate)	3	6	—	—	4
27 cm left of center, 16.5° (Low Flow Rate)	3	2	1	0	4
27 cm right of center, 16.5° (Low Flow Rate)	0	0	0	0	5
27 cm left of center, 33° (Low Flow Rate)	—	—	6	4.5	4

[a] — = rivulet spread not measured.
[b] These data are ignored due to inconsistent behavior – rivulet spread should not occur at the drip location.

Table 7.1-9. Atlas Breached Waste Package Experiments on Rough Mock-Up Surface – Dripping off Crown – Splash Radius Tests

No. Drips	Splash Radius (cm)		Comments
	Left	Right	
Splash Radius Test #4 (33°) (DTN: MO0207EBSATBWP.021 [DIRS 163399])			
31	3.0	3.5	Measured inner cluster (bulk)
82	5.5	6.0	Measured inner cluster (bulk)
158	6.5	6.5	Measured inner cluster (bulk)
Splash Radius Test #5 (16.5°) (DTN: MO0207EBSATBWP.021 [DIRS 163399])			
22	9.0	10.0	Measured inner cluster (bulk)
82	13.0	14.5	Measured inner cluster (bulk)
156	14.0	15.0	Measured inner cluster (bulk)

The experimentally measured fraction of the drip flux that flowed into all breaches (f_{expt}) from off-crown drip locations is given in Table 7.1-10. The breaches that were the focus of a particular test or into which flow was expected have f_{expt} values shown in bold. For f_{expt} values in bold, f_{expt} had a mean of 0.12, with a standard deviation of 0.23. The measured minimum fraction was 0.0 and the maximum was 0.621.

Following the approach used in Section 6.5.1.1.3, the "inner cluster" splash diameter is used for the effective length of the waste package in the validation of the flux splitting algorithm, which is given by Equations 6.3.3.2-1 (or 6.5.1.1.3-2) and 6.3.3.2-3 (or 6.5.1.1.3-1). The form of the equation is:

$$F = \frac{N_b \ell}{L_{WP}} \left(1 + \frac{\tan \alpha}{2} \right) f_{VW}, \qquad \text{(Eq. 7.1.1.2-1)}$$

where F is the fraction of dripping flux that flows through breaches, ℓ is one-half the width of a breach or patch, L_{WP} is the effective length of the waste package (i.e., the length over which dripping or splattering occurs), α is the rivulet spread angle, and f_{VW} is the uncertainty factor

for the waste package developed for validation, corresponding to the waste package uncertainty factor, f_{WP}. For the validation tests, the number of breaches, N_b, is one. f_{VW} is obtained by inserting f_{expt}, the measured fraction of the dripping flux that flowed into breaches, for F in Equation 7.1.1.2-1:

$$f_{VW} = \frac{f_{expt}}{\frac{N_b \ell}{L_{WP}}\left(1+\frac{\tan\alpha}{2}\right)}. \qquad \text{(Eq. 7.1.1.2-2)}$$

Table 7.1-10. Atlas Breached Waste Package Experiments on Rough Mock-Up Surface – Dripping off Crown – Flow into Breaches

Drip Location on Mock-Up	Water Input (g)	Breach 4 Inflow (g)	Breach 4 f_{expt}	Breach 5 Inflow (g)	Breach 5 f_{expt}
81 cm right of center, 16.5°	282.96	0	0	0.76	**0.0027**
27 cm right of center, 16.5°	316.74	0	0	0.35	**0.0011**
27 cm left of center, 16.5°	309.57	0.48	**0.0016**	0.44	0.0014
81 cm left of center, 16.5°	242.56	0.94	**0.0039**	0	0
81 cm right of center, 33°	109.4	0	0	0.22	**0.0020**
27 cm right of center, 33°	108.44	0	0	0.30	**0.0028**
27 cm left of center, 33°	107.33	0.33	**0.0031**	0	0
81 cm left of center, 33°	106.75	0.01	**0.0001**	0	0
54 cm left of center, 33° (Low Flow Rate)	123.13	53.27	**0.4326**	0	0
54 cm left of center, 33° (High Flow Rate)	330.03	204.99	**0.6211**	0	0
27 cm left of center, 33° (High Flow Rate)	339.24	0.06	**0.0002**	0	0
27 cm right of center, 33° (High Flow Rate)	330.22	0.10	0.0003	1.23	**0.0037**
27 cm right of center, 33° (Low Flow Rate)	112.36	0	0	0.80	**0.0071**
27 cm right of center, 16.5° (High Flow Rate)	313.82	0	0	1.14	**0.0036**
27 cm left of center, 16.5° (High Flow Rate)	322.07	1.34	**0.0042**	0.19	0.00059
54 cm left of center, 16.5° (High Flow Rate)	328.27	197.92	**0.6029**	0	0
54 cm left of center, 16.5° (Low Flow Rate)	94.41	57.18	**0.6056**	0	0
27 cm left of center, 16.5° (Low Flow Rate)	115.97	0.34	**0.0029**	0.45	0.0039
27 cm right of center, 16.5° (Low Flow Rate)	119.76	0	0	0.09	**0.0008**
27 cm left of center, 33° (Low Flow Rate)	115.81	0.36	**0.0031**	0	0

DTNs: MO0208EBSATBWP.027 [DIRS 163404], MO0208EBSATBWP.028 [DIRS 163405].

NOTE: For all fexpt values in bold: mean = 0.115; standard deviation = 0.234; median = 0.0031; minimum = 0.00014; maximum = 0.621.

Statistics for f_{expt} are compared in Table 7.1-11 between the smooth surface experimental results used for the waste package flux splitting submodel (Appendix D) and the rough surface results discussed in this section (Table 7.1-10).

Table 7.1-11. Comparison of f_{expt} Statistics for Smooth and Rough Surfaces

Experiments	Mean f_{expt}	Minimum f_{expt}	Maximum f_{expt}	Median f_{expt}
Waste Package (Smooth Surface)	0.295	0.0	1.066	0.0142
WP Validation (Rough Surface)	0.115	0.0001	0.621	0.0031

WP = waste package

With the values for the breach flow fraction (f_{expt}), the effective waste package length (L_{WP}), and the spread angle (α) as determined above using off-crown rough surface test data, the range for f_{VW} is be determined. The half-width of the patch used in the experiments ($\ell = 13.5$ cm) is used to evaluate f_{VW}. The minimum for f_{VW} is obtained using the minimum effective waste package length ($L_{WP} = 6.0$ cm) and the maximum spread angle ($\alpha = 19.0°$), resulting in $f_{VW} = 0.379 f_{expt}$. The maximum for f_{VW} is obtained using the maximum effective waste package length ($L_{WP} = 30$ cm) and the minimum spread angle ($\alpha = 0°$), resulting in $f_{VW} = 2.22 f_{expt}$. Using the mean value of f_{expt} (0.115), f_{VW} for the waste package ranges from 0.044 to 0.26. Over the measured range of f_{expt} (0 to 0.621), f_{VW} ranges from 0.0 to (2.22)(0.621) = 1.38. The range obtained for f_{WP} (0.909 to 2.00), based on the mean smooth surface value of f_{expt} (0.295), is higher. When the measured range of smooth surface f_{expt} values (0.0 to 1.066; see Figure D-10) for the waste package flux splitting analysis is used instead of the mean, f_{WP} ranges from 0.0 to 3.28. The waste package flux splitting submodel (based on smooth surface data) overestimates flow through breaches compared to the model validation estimates (based on rough surface data), which in turn overestimates the advective releases of radionuclides compared to the model validation estimates. The estimated values for f_{WP} and f_{VW} are summarized in Table 7.1-12.

Table 7.1-12. Summary of f_{WP} and f_{VW} Values

	Based on Mean f_{expt}		Based on Minimum f_{expt}	Based on Maximum f_{expt}
	Minimum	Maximum	Minimum	Maximum
f_{WP}	0.909	2.001	0.0	3.28
f_{VW}	0.044	0.26	0.0	1.38

As with the drip shield flux splitting submodel, a final comparison is between f'_{WP}, which lumps the uncertainty in the rivulet spread angle into f_{WP}, and a corresponding parameter for the rough waste package surface, f'_{VW}, where

$$f'_{VW} = \left(1 + \frac{\tan\alpha}{2}\right) f_{VW}. \qquad \text{(Eq. 7.1.1.2-3)}$$

For the rough surface, α ranges from 0° to 19.0°. Applying the maximum value for α results in the range for f'_{VW} of 0 to 0.30, based on the mean value of f_{expt}. For comparison, f'_{WP} was estimated to range from 0 to 2.41. The wider range for f'_{WP} means that the waste package flux splitting submodel tends to overestimate the flow through breaches in the waste package compared to the rough surface validation tests. The overlapping ranges for f'_{WP} and f'_{VW} validate the waste package flux splitting submodel.

Sections 7.1.1.1 and 7.1.1.2 have demonstrated that the drip shield and waste package flux splitting submodels based on experiments using smooth drip shield mock-up surfaces overestimate fluxes when compared to the experimental data using rough drip shield mock-up surfaces. The validations discussed uncertainties in relevant parameters. Based on these validation results, the EBS flow model is adequate for its intended use.

7.1.2 Results of Independent Model Validation Technical Review of the EBS Flow Model

The results of the independent model validation technical review of the EBS flow model are given in a memo presented in Section 7.2.3 that combines the technical reviews of the EBS flow and transport models.

7.2 EBS TRANSPORT MODEL

The transport of radionuclides through the EBS is modeled, using assumptions in Section 5, as a combination of advective and diffusive transport including retardation between a series of three domains:

- Waste form domain
- Corrosion products domain
- Invert domain.

Advective transport is considered when water enters the waste form domain and is able to flow through the EBS and enter the UZ. The EBS flow model (Section 7.1) calculates the water flux between each domain and a separate model provides radionuclide concentrations.

Diffusive transport between each of the domains occurs regardless of whether water is flowing though the EBS, since, by Assumption 5.5, a continuous film of water is always present on all surfaces of internal waste package components and corrosion products in a breached waste package when the temperature is below 100°C. Diffusive transport between each domain is

modeled in one dimension and therefore is dependent upon the following parameters that can vary as a function of time and according to the specific transport pathway:

- Effective diffusion coefficient
- Diffusive area
- Diffusion length.

The effective diffusion coefficient is calculated from Archie's law and is dependent upon the free water diffusion coefficient, porosity, and saturation in each domain. Additionally a temperature correction is made for diffusion in the invert domain. Porosity is either assumed to be constant or is provided by a separate model (e.g., BSC 2005 [DIRS 172895]). Saturation varies with relative humidity. The diffusive area is calculated differently for each domain, but is either a function of the number of breaches in the waste package (corrosion patches or stress corrosion cracks) or it is calculated from the geometry of the different components of the EBS. The diffusive area of breaches also depends on the scenario class being modeled. The diffusion length is either calculated from EBS geometry or is sampled, depending upon the domain.

As stated in Section 7, the level of confidence required for the EBS transport model is Level II. Level II validation is described in Section 7. In Sections 6.3 and 6.5, a detailed explanation and justification is presented on the formulation of the transport model. These sections include a great amount of information that is relevant to Level II validation. In addition, the following sections include auxiliary information aimed to validate further certain components of the transport model.

Section 7.2.1 describes a comparison between the in-package diffusion submodel and two similar, independently developed models of transport from a waste package to the invert. The comparison shows that although each model uses a different set of assumptions, the assumptions used and the final diffusion coefficients calculated by each model generally agree and thus the transport model is valid for its intended purpose.

Section 7.2.2 compares the invert diffusion coefficient of free water diffusivity for radionuclides at different temperatures and with other cations and anions and shows that the self-diffusion coefficient of water at 25°C is an upper bound.

7.2.1 In-Package Diffusion Submodel

Diffusive transport within the waste package will limit the release of radionuclides for those waste packages in a no-seep environment. The in-package diffusion submodel is directly related to the waste isolation attribute, limited release of radionuclides from the engineered barriers, because the model predicts delays in the release of mass from the waste package in comparison to the TSPA-SR model, which immediately mobilized radionuclides at the external surface of the waste package.

Level II validation is appropriate for the in-package diffusion submodel, as it is part of the EBS radionuclide transport model (see Section 7 above). In addition, the in-package diffusion submodel has the following features:

- The in-package diffusion submodel is not extrapolated over large distances or spaces. There is an inherent time extrapolation in the model.

- The in-package diffusion submodel bounds the uncertainties by considering two bounding states. In the first state, the waste package internal components are considered to be in their intact, as-emplaced condition. For the second state, the iron-based waste package internal components are considered to be completely degraded to a porous material. Although these are two bounding end states, uncertainties exist in the time- and spatially-dependent intermediate conditions.

- The in-package diffusion submodel has a minor impact on dose time history in the first 10,000 years, based on sensitivity calculations performed for the prioritization report *Risk Information to Support Prioritization of Performance Assessment Models* (BSC 2003 [DIRS 168796], Sections 3.3.6 through 3.3.11). Those studies indicate that the estimate of mean annual dose in the first 10,000 years has only a minor dependence on in-package conditions that impact diffusion.

The in-package diffusion submodel is validated by comparison to two other models:

- Electric Power Research Institute (EPRI) *Phase 5* report (EPRI 2000 [DIRS 154149])

- A model by Lee et al. (1996 [DIRS 100913]) for diffusive releases from waste package containers with multiple perforations.

The in-package diffusion submodel is based on the one-dimensional diffusion equation, Fick's first law of diffusion (Bird et al. 1960 [DIRS 103524], p. 503):

$$\frac{q_i}{A} = -D\frac{\partial C_i}{\partial x}. \qquad \text{(Eq. 7.2.1-1)}$$

That is, the fundamental process being modeled is diffusion through a porous medium, a process that is well understood and fully accepted throughout the scientific and engineering community.

Certain underlying assumptions need to be addressed. It is assumed that the bulk of the corrosion products inside a waste package is hematite, Fe_2O_3, based simply on the predominance of iron in the composition of internal non-waste form components. This assumption is also used in the EPRI report (EPRI 2000 [DIRS 154149], p. 6-22), based on cited studies (EPRI 2000 [DIRS 154149], p. 6-31) of corrosion products of carbon steel in humid, oxidizing environments that indicate that in the presence of an abundant supply of oxygen, iron would be expected to exist as Fe_2O_3, or FeOOH or $Fe(OH)_3$.

The specific surface area of hematite has been measured by numerous investigators. The range of values obtained varies widely, depending on the morphology of the sample. As can be seen in the expressions for effective saturation and diffusion coefficient, Equations 6.3.4.3.5-5 and 6.3.4.3.5-6, the diffusion coefficient is proportional to the square of the specific surface area, which from Table 6.3-7 varies by about a factor of about 12. This uncertainty is accounted for in the uncertain parameter, Surface_Area_CP (Table 6.5-6), which ranges from 1.0 to 22 $m^2\ g^{-1}$.

The water adsorption isotherm used for the in-package diffusion submodel is compared with another measured isotherm (McCafferty and Zettlemoyer 1971 [DIRS 154378], Figure 3) in Figure 7.2-1, which shows the close agreement between independent investigators. In addition, Figure 6.3-6 shows that hematite over-predicts the amount of water adsorbed compared to nickel oxide, which is one of the other major components of stainless steel (DTN: MO0003RIB00076.000 [DIRS 153044]) that would comprise the products of corrosion of the waste package internal components.

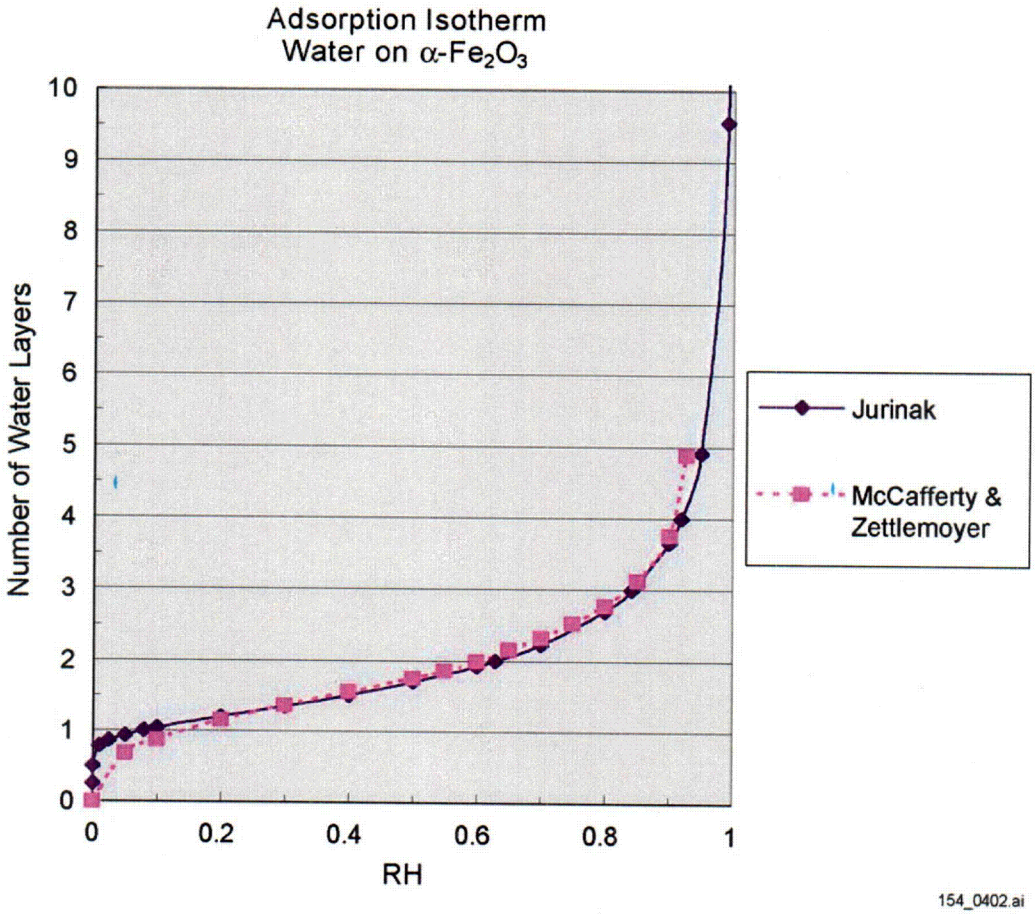

Source: Jurinak curve: Jurinak 1964 [DIRS 154381]; McCafferty and Zettlemoyer curve: McCafferty and Zettlemoyer 1971 [DIRS 154378].

Figure 7.2-1. Adsorption Isotherms for Water Vapor on α- Fe_2O_3

7.2.1.1 Comparison with Electric Power Research Institute 2000

Validation of the in-package diffusion submodel is provided in part by qualitative comparison with a similar model developed independently by a reputable performance assessment program (EPRI 2000 [DIRS 154149]).

The EPRI source-term model, COMPASS2000, implements five compartments–Waste, Corrosion Products, Canister, Invert, Near-Field Rock–of which two (Corrosion Products and Canister) are analogous to portions of the in-package diffusion submodel. The Corrosion

Products compartment represents the porous material that is formed after the basket materials are corroded. The Canister compartment represents the failed metal canisters. As with the GoldSim TSPA-LA model, each compartment is treated as a mixing cell in which radionuclide concentrations are assumed to be uniform. Mass balances in each compartment account for the various processes that comprise the model, including transport by diffusion and advection, radioactive decay and ingrowth, sorption, dissolution, and precipitation.

In the EPRI model, EBS transport parameters are assigned fixed values. Both the Corrosion Products and corroded Canister compartments have a porosity of 0.42 (EPRI 2000 [DIRS 154149], p. 6-21), less than the initial porosity of a CSNF waste package, 0.58, as estimated in Section 6.3.4.3.4. The EPRI value accounts for the volume occupied by the oxide. A lower value for porosity overestimates releases of radionuclides. However, in the in-package diffusion submodel (Equation 6.3.4.3.5-6), the higher value of porosity increases the estimated diffusion coefficient by only a factor of 1.5, which is small compared to other uncertainties in the model.

The EPRI model assumes a fixed water saturation of 0.35 in both the Corrosion Products and corroded Canister compartments (EPRI 2000 [DIRS 154149], p. 6-21). This value is appropriate for modeling cases involving advective transport, but overestimates releases of radionuclides for the expected large fraction of the repository that has no seepage flux, where the only water present is adsorbed water. The in-package diffusion submodel specifically applies to those regions and provides a more realistic estimate of saturation as a function of relative humidity.

The EPRI model uses a fixed value for effective diffusion coefficient of 4.645×10^{-4} $m^2\ yr^{-1}$ in both the Corrosion Products and corroded Canister compartments (EPRI 2000 [DIRS 154149], p. 6-22). This converts to 1.472×10^{-7} $cm^2\ s^{-1}$ or to 1.472×10^{-11} $m^2\ s^{-1}$. For diffusion through a fully degraded waste package (Equation 6.3.4.3.5-5), this corresponds to a relative humidity of 97.9 percent. Thus, when the humidity is high, the EPRI model and the in-package diffusion submodel agree well. In contrast, the in-package diffusion submodel provides humidity-dependent diffusion coefficient values.

The EPRI model also specifies fixed diffusive lengths, which are defined as the distance from the center of the compartment to the interface of the two contacting compartments. For the Corrosion Products compartment, the diffusion length is 0.046 m; for the Canister compartment, the diffusion length is 0.025 m (EPRI 2000 [DIRS 154149], p. 6-22). In a well-degraded waste package, these are reasonable values, comparable to those used in the in-package diffusion submodel. However, the in-package diffusion submodel accounts for the uncertainty in diffusion lengths at all times, and provides special treatment at early times when large masses of corrosion products are not yet formed.

For the conditions assumed in the EPRI model, namely, at later times when the waste package is extensively corroded, the in-package diffusion submodel agrees quite well with the EPRI model. The primary differences are that the in-package diffusion submodel accounts for a wider range of conditions, including times just after breaches first appear in the waste package. In addition, the in-package diffusion submodel accounts explicitly for the relative humidity, which realistically is the only source of water when seepage does not occur. And finally, in contrast to the EPRI model, the in-package diffusion submodel accounts for uncertainty in diffusive path lengths.

Thus, there is agreement between the models, and where differences occur, it is primarily to increase the realism of the diffusive release calculation and to account for uncertainty.

7.2.1.2 Comparison with Lee et al. 1996

Validation of the in-package diffusion submodel is provided in part by comparison with a similar model developed independently and published in technical literature (Lee et al. 1996 [DIRS 100913]).

Lee et al. (1996 [DIRS 100913]) developed a model for steady-state and "quasi-transient" diffusive releases from waste packages into the invert. In this model, perforations in the package are assumed to be cylindrical in shape. The diffusion path consists of the approach to the opening of the perforation from the waste form side; the path through the cylindrical portion of the perforation, which is filled with corrosion products; and the path through the exit disk separating the perforation from the invert. The waste is assumed to be distributed uniformly inside the waste container. The package is approximated by an equivalent spherical configuration, and the underlying invert is represented by a spherical shell surrounding the package.

The model of Lee et al. (1996 [DIRS 100913]) is suitable for the late stages of package degradation, when the waste form has become a mass of porous corrosion products. Although Lee et al. (1996 [DIRS 100913]) assumed the packages failed by localized corrosion, this model should be equally applicable to failure by general corrosion.

The assumption of Lee et al. (1996 [DIRS 100913]) that the waste (i.e., the radionuclide source) is uniformly distributed inside the waste package restricts the applicability of the model and comparison to the in-package diffusion submodel to the times when the waste package has extensively corroded. The object of the in-package diffusion submodel is to provide more realism at earlier and intermediate times, when the waste cannot yet be considered a uniform porous medium. (In the in-package diffusion submodel, the dependence of the diffusive properties of the waste package on the extent of degradation is computed explicitly as a function of time; see Sections 6.3.4.3.5 and 6.5.3.2.) On the other hand, the fundamental assumption that diffusive releases are controlled by diffusion through breaches that are filled with porous corrosion products may be valid over much of the waste package lifetime, including early times, when stress corrosion cracks are the first breaches to appear. Lee et al. (1996 [DIRS 100913], p. 5-67) assume that the porosity of the perforations is $\phi_{CP} = 0.4$, and the volumetric water content is $\Phi = 10$ percent (so the water saturation in the perforations is a constant $S_w = \Phi/(100\phi_{CP}) = 0.25$). Based on data by Conca and Wright (1990 [DIRS 101582]; 1992 [DIRS 100436]), Lee et al. compute a diffusion coefficient, D (cm^2 s^{-1}), for the porous corrosion products filling the perforations (Lee et al. 1996 [DIRS 100913], p. 5-67):

$$\log_{10} D = -8.255(\pm 0.0499) + 1.898(\pm 0.0464)\log_{10}\Phi, \qquad \text{(Eq. 7.2.1.2-1)}$$

where the numbers in parentheses are one standard deviation. From the discussion in Section 6.3.4.1.1, it is likely that this equation, being based on data by Conca and Wright (1990 [DIRS 101582]; 1992 [DIRS 100436]), should be written using $\log_{10}(\phi_{CP} S_w D)$ rather than

$\log_{10} D$; however, this model validation comparison will use the equation as given by Lee et al., since not enough information is available to repeat their analysis.

For $\Phi = 10$ percent (the assumed volumetric water content of the perforations), Equation 7.2.1.2-1 gives $D = 4.4 \times 10^{-7}$ cm^2 s^{-1}. Lee et al. assume that the diffusion coefficient inside the waste package (as opposed to the perforations) is 10^{-5} cm^2 s^{-1} (Lee et al. 1996 [DIRS 100913], p. 5-67). As a comparison, the self-diffusion coefficient for water is 2.299×10^{-5} cm^2 s^{-1} (Mills 1973 [DIRS 133392], Table III), and for many actinides the diffusion coefficient in water is roughly 5×10^{-6} cm^2 s^{-1} (Table 7.2-11). The value for D obtained from Equation 7.2.1.2-1 (4.4×10^{-7} cm^2 s^{-1}) accounts for porosity, saturation, and tortuosity, and thus is comparable to the values for D_s obtained from Equation 6.3.4.3.5-6. Table 6.3-10 tabulates values of $\phi S_w D_s$ using Equation 6.3.4.3.5-6. At appropriate ranges of conditions in Table 6.3-10 for a water content of 10 percent, D_s ranges from about 1.4×10^{-6} cm^2 s^{-1} to about 4.1×10^{-6} cm^2 s^{-1} (in Table 6.3-10, where, for the lower bound on specific surface area of $\bar{s}_{CP} = 1{,}000$ m^2 kg^{-1}, the closest entry for 10 percent water content, ϕS_w, is $\phi S_w D_s = 1.4 \times 10^{-7}$ cm^2 s^{-1}, at RH = 0.9999, and $S_{we} = 0.14$; for the upper bound on specific surface area of $\bar{s}_{CP} = 22{,}000$ m^2 kg^{-1}, at a water content of approximately 10 percent, $\phi S_w D_s = 4.1 \times 10^{-7}$ cm^2 s^{-1}, at RH = 0.95 and $S_{we} = 0.24$). This comparison indicates that the model developed by Lee et al. (1996 [DIRS 100913]) for D represents high relative humidity and reasonable specific surface area (i.e., within the sampled range specified for the *EBS RT Abstraction*) if adsorption is the sole mechanism for water appearing in the corrosion products.

A more detailed calculation can be performed to estimate the surface area of corrosion patches, the amount of water adsorbed at various relative humidity values, the resulting water saturation of the patches, and obtain a diffusion coefficient using Equation 6.3.4.3.5-6. Alternatively, the diffusion coefficient can be obtained using a modification of Equation 7.2.1.2-1, in which the water content, Φ (percent), is:

$$\Phi = 100 S_{we,CP} \phi_{CP} = 1.194(-\ln RH)^{-0.408}. \qquad \text{(Eq. 7.2.1.2-2)}$$

This equation uses a porosity of $\phi_{CP} = 0.4$, but obtains the effective water saturation from Equation 6.3.4.3.5-5, which is based on the assumption that all water comes from adsorption of water vapor onto hematite having a specific surface area of 9.1 m^2 g^{-1}. Then, substituting Equation 7.2.1.2-2 into Equation 7.2.1.2-1:

$$\begin{aligned} \log_{10} D &= -8.255 + 1.898 \log_{10} \Phi \\ &= -8.255 + 1.898[0.07707 - 0.408 \log_{10}(-\ln RH)] \qquad \text{(Eq. 7.2.1.2-3)} \\ &= -8.109 - 0.775 \log_{10}(-\ln RH). \end{aligned}$$

For example, at RH = 0.95, the effective diffusion coefficient for the patch using Archie's law (Equation 6.3.4.3.5-6) is $\phi S_w D_s = 7.03 \times 10^{-12}$ m^2 s^{-1} (for $\phi = 0.4$ and,

from Equation 6.3.4.3.5-5, $S_w = 0.100$), or $D_s = 1.75 \times 10^{-10}\ \mathrm{m^2\ s^{-1}}$, whereas using Equation 7.2.1.2-3, the diffusion coefficient for the corrosion patch is $D = 7.77 \times 10^{-12}\ \mathrm{m^2\ s^{-1}}$.

Thus, for those cases where the release rate is controlled by diffusion through porous corrosion products, the in-package diffusion submodel results in more rapid diffusive releases than the model of Lee et al. (1996 [DIRS 100913]).

If the value obtained by Lee et al. is actually $\log_{10}(\phi_{CP} S_w D)$ rather than $\log_{10} D$, then the two models agree well. For example, at a water content $\phi S_w = \Phi$ of 10 percent, Equation 7.2.1.2-1 would give $\phi S_w D = 4.4 \times 10^{-7}\ \mathrm{cm^2\ s^{-1}}$ or $D = 4.4 \times 10^{-6}\ \mathrm{cm^2\ s^{-1}}$, which compares well with the range of D_s from Table 6.3-10 of $1.4 \times 10^{-6}\ \mathrm{cm^2\ s^{-1}}$ to $4.1 \times 10^{-6}\ \mathrm{cm^2\ s^{-1}}$ at a water content of approximately 10 percent, as discussed earlier in this section.

The in-package diffusion submodel provides a means for quantifying the uncertainty in diffusion coefficients for diffusion of radionuclides from within the waste form to the invert. Whereas other models consider only the times when the waste package is largely degraded, the in-package diffusion submodel presented here also considers earlier times, starting from the time of the initial waste package breach. The time period between initial breach and complete degradation of the internal components may span many thousands of years. Thus, the in-package diffusion submodel fills a major time gap in modeling diffusive releases from a waste package. In effect, it provides a rationale for interpolating between essentially a zero diffusion coefficient (due to the absence of water) when a waste package is first breached to a value at a time when porous corrosion products can be expected to fill the waste package with a degree of water saturation capable of transporting radionuclides. The in-package diffusion submodel is considered validated based on corroborating data for input parameters such as water adsorption isotherms and specific surface areas, and based on the agreement with two other waste package diffusion models in areas where these models apply.

7.2.2 Invert Diffusion Submodel

Level I validation is appropriate for the invert diffusion submodel, as it is part of the mechanisms for radionuclide transport from waste package to the drift wall through the invert (see Section 7). In addition, the invert diffusion submodel has the following features:

- Diffusive release from the engineered barrier system does not result in significant releases from the repository system. Under expected conditions, there is a small probability of waste package breaching, and only limited release at all is likely. Therefore, the diffusion properties of the invert that might affect this release are expected to play a small role in the estimate of performance of the system under these conditions. The invert diffusion coefficient is also expected to play a small role for disruptive conditions under which more significant breaching of the waste package might occur. In this case, transport through the invert would be dominated by advection, and diffusion would therefore provide only a minor contribution. Therefore, the diffusion submodel is not expected to play a major role in the assessment of system performance.

- In addition to the above, the invert diffusion properties submodel is not extrapolated beyond the conditions and distances considered in the development of the model. The model applies only on the scale of the EBS and is not applied to larger scales, for example to the unsaturated zone rock.

The invert diffusion coefficient abstraction considers the free water diffusivity for radionuclides as an upper bound. The validation of each of these factors is considered in the following sections.

Section 6.3.4.1.2 describes modification of the self-diffusion coefficient due to temperature. The modification is based on established principles of diffusion in fluids and thus no validation is necessary. The temperature modification is based on the relationship between diffusion and viscosity and temperature (Cussler 1997 [DIRS 111468], p. 114). The relationship between temperature and viscosity of water is available in text books. Thus, it is straightforward to establish a direct relationship between diffusion coefficient and temperature.

7.2.2.1 Self-Diffusion Coefficient of Water

The self-diffusion coefficient of water at 25°C, 2.299×10^{-5} cm^2 s^{-1} (Mills 1973 [DIRS 133392], Table III), provides an upper bound for the diffusion of ionic and neutral inorganic, and organo-metal species that may be released from a waste package. This assertion is based on the following points, which are discussed in the text following this list:

1. A survey of compiled diffusion coefficients at 25°C shows that simple cation and anion species (excluding the proton and hydroxyl species, which are not appropriate analogs to diffusing radionuclide species) have diffusion coefficients that are smaller than that of water.

2. The self-diffusion coefficient for water at 90°C is larger than compiled diffusion coefficients for simple inorganic species at 100°C.

3. Diffusion coefficients for simple lanthanide and actinide cations are much smaller than the self-diffusion coefficient of water and are expected to be even smaller for their hydroxyl and carbonate complexes.

In a compilation of diffusion coefficients for 97 ionic species , only 3 species, H^+, OH^-, and OD^- have diffusion coefficients at 25°C that are larger than the self-diffusion of water at 25°C (Mills and Lobo 1989 [DIRS 138725], Appendix A, Tables 1.1 to 1.6, pages 314 to 319). Of the 33 ionic species for which Mills and Lobo list diffusion coefficients at 100°C in Tables 1.1 through Table 1.7, only 2 species, H^+ and OH^-, have diffusion coefficients larger than the self-diffusion of water ($H_2{}^{18}O$) at 90°C (Mills and Lobo 1989 [DIRS 138725]; Table 1, page 17). The fact that the self-diffusion of $H_2{}^{18}O$ is less than that of H_2O, and that the self-diffusion of H_2O at 90°C would be greater than that of various ionic species at 100°C, further supports the contention that the self-diffusion of water at 25°C is bounding.

Using the self-diffusion coefficient for water as a bounding value for all radionuclides partially compensates for not accounting for the effect of temperature on the diffusion coefficient in the corrosion product domain. See the discussion at the end of Section 6.3.4.3.5.

The compilation below (Table 7.2-1) lists a selection of diffusion coefficients for some trivalent lanthanides and actinides. Table 7.2-1 also includes some anions not listed in most compilations but relevant and/or analogous to those expected for radionuclides released from the waste package. The listing shows that the diffusion coefficients for these species are all smaller than the self-diffusion of water, by factors ranging from 1.6 to 14.7. In the case of uranium, the carbonate complexes of the metal species have even smaller diffusion coefficients. Based on the Stokes-Einstein equation (Bird et al. 1960 [DIRS 103524], p. 514, Equation 16.5-4), the diffusivity of a solute in a liquid is inversely proportional to the radius of the diffusing particles. It is therefore expected that other carbonate and hydroxyl complexes, on the basis of the greater size of the complexes relative to the metal species, will also have smaller diffusion coefficients than the metal species listed in Table 7.2-1.

As an alternative, four diffusion coefficients could be used. One coefficient could be used for each charge (mono-, di-, and tri-valent species) and one for the hydroxyl and carbonate complexes of the actinides and lanthanides. At 25°C, the mono-, di-, and trivalent species have bounding values of $2.2 \times 10^{-5}\,cm^2\,s^{-1}$, $1.2 \times 10^{-5}\,cm^2\,s^{-1}$, $0.7 \times 10^{-5}\,cm^2\,s^{-1}$, respectively, as shown in Figure 7.2-2. Although this alternative model is not used for TSPA-LA, it provides further evidence that the use of the self-diffusion coefficient of water bounds the diffusion coefficients of diffusing radionuclide species in the EBS.

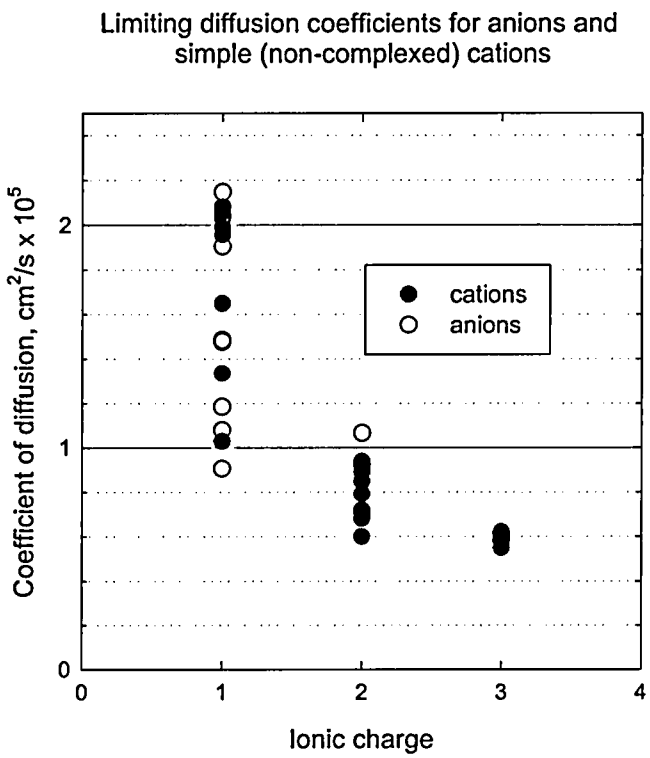

Source: Selected from Mills and Lobo 1989 [DIRS 138725], Appendix I, Tables 1.1 to 1.6; pp. 314 to 319.

Figure 7.2-2. Limiting Diffusion Coefficients for Anions and Simple (Non-Complexed) Cations

Table 7.2-1. Compilation of Diffusion Coefficients for Yttrium, Technetium, Molecular Iodine, and Lanthanide and Actinide Species

Species	D^*, $cm^2\ s^{-1}$	Comments	Reference
Y^{3+}	$5.7 \pm 0.06 \times 10^{-6}$	25°C	Mills and Lobo 1989 [DIRS 138725], p. 220.
TcO_4^-	$1.48 \pm 0.01 \times 10^{-5}$	25°C	Mills and Lobo 1989 [DIRS 138725], p. 105.
I_2	$1.36 \pm 0.04 \times 10^{-5}$	25°C; 0.075 M H_2SO_4	Cantrel et al. 1997 [DIRS 138551], Table 5.
La^{3+}	5.42×10^{-6}	25°C; 0.1 M $NaClO_4$; $u = 6.33\ cm^2\ s^{-1}\ V^{-1}$	Rosch and Khalkin 1990 [DIRS 138739], calculated from mobility data reported in Table 1, p. 103.[a]
La^{3+}	$6.18 \pm 0.06 \times 10^{-6}$	25°C	Mills and Lobo 1989 [DIRS 138725], p. 93.
Ce(III)-carbonate	$2.68 \pm 0.12 \times 10^{-6}$	5.5 M K_2CO_3, pH 13, presumably at 25°C.	Haltier et al. 1990 [DIRS 138643], p. 111.
Ce(IV)-carbonate	$1.56 \pm 0.07 \times 10^{-6}$	5.5 M K_2CO_3, pH 13, presumably at 25°C.	Haltier et al. 1990 [DIRS 138643], p. 111.
Eu^{3+}	4.38×10^{-6}	25°C; 0.1 M $NaClO_4$; $u = 5.12\ cm^2\ s^{-1}\ V^{-1}$	Rosch and Khalkin 1990 [DIRS 138739]; calculated from mobility data reported in Table 1, p. 103.[a]

Table 7.2-1. Compilation of Diffusion Coefficients for Yttrium, Technetium, Molecular Iodine, and Lanthanide and Actinide Species (Continued)

Species	D^*, $cm^2\ s^{-1}$	Comments	Reference
Gd^{3+}	5.24×10^{-6}	25°C; 0.1 M $NaClO_4$; $u = 6.12\ cm^2\ s^{-1}\ V^{-1}$	Rosch and Khalkin 1990 [DIRS 138739]; calculated from mobility data reported in Table 1, p. 103.[a]
Tb^{3+}	5.01×10^{-6}	25°C; 0.1 M $NaClO_4$; $u = 5.85\ cm^2\ s^{-1}\ V^{-1}$	Rosch and Khalkin 1990 [DIRS 138739]; calculated from mobility data reported in Table 1, p. 103.[a]
Tm^{3+}	5.10×10^{-6}	25°C; 0.1 M $NaClO_4$; $u = 5.96\ cm^2\ s^{-1}\ V^{-1}$	Rosch and Khalkin 1990 [DIRS 138739], calculated from mobility data reported in Table 1; p. 103.[a]
Yb^{3+}	5.23×10^{-6}	25°C; 0.1 M $NaClO_4$; $u = 6.11\ cm^2\ s^{-1}\ V^{-1}$	Rosch and Khalkin 1990 [DIRS 138739], calculated from mobility data reported in Table 1; p. 103.[a]
Lu^{3+}	5.01×10^{-6}	25°C; 0.1 M $NaClO_4$; $u = 5.85\ cm^2\ s^{-1}\ V^{-1}$	Rosch and Khalkin 1990 [DIRS 138739], calculated from mobility data reported in Table 1; p. 103.[a]
$UO_2(CO_3)_3^{4-}$	3.6×10^{-6}	1 M total carbonate, 22°C	Perry et al. 1988 [DIRS 138732], p. 302.
$UO_2(CO_3)_3^{4-}$	$3.0 \pm 0.7 \times 10^{-6}$	0.2 M total carbonate, pH 9.8, 25°C	Perry et al. 1988 [DIRS 138732], p. 302.
$UO_2(CO_3)_3^{5-}$	$3.81 \pm 0.26 \times 10^{-6}$	0.75 M Na_2CO_3, 0.6 M $NaClO_4$, pH 11.5, presumably at 25°C	Haltier et al. 1990 [DIRS 138643], p. 110.
UO_2^{++}	6.8×10^{-6}	25°C	Millard and Hedges 1996 [DIRS 138677], p. 2141.
UO_2-carbonate	1.9×10^{-6}	Calculated using Stokes-Einstein with a radius of 8 Å at 10°C	Millard and Hedges 1996 [DIRS 138677], p. 2141.
Np(V)-carbonate	7×10^{-6}	Calculated using Stokes-Einstein with a radius of 3.4 Å at 25°C	Tsukamoto et al. 1994 [DIRS 138747]; p. 469.
Am^{3+}	5.78×10^{-6}	25°C; 0.1 M $NaClO_4$; $u = 6.75\ cm^2\ s^{-1}\ V^{-1}$	Rosch and Khalkin 1990 [DIRS 138739]; calculated from mobility data reported in Table 1; p. 103.[a]
Am^{3+}	$5.95 \pm 0.06 \times 10^{-6}$	25°C, in 0.0002 M $Nd(ClO_4)_3$	Mills and Lobo 1989 [DIRS 138725]; p. 131.
Cf^{3+}	4.39×10^{-6}	25°C; 0.1 M $NaClO_4$; $u = 5.13\ cm^2\ s^{-1}\ V^{-1}$	Rosch and Khalkin 1990 [DIRS 138739]; calculated from mobility data reported in Table 1; p. 103.[a]
Cf^{3+}	$5.50 \pm 0.06 \times 10^{-6}$	25°C, in 0.0002 M $Nd(ClO_4)_3$	Mills and Lobo 1989 [DIRS 138725]; p. 132.
Es^{3+}	$5.50 \pm 0.06 \times 10^{-6}$	25°C, in 0.0002 M $Nd(ClO_4)_3$	Mills and Lobo 1989 [DIRS 138725]; p. 132.

[a] Calculation of diffusion coefficients from reported ionic mobilities (Rosch and Khalkin 1990 [DIRS 138739]; Table 1). The mobilities (u) were measured in 0.1 M NaClO4 at various pHs (below the pH of hydrolysis) and were slightly larger at pHs greater than 5, and these are the data that were used for the calculation. The equation used to calculate the diffusion coefficient is: $D^* = (kT/(|z|e))\ u$, where k is Boltzmann constant ($J\ K^{-1}$), T is the temperature (K), z is the valence of the ion, e is the elementary charge (C), and u is the mobility ($cm^2\ s^{-1}\ V^{-1}$) (Atkins 1990 [DIRS 111464], Box 25.1, Einstein relation, p. 765).

7.2.2.2 Modification for Porosity and Saturation

Validation of the dependence of invert diffusion coefficient on porosity and saturation is provided by comparison with measured data obtained independently of the data used for model development. Data used for validation are obtained from diffusivity measurements for crushed tuff using electrical conductivity measurements (CRWMS M&O 2000 [DIRS 156680]) and from direct measurements of diffusivity between machined cubes of tuff (Hu et al. 2001 [DIRS 161623]).

Conca and Wright (1992 [DIRS 100436]) and Conca et al. (1993 [DIRS 170709]) obtained diffusion coefficients from electrical conductivity measurements for various granular materials, including tuff, with volumetric moisture content ranging from 0.5 percent to 66.3 percent. A statistical fit of the data (Conca and Wright 1992 [DIRS 100436], Figure 2; Conca et al. 1993 [DIRS 170709], Figure 2; listed in Table 4.1-17) ranging from 1.5 percent to 66.3 percent volumetric moisture content, based on Archie's law, results in the model used in TSPA-LA (Section 6.3.4.1.1 and Appendix G):

$$\begin{aligned} \theta D_l &= D_0 \phi^{1.863} S_w^{1.863} 10^{ND(\mu=0.033,\sigma=0.218)} \\ &= D_0 \theta^{1.863} 10^{ND(\mu=0.033,\sigma=0.218)} \end{aligned} \qquad \text{(Eq. 7.2.2.2-1)}$$

where $\theta = \phi S_w$ is the volumetric moisture content (fraction: m^3 water m^{-3} rock), and ND represents a normal distribution with a mean, μ, of 0.033 and a standard deviation, σ, of 0.218. The object of this validation is to show that the diffusion coefficient given by Equation 7.2.2.2-1 obtained from the electrical conductivity measurements of Conca and Wright (1992 [DIRS 100436]) and Conca et al. (1993 [DIRS 170709]) tends to overestimate the diffusivity of invert materials.

The diffusion coefficient has also been determined specifically for tuff, also using electrical conductivity measurements (CRWMS M&O 2000 [DIRS 156680], Tables A-1 and A-2). These data are listed in Table 7.2-2 and are plotted in Figure 7.2-3, along with the mean value and plus and minus three standard deviations from Equation 7.2.2.2-1. This plot shows that the fit to the measured diffusion coefficient data (Equation 7.2.2.2-1) overestimates the diffusion coefficient relative to *The Determination of Diffusion Coefficient of Invert Materials* (CRWMS M&O 2000 [DIRS 156680], Tables A-1 and A-2). This plot was created using Microsoft Excel; see Appendix G, Worksheet: Validation, p. VII-10.

The electrical conductivity measurements by Conca and Wright (1992 [DIRS 100436]) and Conca et al. (1993 [DIRS 170709]) use conductivity as an analog for diffusivity. While the analog is known to be valid in fully saturated media, its application to unsaturated media, particularly at low moisture contents, is questionable due to the difficulty in preparing samples and in making reliable electrical contact between the electrical leads and the samples. To avoid these problems, Hu et al. (2001 [DIRS 161623]) measured diffusive tracer concentrations in tuff cubes directly using laser ablation coupled with inductively coupled plasma-mass spectrometry (LA-ICP-MS), rather than relying on electrical analogs.

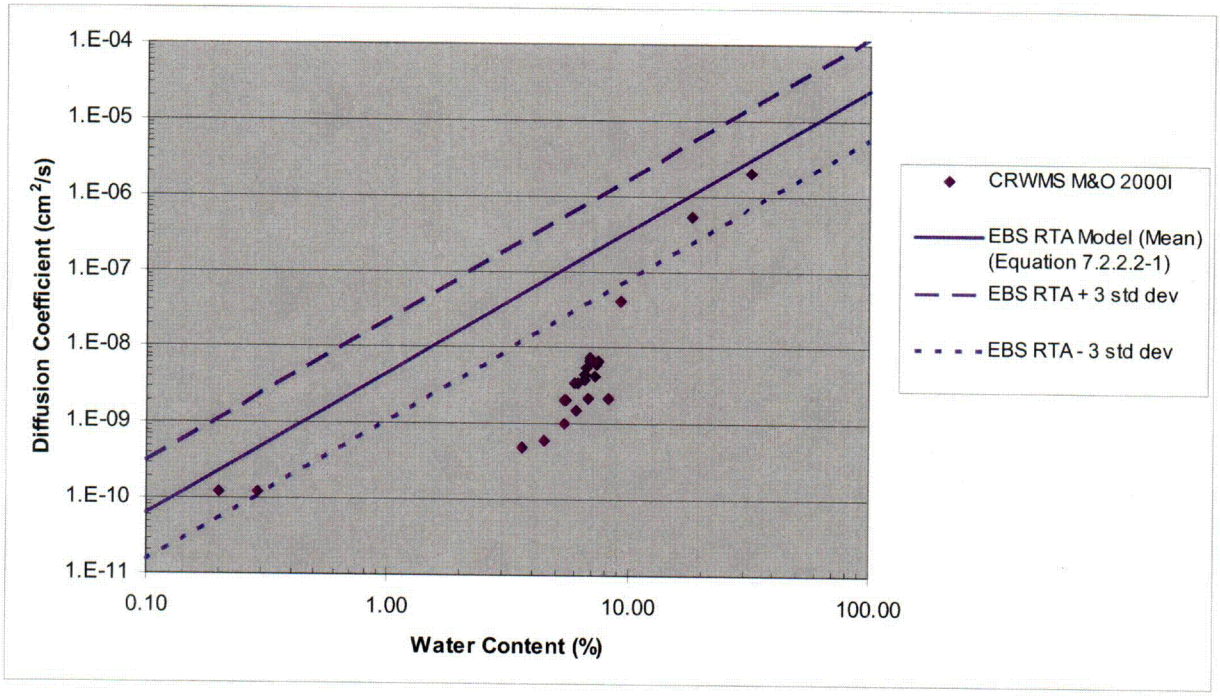

Source: CRWMS M&O 2000 [DIRS 156680].

Figure 7.2-3. Comparison of EBS Radionuclide Transport Abstraction Invert Diffusion Submodel (Equation 7.2.2.2-1) with Measured Diffusion Coefficients for Tuff

Table 7.2-2. Diffusion Coefficient of Crushed Tuff Invert Materials

Sample	Volumetric Moisture Content (%)	Diffusion Coefficient ($cm^2\ s^{-1}$)
1	32.13	2.02×10^{-6}
2	18.15	5.40×10^{-7}
3	9.26	4.05×10^{-8}
4	7.03	6.75×10^{-9}
5	6.97	7.45×10^{-9}
6	6.89	6.73×10^{-9}
7	6.75	5.42×10^{-9}
8	6.63	4.39×10^{-9}
9	6.63	3.76×10^{-9}
10	6.23	3.40×10^{-9}
11	6.00	3.43×10^{-9}
12	5.55	2.04×10^{-9}
13	5.46	2.04×10^{-9}
14	8.29	2.24×10^{-9}

Table 7.2-2. Diffusion Coefficient of Crushed Tuff Invert Materials (Continued)

Sample	Volumetric Moisture Content (%)	Diffusion Coefficient ($cm^2 s^{-1}$)
15	7.54	6.81×10^{-9}
16	7.36	6.21×10^{-9}
17	7.22	4.38×10^{-9}
18	6.84	2.19×10^{-9}
19	6.11	1.55×10^{-9}
20	5.41	9.97×10^{-10}
21	4.45	6.19×10^{-10}
22	3.64	5.00×10^{-10}
23	0.29	1.24×10^{-10}
24	0.20	1.25×10^{-10}

Source: CRWMS M&O 2000 [DIRS 156680], Tables A-1 and A-2.

LA-ICP-MS has recently evolved as a powerful analytical tool for solid samples (Russo et al. 2000 [DIRS 155697]). It can simultaneously determine a large number of chemical elements with low detection limits. Laser ablation uses an intense burst of energy delivered by a short laser pulse to vaporize a minute sample (in the range of nanograms) from a small area. Several spot sizes can be selected (from 25 μm to 200 μm in diameter), allowing a choice of appropriate spot size for different applications. A smaller spot size will sample less solid material, leading to lower analytical precision, but allowing more heterogeneity to be observed. A single laser pulse reveals surface compositions, while multiple pulses allows compositions to measured at various depths below the surface, with the crater depth proportional to the number of laser pulses applied. For example, two pulses reach about 4 μm into the tuff matrix (Hu et al. 2001 [DIRS 161623], p. 22), and 50 pulses ablates to a depth of about 35 μm (Hu et al. 2001 [DIRS 161623], Figure 6).

In the approach of Hu et al. (2001 [DIRS 161623]), a machined 1.5-cm tuff cube containing a tracer was placed in contact with a cube not containing the tracer, both under the same thermodynamic conditions. The tracer is allowed to diffuse from the tracer-containing cube to the other. Tracers were chosen based on their chemical similarity to radionuclides of interest. The source cube was vacuum-saturated with a tracer solution mixture of NaBr, $NaReO_4$, CsBr, and RbBr; both Br^- and perrhenate (ReO_4^-) act as nonsorbing tracers. The sink cube was also vacuum-saturated, but had no tracers. Source and sink cubes were separately placed inside a humidity chamber within an incubator maintained at 22°C until the cubes equilibrated to a constant weight (13 days). The cubes were then clamped together in the relative humidity (*RH*) chamber to start the diffusion test. After 87 days, the diffusion test was stopped by separating the source and sink cubes. The surface and depth distribution of the tracer was then mapped using LA-ICP-MS. The mapping was done on the interface, the far side face (opposite side from the interface), and along the side perpendicular to the interface.

Measurements along the outside surface of the sink cube indicated that a nonsorbing tracer (ReO_4^-) diffused along the surface at a rate similar to its aqueous diffusion rate in bulk water (Hu et al. 2001 [DIRS 161623], pp. 21 and 22). This result was reasonable because the tuff cubes were located in the high-RH chamber, with the likely presence on the outside of the cube

of a thick water film that behaves like bulk water. These measurements provided a bounding value for the diffusivity of the tracer, comparable to the diffusion coefficient of 1.48×10^{-5} cm^2 s^{-1} (Table 7.2-1) for its analog, TcO_4^-. In other words, in regions on the tuff samples that were saturated or at least had high water saturation, the direct diffusivity measurements agreed with theoretical predictions.

Hu et al. also measured tracer concentrations at greater depths into the cube by using the laser ablation technique to probe into the surface. They found that internal diffusion coefficients, at depths of 60-410 μm, were on the order of 10^{-12} cm^2 s^{-1} (Hu et al. 2001 [DIRS 161623], p. 22). The measured volumetric water content of the tuff matrix was 8.9 percent (Hu et al. 2001 [DIRS 161623], p. 25). The mean diffusion coefficient predicted by the invert diffusion properties submodel (Equation 7.2.2.2-1) would then be 2.6×10^{-7} cm^2 s^{-1}. This is a factor of 10^5 larger than the measurement. Thus, the diffusion coefficient throughout most of a grain of crushed tuff is lower than that predicted by the invert diffusion properties submodel. This provides corroborating evidence that the invert diffusion properties submodel overestimates releases of radionuclides from the EBS. These data also show that the overestimation of diffusivities in the invert diffusion properties submodel may be excessive. However, insufficient data exist to reduce the uncertainty in this model, and, if this additional uncertainty were included in the invert diffusion submodel, estimated releases of radionuclides from the EBS would be reduced and no longer be bounding. Because the model has a low impact on repository performance, the degree of uncertainty in this model is acceptable for TSPA-LA.

The study by Hu et al. (2001 [DIRS 161623]) was primarily a development of the technique for using LA-ICP-MS of microscale profiling of the distribution of diffusing tracers. However, in the process, some preliminary data were obtained that can be used to corroborate the electrical conductivity measurements of Conca and Wright (1992 [DIRS 100436]) and Conca et al. (1993 [DIRS 170709]).

Sections 7.2.1 and 7.2.2 have demonstrated that the component models of the EBS transport model meet Level II validation. Based on the validation results, the EBS transport model is adequate for its intended use.

7.2.3 Results of Independent Model Validation Technical Review of the EBS Flow and Transport Models

An independent model validation technical review of the EBS flow and transport models was conducted, as specified in the TWP (BSC 2005 [DIRS 173617], Section 2.2.3). This model validation approach is justified based on requirements of LP-SIII.10Q-BSC, Section 5.3.2c), where independent technical review is listed as an appropriate method for model validation. The results of the independent model validation technical review of the EBS flow and transport models are presented in a memo, a facsimile of which follows.

BECHTEL SAIC COMPANY, LLC

Interoffice Memorandum

QA: QA

To:	James D. Schreiber, Ernest Hardin	**No.:**	0801056250
From:	James A. Blink JAB	**Date:**	16 Aug 05
Re:	Independent Model Validation Review of ANL-WIS-PA-000001 Rev 2	**CC:**	W. J. Duffy, E. F. Loros, Roberta Stambaugh

This IOM was included in draft form in the 2.14 review of the subject AMR. It was finalized prior to final checking.

I have completed the independent model validation review of the "*Engineered Barrier System Radionuclide Transport Abstraction*" AMR, ANL-WIS-PA-000001 Rev 2.

This review was conducted in accordance with *"Technical Work Plan for: Near-Field Environment and Transport: Engineered Barrier System: Radionuclide Transport Abstraction Model Report Integration"*, TWP-MGR-PA-000020 Rev 1.

REVIEWER QUALIFICATIONS:

I have met the qualification requirements to do this review, as established by Section 2.2.4 of the cited TWP, as follows:

- "Reviewer shall not have contributed to the development of model assumptions, parameters, or implementing algorithms." I was not on the author team and have not had a management relationship with that team for the past three years.
- "Reviewer shall have an appropriate technical background (i.e., advanced degree in an appropriate technical field) and demonstrated expertise in fluid flow and transport of radionuclides in porous media." I have a B.S. in Engineering Science from the University of Nevada, Reno; an M.S. in Nuclear Engineering from the Georgia Institute of Technology, and a Ph.D. in Engineering from the University of California – Davis. In addition to a variety of courses in physics and engineering that are pertinent to this subject, my nuclear engineering coursework included formal training in neutron transport, which uses the same mathematical methods as this AMR. Further, I have over 33 years of engineering experience in the U.S. Army and at Lawrence Livermore National Laboratory. That experience includes over 15 years of experience on the Yucca Mountain Project in a variety of technical areas, including the Engineered Barrier System and Design Basis

0801056250
Page 2

Models. My education and experience are included in records submitted to the Record Information System by Lawrence Livermore National Laboratory.

REVIEW REQUIREMENTS:

The TWP requires me, as the independent model validation technical reviewer, to do the following:

- "Review the validation criteria in this TWP." I have reviewed those criteria, which are listed below.
- "Review relevant sections of the RTA report and meet with the document author and representatives from TSPA organization in order to obtain a full understanding of the model(s) and TSPA implementation." I have read the entire report in detail, with the exception of the spreadsheet details listed in Appendices A, C, D, E, F, and G. I have had a number of discussions with the author (J. Schreiber) and the TSPA Analyst (S. Mehta). The author was also an appropriate TSPA-implementation point of contact for this AMR because the implementation was controlled using one or more Parameter Entry Forms accepted by the author, the TSPA implementing analyst and the TSPA Inputs Manager.
- "Assess whether or not the model(s) as documented in the RTA report meet the validation criteria." My assessment is documented below in this memorandum.
- "Assess whether or not the model(s) are adequate for their intended use, meet with the author to resolve comments, and recommend actions, as appropriate, to resolve any inadequacies found as part of the review." My assessment is documented below in this memorandum.
- "Document this review process as a memo to be included in the records package for the RTA report." My review is documented in this memorandum.

REVIEW CRITERIA:

The TWP specifies the following validation criteria for the EBS Flow Model and the EBS Transport Model: "Criteria ... are as follows. Each shall be confirmed by the independent model validation technical reviewer."

- "The approach and algorithms described in the document and provided to TSPA capture all known flow pathways into and from the EBS components." [Flow Model]
- "The approach and algorithms described in the document and provided to TSPA address all known modes of radionuclide transport within and from the EBS components." [Transport Model]
- "Modeling assumptions are clearly defined, discussed, and justified as appropriate for the intended use of the model." [Both models]

0801056250
Page 3

- "Uncertainties in parameters, processes, and assumptions are sufficiently described, and impacts of these uncertainties discussed." [Both models]
- "The overall technical credibility of the approach, including assumptions, parameters, equations, and the TSPA implementation, are sufficient for the model's intended use." [Both models]

The TWP also includes a separate criterion for the EBS-UZ Interface Model, which was reviewed by another reviewer in Revision 01 of the AMR. I have read the memorandum of that review which was included in the draft of Revision 02, and concur with it. In addition, my review of the Flow Model includes its lower boundary condition, which is described as the EBS-UZ Interface Model in the AMR and TWP.

CONCEPTUAL MODEL:

Based on the discussion below, I conclude that the conceptual models for EBS Flow, EBS Transport, and the EBS-UZ Interface are technically credible, are appropriate for their intended TSPA use, and that they capture the known flow pathways and transport modes.

Sections 6.1.2 and 6.7.1 state that this AMR applies only to the nominal scenario class, and it cites igneous and seismic AMRs to be used for the igneous and seismic scenario classes. It then discusses how those AMRs calculate EBS Flow and Transport, as follows: The igneous eruption modeling case results in waste being moved by the event to the mountain surface, making the EBS flow and transport models non-relevant. The igneous intrusion modeling case destroys the drip shield and waste packages in the affected repository area and makes the radionuclides available for transport into the UZ as calculated by the cited Dike/Drift Interactions AMR. The (low-probability) seismic scenario class also has two modeling cases: mechanical damage failure of waste packages and later failure of waste packages due to corrosion (primarily stress corrosion cracking due to seismically-induced stresses). Section 6.1.2 cites the Seismic Consequence Abstraction AMR and the Characterize Framework for Seismicity and Structural Deformation at Yucca Mountain, Nevada AMRs for these modeling cases. Section 6.5.3.1.1.2 discusses the WP breach area and its influence on the flow model for each scenario class and modeling case:

- Nominal scenario class with no early failures modeling case: The breach area comes from the cited WAPDEG Analysis of Waste Package and Drip Shield Degradation AMR. However, Section 7.1.1 notes that no waste packages fail due to general corrosion within 10,000 years. Beyond 10,000 yr, if the TSPA-LA model were to be extended, the drip shield general corrosion is modeled as a single patch, and the EBS Flow model would then become dripping from the drift crown onto the waste package crown
- Nominal scenario class early failure modeling case: The entire waste package surface area is breached (WAPDEG Analysis of Waste Package and Drip Shield Degradation AMR),

and conservatively unfolds onto the invert for diffusive transport calculation purposes. However, Section 7.1.1 notes that no drip shields fail within 10,000 years and hence the waste package breach area receives no seepage flux that can drive advection.

- Igneous intrusion modeling case: The entire waste package area is breached and there is no cladding protection. Transport begins at the top of the invert.
- Seismic ground motion modeling case: The cited Seismic Consequence Abstraction AMR calculates the breach area, and transport is sequentially through the waste package plan area (diameter times length) and then the breached area of the outer shell.
- Seismic localized corrosion modeling case: The breach area is calculated by the cited AMR (General Corrosion and Localized Corrosion of Waste Package Outer Barrier). The drip shield also is breached by stress corrosion cracking. However, the drip shield cracks are too small to support advective flux and no seepage is received by the waste package breaches.

The conceptual models for EBS Flow, EBS Transport, and the EBS/UZ Interface are discussed in Sections 1, 6.3, 6.5, and 7, and Appendix B. Section 8.1 (in the Conclusions chapter) provides a succinct summary of the conceptual models. These models are briefly summarized below, including notation of conservatism used to simplify the models.

The Flow Model is based on conservation of mass for the TSPA nominal scenario class. Three potential sources of moisture to the EBS (which is defined by the perimeter of the excavated emplacement drifts) were identified (seepage, condensation, and flow from the rock to the invert). One significant sink for water leaving the emplacement drifts was identified (flow into the UZ). The minor sink by evaporation and movement of vapor from the EBS into the rock or longitudinally into the mains was conservatively neglected.

Within the EBS, the movement of water is calculated along potential pathways. The analysis included diversion by the drip shield and flow through breaches in the drip shield. Condensation under the drip shield was excluded as a FEP in the EBS FEP AMR. Water moving through the breaches in the drip shield could be diverted by the waste package or enter the waste package through breaches. The invert receives water from these three sources (drip shield diversion, waste package diversion, and flow through waste package), as well as receiving water from the UZ.

Conservatism is used in the EBS Flow model as follows:

- All seepage (and in-drift condensation) is assumed to be from the crown (with the largest probability of reaching breaches). Dripping outboard of the drip shield and film flow down the drift wall are conservatively ignored (their flux is part of the conservatively consolidated crown seepage).
- All flow through the drip shield breaches is assumed to drip on the waste package crown. Dripping outboard of the waste package and film flow down the underside of the drip

shield are conservatively ignored (their flux is part of the conservatively consolidated dripping on the waste package crown).

- All flow into the waste package is assumed to contact the waste form and then move through the corrosion products to an exit breach from the waste package
- No seepage liquid evaporates after it enters the drift
- The exit breach from the waste package is assumed to be in direct contact with the invert
- Flow through the invert is assumed to be through the tuff ballast, with the oxidized steel components not being contacted; this reduces the sorption in the invert

The neglect of condensation on the underside of the drip shield is non-conservative, but the AMR states in Sections 6.3.3.2, 6.3.3.3 and 6.7.1 that a cited FEP AMR justifies its neglect based on low consequence.

The EBS Transport conceptual model includes all the significant processes that contribute either positively or negatively to radionuclide transport. These are advective transport in solution, diffusive transport in solution, reversible and irreversible sorption on immobile solids, reversible and irreversible sorption on colloids, and both advective and diffusive movement of colloids. The implemented numerical model conservatively neglects reversible sorption on immobile solids.

Conservatism is used in the EBS Transport model as follows:

- Lateral and longitudinal dispersion are neglected (Section 6.3.1.2) which results in somewhat more focused transport than the real situation. However, the effect is justified as being small because the EBS is such a small part of the overall transport path.
- Advective flux into the UZ just below the invert is the greater of the steady state UZ flux and F_8. At locations with flow focusing, the (higher) focused flow will be used for transport calculation, and at locations with flow defocusing, the steady state (no flow defocusing) value will be used. The overall result is more flow from the EBS into the UZ than enters the EBS from the UZ, which will conservatively increase radionuclide release from the EBS.
- Reversible sorption of radionuclides onto stationary corrosion products is neglected (Sections 1, 6.3.4.2.3, 6.5.1.2, and Appendix B).
- Physical filtering and gravitational settling of colloids during transport is neglected (Section 6.5.1.2).
- For waste packages with early failures, the diffusion cross sectional area between the corrosion products domain and the invert domain is the entire waste package surface area.
- No sorption on oxidized iron components of the invert is calculated.
- A continuous path of water film is assumed within the waste package and invert when the temperature is below 100°C, allowing diffusion from shortly after the waste package breaches.
- Reduction in diffusion effectiveness due to discontinuous intergranular films at low humidity in the invert is not included in the model.

0801056250
Page 6

The EBS/UZ Interface model has two key features. The first is that the location of zero-concentration sink is significantly (about three drift diameters) below the bottom of the invert and extends laterally one drift diameter on each side (the domain of the interface model is three drift diameters wide and about three high). Second, the invert is a single (equivalent) continuum that couples to the dual fracture-matrix continuum of the UZ. Diffusion from the invert independently enters both UZ continua below the drift and can also diffuse, in the UZ, both between continua and laterally. Advective flux in the invert has two distinct sources, seepage from above (including the flux which transits a breached waste package) and percolation from the drift wall. The percolation flux into the invert exits the invert into the UZ matrix, and the seepage flux into the invert exits the invert into the UZ fractures.

The EBS/UZ Interface model uses the same properties as the UZ transport model and results in a radionuclide flux into the UZ at the bottom of the invert. That flux is the time-dependent boundary condition for the UZ transport model.

The EBS/UZ Interface model conservatively ignores the drift shadow effect, in which advective fluxes below the drift are expected to be less than those in the pillars between the drifts.

NUMERICAL MODEL:

Based on the discussion below, I conclude that the numerical implementation of the conceptual models for EBS Flow, EBS Transport, and the EBS-UZ Interface are technically credible, are appropriate for their intended TSPA use, and that they capture the known flow pathways and transport modes.

The conceptual models for EBS Flow, EBS Transport, and the EBS/UZ Interface are implemented in numerical models. Because these models will be run as part of the TSPA-LA runs (using TSPA software), the EBS Radionuclide Transport Abstraction AMRs develops the equations and the input parameters for those equations, and provides them to TSPA. The numerical implementation to be used by TSPA is discussed in Sections 6.5.1 and 6.5.3.

The development of the equations of flow through breaches in the waste package and drip shield in Section 6.5.1.1 is rigorous and clear. The development of the transport equations in Section 6.5.1.2 is extremely thorough and easy to follow. The derivation is supplemented by additional equation development in Appendix B, to produce models that were used to verify the accuracy of the base case derivation; readers seeking additional explanation of the development in Section 6.5.1.2 can find that information in Appendix B. Section 6.5.3 is a step-by-step prescription for implanting the numerical model in TSPA. Equation B-72 is also directly used by TSPA, using input parameters from controlled sources or calculated within the TSPA model.

0801056250
Page 7

Dimensional units are provided throughout the AMR for each symbol in each equation, and Section 6.5.1.3 is a comprehensive listing of the symbols used throughout the report. The authors did an excellent job of remaining consistent in their choice of symbols, and they avoided reader confusion by not reusing symbols to represent different quantities in different sections of the AMR.

Section 8.2 (in the Conclusions chapter) includes a succinct summary of the equations to be implemented in TSPA.

PARAMETERS USED IN NUMERICAL MODEL:

Based on the discussion below, I conclude that the numerical parameters developed for the numerical models for EBS Flow, EBS Transport, and the EBS-UZ Interface are technically credible and are appropriate for their intended TSPA use.

Section 6.5.2 provides an overview of the parameters to be used in the models, and the parameters are listed in Section 8.2 (in the Conclusions chapter).

The EBS Flow model parameters are based on experimental data that are analyzed in the AMR (Sections 6.5.1.1.2 and 7.1.1, and Appendices C, D, and E). The diffusion coefficient data are developed in Sections 6.3.4.1, 6.3.4.3, 6.5.2.1, and 6.5.2.4, and in Appendices G and H. The sorption parameters for the EBS Transport model are discussed in Sections 6.3.4.2, 6.5.2.3, and 6.5.3.2, through 6.5.3.4, and Appendix J.

The carbon steel corrosion rates used in developing the characteristics of the corrosion products domain are taken from 1 yr data, and are applied as if the corrosion of the stainless steel inner vessel or the waste package internal components is from one side only. Carbon steel corrosion rates are known to decrease until an equilibrium oxide thickness is reached (signifying a nominal equilibrium between periodic flaking of oxide and additional oxide layer formation at the interface with the base metal. The equilibrium oxide thickness depends on a number of difficult-to-quantify parameters, including the stress state of the component and the frequency and intensity of seismic events. It is possible that the overall average corrosion rate for the time to completely corrode the carbon steel components is lower than that used in this AMR. The influence of a lower corrosion rate is the following:

- For failed cladding, the early release of iodine and technetium will be prior to significant carbon steel corrosion for both the AMR's corrosion rate or a lower corrosion rate. There will be a low amount of corroded surface area and hence a low volume of adsorbed water (which may or may not be sufficient to form a thin continuous film and thus may or may not lead to diffusion). There will then be a high concentration of the radionuclide source and rapid diffusion of these radionuclides (assuming the concentration gradient factor is

more important than other diffusion factors, and that there is a continuous water film pathway for diffusion).

- For intact cladding, the failure time of the cladding will likely be much later than the corrosion time of the carbon steel, and there will be little effect on diffusion of fast-release of iodine and technetium.
- For failed cladding, the release of plutonium and americium will be slow because of the slow dissolution rate of the SNF matrix. The carbon steel corrosion rate will almost certainly be faster than the SNF matrix dissolution rate. Prior to full corrosion of the carbon steel, there are competing effects of different corrosion rates. Slower corrosion of the carbon steel leads to less surface area, less water volume, higher source concentrations, and faster diffusion (assuming the concentration factor is more important than other diffusion factors), just as for iodine and technetium. Slower corrosion of the carbon steel also leads to less irreversible sorption of the plutonium and americium, which results in less colloidal transport but also less removal onto the fixed corrosion products. Eventually, the carbon steel corrosion will be complete, and the remainder of the plutonium and americium releases will be unaffected by the prior corrosion rates.
- For TSPA, the effect will not be noticeable with respect to meeting the regulatory dose limits because of the small fraction of failed cladding and the small number of waste packages that fail during the 10,000-year TSPA calculation.

Transport requires a number of parameters in the following areas:

- The saturation in all three domains is 100%, except for the CSNF Corrosion Product (CP) domain in regions of no seepage. The saturation is calculated from relative humidity for that situation, and the humidity is an input from another AMR.
- Release of radionuclides from the waste form into the aqueous phase is calculated based on input from other AMRs, including solubility and WF degradation rate. The concentration of the radionuclides in the Waste Form (WF) domain is based on the amount of water in that domain, which is calculated from on the CSNF rind volume and porosity, HLW rind volume and porosity, and 1 m^3 of DSNF volume with porosity of 20% (all from other AMRs).
- WF colloids are generated in the WF domain, based on another AMR, and include embedded radionuclides.
- The water content of the CP domain is calculated as a function of time based on the corrosion of the iron-based materials (see above) and the resulting surface area (uniform distribution of 1.0 – 22 m^2/g to account for uncertainty).
- FeOx colloids are generated in the CP domain based on another AMR. Groundwater colloids enter the transport model at the CP domain.
- Dissolved radionuclides advect from the WF domain to the CP domain based on aqueous concentration and on flow rate. For CDSP waste packages, the advection is sequentially from the HLW WF subdomain to the DSNF WF subdomain, and then to the CP domain. For CSNF waste packages, the advection is from the WF domain to the CP domain

0801056250
Page 9

Dissolved radionuclides diffuse through the same pathways, based on concentrations, diffusion coefficients, path lengths, and diffusion areas. These parameters are provided in Section 8 of the AMR, with some being single valued and others being distributions.

- In the CP domain, radionuclides can irreversibly sorb onto stationary FeOx, can irreversibly and reversibly sorb onto FeOX and waste form colloids, and can reversibly sorb onto groundwater colloids. The reversible Kd values are taken from another AMR's DTN and are listed in Table 6.3-11, with smectite being representative of both waste form and groundwater colloids. Table 6.3-11 includes 100x reductions in the Kds for Pu and Am on FeOx to be compatible with the mechanistic sorption model in another AMR. The irreversible reaction rates are a range taken from another AMR's DTN for locations without seepage. In seepage locations, the flux-out ratio is sampled from 90 to 99% based on another AMR, and the irreversible reaction rate is calculated from an expression derived in this AMR, using parameters available in TSPA from this AMR or other AMRs. Eq. B-72 in this AMR defines the parameters; those from this AMR are listed in Section 8.
- FeOx, WF, and groundwater colloids advect and diffuse from the CP domain to the Invert domain, with the colloid diffusion coefficient being 100x smaller than the aqueous diffusion coefficient.
- Dissolved radionuclides and WF and FeOx colloids advect and diffuse from the CP domain to the invert domain, with no credit taken for path length between the edge of the waste package breach and the top of the invert. Diffusion out of the corrosion products uses a sampled path length between the outer barrier thickness and the waste package radius, with the diffusion area depending on the scenario class and modeling case, as described under "conceptual model" above. The aqueous diffusion coefficient in the Invert domain is calculated (based on experimental data) from the water content and temperature (both obtained from another AMR), and includes a normal distribution for uncertainty that is truncated at ± 3 standard deviations.
- The Invert domain is modeled as a rectangular cross section that is 1 WP long. The cross section width is the same as the actual invert top surface, and the depth is that which preserves the overall volume of the invert. The small (10 cm) axial gap between waste packages does not contribute radionuclide transport in the invert, for this model.
- The invert is modeled as a single continuum with a thin interface zone at its lower surface. The interface zone is the starting point for diffusion and advection into the two continua of the UZ, which is assumed to be at zero concentration about three drift diameters below the invert.
- The near field of the UZ is modeled as three columns of cells, with each column being one drift diameter wide. (The middle column is as wide as the drift diameter, rather than the rectangular width of the invert domain, to facilitate linkage to the domain for the seepage flux.) Advective transport of the seepage plus condensation flux (F_6) in the invert moves into the fracture continuum of the middle column. Advective transport of the water that directly enters the invert from the UZ (F_7) moves into the matrix continuum of the middle column. Diffusive transport from the invert interface zone moves radionuclides and

colloids into both continua of the middle column. Within the three columns of four zones in the EBS/UZ boundary model domain, advection is calculated vertically in both continua, and diffusion is calculated between adjacent vertical and horizontal matrix zones and between matrix and fracture continua in each zone. All three columns of zones (in both continua) end in a single zero-concentration collector cell.

- The TSPA model calculates the transport through the coupled WF, CP, Invert, and UZ boundary domains to the collector cell in a self-consistent manner, using the parameters from this AMR and other AMRs. The resulting time-dependent radionuclide fluxes into the UZ from the invert interface zone are the starting point for the UZ transport model.

ALTERNATIVE CONCEPTUAL AND NUMERICAL MODELS:

The AMR includes a number of alternative conceptual models, for the purpose of evaluating whether the base model is adequate for TSPA. These models are well described and justify use of the base model in the TSPA.

The alternative models include the following:

- Treatment of the water flow through the waste package as a bathtub conceptual model rather than a steady state flow model. Variations of this alternative model include changing the inflow rate, changing the inflow chemistry, and changing the corrosion patch geometry (formation of a draining patch after the waste package "bathtub" fills).
- Limiting water vapor and oxygen diffusion rates into the waste package. These scoping calculations uses an atmospheric pressure at sea level; however, this inaccuracy does not affect the conclusion of the alternative model.
- Treating the invert as a dual continuum with intragranular and intergranular porosities.
- Single and dual continuum invert diffusion coefficients. The single continuum alternative diffusion coefficient was modeled as decreasing more rapidly than the base case as saturation decreases, at the dry end of the saturation spectrum.
- Reversible sorption onto corrosion products within the waste package.
- Slow desorption of irreversibly sorbed radionuclides.

MODEL VALIDATION AND MODEL TESTING RESULTS IN THE AMR:

Based on the discussion below, I conclude that the model validation activities and model testing of the numerical models for EBS Flow, EBS Transport, and the EBS-UZ Interface are technically credible and support the use of these models in TSPA. All of the comparisons with alternative data sources and models described below had reasonable results.

0801056250
Page 11

Flow Through Breaches in the WP and DS:

For the EBS Flow model, four series of tests were performed on a full-scale mock-up of one side of a drip shield. Two of the series of tests were configured to represent dripping from the drift crown onto the drip shield crown, and the other two tests were configured to represent dripping from the drip shield [or drift wall] onto the waste package crown. For each pair of test series, the initial tests were done with smooth mock-up surfaces, and the data were used to predict the splitting of flow between the outside of the drip shield and through the breaches. Then, the tests were repeated with a rough mock-up surface, and the results were compared to the smooth surface results as a means of model validation. The fraction of water through the breaches is expressed as a fraction of half the dripping water, since there is equal probability of dripping down either side of the crown of a full drip shield or waste package. Therefore, the results can conceivably range between 0 and 200%. The test results (rounded to integers for values >1%) were the following:

- Smooth drip shield test: Range 1% to 28%, Mean 11%, Median 5%
- Rough drip shield test: Range 0% to 117%, Mean 11%, Median 0.5%
- Smooth WP test: Range 0% to 107%, Mean 30%, Median 1%
- Rough WP test: Range 0.01% to 62%, Mean 12%, Median 0.3%

The values in these results were compared to a geometric prediction and to develop a multiplier range on that prediction (including the incorporation of uncertainty into the multiplier range). The actual values of the test results shown above are dependent on the selected combinations of drip and breach locations; however, the similarity and differences of the smooth and rough surface results are a combination of validation (repeatability), adequate statistics, and physical differences due to the surface texture itself. The experimental results are difficult to use to directly predict the splitting of flow because the initial drip splashing results in a distributed source of rivulets, because the flow is in rivulets with a variety of angles from the most downward, and because the experiment ends with a portion of the drip still on the surface as small mini-droplets which have neither run-off nor gone through breaches.

The model for the fraction entering breaches is a uniform distribution from zero to the computed maximum (but limited to no more than 100% of the total, both sides, source). The computed maximum is based on three multiplicative factors. The first factor is the geometric area fraction of the breach(es) length divided by the actual component length. The second factor, which normalizes the measured data, is based on three measured ranges for the smooth surface data for the component (drip shield or waste package). These three measured ranges are reduced to single values that result in a maximum multiplicative factor. The mean of the experimental breach fraction results (the first measured range) is used since it is larger than the median (it has a theoretical maximum of 200% of the single side source). The *minimum* of the measured rivulet spread angle (the second measured range) is used as it appears in the denominator of the multiplicative factor. The diameter of the inner cluster of splash mini-droplets is the third

measured range; the maximum was used and was the source of the "effective component (DS or WP) length". The final factor in the calculation depends on the rivulet-spread angle, and it is independently maximized by using the *maximum* of the measured angle, even though the minimum of that angle was used in the second factor. The inconsistency in selection of the measured angle adds conservatism to the results as the maximizing end of the range is different in the second and third factors.

The net result passed to TSPA is the following:

- For the drip shield, breach flow is sampled between 0 and 85% of the source multiplied by one-half of the geometric fraction of the breach length divided by the drip shield segment length (the one-half factor accounts for only half the source flow going toward the breach side of the drip shield).
- For the waste package, breach flow is sampled between 0 and 241% of the source multiplied by the one-half of the geometric fraction of the breach length.
- In both cases, any sampled breach flow larger than the source is reduced to 100% of the source.

The drip shield multiplier maximum is somewhat less than the nominal expected maximum of 100%, reflecting the combination of the experimental issues (such as remaining liquid on the surface) and the choice of maximizing measured factors in the development of the multiplier. The waste package multiplier maximum is greater than 100%, reflecting the dominance of the conservatisms in the data reduction and the lesser effect of the remaining liquid issue when some of the drips are onto the sloping side surfaces.

The analysis of the rough surface (validation) experimental data resulted in maximum multipliers of 77% for the drip shield and 30% for the waste package. The drip shield breach flow model results are similar for the two surface textures, but the waste package breach flow results are much lower for the rough surface used in the validation tests. Since the TSPA model will use the larger values in both the DS and WP cases, the data selection for the TSPA is conservative (larger breach flow leads to more radionuclide transport).

Transport Model:

The EBS/UZ boundary condition involves bifurcation from a single continuum into a dual continuum. Two approaches were developed for this situation. The first is rigorous but difficult to implement efficiently. The second uses a thin interface layer at the base of the single continuum and is computationally efficient. Section 6.6.4.4 presents a test of the two methods for a simplified situation. Figures 6.6-4 and 6.6-5 present the results, which show that the two methods are in close agreement and that the GoldSim software implementation of the interface-layer method in TSPA matches a spreadsheet implementation of the same method. In addition, an alternative

model from the Drift-Scale Radionuclide Transport AMR (the fracture-matrix partitioning model) was compared to the results from this AMR.

For in-package diffusion, Section 7.2.1 compares the results with two published alternative models, including one developed by the Electric Power Research Institute. Section 7.2.2 compares the electrical analog tuff diffusion experimental results to results from direct measurements of diffusivity between machined cubes of tuff.

Finally, in Appendices B and F, the differential equations from the base case model were converted into a finite difference model and implemented in a spreadsheet program (with some simplifications compared to the base case model). The resulting model was exercised using reasonable input parameter values, and the results were analyzed in terms of the fraction of the release carried by irreversible sorption on colloids, and also of the temporal behavior of the modeled system.

CONCLUSION:

Based on the information above, I conclude that

- The approach and algorithms described in the document and provided to TSPA capture all known flow pathways into and from the EBS components.
- The approach and algorithms described in the document and provided to TSPA address all known modes of radionuclide transport within and from the EBS components.
- Modeling assumptions are clearly defined, discussed, and justified as appropriate for the intended use of the three models. Major assumptions are documented in Section 5 of the AMR, and the text discusses other assumptions as they occur.
- Uncertainties in parameters, processes, and assumptions are sufficiently described, and impacts of these uncertainties discussed. The organization of Section 8 of the AMR into single-value parameters and sampled parameters makes the treatment of uncertainty easy to follow.
- The overall technical credibility of the approach, including assumptions, parameters, equations, and the TSPA implementation, are sufficient for the model's intended use.

7.3 EBS-UZ INTERFACE MODEL

The output of the invert domain feeds into the unsaturated zone through the EBS-UZ interface model. In the *EBS RT Abstraction*, the invert is modeled as a single-continuum porous medium whereas the adjacent UZ is modeled as a dual continuum fracture-matrix medium. The model is described in detail in Section 6.5.3.6.

The mass flux from the invert flows into the top layer of the middle zone in the UZ. The portion of the advective flux from the invert that is attributable to the seepage flux (F_1) flows into the UZ fractures. The imbibition flux into the invert (F_7) flows out of the invert into the UZ matrix. The diffusive flux from the invert can go into both UZ continua based on the concentration gradient and effective diffusion coefficient. The diffusive area remains the same because they are overlapping continua. The advective flux flowing through the UZ fracture cells in the middle zone is given by the greater of the advective flux out of the invert and the steady state UZ fracture flux. The advective flux in the two outer zones is given by the steady state UZ flow in each continuum at the repository horizon; the drift shadow effects are ignored.

For TSPA-LA, a semi-infinite zero concentration boundary condition is used for the EBS-UZ interface. This is approximated by applying an effective zero-concentration boundary at approximately three drift diameters below the invert-UZ boundary into the UZ. By moving the zero concentration boundary some distance below the invert, a more realistic diffusive gradient through the invert is achieved.

The EBS-UZ interface model of the *EBS RT Abstraction* provides input to the unsaturated zone radionuclide transport model in *Particle Tracking Model and Abstraction of Transport Processes* (BSC 2004 [DIRS 170041]). The appropriate level of confidence identified for unsaturated zone radionuclide transport is Level II. Therefore, Level II also represents appropriate level of confidence for the EBS-UZ interface model of the *EBS RT Abstraction.*

Section 7.3.1.1 describes the semi-analytical fracture-matrix partitioning model that is used to validate the EBS-UZ interface model of the *EBS RT Abstraction.* Section 7.3.1.2 compares the two interface models, and Section 7.3.1.3 provides an evaluation of differences between the two models and discussion of the applicability and suitability of the EBS-UZ interface model for TSPA-LA transport modeling.

7.3.1 Validation of EBS-UZ Boundary Condition Implementation in TSPA-LA

In this section, the predictions of the analytical fracture-matrix partitioning model developed in *Drift-Scale Radionuclide Transport* (BSC 2004 [DIRS 170040]) are compared with the fracture-matrix partitioning at the EBS-UZ boundary predicted by the *EBS RT Abstraction* (Section 6.5.3.6). Because the two models are conceptually different, exact agreement in their results is not expected. The objective of the validation is to demonstrate qualitative agreement, i.e., that the trends and general qualitative behavior of the EBS-UZ boundary condition implementation in the *EBS RT Abstraction* are also seen in a model that has been independently developed and uses a completely different solution approach.

7.3.1.1 Description of Fracture-Matrix Partitioning Model

The fracture-matrix partitioning model, described in *Drift-Scale Radionuclide Transport* (BSC 2004 [DIRS 170040]), is developed for the case where there is no seepage inside the drift. It may be used to compute the relative fraction of the radionuclide mass entering the UZ matrix and UZ fracture from the invert by the process of diffusion. The fracture-matrix partitioning model is extended to the case where there is seepage through the drift by specifying that all mass leaving the invert by advection enters the UZ fractures, i.e., there is no partitioning in this case.

The fracture-matrix partitioning model considers only that part of the invert that is directly underneath the waste package, and effectively treats the invert as a single continuum by assuming zero saturation in the intergranular pores of the invert and a fully saturated intragranular invert continuum, in order to compute a single continuum (or bulk) water content. A rectangular geometry is used for the invert, with a vertical length sampled from a uniform distribution whose maximum is the maximum thickness of the invert directly under the package and whose minimum is the thickness of the invert under the projected edges of the package. The invert width is defined to be equal to the half-fracture spacing in the UZ, which is the reciprocal of the sampled value of the fracture frequency. The model assumes two-dimensional steady state diffusion in a homogeneous invert material. The governing mass transport equation is the Laplace equation:

$$\nabla^2 C_i(x,y) = 0. \qquad \text{(Eq. 7.3.1.1-1)}$$

Both lateral boundaries are considered lines of symmetry and treated as no-flow boundaries (BSC 2004 [DIRS 170040], Section 6.4.1 and Figure 6-10). Along the top of the invert, a constant concentration boundary condition is imposed. At the bottom of the invert, two flux boundary conditions are imposed – one across the interface between the invert and the saturated width of the single UZ fracture (i.e., the water film thickness), and one for the interface of the invert with UZ matrix. The model only considers a single fracture in the UZ, located directly under the left boundary of the invert. The remaining width (the half fracture spacing minus the fracture water film thickness) interfaces with the UZ matrix. Within the single UZ fracture, only diffusive transport is allowed for a vertical distance below the invert that is sampled uniformly between zero and the fracture spacing. Beneath that point, only advective transport in the fracture is allowed. The imposed boundary condition is such that the diffusive flux in the fracture is equal to the downward advective flux in the fracture at this sampled transition point between diffusion and advection. For the UZ matrix, only advective transport is allowed, and the boundary condition is such that the diffusive flux from the invert to the UZ matrix is equal to the UZ matrix advective mass flux.

The fracture-matrix partitioning first formulates the above partial differential equation for concentration with boundary conditions in dimensionless form, which is then solved analytically by infinite series expansion in cosines and hyperbolic tangent functions. The flux to the fracture is then determined by integration at the invert-UZ boundary of the gradient of the concentration. The integral over the UZ fracture portion of the UZ represents the flux to the UZ fracture, while integration of the concentration gradient over the UZ matrix portion of the boundary provides the flux to the UZ matrix.

7.3.1.2 Comparison of Results from Fracture-Matrix Partitioning Model with Results from the Modified *EBS RT Abstraction*

The two models are compared for the predictions of the fraction of mass of radionuclides released to fractures of the unsaturated zone. The comparison is based on the results of the Fracture-Matrix Partitioning Model reported in Section 6.4.6 of the *Drift-Scale Radionuclide Transport* (BSC 2004 [DIRS 170040]). In that report, calculations are done for the three infiltration rates (lower, mean and upper) of the glacial transition climate. The calculations include parameter uncertainty. The EBS-UZ interface model is modified, as discussed below, to allow comparison of the two models without changing the conceptual design or solution algorithm. GoldSim V8.01 (Golder Associates 2003 [DIRS 166572]) is used for the *EBS RT Abstraction* calculations. The GoldSim run files and the analysis of the results in an Excel spreadsheet are found in DTN: MO0508SPAFRAPM.000. The results of the comparison are shown in Figure 7.3-1.

In order to compare the *EBS RT Abstraction* with the fracture-matrix partitioning model, all sampled and time-varying parameters in the EBS and UZ in the TSPA-LA system model are made consistent with the parameters used in the fracture-matrix partitioning model. Additional modifications made to the *EBS RT Abstraction* are listed below:

1. Delete the upstream waste form and corrosion products domains.

2. Apply uniform concentration at the top of the invert domain (1000 mg/L). For this purpose, the radionuclide chosen is ^{99}Tc, because it has no sorption in the invert and UZ. The inventory for all other radionuclides is set to zero.

3. Set the seepage flux entering the invert domain to zero, so that the only transport mechanism is diffusion.

4. Set the water saturation of invert intragranular continuum to 1.0 (fully saturated) and the water saturation of the intergranular continuum to zero. For the single continuum representation of the invert, the bulk water content is computed.

5. Turn off the imbibition flux entering the invert domain.

6. Change the diffusive property of the invert domain to match Equation E-1 of *Drift-Scale Radionuclide Transport* (BSC 2004 [DIRS 170040]).

7. Change the free water diffusion coefficient (D_0) to a lognormal distribution with the mean of $\log D_0$ of 4.69 and standard deviation of $\log D_0$ of 0.150, where D_0 is in units of mm^2 yr^{-1} (thus, the value of D_0 corresponding to the mean of $\log D_0$ is $10^{4.69}$ = 4.90×10^4 mm^2 yr^{-1}, or 1.55×10^{-5} cm^2 s^{-1}), consistent with the approach adopted in *Drift-Scale Radionuclide Transport* (BSC 2004 [DIRS 170040], p. E-2 of Appendix E).

8. Change the diffusive thickness in the invert to a uniform distribution between 0.675 m and 0.806 m, as shown in *Drift-Scale Radionuclide Transport* (BSC 2004 [DIRS 170040], Appendix G, p. G-8).

9. Set the diffusive outflow area of the UZ matrix cells to zero, consistent with the boundary conditions imposed by the fracture-matrix partitioning model *Drift-Scale Radionuclide Transport* (BSC 2004 [DIRS 170040], Section 6.4.1). As a result, only diffusive transport occurs from invert domain to the UZ matrix continuum, and only advective transport occurs in the UZ matrix continuum.

10. The distance where the flow occurs in the UZ fracture is uniformly sampled between 0 m and the fracture spacing (inverse of fracture frequency). For the UZ matrix, the flow occurs immediately under the invert. Residual saturation is applied to the UZ fracture for the part where there is no flow. For the UZ matrix, the flow occurs immediately under the invert and thus the diffusive thickness of the first layer of the UZ matrix is set to a small value equal to 1×10^{-5} m.

11. Set the diffusive mass transfer term between the UZ matrix and fracture continuum to zero.

12. Ignore the transverse diffusion to the side UZ matrix and fracture cells from the UZ cells in the middle zone (These zones and cells in the EBS-UZ interface model are described in Section 6.5.3.6 and Figure 6.5-4).

13. Instead of setting the thickness of the second UZ layer as twice that of the first layer, the thickness of the second layer is changed to 1 m.

Figure 7.3-1 (shown below) compares the fraction of the radionuclide mass released to the fractures as predicted by the fracture-matrix partitioning model (labeled as "F-M Partitioning Model" in Figure 7.3-1) with the fraction predicted by the EBS-UZ boundary condition implementation for TSPA-LA in the modified *EBS RT Abstraction* (labeled as "EBS RT Model" in Figure 7.3-1). The cumulative distribution function from the *EBS RT Abstraction* (thick red and green curves) is based on 100 realizations, while that for fracture-matrix partitioning model is based on 24 random samples selected for each infiltration case, as discussed in Section 6.4.6 of *Drift-Scale Radionuclide Transport* (BSC 2004 [DIRS 170040]). The 24 samples are the minimum required to ensure sampling of hydrologic parameters from each of the four host rock units (TSw33, TSw34, TSw35, and TSw36). Based on this sample size, it is estimated that for 95 percent confidence limit, the sample mean is within $\pm 0.41\sigma_s$ of the population mean, where σ_s is the sample standard deviation. Increasing the sample size narrows the estimated spread around the true mean and improves the accuracy of estimation. For the 100 realizations performed by the modified *EBS RT Abstraction*, the estimate of the sample mean for 95 percent confidence limit is within $\pm 0.2\sigma_s$ of the population mean. The uncertain parameters for the 100 realizations are sampled using the Latin Hypercube Sampling methodology employed by GoldSim.

The results for the fracture-matrix partitioning model for the three infiltration cases have been combined (weighted by the probability of each infiltration case) into a single curve (thick blue curve – "Combined Infiltration") for comparison with the EBS-UZ boundary condition implementation for TSPA-LA *EBS RT Abstraction.* The thick red curve shows the results for the modified *EBS RT Abstraction* using the single continuum representation of the invert, which is the base case model used in TSPA-LA. (Though not pertinent to model validation, the modified *EBS RT Abstraction* was also run using the dual continuum representation of the invert, an alternative conceptual model; results are shown as the thick green curve. These thick red and green curves virtually overlap showing little effect on the mass fraction released to fractures.)

In general, the modified *EBS RT Abstraction* predicts approximately the same mass fraction released to fractures compared to the fracture-matrix partitioning model. The difference is due to the fact that the two models are conceptually different with regard to the placement of fracture and matrix medium underneath the invert and in computing the flux out of the invert. The fracture-matrix partitioning model solves the transport equation semi-analytically, whereas the modified *EBS RT Abstraction* model uses a finite difference approach. Because of these differences, a perfect match between the two models is not expected. Nevertheless, the comparison shows a similar qualitative and quantitative behavior between the two models.

The modified *EBS RT Abstraction* and the fracture-matrix partitioning model (combined infiltration curve) agree within a factor about of three. The uncertainty in the three infiltration curves, shown as error bars in Figures 6-26b and 6-28 of *Drift-Scale Radionuclide Transport* (BSC 2004 [DIRS 170040]), is bounded by the "Upper Error Margin" and "Lower Error Margin" curves in Figure 7.3-1. The thick red (or green) curve falls within the "error margins" of the individual infiltration case curves, indicating a close match between the modified *EBS RT Abstraction* and the fracture-matrix partitioning model.

Although conceptual differences exist between the fracture-matrix partitioning model and the EBS-UZ interface model in the *EBS RT Abstraction,* with appropriate modifications to bring them into closer conceptual alignment, the two models display similar qualitative and quantitative behavior. The similarity in the results gives confidence that the EBS-UZ interface model is valid for use in TSPA-LA.

7.3.1.3 Applicability of EBS-UZ Interface Model in TSPA-LA in Comparison with Fracture-Matrix Partitioning Model

The EBS-UZ interface model of the *EBS RT Abstraction* is more suitable for TSPA-LA compared to the fracture-matrix partitioning model for the following reasons:

- The fracture-matrix partitioning model assumes steady state mass transport and is solved with a semi-analytic solution to the Laplace equation, assuming a constant concentration boundary at the top of the invert and a variable flux boundary at the bottom. This approach is restrictive compared to the *EBS RT Abstraction,* wherein the radionuclide concentrations will be varying with time. Thus, important transient effects related to fuel degradation, thermal-hydrology, in-drift chemistry, and seepage are captured in the *EBS RT Abstraction,* but may not be captured adequately in the fracture-matrix partitioning model.

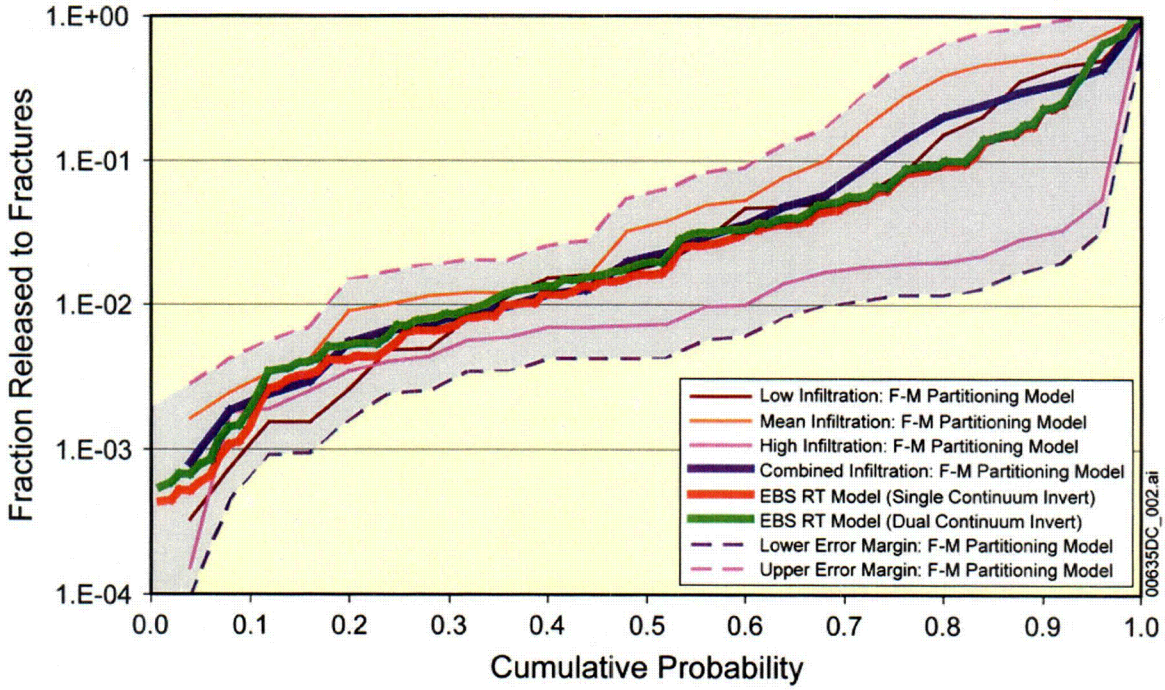

Fracture-Matrix Partitioning Model Error Margins: BSC 2004 [DIRS 170040], Figures 6-26b and 6-28b.

Output DTN: MO0508SPAFRAPM.000.

Figure 7.3-1. Fracture-Matrix Partitioning for No Seepage Case

- The *EBS RT Abstraction* is a finite difference type model that treats the EBS processes and the near-field UZ processes as a coupled system. The upstream boundary condition is provided by a specified mass flux based on the degradation rate of the waste form and the radionuclide solubility limits, while the downstream boundary is provided by assuming a zero concentration boundary at some distance (~3 drift diameters) from the invert in the UZ. Consequently, the mass flux of radionuclides from the waste package to the invert and from the invert to the UZ is based on solving the coupled system of differential equations with realistic boundary conditions. Since the mass flux from the invert to the UZ is based on the EBS-UZ boundary condition implementation for TSPA-LA in the *EBS RT Abstraction*, to be consistent, the mass flux partitioning into the far-field UZ transport model (FEHM) should also be based on the *EBS RT Abstraction*, rather than on the fracture-matrix partitioning model.

- The fracture-matrix partitioning model assumes a discrete fracture network with no coupling between the fracture and matrix domains. In contrast, the EBS-UZ boundary condition implementation for TSPA-LA in the *EBS RT Abstraction* treats the UZ as a dual continuum (overlapping UZ fracture and matrix continua), with diffusive mass transfer capability between the two continua. This dual continuum modeling approach is consistent with the various process-level UZ flow and transport models created for the YMP.

- The imbibition flux from the surrounding host rock into the intragranular continuum is modeled in the *EBS RT Abstraction*, whereas its contribution in the fracture-matrix

partitioning model is ignored. This flux could potentially carry some radionuclide mass into the UZ matrix that could lower the partitioning to the fracture continuum, which is realistic. The fracture-matrix partitioning model may overestimate the fraction released to the fractures where imbibition flux is significant.

- In the regions of the repository where water seeps through the drift, the fracture-matrix partitioning model arbitrarily proposes putting all the mass from the invert into the UZ fracture. This is a bounding approach and ignores the matrix pathway, which occupies most of the area under the invert. The EBS-UZ boundary condition implementation for TSPA-LA in the *EBS RT Abstraction*, however, applies a more realistic approach, computing the fracture-matrix partitioning based on the appropriate set of boundary conditions in drifts with seepage and including transport in the UZ matrix, as discussed in the second bullet above. Sections 6.5.3.5 and 6.5.3.6 discuss how the advective flux from the invert is apportioned between fractures and matrix in the UZ.

The above comparisons of the results of the two models and their comparative suitability for TSPA-LA have demonstrated that the EBS-UZ interface model meets Level II validation criteria. Based on the validation results, the EBS-UZ interface model is suitable for its intended use.

7.3.2 Results of Independent Model Validation Technical Review of the EBS-UZ Interface Model

An independent model validation technical review of the EBS-UZ interface model was conducted, as specified in the TWP (BSC 2005 [DIRS 173617], Section 2.2.3). This model validation approach is justified based on requirements of LP-SIII.10Q-BSC, Section 5.3.2 c), where independent technical review is listed as an appropriate method for model validation. The results of the independent model validation technical review of the EBS-UZ interface model are presented in a memo (Baker and Grisak 2004 [DIRS 170953]), a verbatim copy of which follows.

MEMO

Date: July 27, 2004

To: James Schreiber and Cliff Howard, Yucca Mountain Project

Cc:

From: Noreen A. Baker, Gerald E. Grisak, INTERA Inc., Austin, Texas

RE: **Independent Model Validation Technical Review of the EBS-UZ Interface Sub-Model of the Radionuclide Transport Abstraction Model for the Yucca Mountain Project**

MEMO (Continued)

Pursuant to your request to perform an independent model validation technical review of three sub-models of the Engineered Barrier System (EBS) Radionuclide Transport Abstraction (RTA) model as documented in ANL-WIS-PA-000001 Rev 01K, we have performed and documented the review consistent with the requirements of the Technical Work Plan TWP-MGR-PA-000020 Rev 00. We reviewed the EBS-UZ interface sub-model of the EBS RTA report, and the results of the review are provided in this memo.

Review Qualifications

Section 2.2.4 of the Technical Work Plan TWP-MGR-PA-000020 Rev 00 describes the qualifications and responsibilities the independent model validation technical reviewer. We are qualified to perform the work described for the following reasons. (1). we have not contributed to the development of the model assumptions, parameters, or implementing algorithms documented in ANL-WIS-PA-000001 Rev 01K, (2). Noreen A. Baker has a BS and MS degree in Geology with specialties in Engineering Geology and Hydrogeology, respectively, with more than ten years of professional experience modeling fluid flow and transport in geologic media (3) G. E. Grisak has BS (Geology) and MS (Hydrogeology) degrees, and over 30 years experience evaluating and modeling fluid flow and transport in geologic media, including several publications on fracture/matrix flow and transport, (3) Both N. A. Baker and G. E. Grisak are licensed Professional Geoscientists in the State of Texas. More detailed information regarding credentials can be found in the resumes attached.

Appropriateness and Adequacy of the EBS-UZ Interface Sub-Model Conceptual Model

Discussion of the EBS-UZ interface sub-model is provided in Section 6.5.3.6. Discussion of the EBS-UZ interface sub-model is provided in Section 6.5.3.6. In the EBS-UZ interface sub-model, the near-field UZ is modeled as a dual continuum of overlapping UZ-matrix and UZ-fracture media. This approach is consistent with current technical approaches to modeling flow and transport in fractured geologic media (Liu et al., 1998; Nitao, 1991). The matrix and fracture continua are represented by a two dimensional vertical array of cells oriented parallel to a cross section of a drift and located immediately beneath a drift. The array consists of three vertical zones, with each zone containing both a fracture cell and a matrix cell. The vertical zones are four layers deep in the vertical direction. The invert is in direct communication with the center zone of UZ matrix/fracture cells. A semi-infinite zero concentration boundary condition at the EBS-UZ interface is approximated by setting a zero concentration boundary at a distance of 3 drift diameters below the invert-UZ boundary.

The mass flux from the invert flows into the top layer of the middle zone in the UZ. The mass flux from the invert is routed to both the fracture cell and the matrix cell in the center zone beneath the invert, with the advective flux routed to the fracture and matrix cells in a manner that is consistent with physical reality. That is, the advective flux coming out of the invert, which is attributable to the dripping flux is routed to the fracture cell in the middle zone, while the imbibition flux is routed to the matrix. The diffusive flux is allowed to enter both the matrix and the fracture cells. The advective flux in the fractures is taken as the larger of the steady-state advective flux in the fractures and the advective flux out of the invert.

The mass flux that enters the center zone cells in the UZ below the invert is then transported by advection and diffusion throughout the modeled area. The advective flux in the two outer zones is given by the steady state UZ flow in the fractures and the matrix at the repository horizon. Advection occurs downward only, from the fracture cell of one layer to the fracture cell of the underlying layer in the same zone, and from the matrix cell of one layer to the matrix cell of the underlying layer in the same zone. Advection does not occur across zones. The fracture and

MEMO (Continued)

matrix cells of each zone interact via diffusion. The entire modeled area interacts through the matrix cells via diffusion, with the matrix cells of one zone interacting via diffusion with the matrix cells of adjacent zones, and the matrix cells of one layer in a zone interacting with adjacent overlying and underlying matrix cells in the same zone.

The conceptual model of how the EBS and UZ interface is well captured by the EBS-UZ interface model. The conceptual model recognizes the physical reality by considering both an advective and diffusive flux and by treating the UZ as a dual-permeability medium with both fracture and matrix continua. This modeling approach is consistent with the manner in which dual-permeability continua are modeled (Pruess, 2003). The conceptual model is appropriate for describing the interconnection between the EBS and the UZ because it considers the important components of mass flux out of the EBS and it conserves all the mass flux from the EBS and transfers it to the UZ. The mass transfer to the UZ also captures temporal variations, which may be due to variable radionuclide concentrations in the waste, production of corrosion products, or varying water flux through the EBS. The mass is distributed to the fractures and the matrix in the EBS-UZ interface sub-model in a manner that is conceptually logical. The mass is finally gathered from the EBS-UZ interface sub-model into a collector cell for delivery to the UZ transport model. The delivery from the collector cell to the UZ transport model retains the relative fractions of mass in the fractures and the matrix that is determined within the EBS-UZ interface sub-model.

Appropriateness of the Mathematical Representation of the EBS-UZ Interface Sub-Model

The EBS-UZ interface sub-model represents the UZ immediately below the invert as a dual continuum of UZ matrix and UZ fracture media. The dual permeability modeling approach is an appropriate way to model transport in fractured media. Mass is tracked and accounted for in the model in both fracture and matrix cells and the fracture and matrix cells have physical dimensions which adequately approximate the physical hydrogeologic system. The mathematical formulation of the dual permeability modeling approach is described in *Particle Tracking Model and Abstraction of Transport Processes* (BSC 2003w).

EBS-UZ Interface Sub-Model Assumptions and Boundary Conditions

The EBS-UZ sub-model assumptions and comments are provided below.

Assumptions/Boundary Condition	Comments
1. A semi-infinite zero concentration boundary condition is used for the EBS-UZ interface. The boundary condition is set at a distance of 3 drift diameters below the invert-UZ boundary.	We agree with the boundary condition and with the manner in which it is implemented. Placing the boundary condition at the interface would result in an unrealistically high diffusive flux from the invert to the UZ.
2. With respect to the advective flux in the outer two zones of cells, drift shadow effects are ignored.	We agree with the assumption. Drift shadow effects would increase the advective flux in the two outer zones and result in dilution of radionuclide concentrations entering the UZ immediately below the invert.

Evaluation of Model Validation

Documentation of the model validation is presented in Section 7.3.1. The EBS-UZ sub-model is validated by comparison with an alternative mathematical model developed for a closely

MEMO (Continued)

comparable description of the EBS-UZ interface. The alternative model used for the comparison is the fracture-matrix partitioning model described in *Drift-Scale Radionuclide Transport* (BSC 2004m). The primary validation criterion is corroboration of the model results with an alternative mathematical model, as described in TWP-MGR-PA-000020 Rev 00. This is a common approach to model validation where site specific or generic field or laboratory data or experiments do not adequately capture the processes involved. The EBS-UZ interface sub-model involves coupling the porous medium invert to the dual-permeability UZ with a numerical solution of a discretized model. In the fracture-matrix partitioning model, the coupling is accomplished by formulating the problem as a partial differential equation for concentration and deriving an analytical solution to the problem. In order to compare the two models, all sampled and time-varying parameters in the EBS-UZ interface sub-model are made consistent with the parameters used in the fracture-matrix partitioning model. Additionally, other changes to the EBS-UZ interface sub-model were made to more closely approximate conditions in the fracture-matrix partitioning model. The EBS-UZ interface sub-model was also run using an alternative conceptualization for the invert as a dual continuum. The results of the CDFs of the fraction released to fractures are then compared. This is a technically reasonable and appropriate approach to model validation.

Evaluation of Model Validation Criteria

In Section 2.2.4 of Technical Work Plan TWP-MGR-PA-000020 Rev 00, provides validation criteria for the EBS-UZ interface sub-model. The table below provides our assessment of these criteria.

Criteria	Criteria met?	Response
1. The results of the UBS-UZ interface sub-model shall show qualitative agreement with the results of the fracture-matrix partitioning model.	Yes	The two models display similar qualitative results, and in addition are reasonably similar quantitatively, in that the results of the EBS-UZ interface sub-model fall within the shadow of the error bars of the low, mean and high infiltration cases of the fracture-matrix partitioning model.
2. The report shall document equivalent trends and correlations between input parameter variation and predicted results	Yes	Equivalent trends and correlations between input parameter variations and predicted results are visually obvious on the graphical comparison between the two methods. Either the single or dual continuum representation of the invert by the EBS-UZ interface sub-model is adequate.
3. Identification of differences between model results.	Yes	Differences between model results and the reasons for the differences are provided in section 7.3.1.2
4. Demonstrate that the EBS-UZ interface sub-model does not underestimate radionuclide transport from the EBS to the UZ.	Yes	The suitability and applicability of the EBS-UZ interface sub-model is discussed and justified in Section 7.3.1.3. The sub-model is suitable for its intended use.

MEMO (Continued)

Conclusions

The EBS-UZ interface sub-model documented in report ANL-WIS-PA-000001 Rev 01K incorporates all the significant aspects contributing to mass flux from the invert to the UZ. The sub-model is validated against an alternative model developed for similar purposes and the results are comparable. The advective flux is the primary uncertainty in the mass flux to the fractures, and this uncertainty has been adequately and realistically bounded by the low, mean and high infiltration cases used in the fracture-matrix partitioning model in the validation comparison. It is our professional judgment that the EBS flow sub-model is appropriate for use in the Radionuclide Transport Abstraction.

References

Liu, H.H., C. Doughty and G.S. Bodvarsson, 1998, "An active fracture model for unsaturated flow and transport in fractured rock," Water Resources Research, vol. 34, no. 10, pages 2633-2646.

Nitao, J.J., 1991, "Theory of matrix and fracture flow regimes in unsaturated, fractured media," Proc., Second International High Level Radioactive Waste Management Conference, Las Vegas, NV, April 29-May 3, 1991.

Pruess, K. (editor), 2003, Proceedings, TOUGH Symposium 2003, Lawrence Berkeley National Laboratory, CA, May 12-14.

7.4 VALIDATION SUMMARY

The *EBS RT Abstraction* has been validated by applying acceptance criteria based on an evaluation of the model's relative importance to the potential performance of the repository system. All validation requirements defined in the *Technical Work Plan for: Near-Field Environment and Transport: Engineered Barrier System: Radionuclide Transport Abstraction Model Report Integration* (BSC 2005 [DIRS 173617]), Sections 2.2.1, 2.2.2, and 2.2.3 have been fulfilled. Requirements for confidence building during model development have also been satisfied. The model development activities and post-development validation activities described establish the scientific bases for the *EBS RT Abstraction*. Based on this, the *EBS RT Abstraction* is considered to be sufficiently accurate and adequate for the intended purpose and to the level of confidence required by the model's relative importance to the performance of the proposed repository system.

8. CONCLUSIONS

This abstraction defines the conceptual model used to determine the rate of release of radionuclides from the EBS to the unsaturated zone in the TSPA-LA given the assumptions listed in Section 5. The *EBS RT Abstraction* includes algorithms used in the TSPA-LA for computing the flow of water and the transport of radionuclides through the EBS and specifies how parameters used in the model are calculated or from what other models they are obtained. This model is reasonably bounding because it overestimates flow through the drip shield and into the waste package and transport out of the EBS. At the same time, wherever possible, it is realistic, not just bounding, within the appropriate range of uncertainty for TSPA-LA calculations.

8.1 CONCEPTUAL MODEL SUMMARY

This section summarizes the conceptual model for transport of radionuclides from the EBS as modeled in TSPA-LA. Radionuclide transport out of the waste form and waste package, through the invert, and into the unsaturated zone is dependent on a complex series of events in the repository. After the waste packages are emplaced, radioactive decay of the waste will heat the drifts and locally perturb the normal percolation of water through the mountain. As the drifts cool, some of the water percolating through the mountain may drip into the drifts and subsequently contact some of the drip shields. Over time, the drip shield, waste package, and other components of the EBS are expected to degrade, leading to contact between the water and the waste form, resulting in the mobilization and transport of radionuclides through the EBS to the unsaturated zone. The primary transport medium through the EBS is anticipated to be water. Either a thin film of water or moving water is necessary for radionuclides to be transported out of the waste package and through the invert to the unsaturated zone.

A number of key factors will affect the mobilization and transport of radionuclides through the EBS, including barrier effectiveness and transport behavior:

- Performance of the drip shields
- Performance of the waste packages
- Protection provided by cladding
- Waste form degradation rates
- Entry and movement of water through waste packages
- Solubilities of radionuclides
- Transport of radionuclides through and out of the waste packages
- Transport of radionuclides through the invert below the waste packages
- Colloidal transport of radionuclides.

Once the drip shield is breached, water may contact the waste packages. Once a waste package is breached, water may enter the package as water vapor or as drips. If the cladding around spent fuel rods or the canister around a vitrified waste form is also breached, radionuclides may start to dissolve in the water. The concentration of each radionuclide mobilized from the waste form cannot exceed the radionuclide solubility limit, unless suspended colloids are included. Colloids are important for two reasons: they may potentially increase the release of radionuclides from the waste package, and they may potentially increase the transport velocity of radionuclides.

Radionuclides mobilized in water as dissolved species or in association with colloidal species may then be transported by advection and/or diffusion from the waste form, through the waste package, and out of breaches in the waste packages. Once outside the package, the radionuclides may be transported through the invert predominantly by diffusion, if water is not flowing through the invert, or by advection, if water is flowing through the invert.

The conceptual model for flow of water through the EBS identifies eight key flow pathways. These pathways and their relationships are summarized in the following list and in Table 8.1-1. Sections 6.3.1.1, 6.3.2, 6.3.3, and 6.5.1.1 contain detailed technical discussions of the EBS flow abstraction portion of the *EBS RT Abstraction.*

- **Total Dripping Flux**—This is the input flux or boundary condition; it is a time- and location-dependent input to this model provided by *Abstraction of Drift Seepage* (BSC 2004 [DIRS 169131]). Any condensation that may occur on the walls of the drift above the drip shield is added to the seepage flux (BSC 2004 [DIRS 164327], Section 8.3.1).
- **Through the Drip Shield to the Waste Package**—Flux through the drip shield is proportional to the ratio of the axial lengths of breaches in the drip shield to the total axial length of the drip shield, multiplied by a sampled factor that accounts for uncertainty in the fraction of the flux that is diverted by the drip shield. This flux splitting submodel for the drip shield should only be applied when there is a time-varying failure of the drip shield.
- **Drip Shield to Invert (Diversion around the Drip Shield)**—Any seepage and wall condensation flux that does not go through the drip shield flows directly into the invert.
- **Through the Waste Package to the Waste Form**—Flux into the waste package is proportional to the product of the flux through the drip shield and the ratio of the lengths of breaches in the waste package to the total axial length of the waste package, multiplied by a sampled factor that accounts for uncertainty in the fraction of the flux that is diverted by the waste package. The number of corrosion patches in the waste package is calculated in *WAPDEG Analysis of Waste Package and Drip Shield Degradation* (BSC 2004 [DIRS 169996]).
- **Waste Package to Invert (Diversion around the Waste Package)**—Flow that does not go through the waste package is diverted directly to the invert.
- **Waste Package to Invert**—All of the flux from the waste package flows directly to the invert, independent of breach location on the waste package. The presence of the emplacement pallet, which maintains an air gap between the waste package and the invert and could potentially interfere with flow to the invert, is ignored in order to bound the water flow through this pathway.
- **Imbibition to Invert**—Water can be imbibed from the host rock matrix into the invert.
- **Invert to Unsaturated Zone**—All of the flux into the invert is released into the unsaturated zone.

In the conceptual model of radionuclide transport through the EBS, the waste form is the source of all radionuclides in the repository system. Radionuclides can be transported downward, through corrosion products in the waste package, through the invert, and into the unsaturated zone. Transport can occur through advection when there is a liquid flux through the waste package, and by diffusion through any water present in the waste package. Diffusion can occur in a seep environment, when advective transport also takes place, as well as in a no-seep environment where no advective transport occurs; thin films of water are assumed to be present on all surfaces. If the only breaches in a waste package are stress corrosion cracks, advective transport does not occur, but diffusion of radionuclides out of the waste package can still take place. The concentration of each radionuclide during transport is limited by the sum of its solubility limit and the presence of any colloidal particles that may act as reversible or irreversible carriers for the radionuclide. The transport pathways and transport processes (advection or diffusion) are summarized in Table 8.1-2. Sections 6.3.4, 6.5.1.2, and 6.5.3 contain a detailed technical discussion of the EBS transport abstraction.

Table 8.1-1. Summary of EBS Flow Abstraction

Flow Pathway, Pathway Flux	Flow Parameters	Data Sources and Notes
1. Total dripping flux (seepage + wall condensation), F_1	Total dripping flux is a function of fracture properties, rock properties, air and water properties, and the percolation flux.	*Abstraction of Drift Seepage* (BSC 2004 [DIRS 169131]) and *In-Drift Natural Convection and Condensation Model* (BSC 2004 [DIRS 164327]) provide time- and location-dependent values of total dripping flux.
2. Flux through the drip shield, F_2	L_{DS_Patch} is axial half-length of each patch due to general corrosion of Ti. L_{DS} is axial length of the drip shield. N_{bDS} is number of corrosion patches of length L_{DS_Patch} in the drip shield. f'_{DS} is sampled uncertain parameter, Flux_Split_DS_Uncert. $F_2 = \min[F_1 N_{bDS} L_{DS_Patch} f'_{DS}/L_{DS}, F_1]$	This flux splitting submodel for the drip shield should only be applied when there is a time-varying failure of the drip shield. For the seismic scenario class, the opening area is computed based on the drip shield damage fraction multiplied by the area of the drip shield.
3. Diversion around drip shield, F_3	$F_3 = F_1 - F_2$.	Continuity of liquid flux.
4. Flux into the WP, F_4	L_{WP_Patch} is axial half-length of each patch due to general corrosion of Alloy 22. L_{WP} is axial length of the WP. N_{bWP} is number of corrosion patches in the waste package. f'_{WP} is sampled uncertain parameter, Flux_Split_WP_Uncert. $F_4 = \min[F_2 N_{bWP} L_{WP_Patch} f'_{WP}/L_{WP}, F_2]$	WAPDEG (BSC 2004 [DIRS 169996]) provides the number of patches and stress corrosion cracks on the WP. No significant flow through stress corrosion cracks due to plugging (BSC 2005 [DIRS 173781], Section 6.2.63). Steady state flow through WP (outflow = inflow in steady state; this is bounding for release).
5. Diversion around the WP, F_5	$F_5 = F_2 - F_4$	Continuity of liquid flux.
6. Flux to the invert, F_6	$F_6 = F_5 + F_4 + F_3$ $= F_1$	All advective flux enters the invert. Only F_4 can transport radionuclides into the invert.
7. Imbibition flux from the host rock matrix into the invert, F_7	F_7 is an input to the EBS flow model.	Imbibition flux is provided by *Multiscale Thermohydrologic Model* calculations (BSC 2005 [DIRS 173944]).

Table 8.1-1. Summary of EBS Flow Abstraction (Continued)

Flow Pathway, Pathway Flux	Flow Parameters	Data Sources and Notes
8. Flux from the invert into to the unsaturated zone, F_8	$F_8 = F_6 + F_7$ $= F_1 + F_7$	Total dripping flux portion (F_1) of advective flux from the invert flows into the UZ fractures, imbibition flux (F_7) flows into the UZ matrix.

Output DTN: SN0410T0507703.018.

WP = waste package.

In the transport abstraction, the EBS is modeled as consisting of three domains. The first domain is the source (i.e., SNF or HLW). The second domain consists of corrosion products from the degradation of steel waste package internal components. The third domain is the invert. The physical and chemical properties and conditions are uniform throughout each domain, as though the contents of the domain were thoroughly and continuously stirred.

Parameters that define the size of the two waste package domains, specifically the volumes and diffusive path lengths, are summarized in Table 8.2-1. Parameter values that are provided by other models are identified there. The path length for diffusion through the invert is set to the average thickness of the invert, 0.597 m.

The mass of corrosion products is a function of time and depends on the corrosion rates of carbon steel and stainless steel, which are uncertain parameters with values that are sampled in TSPA-LA. In a seep environment, the corrosion products are fully saturated with water. In a no-seep environment for CSNF, the water saturation is based on the amount of water adsorbed onto iron oxide surfaces, which is a function of the relative humidity. The RH is an input to the transport model that depends on time and location in the repository. Calculation of corrosion products mass and saturation is discussed in Section 6.5.3.2.

The diffusion coefficient in the corrosion products is based on the self-diffusion coefficient of water at 25°C as a bounding value for all radionuclides, modified for the porosity and time-dependent water saturation.

The diffusion coefficient in the invert is also based on the self-diffusion coefficient of water at 25°C as a bounding value for all radionuclides. The effects of porosity and time-dependent saturation in the invert are incorporated, based on experimental data. The effect of temperature is also incorporated into the abstraction for the diffusion coefficient. The diffusion coefficient for colloids is assumed to be $1/100^{th}$ of the diffusion coefficient for a dissolved species (Section 6.3.4.4).

Sorption of radionuclides may occur on corrosion products in the waste package and on crushed tuff in the invert. Values for sorption distribution coefficients on corrosion products and on crushed tuff for all radionuclides of interest are determined in Section 6.3.4.2. K_d values for sorption on corrosion products are set to zero for all radionuclides as a bounding approach; i.e., no credit is taken for retardation due to reversibly sorbed radionuclides on stationary corrosion products.

Table 8.1-2. Summary of EBS Transport Abstraction

Transport Pathway	Transport Modes	Transport Parameters and Data Sources
1. Waste form and corrosion products domains	Waste form domain: Diffusion and advection (when possible) through the waste form rind. Corrosion product domain: Diffusion through stress corrosion cracks (no advective transport through stress corrosion cracks). Diffusion and advection through corrosion products and corrosion patches.	No lateral or forward dispersion. Colloidal particles will transport radionuclides. Diffusive area for each stress corrosion crack is 7.7×10^{-6} m^2 (see Section 6.3.3.1.2.1). Diffusion coefficient (all radionuclides): • Free water diffusion coefficient: 2.299×10^{-5} cm^2 s^{-1} at 25°C (Mills 1973 [DIRS 133392], Table III) • Modified for porosity and saturation (see Section 6.3.4.3.5); not modified for temperature • Reduced by a factor of 100 if radionuclide is bound to a colloid (see Section 6.3.4.4). The cross-sectional area for radionuclide transport is dependent on the scenario class (see Sections 6.5.3.1.1 and 6.5.3.1.2). Irreversible sorption of Pu and Am onto corrosion products; time-dependent mass of corrosion products available for sorption is calculated based on corrosion rates of carbon and stainless steels. See Section 6.5.3 for further details.
2. Invert	Diffusion and advection (F_6) from corrosion products domain into the invert.	Liquid flux for advection = F_6 = F_5 (diverted by WP) + F_4 (flux through WP) + F_3 (diverted by drip shield). Diffusion coefficient (all radionuclides): • Free water diffusion coefficient: 2.299×10^{-5} cm^2 s^{-1} at 25°C (Mills 1973 [DIRS 133392], Table III) • Modified for porosity and saturation (see Section 6.3.4.1) • Temperature modification defined in Section 6.3.4.1.2; invert temperature is provided by *Multiscale Thermohydrologic Model* calculations (BSC 2005 [DIRS 173944] • Reduced by a factor of 100 if radionuclide is bound to a colloid (see Section 6.3.4.4). The cross-sectional area for radionuclide transport is the width of the invert times the waste package length. Transport of radionuclides is retarded by sorption onto crushed tuff in invert. See Section 6.5.3 for further details.
3. Invert-UZ interface	Advection from the invert to UZ fractures (F_6) and UZ matrix (F_7); total flux is F_8. Diffusion from the invert to UZ fractures and matrix.	The invert diffusion calculation uses radionuclide concentrations in the WP corrosion products domain as the boundary condition at the top of the invert and a series of unsaturated zone computational cells below the invert that provide a gradient to a zero radionuclide concentration at some distance from the bottom of the invert. See Section 6.5.3.6.

Output DTN: SN0410T0507703.018.

WP = waste package.

8.2 MODEL OUTPUTS

Table 8.2-1 summarizes parameters that define the three-domain EBS transport abstraction, which is described in more detail in Section 6.5.3. These domains are comprised of:

- *The waste form.* In the case of CSNF waste packages, this consists of fuel rods. In codisposal waste packages, the waste form is a composite of HLW glass and DSNF and thus there are two waste form subdomains one each for HLW glass and for DSNF. Transport processes that occur in the waste form domain(s) are the dissolution of radionuclides and advection and diffusion to the corrosion products domain. Waste form colloids are generated from the alteration of HLW glass and carry radionuclides that are both reversibly and irreversibly bound to the colloid.

- *Corrosion products inside the waste package.* These are the result of corrosion of steel internal waste package components such as baskets, canisters, and the inner stainless steel vessel. The stationary iron-oxide-based corrosion products are strong sorbers, so irreversible sorption of Pu and Am is modeled on the corrosion products. In addition, iron oxyhydroxide colloids (released from corrosion products) and groundwater colloids (from seepage water) are available in this domain. Both reversible and irreversible sorption is modeled on iron oxyhydroxide colloids but only reversible sorption is modeled on groundwater colloids. Precipitation and dissolution can also take place in this domain. Diffusion transports radionuclides into this domain from the waste form domain and from this domain to the invert domain. In a codisposal waste package, the degraded DSNF is conceptualized to be in a powdered form mixed in with steel corrosion products and provides the minimum water volume in the domain. Once the water volume associated with corrosion products exceeds the water volume associated with DSNF, the corrosion products water volume is used.

- *Invert.* Advection and diffusion transport radionuclides into this domain from the corrosion products domain and from this domain to the unsaturated zone. Groundwater colloids are also available in this domain if there is any water flow. Reversible sorption of radionuclides is modeled on these colloids. Because the chemical environment of the invert may be different from the corrosion products domain, colloid stability may be affected and dissolution or precipitation of radionuclides may take place. The submodel for transport through the invert is summarized in transport pathway 3 of the transport abstraction summary, Table 8.1-2.

Transport is affected by the parameters that define the physicochemical environment, including the porosity and pore volume, water saturation, interfacial diffusive areas, diffusive path lengths, and diffusion coefficients. These diffusive transport parameters are discussed in Section 6.5.3.

Output from the *EBS RT Abstraction*, including algorithms and parameters, is summarized in three output DTNs: SN0410T0507703.018, SN0508T0503305.003, and MO0506SPAINPAR.000. DTN: SN0410T0507703.018 contains the tables in Sections 8.1 and 8.2 of this report (except for some of the entries in Table 8.2-3); in addition, this DTN includes the K_d values from Table 6.6-7 for the alternative conceptual model for reversible sorption onto corrosion products. DTN: MO0506SPAINPAR.000 contains the parameters in Table 8.2-3 that

are not included in DTN: SN0410T0507703.018, as well as the zero K_d values specified for corrosion products. DTN: SN0508T0503305.003 contains sorption data for goethite and HFO that are summarized in Table 6.3-6.

In addition, three preliminary output DTNs were created prior to final approval of this report: DTNs: SN0403T0507703.015, SN0409T0507703.017, and SN0503T0503305.001. DTNs: SN0410T0507703.018 and MO0506SPAINPAR.000 consist of the tables found in Sections 8.1 and 8.2 of the *EBS RT Abstraction*. Differences between the preliminary and final DTNs are described in Appendices I and J. Both of the preliminary DTNs: SN0403T0507703.015 and SN0409T0507703.017 have been superseded by the final output DTN: SN0410T0507703.018. These two preliminary output DTNs are discussed in Appendix I solely to provide transparency and traceability for TSPA-LA applications that were initially developed based on the preliminary DTNs. These two DTNs are not intended for any other application. Preliminary DTN: SN0503T0503305.001 is used in TSPA-LA and is not intended for any other application.

Table 8.2-1. Parameters for EBS Transport Abstraction

Waste Type	Transport Properties	Seep Case	No-Seep Case
		Waste Form Domain (Fuel Rods, HLW, DSNF)	
CSNF	Rind volume and water volume	Waste form domain consists of fuel rods. • Rind volume provided by *Cladding Degradation Summary for LA* (BSC 2005 [DIRS 172895]) • S_w = water saturation in rind = 1.0	• Same as Seep Case
	Advection and Diffusion	Advective flux = volumetric flow rate through the WP Diffusive area of Waste Form Domain: • Total exposed surface area of all failed (axially split) fuel rods, limited to the total surface area of the waste package. • Provided by *Cladding Degradation Summary for LA* (BSC 2005 [DIRS 172895]) Diffusion path length: • Thickness of rind; function of time. • Provided by *Cladding Degradation Summary for LA* (BSC 2005 [DIRS 172895]) Diffusion coefficient in Waste Form Domain, D_{WF}: • $\phi S_w D_{WF} = \phi^{1.3} S_w^2 D_0$ • ϕ = porosity of rind (BSC 2005 [DIRS 172895]) • S_w = water saturation in rind = 1.0 • D_0 = free water diffusion coefficient (D_{WF} is an effective value defined in the same manner as D_s in Equation 6.3.4.3.5-2.)	• No advective flux • Diffusive properties same as Seep Case

Table 8.2-1. Parameters for EBS Transport Abstraction (Continued)

Waste Type	Transport Properties	Seep Case	No-Seep Case
		Waste Form Domain (Fuel Rods, HLW, DSNF)	
Codisposal	Rind volume and water volume	Waste form domain is divided into two subdomains: HLW and DSNF subdomains. HLW Subdomain: • Volume of HLW rind provided as function of time by *Defense HLW Glass Degradation Model* (BSC 2004 [DIRS 169988], Section 8.1, Eq. 54) • Porosity of HLW rind provided by *Defense HLW Glass Degradation Model* (BSC 2004 [DIRS 169988], Table 8-1) • S_w = water saturation = 1.0 DSNF Subdomain: • Volume of degraded DSNF (rind), V_{DSNF} = 1 m^3 provided by *DSNF and Other Waste Form Degradation Abstraction* (BSC 2004 [DIRS 172453], Table 8-1) • Porosity of DSNF rind, ϕ_{DSNF} = 0.2 • S_w = water saturation in DSNF = 1	• No advective flux • Diffusive properties same as Seep Case
	Advection and Diffusion	Advective flux = volumetric flow rate through the WP. HLW Subdomain: Diffusive area: • Total initial surface area of 5 glass logs • Provided by *Defense HLW Glass Degradation Model* (BSC 2004 [DIRS 169988], Section 8.1) Diffusion path length: • Thickness of degraded glass layer; function of time. • Provided by *Defense HLW Glass Degradation Model* (BSC 2004 [DIRS 169988], Section 8.1, Eq. 56) Diffusion coefficient in Waste Form Domain, D_{WF}: • $\phi S_w D_{WF} = \phi^{1.3} S_w^2 D_0$ • ϕ = rind porosity • S_w = water saturation = 1.0 • D_0 = free water diffusion coefficient (D_{WF} is an effective value defined in the same manner as D_s in Equation 6.3.4.3.5-2.)	• No advective flux • Diffusive properties same as Seep Case

Table 8.2-1. Parameters for EBS Transport Abstraction (Continued)

Waste Type	Transport Properties	Seep Case	No-Seep Case
	Advection and Diffusion	DSNF Subdomain: Diffusive area: • Same as the diffusive area in the corrosion product domain (= WP breach area). Diffusion path length: • V_{DSNF} (= 1 m^3) / Diffusive area Diffusion coefficient in Waste Form Domain, D_{WF}: • $\phi S_w D_{WF} = \phi S_w D_0$ • ϕ = rind porosity • S_w = water saturation = 1.0 • D_0 = free water diffusion coefficient (D_{WF} is an effective value defined in the same manner as D_s in Equation 6.3.4.3.5-2.)	
		Corrosion Product Domain	
CSNF	Bulk volume and water volume	Pore volume of corrosion products, V_{CP}: • Mass of corrosion products, m_{CP}, is function of time, Table 8.2-4, Equation 8-7 • Porosity ϕ_{CP} = 0.4 • V_{CP} from Table 8.2-4, Equation 8-6	• Same as Seep Case
		Volume of water: • S_w = water saturation in CP = 1.0 • Water volume = $S_w V_{CP}$	Volume of water: • $S_{we,CP}$ = effective water saturation in CP from adsorbed water (in-package diffusion submodel); Table 8.2-4, Equation 8-5 • $S_{we,CP}$ function of RH and sampled specific surface area of CP CP_Spec_Surf_Area • Water volume = $S_{we,CP} V_{CP}$
	Advection and Diffusion	Advective flux = volumetric flow rate through the WP	• No advective flux
		Diffusive area: • Total area of all waste package breaches	• Same as Seep Case
		Diffusion path length: • Sampled parameter Diff_Path_Length_CP_CSNF	• Same as Seep Case

Table 8.2-1. Parameters for EBS Transport Abstraction (Continued)

Waste Type	Transport Properties	Seep Case	No-Seep Case
	Advection and Diffusion	Diffusion coefficient in corrosion products, D_{CP}: • $\phi_{CP}S_wD_{CP} = \phi_{CP}^{1.3}S_w^2D_0$ • ϕ_{CP} = porosity of CP = 0.4 • S_w = water saturation in CP = 1.0 • D_0 = free water diffusion coefficient (D_{CP} is an effective value defined in the same manner as D_s in Equation 6.3.4.3.5-2.)	Diffusion coefficient in corrosion products, D_{CP}: • $\phi_{CP}S_{we,CP}D_{CP} = \phi_{CP}^{1.3}S_{we,CP}^2D_0$ • $S_{we,CP}$ = effective water saturation in CP from adsorbed water (in-package diffusion submodel); Table 8.2-4, Equation 8-5 • $S_{we,CP}$ function of RH and sampled specific surface area of CP CP_Spec_Surf_Area • ϕ_{CP} = porosity of CP = 0.4 • D_0 = free water diffusion coefficient
Codisposal	Bulk volume and water volume	Pore volume of corrosion products, V_{CP}: • Same as for CSNF Seep Case • ϕ_{CP} = porosity of CP = 0.4 • S_w = water saturation in CP = 1.0	• Same as Seep Case
		Volume of water: • Water volume = max[S_wV_{CP}, $S_w\phi_{DSNF}V_{DSNF}$]	• Same as Seep Case
	Advection and Diffusion	Advective flux = volumetric flow rate through the WP Diffusive area: • Same as for CSNF Seep Case Diffusion path length: • Sampled parameter Diff_Path_Length_CP_CDSP Diffusion coefficient in corrosion products, D_{CP}: • $\phi_{CP}S_wD_{CP} = \phi_{CP}^{1.3}S_w^2D_0$ • ϕ_{CP} = porosity of CP = 0.4 • S_w = water saturation = 1.0 • D_0 = free water diffusion coefficient (D_{CP} is an effective value defined in the same manner as D_s in Equation 6.3.4.3.5-2.)	• No advective flux • Diffusive properties same as Seep Case

Output DTN: SN0410T0507703.018.

CP = corrosion products; DSNF = defense spent nuclear fuel.

As a bounding approach, no credit is taken for retardation due to reversibly sorbed radionuclides on waste package corrosion products. Thus, sorption distribution coefficients are set to zero for all radionuclides (Table 8.2-3; output DTN: MO0506SPAINPAR.000). Nonzero K_d values, an alternative conceptual model described in Section 6.6.6, are given in DTN: SN0410T0507703.018.

The ranges and distributions of radionuclide sorption distribution coefficients for sorption on devitrified unsaturated zone tuff given in Table 4.1-15 (DTN: LA0408AM831341.001 [DIRS 171584]) are assigned to K_d values on crushed tuff in the invert. Correlations for sampling sorption distribution coefficient probability distributions for devitrified UZ tuff given in Table 4.1-16 (DTN: LA0311AM831341.001 [DIRS 167015]) are assigned to invert crushed tuff.

Sorption distribution coefficient (K_d) values and interval probabilities used for reversible radionuclide sorption on colloids in TSPA-LA calculations are provided by DTN: SN0306T0504103.006 [DIRS 164131], Table 1.

Parameter ranges and distributions for irreversible sorption of plutonium and americium onto stationary waste package corrosion products are given in Table 6.3-6 and summarized in output DTN: SN0508T0503305.003.

Table 8.2-2 summarizes various sampled parameters to be used in the EBS radionuclide transport abstraction, with the range and distribution of each parameter provided. This table is itself a summary of Table 6.5-6, which, along with the rest of Section 6.5.2, gives further details about each parameter and the location in this document where the parameter is developed. A summary of fixed, single-value parameters to be used in the EBS radionuclide transport abstraction is given in Table 8.2-3 (output DTNs: SN0410T0507703.018 and MO0506SPAINPAR.000). Equations used to compute various parameters in the EBS radionuclide transport abstraction are shown in Table 8.2-4.

Table 8.2-2. Sampled Model Inputs Used in the EBS Radionuclide Transport Abstraction

Input Name	Input Description	Range	Distribution
Invert_Diff_Coeff_Uncert	Invert diffusion coefficient uncertainty; Table 8.2-4, Equation 8-1	Range: $10^{\mu \pm 3\sigma}$ (dimensionless) Mean: $\mu = 0.033$; Std. Dev. $\sigma = 0.218$	10ND
SS_Corrosion_Rate	Stainless steel corrosion rate (DTN: MO0409SPAACRWP.000 [DIRS 172059]; Spreadsheet "ECDF_metals2.xls"; Worksheet "316 ss", Columns L & M, Rows 5–15); cumulative distribution function	**Rate (μm yr^{-1})** 0.03699 0.037 0.1016 0.109 0.1524 0.154 0.1778 0.2032 0.2286 0.254 0.2794 0.51	**CDF** 0.000 0.063 0.125 0.188 0.250 0.313 0.375 0.438 0.563 0.750 0.813 1.000
CS_Corrosion_Rate	Carbon steel corrosion rate (DTN: MO0409SPAACRWP.000 [DIRS 172059]; Spreadsheet "ECDF_metals2.xls"; Worksheet "A516-Carbon Steel", Columns B & C, Rows 5-30);cumulative distribution function	**Rate (μm yr^{-1})** 65.76 65.77 66.75 69.84 70.00 71.25 72.21 72.64 72.87 72.89 73.47 74.29 74.51 74.60 75.41 77.31 79.29 80.00 80.87 83.26 83.66 83.74 85.68 90.97 106.93	**CDF** 0.000 0.042 0.083 0.125 0.167 0.208 0.250 0.292 0.333 0.375 0.417 0.458 0.500 0.542 0.583 0.625 0.667 0.708 0.750 0.792 0.833 0.875 0.917 0.958 1.000
Diff_Path_Length_CP_CSNF	Diffusive path length through corrosion products domain for CSNF packages	0.02 – 0.859 m	Uniform
Diff_Path_Length_CP_CDSP	Diffusive path length through corrosion products domain for codisposal packages	0.025 – 1.063 m	Uniform
CP_Spec_Surf_Area	Specific surface area of Fe_2O_3 corrosion products	1.0 – 22 m^2 g^{-1}	Uniform
DS_Flux_Uncertainty	Drip shield flux splitting uncertainty factor	0 – 0.85 (dimensionless)	Uniform

Table 8.2-2. Sampled Model Inputs Used in the EBS Radionuclide Transport Abstraction (Continued)

Input Name	Input Description	Range	Distribution
WP_Flux_Uncertainty	Waste package flux splitting uncertainty factor	0 – 2.41 (dimensionless)	Uniform
Fracture_Frequency	Unsaturated zone fracture frequency (BSC 2004 [DIRS 170040], Appendix A, Table A-1)	Mean=3.16 m^{-1} Std. Dev.=2.63 m^{-1}	Log-normal
UZ_Fracture_Fraction	Unsaturated zone fracture porosity (BSC 2004 [DIRS 170040], Appendix D, Table D-1)	0 – 1 (fraction); $E(x)=9.6 \times 10^{-3}$; $\sigma(x)=2.82 \times 10^{-3}$	Beta
UZ_Matrix_Porosity	Unsaturated zone matrix porosity (BSC 2004 [DIRS 170040], Appendix D, Table D-1)	0 – 1 (fraction); $E(x)=0.131$; $\sigma(x)=0.031$	Beta
Fracture_Saturation	Unsaturated zone fracture saturation (DTN: LB0307FMRADTRN.001 [DIRS 165451])	Uniform sampling from 433 locations for each infiltration case	Provided in source DTN
Fracture_Residual_Sat	Unsaturated zone fracture residual saturation (DTN: LB0307FMRADTRN.001 [DIRS 165451])	Uniform sampling from 433 locations	Provided in source DTN
Fracture_Percolation_Flux	Unsaturated zone fracture percolation flux (DTN: LB0307FMRADTRN.001 [DIRS 165451])	Uniform sampling from 433 locations for each infiltration case	Provided in source DTN
Flow_Focus_Factor	Unsaturated zone fracture percolation flow-focusing factor (DTN: LB0307FMRADTRN.001 [DIRS 165451])	Uniform sampling from 433 locations for each infiltration case	Provided in source DTN
UZ_Matrix_Saturation	Unsaturated zone matrix saturation (DTN: LB0307FMRADTRN.001 [DIRS 165451])	Uniform sampling from 433 locations for each infiltration case	Provided in source DTN
Matrix_Percolation_Flux	Unsaturated zone matrix percolation flux (DTN: LB0307FMRADTRN.001 [DIRS 165451])	Uniform sampling from 433 locations for each infiltration case	Provided in source DTN
Matrix_Rel_Perm_Low, Matrix_Rel_Perm_Mean, Matrix_Rel_Perm_High	Unsaturated zone matrix relative permeability for all three infiltration cases (DTN: LB0307FMRADTRN.001 [DIRS 165451])	Uniform sampling from 433 locations for each infiltration case	Provided in source DTN

Output DTN: SN0410T0507703.018.

NOTES: ND = Truncated normal distribution
$E(x)$ = Expected value
$\sigma(x)$ = Standard deviation
CDF = cumulative distribution function.

Table 8.2-3. Fixed Model Inputs Used in the EBS Radionuclide Transport Abstraction

Input Name	Input Description	Source, or Developed in *EBS RT Abstraction*	Value
Max_Mass_CP_CSNF	Mass of corrosion products in CSNF waste package	Developed: Table 6.3-4	19,440 kg
Max_Mass_CP_HLW	Mass of corrosion products in CDSP waste package	Developed: Table 6.3-4	14,230 kg
Max_Thick_CS	Maximum thickness of carbon steel waste package internal components	IED BSC 2004 [DIRS 169472]	10 mm
Max_Thick_SS	Maximum thickness of stainless steel waste package internal components	IED BSC 2004 [DIRS 167394]	50.8 mm
DS_Total_Length	Length of drip shield	IED BSC 2005 [DIRS 173303], Table 1	5,805 mm
Density_CP	Density of corrosion products	Weast 1985 [DIRS 111561]	5,240 kg m^{-3}
Porosity_CP	Porosity of corrosion products	Developed: Section 6.3.4.3.4	0.4 (fraction)
Width_Invert	Width of invert	Developed: Equation 6.5.3.3-1	4.00 m
Thick_Invert	Average thickness of invert (flow and diffusive path length)	Developed: Equation 6.5.3.3-5	0.597 m
Vert_Cross_Sect_Area_Invert	Vertical cross sectional area of invert	Developed: Equation 6.5.3.3-2	2.39 m^2
Density_Water	Water density at 25°C	Weast 1985 [DIRS 111561]	997.0449 kg m^{-3}
Viscosity_Water	Water viscosity at 25°C	Lide 2000 [DIRS 162229]	0.890×10^{-3} Pa s (0.000890 kg m^{-1} s^{-1})
Intergranular_Porosity_Invert	Porosity of crushed tuff invert ballast	BSC 2005 [DIRS 173944], Appendix X	0.45 (fraction)
Invert_Viscosity_Ref_Temp	Reference temperature for viscosity giving temperature dependence of invert diffusion coefficient	Reference temperature for free water diffusion coefficient (25°C)	298.15 K
Interface_Scale_Factor	Scale factor used in numerical approximation for computing mass flux distribution from single-continuum to dual-continuum medium	Developed: Section 6.5.3.5	1×10^{-6} (dimensionless)
Intragranular_Porosity_Invert	Porosity of TSw35 tuff rock matrix (used in dual-continuum invert alternative conceptual model)	DTN: LB0207REVUZPRP.002 [DIRS 159672], Spreadsheet "Matrix_Props.xls", Row 20, Column C	0.131 (fraction)
Fracture_Aperture	Unsaturated zone fracture aperture	DTN: LB0205REVUZPRP.001 [DIRS 159525], Spreadsheet "FRACTURE_PROPERTY .xls," Row 20, Column L	1.5×10^{-4} m

Table 8.2-3. Fixed Model Inputs Used in the EBS Radionuclide Transport Abstraction (Continued)

Input Name	Input Description	Source, or Developed in *EBS RT Abstraction*	Value
Fracture_Interface_Area	Unsaturated zone fracture interface area	DTN: LB0205REVUZPRP.001 [DIRS 159525], Spreadsheet "FRACTURE_PROPERTY .xls," Row 20, Column R	9.68 m^2 m^{-3}
Active_Fracture_Parameter	Unsaturated zone active fracture parameter for TSw35 for all three infiltration cases	DTN: LB03013DSSCP3I.001 [DIRS 162379]	Low=0.476 Mean=0.569 High=0.570 (dimensionless)
Matrix_Perm_TSW33	Unsaturated zone matrix permeability for TSw33 for all three infiltration cases	DTNs: LB0208UZDSCPLI.002 [DIRS 161788]	Low=1.60 × 10^{-18} m^2
		LB0208UZDSCPMI.002 [DIRS 161243]	Mean=6.57 × 10^{-18} m^2
		LB0302UZDSCPUI.002 [DIRS 161787]	High=2.39 × 10^{-17} m^2
Matrix_Perm_TSW34	Unsaturated zone matrix permeability for TSw34 for all three infiltration cases	DTNs: LB0208UZDSCPLI.002 [DIRS 161788];	Low=1.38 × 10^{-19} m^2
		LB0208UZDSCPMI.002 [DIRS 161243]	Mean=1.77 × 10^{-19} m^2
		LB0302UZDSCPUI.002 [DIRS 161787]	High=2.96 × 10^{-19} m^2
Matrix_Perm_TSW35	Unsaturated zone matrix permeability for TSw35 for all three infiltration cases	DTNs: LB0208UZDSCPLI.002 [DIRS 161788]	Low=2.33 × 10^{-18} m^2
		LB0208UZDSCPMI.002 [DIRS 161243]	Mean=4.48 × 10^{-18} m^2
		LB0302UZDSCPUI.002 [DIRS 161787]	High=8.55 × 10^{-18} m^2
Matrix_Perm_TSW36	Unsaturated zone matrix permeability for TSw36 for all three infiltration cases	DTNs: LB0208UZDSCPLI.002 [DIRS 161788]	Low=5.58 × 10^{-19} m^2
		LB0208UZDSCPMI.002 [DIRS 161243]	Mean=2.00 × 10^{-19} m^2
		LB0302UZDSCPUI.002 [DIRS 161787]	High=7.41 × 10^{-19} m^2
UZ_Matrix_Density	Unsaturated zone dry matrix density for TSw35	DTN: SN0404T0503102.011 [DIRS 169129]	1,980 kg m^{-3}
Diff_Thick_OB_CDSP	Outer barrier thickness for CDSP waste package	Section 6.5.2.4	0.025 m
Diff_Thick_OB_CSNF	Outer barrier thickness for CSNF waste package	Section 6.5.2.4	0.02 m
DS_Patch_Area	Area of a drip shield patch for analysis of the flux splitting experiments	Section 6.5.1.1.1	7.214 × 10^4 mm^2
DS_Total_Width	Width of unfolded drip shield	Figure 4.1-1	4880 mm

Table 8.2-3. Fixed Model Inputs Used in the EBS Radionuclide Transport Abstraction (Continued)

Input Name	Input Description	Source, or Developed in *EBS RT Abstraction*	Value
Porosity_DSNF	DSNF porosity	Table 8.2-1	0.2 (dimensionless)
Rind_Saturation_CDSP	Saturation of the CDSP waste form rind	Table 8.2-1	1 (dimensionless)
Rind_Saturation_CSNF	Saturation of the CSNF waste form rind	Table 8.2-1	1 (dimensionless)
WP_Crack_Area	Area of a single crack on the waste package	Section 6.3.3.1.2.1	7.7×10^{-6} m^2
X_length_1	Width of cells to the left and right of the middle cells	Section 6.5.3.6	5.5 m
Z_length_1	Depth of first layer of matrix-fracture cells	Section 6.5.3.6	0.6567 m
Z_length_2	Depth of second layer of matrix-fracture cells	Section 6.5.3.6	1.3134 m
Z_length_3	Depth of third layer of matrix-fracture cells	Section 6.5.3.6	5 m
Z_length_4	Depth of fourth layer of matrix-fracture cells	Section 6.5.3.6	10 m
Kd_Ac_FeOx_CP_a	K_d value for reversible sorption of Ac onto stationary corrosion products	Section 6.3.4.2.3	0 ml g^{-1}
Kd_Am_FeOx_CP_a	K_d value for reversible sorption of Am onto stationary corrosion products	Section 6.3.4.2.3	0 ml g^{-1}
Kd_C_FeOx_CP_a	K_d value for reversible sorption of C onto stationary corrosion products	Section 6.3.4.2.3	0 ml g^{-1}
Kd_Cs_FeOx_CP_a	K_d value for reversible sorption of Cs onto stationary corrosion products	Section 6.3.4.2.3	0 ml g^{-1}
Kd_I_FeOx_CP_a	K_d value for reversible sorption of I onto stationary corrosion products	Section 6.3.4.2.3	0 ml g^{-1}
Kd_Np_FeOx_CP_a	K_d value for reversible sorption of Np onto stationary corrosion products	Section 6.3.4.2.3	0 ml g^{-1}
Kd_Pu_FeOx_CP_a	K_d value for reversible sorption of Pu onto stationary corrosion products	Section 6.3.4.2.3	0 ml g^{-1}
Kd_Tc_FeOx_CP_a	K_d value for reversible sorption of Tc onto stationary corrosion products	Section 6.3.4.2.3	0 ml g^{-1}
Kd_Th_FeOx_CP_a	K_d value for reversible sorption of Th onto stationary corrosion products	Section 6.3.4.2.3	0 ml g^{-1}
Kd_U_FeOx_CP_a	K_d value for reversible sorption of U onto stationary corrosion products	Section 6.3.4.2.3	0 ml g^{-1}

Table 8.2-3. Fixed Model Inputs Used in the EBS Radionuclide Transport Abstraction (Continued)

Input Name	Input Description	Source, or Developed in *EBS RT Abstraction*	Value
Kd_Pa_FeOx_CP_a	K_d value for reversible sorption of Pa onto stationary corrosion products	Section 6.3.4.2.3	0 ml g^{-1}
Kd_Ra_FeOx_CP_a	K_d value for reversible sorption of Ra onto stationary corrosion products	Section 6.3.4.2.3	0 ml g^{-1}
Kd_Sr_FeOx_CP_a	K_d value for reversible sorption of Sr onto stationary corrosion products	Section 6.3.4.2.3	0 ml g^{-1}

Output DTNs: SN0410T0507703.018 and MO0506SPAINPAR.000.

IED = information exchange drawing

Table 8.2-4. Calculated Model Inputs Used in the EBS Radionuclide Transport Abstraction

Input Description	Input Equation and Parameter Description
Equation 8-1 Invert diffusion coefficient (Equation 6.3.4.1.1-22)	$\phi S_w D_I = D_0 \phi^{1.863} S_w^{1.863} 10^{ND(\mu=0.033,\sigma=0.218)}$ D_I = effective invert diffusion coefficient ($cm^2\ s^{-1}$) D_0 = free water diffusion coefficient ($cm^2\ s^{-1}$) ϕ = invert bulk porosity (fraction) S_w = invert water saturation (fraction) ND = truncated normal distribution (±3 standard deviations from the mean) μ = mean σ = standard deviation (D_I is an effective value that includes the effects of tortuosity.)
Equation 8-2 Temperature modification for invert diffusion coefficient (Equation 6.3.4.1.2-4)	$D_T = D_{T_0} \frac{T}{T_0} 10^{\left[\frac{1.3272(293.15-T_0)-0.001053(T_0-293.15)^2}{T_0-168.15}\right]-\left[\frac{1.3272(293.15-T)-0.001053(T-293.15)^2}{T-168.15}\right]}$ D_T = invert diffusion coefficient at temperature T ($cm^2\ s^{-1}$) D_{T_0} = invert diffusion coefficient at temperature T_0 ($cm^2\ s^{-1}$) T = temperature (K); valid range: 293.15 K ≤ T ≤ 373.15 K T_0 = reference temperature (K) (Invert_Viscosity_Ref_Temp)
Equation 8-3 Diffusion coefficient of unsaturated zone matrix and fractures (Equation 6.5.3.6-2)	$\log_{10} D_{ms} = -3.49 + 0.0138\theta_m + 0.165 \log_{10} k_{me}$ D_{ms} = diffusion coefficient of unsaturated zone matrix ($cm^2\ s^{-1}$) θ_m = unsaturated zone matrix water content (percent) k_{me} = effective permeability of unsaturated zone matrix (m^2) (D_{ms} is an effective value that includes the effects of tortuosity in the rock matrix.)

Table 8.2-4. Calculated Model Inputs Used in the EBS Radionuclide Transport Abstraction (Continued)

Input Description	Input Equation and Parameter Description
Equation 8-4 Effective permeability of unsaturated zone matrix (Equation 6.5.3.6-3)	$k_{me} = k_{rm} k_m$ k_{me} = effective permeability of unsaturated zone tuff matrix (m^2) k_{rm} = relative permeability of unsaturated zone tuff matrix (dimensionless) k_m = intrinsic permeability of unsaturated zone tuff matrix (m^2) (Matrix_Perm_TSWxx, xx = 33, 34, 35, 36)
Equation 8-5 Effective water saturation of corrosion products (Equation 6.3.4.3.5-5)	$S_{we,CP} = 3.28 \times 10^{-6} \bar{s}_{CP} (-\ln RH)^{-1/2.45}$ $S_{we,CP}$ = effective water saturation of corrosion products $\bar{s}_{CP}$ = specific surface area of corrosion products (m^2 kg^{-1}) (CP_Spec_Surf_Area) RH = relative humidity
Equation 8-6 Pore volume of corrosion products (Equation 6.5.3.1.1-1)	$V_{CP} = \frac{m_{CP}}{\rho_{FeOx}} \left(\frac{\phi_{CP}}{1 - \phi_{CP}} \right)$ V_{CP} = pore volume of corrosion products (m^3) m_{CP} = mass of corrosion products (kg) ρ_{FeOx} = density of corrosion products (kg m^{-3}) (Density_CP) ϕ_{CP} = porosity of corrosion products (m^3 void m^{-3} bulk volume) (Porosity_CP)

Table 8.2-4. Calculated Model Inputs Used in the EBS Radionuclide Transport Abstraction (Continued)

Input Description	Input Equation and Parameter Description
Equation 8-7 Mass of corrosion products (Equations 6.5.3.2-1 to 6.5.3.2-5)	$m_{CP}(t) = m_{CP1} + m_{CP2}$ m_{CP} = mass of corrosion products (kg) t = time since waste package emplacement (yr) t_0 = time when waste package breach occurs (yr) $m_{CP1} = \begin{cases} \left(\frac{t-t_0}{t_{f1}}\right)\frac{1}{3}m_{CPf}, & t-t_0 \le t_{f1} \\ \frac{1}{3}m_{CPf}, & t-t_0 > t_{f1} \end{cases}$ m_{CPf} = mass of corrosion products when internal components are fully degraded (kg) (Max_Mass_CP_CSNF or Max_Mass_CP_HLW) t_{f1} = lifetime of carbon steel (yr) $= \frac{1000\,(\text{Max_Thick_CS})}{r_1}$ r_1 = corrosion rate of carbon steel (μm yr^{-1}) (CS_Corrosion_Rate) $m_{CP2} = \begin{cases} \left(\frac{t-t_0}{t_{f2}}\right)\frac{2}{3}m_{CPf}, & t-t_0 \le t_{f2} \\ \frac{2}{3}m_{CPf}, & t-t_0 > t_{f2} \end{cases}$ t_{f2} = lifetime of stainless steel (yr) $= \frac{1000\,(\text{Max_Thick_SS})}{r_2}$ r_2 = corrosion rate of stainless steel (μm yr^{-1}) (SS_Corrosion_Rate)

Output DTN: SN0410T0507703.018.

Input parameters for the dual-continuum invert alternative conceptual model are listed in Table 8.2-5. Equations for calculating the intergranular and intragranular diffusion coefficients are listed in Table 8.2-6.

Table 8.2-5. Invert Diffusion Coefficient Alternative Conceptual Model Parameters

Input Name	Input Description	Where Developed in *EBS RT Abstraction*	Value
Invert_Geometry_Coef	Dimensionless geometry-dependent coefficient for intergranular-intragranular mass transfer coefficient	Section 6.6.4.1	8 - 21 (dimensionless) Uniform
Diff_Length_Inv_Inter_Intra	Characteristic length of the matrix structure	Section 6.6.4.1	5 mm
Crit_Moisture_Content_Intra	Critical moisture content of invert intragranular continuum	Section 6.6.5.1	0.089 (fraction)
Crit_Moisture_Content_Inter	Critical moisture content of invert intergranular continuum	Section 6.6.5.1	0.00932 – 0.0612 Uniform
Diff_Threshold_Invert	Threshold value of diffusion coefficient in intragranular invert continuum	Section 6.6.5.2	1×10^{-12} cm^2 s^{-1}
Sat_Diff_Coeff_Matrix	Diffusion coefficient in saturated UZ matrix	Section 6.6.5.2	9.24×10^{-7} cm^2 s^{-1}

Output DTN: SN0410T0507703.018.

Table 8.2-6. Calculated Model Inputs Used in the EBS Radionuclide Transport Abstraction Invert Diffusion Coefficient Alternative Conceptual Model

Input Description	Input Equation and Parameter Description
Equation 8-8 Invert intergranular continuum diffusion coefficient (Equation 6.6.5.2-3)	$D_{inter} = 0.45 D_0 \left(\frac{\theta}{100\phi_{inter}}\right)\left(\frac{\theta - \theta_C}{100\phi_I - \theta_C}\right), \quad \theta \geq \theta_C$ $D_{inter} = D_{limit}, \quad \theta < \theta_C$ D_0 = free water diffusion coefficient (cm^2 s^{-1}) D_{inter} = invert intergranular continuum diffusion coefficient (cm^2 s^{-1}) $\phi_I = \phi_{inter} + (1 - \phi_{inter})\phi_{intra}$ = bulk porosity of invert (fraction) ϕ_{inter} = invert intergranular continuum porosity (fraction) (Intergranular_Porosity_Invert) ϕ_{intra} = invert intragranular continuum porosity (fraction) (Intragranular_Porosity_Invert) θ = invert bulk moisture content (percent) θ_C = invert intergranular continuum critical moisture content (percent) (Crit_Moisture_Content_Inter)

Table 8.2-6. Calculated Model Inputs Used in the EBS Radionuclide Transport Abstraction Invert Diffusion Coefficient Alternative Conceptual Model (Continued)

Input Description	Input Equation and Parameter Description
Equation 8-9 Invert intragranular continuum diffusion coefficient (Equations 6.6.5.2-5 and 6.6.5.2-6)	$D_{intra} = D_{ms}\left(\frac{\theta_{intra}}{100\phi_{intra}}\right)^p, \quad \theta_{intra} \geq \theta_{min}$ $D_{intra} = D_{limit}, \quad \theta_{intra} < \theta_{min}$ D_{intra} = invert intragranular continuum diffusion coefficient ($cm^2\ s^{-1}$) D_{ms} = tuff matrix saturated diffusion coefficient ($cm^2\ s^{-1}$) (Sat_Diff_Coeff_Matrix) D_{limit} = threshold value of diffusion coefficient in intragranular invert continuum ($cm^2\ s^{-1}$) (Diff_Threshold_Invert) θ_{intra} = invert intragranular continuum moisture content (percent) ϕ_{intra} = invert intragranular continuum porosity (fraction) (Intragranular_Porosity_Invert) $p = \frac{\log_{10} D_{limit} - \log_{10} D_{ms}}{\log_{10}\left(\frac{\theta_{min}}{100}\right) - \log_{10}\phi_{intra}}$ θ_{min} = critical moisture content of invert intragranular continuum (percent) (Crit_Moisture_Content_Intra)

Output DTN: SN0410T0507703.018.

8.3 EVALUATION OF YUCCA MOUNTAIN REVIEW PLAN CRITERIA

This model report documents the abstraction model for flow of liquid and transport of radionuclides through the EBS. This section provides responses to the *Yucca Mountain Review Plan, Final Report* acceptance criteria applicable to this model report. Being conceptual in nature, it is not possible to evaluate quantitatively many of the *Yucca Mountain Review Plan, Final Report* (NRC 2003 [DIRS 163274]) acceptance criteria in Section 4.2.1.

The relevance of this model report to *Yucca Mountain Review Plan, Final Report* (NRC 2003 [DIRS 163274], Section 2.2.1.3.3) criteria for "Quantity and Chemistry of Water Contacting Engineered Barriers and Waste Forms," which are based on meeting the requirements of 10 CFR 63.114(a)–(c) and (e)–(g) [DIRS 173273], is as follows:

Acceptance Criterion 1–System Description and Model Integration are Adequate.

(1) Total system performance assessment adequately incorporates important design features, physical phenomena, and couplings, and uses consistent and appropriate assumptions throughout the quantity and chemistry of water contacting engineered barriers and waste forms abstraction process.

Response: The EBS radionuclide transport abstraction incorporates important design features, physical phenomena, and couplings, and uses consistent assumptions throughout the evaluation of the quantity of water contacting engineered barriers and waste forms. Sections 6.3.2 and 6.3.3 describe the conceptual model for water flux through the EBS. Section 6.5.1 describes the mathematical description of the EBS flow model. These sections provide information on seepage, effectiveness of the EBS components and mechanisms for breach or failure of the drip shield and waste package. Important general technical information related to water flow through the EBS can also be found throughout Section 6.

(2) The abstraction of the quantity and chemistry of water contacting engineered barriers and waste forms uses assumptions, technical bases, data, and models, that are appropriate and consistent with other related U.S. Department of Energy abstractions. For example, the assumptions used for the quantity and chemistry of water contacting engineered barriers and waste forms are consistent with the abstractions of "Degradation of Engineered Barriers" (NRC 2003 [DIRS 163274], Section 2.2.1.3.1); "Mechanical Disruption of Engineered Barriers" (NRC 2003 [DIRS 163274], Section 2.2.1.3.2); "Radionuclide Release Rates and Solubility Limits" (Section 2.2.1.3.4); "Climate and Infiltration" (NRC 2003 [DIRS 163274], Section 2.2.1.3.5); and "Flow Paths in the Unsaturated Zone" (NRC 2003 [DIRS 163274], Section 2.2.1.3.6). The descriptions and technical bases provide transparent and traceable support for the abstraction of quantity and chemistry of water contacting engineered barriers and waste forms.

Response: The EBS radionuclide transport abstraction uses assumptions, technical bases, data, and models that are consistent with other related U.S. Department of Energy abstractions. Sections 6.3.2, 6.3.3 and 6.5.1 of this model report provide descriptions and technical bases to support the quantity-related portion of the abstraction of quantity and chemistry of water contacting engineered barriers and waste forms. Section 5 provides assumptions that are relevant to the EBS flow model.

(3) Important design features, such as waste package design and material selection, drip shield, ground support, thermal loading strategy, and degradation processes, are considered during the determination of initial and boundary conditions for calculations of the quantity of water contacting engineered barriers and waste forms.

Response: Sections 6.3 and 6.5 provide the technical bases and details of model features for the EBS flow model. Section 6.3.2 describes drip shield design, effectiveness and breaching. Section 6.3.3 describes waste package design, breaching and impact of heat generation. Sections 6.3.3 and 6.5.3 provide invert model features.

(4) The U.S. Department of Energy reasonably accounts for the range of environmental conditions expected inside breached waste packages and in the engineered barrier environment surrounding the waste package. For example, the U.S. Department of Energy should provide a description and sufficient technical bases for its abstraction of changes in hydrologic properties in the near field, caused by coupled thermal-hydrologic-mechanical-chemical processes.

Response: Spatial and temporal abstractions address physical couplings (thermal-hydrologic-mechanical-chemical). Sections 6.3 and 6.5 provide descriptions of coupled effects for the flow model. These effects include heat generation inside the waste package and condensation on the drip shield surface. The seepage and imbibition fluxes are also the product of coupled thermal-hydrologic-mechanical-chemical processes.

(5) Sufficient technical bases and justification are provided for total system performance assessment assumptions and approximations for modeling coupled thermal-hydrologic mechanical-chemical effects on seepage and flow, the waste package chemical environment, and the chemical environment for radionuclide release. The effects of distribution of flow on the amount of water contacting the engineered barriers and waste forms are consistently addressed, in all relevant abstractions.

Response: The technical bases and justification are provided for total system performance assessment assumptions and approximations for modeling coupled thermal-hydrologic-mechanical-chemical effects on flow and radionuclide release throughout Sections 5 and 6. The effects of distribution of flow on the amount of water contacting the engineered barriers and waste forms are consistently addressed in Sections 6.3 and 6.5.

(6) The expected ranges of environmental conditions within the waste package emplacement drifts, inside of breached waste packages, and contacting the waste forms and their evolution with time are identified.

Response: These are provided in Sections 6.3, 6.5 and 6.7. Examples include the effects of the drip shield on the quantity of water (Sections 6.3.2 and 6.5.1); conditions that promote corrosion of engineered barriers and degradation of waste forms (Sections 6.3 and 6.5); wet and dry cycles; and size and distribution of penetrations of engineered barriers.

(7) The model abstraction for quantity and chemistry of water contacting engineered barriers and waste forms is consistent with the detailed information on engineered barrier design and other engineered features. For example, consistency is demonstrated for: (i) dimensionality of the abstractions; (ii) various design features and site characteristics; and (iii) alternative conceptual approaches. Analyses are adequate to demonstrate that no deleterious effects are caused by design or site features that the U.S. Department of Energy does not take into account in this abstraction.

Response: The EBS radionuclide transport abstraction is consistent with detailed information on engineered barrier design and other engineered features. Analysis discussions in Section 6 demonstrate that no deleterious effects are caused by design or site features that are not taken into account in this abstraction. Section 6.7 provides a summary discussion on the capability of the engineered barriers.

(8) Adequate technical bases are provided, including activities such as independent modeling, laboratory or field data, or sensitivity studies, for inclusion of any thermal-hydrologic-mechanical-chemical couplings and features, events, and processes.

Response: Technical bases are provided, including activities such as independent modeling, laboratory or field data, or sensitivity studies, for inclusion of any thermal-hydrologic-mechanical-chemical couplings and features, events, and processes. These are provided throughout Sections 6 and 7.

(9) Performance-affecting processes that have been observed in thermal-hydrologic tests and experiments are included into the performance assessment. For example, the U.S. Department of Energy either demonstrates that liquid water will not reflux into the underground facility or incorporates refluxing water into the performance assessment calculation, and bounds the potential adverse effects of alteration of the hydraulic pathway that result from refluxing water.

Response: Performance-affecting processes that have been observed in thermal-hydrologic tests and experiments are included primarily through the inputs (e.g., seepage values from *Abstraction of Drift Seepage* (BSC 2004 [DIRS 169131]), described in Section 6.3.2 of this model report, required to implement the EBS radionuclide transport abstraction.

Acceptance Criterion 2–Data are Sufficient for Model Justification.

(1) Geological, hydrological, and geochemical values used in the license application are adequately justified. Adequate description of how the data were used, interpreted, and appropriately synthesized into the parameters is provided.

Response: The EBS radionuclide transport abstraction provides the technical justification for geological, hydrological, and geochemical values used. There is also a description of how the data were used, interpreted, and synthesized into associated parameter values. Section 6.5.2 provides a summary discussion on the use and interpretation of data used in the EBS flow and transport models. The discussion includes the range, distribution and uncertainty of model data. Detailed description of data and technical justification of values used are provided throughout Sections 6.3 and 6.5.

(2) Sufficient data were collected on the characteristics of the natural system and engineered materials to establish initial and boundary conditions for conceptual models of thermal-hydrologic-mechanical-chemical coupled processes, that affect seepage and flow and the engineered barrier chemical environment.

Response: Data and sources of data are provided in Section 4.1 on the characteristics of the natural system and engineered materials needed to establish initial and boundary conditions for conceptual models of thermal-hydrologic-mechanical-chemical coupled processes that affect flow. Collection of input data used in this model report was done using acceptable techniques under the YMP quality assurance plan; specific techniques are provided in Sections 4.1.1 to 4.1.3.

(4) Sufficient information to formulate the conceptual approach(es) for analyzing water contact with the drip shield, engineered barriers, and waste forms is provided.

Response: Information required to formulate the conceptual approaches for analyzing water contact with the drip shield, engineered barriers, and waste forms is provided in Sections 6.3 and 6.5. Sections 6.3.2, 6.3.3 and 6.5.1 present the conceptual models used for water flux through the Engineered Barrier System, together with information on drip shield effectiveness, drip shield and waste package breaching, seepage and imbibition flux from the unsaturated zone matrix.

Acceptance Criterion 3–Data Uncertainty Is Characterized and Propagated Through the Model Abstraction.

(1) Models use parameter values, assumed ranges, probability distributions, and bounding assumptions that are technically defensible, reasonably account for uncertainties and variabilities, and do not result in an under representation of the risk estimate.

Response: The EBS radionuclide transport abstraction uses parameter values, assumed ranges, probability distributions, and bounding assumptions that account for uncertainties and variabilities, and that do not result in an under-representation of the risk estimate. Section 4.1 lists the data and parameters used, together with their sources. Section 6.5.2 provides a summary of the base case model inputs together with associated uncertainties.

(2) Parameter values, assumed ranges, probability distributions, and bounding assumptions used in the total system performance assessment calculations of quantity and chemistry of water contacting engineered barriers and waste forms are technically defensible and reasonable, based on data from the Yucca Mountain region (e.g., results from large block and drift-scale heater and niche tests), and a combination of techniques that may include laboratory experiments, field measurements, natural analog research, and process-level modeling studies.

Response: Parameter values, assumed ranges, probability distributions, and bounding assumptions used in the total system performance assessment calculations of quantity of water contacting engineered barriers and waste forms are based on data from the Yucca Mountain region, laboratory experiments, field measurements, natural analog research, and process-level modeling studies. Section 4.1 lists the data and parameters used, together with their sources. Section 6.5.2 provides a summary of the base case model inputs together with associated uncertainties.

(3) Input values used in the total system performance assessment calculations of quantity and chemistry of water contacting engineered barriers (e.g., drip shield and waste package) are consistent with the initial and boundary conditions and the assumptions of the conceptual models and design concepts for the Yucca Mountain site. Correlations between input values are appropriately established in the U.S. Department of Energy total system performance assessment. Parameters used to define initial conditions, boundary conditions, and computational domain in sensitivity analyses involving coupled thermal-hydrologic-mechanical-chemical effects on seepage and flow, the waste package chemical environment, and the chemical environment for radionuclide release, are consistent with available data. Reasonable or conservative ranges of parameters or functional relations are established.

Response: Input values used in the total system performance assessment calculations of quantity of water contacting engineered barriers (e.g., drip shield and waste package) are consistent with the initial and boundary conditions and the assumptions of the conceptual models and design concepts for the Yucca Mountain site. Reasonable or conservative ranges of parameters or functional relations have been established. Section 4.1 lists the data and parameters used, together with their sources. Section 6.5.2 provides a summary of the base case model inputs together with associated uncertainties.

(4) Uncertainty is adequately represented in parameter development for conceptual models, process models, and alternative conceptual models considered in developing the abstraction of radionuclide release rates and solubility limits, either through sensitivity analyses or use of bounding analyses.

Response: Adequate representation of uncertainties in the characteristics of the natural system and engineered materials is provided in parameter development for conceptual models, process-level models, and alternative conceptual models. In some instances, uncertainty is constrained using conservative limits. Parameter development for the models described in this model report is provided throughout Sections 6.3, 6.4, 6.5 and 6.6.

Acceptance Criterion 4–Model Uncertainty Is Characterized and Propagated Through the Model Abstraction.

(1) Alternative modeling approaches of features, events, and processes are considered and are consistent with available data and current scientific understanding, and the results and limitations are appropriately considered in the abstraction.

Response: Alternative modeling approaches of features, events, and processes are considered in Sections 6.4 and 6.6 and are consistent with available data and current scientific understanding, and the results and limitations are considered.

(2) Alternative modeling approaches are considered and the selected modeling approach is consistent with available data and current scientific understanding. A description that includes a discussion of alternative modeling approaches not considered in the final analysis and the limitations and uncertainties of the chosen model is provided.

Response: Alternative modeling approaches are considered in Sections 6.4 and 6.6. The selected modeling approach is consistent with available data and current scientific understanding. A description that includes a discussion of alternative modeling approaches not considered in the final analysis and the limitations and uncertainties of the chosen model is provided.

(3) Consideration of conceptual model uncertainty is consistent with available site characterization data, laboratory experiments, field measurements, natural analog information and process-level modeling studies; and the treatment of conceptual model uncertainty does not result in an under-representation of the risk estimate.

Response: Consideration of conceptual model uncertainty is consistent with available site characterization data, laboratory experiments, field measurements, natural analog information and process-level modeling studies. The fundamental relationships, e.g., mass balance and flow equations, upon which the EBS radionuclide transport abstraction is based, are well-established with a long history of use in the scientific community and as such are not subject to significant uncertainty. In addition, the alternative conceptual models have been screened out (Section 6.4), thereby increasing confidence in the selected conceptual model. Other sources of uncertainty involve modeling choices (e.g., assumptions, geometry) that, because of their conservative nature, effectively bound uncertainty. This treatment of conceptual model uncertainty does not result in an under-representation of the risk estimate.

(4) Adequate consideration is given to effects of thermal-hydrologic-mechanical-chemical coupled processes in the assessment of alternative conceptual models. These effects may include: (i) thermal-hydrologic effects on gas, water, and mineral chemistry; (ii) effects of microbial processes on the engineered barrier chemical environment and the chemical environment for radionuclide release; (iii) changes in water chemistry that may result from the release of corrosion products from the engineered barriers and interactions between engineered materials and groundwater; and (iv) changes in boundary conditions (e.g., drift shape and size) and hydrologic properties, relating to the response of the geomechanical system to thermal loading.

Response: Consideration is given in Sections 6.4 and 6.6 to effects of thermal-hydrologic-mechanical-chemical coupled processes in the assessment of alternative conceptual models.

Acceptance Criterion 5–Model Abstraction Output Is Supported by Objective Comparisons.

(1) The models implemented in this total system performance assessment abstraction provide results consistent with output from detailed process-level models and/or empirical observations (laboratory and field testings and/or natural analogs).

Response: The models implemented in this total system performance assessment abstraction provide results consistent with output from detailed process-level models and/or empirical observations (laboratory testings). For example, Sections 6.5.1 and 7.1 provide comparison of the drip shield and waste package flux splitting models with breached drip shield and waste package experiments.

(2) Abstracted models for coupled thermal-hydrologic-mechanical-chemical effects on seepage and flow and the engineered barrier chemical environment, as well as on the chemical environment for radionuclide release, are based on the same assumptions and approximations demonstrated to be appropriate for process-level models or closely analogous natural or experimental systems. For example, abstractions of processes, such as thermally induced changes in hydrological properties, or estimated diversion of percolation away from the drifts, are adequately justified by comparison to results of process-level modeling, that are consistent with direct observations and field studies.

Response: Abstracted models for coupled thermal-hydrologic-mechanical-chemical effects on flow and radionuclide release are based on the same assumptions and approximations demonstrated to be appropriate for process-level models or closely analogous natural or experimental systems, as demonstrated throughout Sections 5 and 6.

(3) Accepted and well-documented procedures are used to construct and test the numerical models that simulate coupled thermal-hydrologic-mechanical-chemical effects on seepage and flow, engineered barrier chemical environment, and the chemical environment for radionuclide release. Analytical and numerical models are appropriately supported. Abstracted model results are compared with different mathematical models, to judge robustness of results.

Response: The EBS radionuclide transport abstraction uses accepted and well-documented procedures to construct and test the numerical models that simulate coupled thermal-hydrologic-mechanical-chemical effects on flow and radionuclide release, as provided throughout Sections 6 and 7. Technical support is presented for analytical and numerical models.

The relevance of this model report to the *Yucca Mountain Review Plan* criteria for "Radionuclide Release Rates and Solubility Limits" (NRC 2003 [DIRS 163274], Section 2.2.1.3.4), which are based on meeting the requirements of 10 CFR 63.114(a)–(c) and (e)–(g) [DIRS 173273], is as follows:

Acceptance Criterion 1–System Description and Model Integration Are Adequate.

(1) Total system performance assessment adequately incorporates important design features, physical phenomena, and couplings, and uses consistent and appropriate assumptions throughout the radionuclide release rates and solubility limits abstraction process.

Response: Total system performance assessment adequately incorporates important design features, physical phenomena, and couplings, and uses consistent and appropriate assumptions throughout the radionuclide release rates and solubility limits abstraction process. Section 6.3.4 describes the conceptual model for EBS transport model. Sections 6.5.1 and 6.5.3 describe the mathematical description of the EBS transport model components. These sections provide information on diffusion, retardation, transport through stress corrosion cracks and EBS-UZ boundary condition implementation. Important general technical information related to radionuclide transport through the EBS can also be found throughout Section 6.

(2) The abstraction of radionuclide release rates uses assumptions, technical bases, data, and models that are appropriate and consistent with other related U.S. Department of Energy abstractions. For example, the assumptions used for this model abstraction are consistent with the abstractions of "Degradation of Engineered Barriers" (NRC 2003 [DIRS 163274], Section 2.2.1.3.1); "Mechanical Disruption of Engineered Barriers" (NRC 2003 [DIRS 163274], Section 2.2.1.3.2); "Quantity and Chemistry of Water Contacting Engineered Barriers and Waste Forms" (NRC 2003 [DIRS 163274], Section 2.2.1.3.3); "Climate and Infiltration" (NRC 2003 [DIRS 163274], Section 2.2.1.3.5); and "Flow Paths in the Unsaturated Zone" (NRC 2003

[DIRS 163274], Section 2.2.1.3.6). The descriptions and technical bases provide transparent and traceable support for the abstraction of radionuclide release rates.

Response: The EBS radionuclide transport abstraction uses assumptions, technical bases, data, and models consistent with other related U.S. Department of Energy abstractions. The descriptions and technical bases described in Sections 6.3.4, 6.5.1, and 6.5.3 provide support for the abstraction of radionuclide release rates. Section 5 provides assumptions that are relevant to the EBS transport model.

(3) The abstraction of radionuclide release rates provides sufficient, consistent design information on waste packages and engineered barrier systems. For example, inventory calculations and selected radionuclides are based on the detailed information provided on the distribution (both spatially and by compositional phase) of the radionuclide inventory, within the various types of high-level radioactive waste.

Response: The EBS radionuclide transport abstraction provides consistent design information on waste packages and engineered barrier systems (Section 4.1 and throughout Section 6). Selected radionuclides are based on the detailed information provided on the distribution (both spatially and by compositional phase) of the radionuclide inventory, within the various types of high-level radioactive waste. Input data on radionuclides are provided in Section 4.1 and 6.5.2.

(4) The U.S. Department of Energy reasonably accounts for the range of environmental conditions expected inside breached waste packages and in the engineered barrier environment surrounding the waste package. For example, the U.S. Department of Energy should provide a description and sufficient technical bases for its abstraction of changes in hydrologic properties in the near field, caused by coupled thermal-hydrologic-mechanical-chemical processes.

Response: The EBS radionuclide transport abstraction accounts for the range of environmental conditions expected inside breached waste packages and in the engineered barrier environment surrounding the waste package. Sections 6.3 and 6.5 describe provisions for thermal, chemical, and hydrologic conditions inside and surrounding the waste package.

(5) The description of process-level conceptual and mathematical models is sufficiently complete, with respect to thermal-hydrologic processes affecting radionuclide release from the emplacement drifts. For example, if the U.S. Department of Energy uncouples coupled processes, the demonstration that uncoupled model results bound predictions of fully coupled results is adequate.

Response: The description of process-level conceptual and mathematical models, with respect to thermal-hydrologic processes affecting radionuclide release from the emplacement drifts is provided in Section 6.5.

(6) Technical bases for inclusion of any thermal-hydrologic-mechanical-chemical couplings and features, events, and processes in the radionuclide release rates and solubility Review Plan for Safety Analysis Report limits model abstraction are adequate. For example, technical bases may include activities, such as independent modeling, laboratory or field data, or sensitivity studies.

Response: Technical bases for inclusion of thermal-hydrologic-mechanical-chemical couplings and the disposition of features, events, and processes in the EBS radionuclide transport abstraction are summarized in Section 6.2.

Acceptance Criterion 2–Data Are Sufficient for Model Justification.

(1) Geological, hydrological, and geochemical values used in the license application are adequately justified. Adequate description of how the data were used, interpreted, and appropriately synthesized into the parameters is provided.

Response: Technical justification for the geological, hydrological, and geochemical values used in the EBS radionuclide transport abstraction is provided. There is also a discussion of how the data are used, interpreted, and synthesized into associated parameters values. Section 6.5.2 provides a summary discussion on the use and interpretation of data used in the EBS flow and transport models. The discussion includes the range, distribution and uncertainty of model data. Detailed descriptions of data and technical justification of values used are provided throughout Sections 6.3 and 6.5.

(2) Sufficient data have been collected on the characteristics of the natural system and engineered materials to establish initial and boundary conditions for conceptual models and simulations of thermal-hydrologic-chemical coupled processes. For example, sufficient data should be provided on design features, such as the type, quantity, and reactivity of materials, that may affect radionuclide release for this abstraction.

Response: Section 4.1 provides data on characteristics of the natural system and engineered materials needed to establish initial and boundary conditions for the EBS radionuclide transport abstraction conceptual models and simulations of thermal-hydrologic-chemical coupled processes.

(4) The corrosion and radionuclide release testing program for high-level radioactive waste forms intended for disposal provides consistent, sufficient, and suitable data for the in-package and in-drift chemistry used in the abstraction of radionuclide release rates and solubility limits. For expected environmental conditions, the U.S. Department of Energy provides sufficient justification for the use of test results, not specifically collected from the Yucca Mountain site, for engineered barrier components, such as high-level radioactive waste forms, drip shield, and backfill.

Response: The corrosion and radionuclide release testing program for HLW forms intended for disposal provides data for the in-package and in-drift chemistry used in the EBS radionuclide transport abstraction (Section 4.1). For expected environmental conditions, the EBS radionuclide transport abstraction provides justification for the use of test results, not specifically collected from the Yucca Mountain site, for engineered barrier components, such as HLW forms and drip shield (Sections 6.3 and 6.5).

Acceptance Criterion 3–Data Uncertainty Is Characterized and Propagated Through the Model Abstraction.

(1) Models use parameter values, assumed ranges, probability distributions, and bounding assumptions that are technically defensible, reasonably account for uncertainties and variabilities, and do not result in an under representation of the risk estimate.

Response: The EBS radionuclide transport abstraction uses parameter values, assumed ranges, probability distributions, and/or bounding assumptions that account for uncertainties and variabilities, and that do not cause an under-representation of the risk estimate. Section 4.1 lists the data and parameters used, together with their sources. Section 6.5.2 provides a summary of the base case model inputs together with associated uncertainties.

(2) Parameter values, assumed ranges, probability distributions, and bounding assumptions used in the abstractions of radionuclide release rates and solubility limits in the total system performance assessment are technically defensible and reasonable based on data from the Yucca Mountain region, laboratory tests, and natural analogs. For example, parameter values, assumed ranges, probability distributions, and bounding assumptions adequately reflect the range of environmental conditions expected inside breached waste packages.

Response: Parameter values, assumed ranges, probability distributions, and bounding assumptions used in the abstractions of radionuclide release rates and solubility limits in the total system performance assessment are based on data from the Yucca Mountain region, laboratory tests, and natural analogs. Parameter values, assumed ranges, probability distributions, and bounding assumptions reflect the range of environmental conditions expected inside breached waste packages. Section 4.1 lists the data and parameters used, together with their sources. Section 6.5.2 provides a summary of the base case model inputs together with associated uncertainties.

(3) DOE uses reasonable or conservative ranges of parameters or functional relations to determine effects of coupled thermal-hydrologic-chemical processes on radionuclide release. These values are consistent with the initial and boundary conditions and the assumptions for the conceptual models and design concepts for natural and engineered barriers at the Yucca Mountain site. If any correlations between the input values exist, they are adequately established in the total system performance assessment. For example, estimations are based on a thermal loading and ventilation strategy; engineered barrier system design (including drift liner, backfill, and drip-shield); and natural system masses and fluxes that are consistent with those used in other abstractions.

Response: The EBS radionuclide transport abstraction uses reasonable or conservative ranges of parameters or functional relations to determine effects of coupled thermal-hydrologic-chemical processes on radionuclide release. These values are consistent with the initial and boundary conditions and the assumptions for the conceptual models and design concepts for natural and engineered barriers at the Yucca Mountain site. Section 4.1 lists the data and parameters used, together with their sources. Section 6.5.2 provides a summary of the base case model inputs together with associated uncertainties.

(4) Uncertainty is adequately represented in parameter development for conceptual models, process models, and alternative conceptual models considered in developing the abstraction of radionuclide release rates and solubility limits, either through sensitivity analyses or use of bounding analyses.

Response: Uncertainty is represented in parameter development for conceptual models, process models, and alternative conceptual models considered in developing the abstraction of radionuclide release rates and solubility limits. Parameter development for the models described in this model report is provided throughout Sections 6.3, 6.4, 6.5, and 6.6.

(5) Parameters used to describe flow through and out of the engineered barrier, sufficiently bound the effects of backfill, excavation-induced changes, and thermally induced mechanical changes that affect flow.

Response: The EBS radionuclide transport abstraction considers the uncertainties, in the characteristics of the natural system and engineered materials, such as the type, quantity, and reactivity of material, in establishing initial and boundary conditions for conceptual models and simulations of thermal-hydrologic-chemical coupled processes that affect radionuclide release. Parameter development for the models described in this model report is provided throughout Sections 6.3, 6.4, 6.5, and 6.6.

(8) DOE adequately considers the uncertainties, in the characteristics of the natural system and engineered materials, such as the type, quantity, and reactivity of material, in establishing initial and boundary conditions for conceptual models and simulations of thermal-hydrologic-chemical coupled processes that affect radionuclide release.

Response: Parameters used to describe flow through and out of the engineered barrier bound the effects of excavation-induced changes and thermally induced mechanical changes that affect flow.

Acceptance Criterion 4–Model Uncertainty Is Characterized and Propagated Through the Model Abstraction.

(1) Alternative modeling approaches of features, events, and processes are considered and are consistent with available data and current scientific understanding, and the results and limitations are appropriately considered in the abstraction.

Response: Alternative modeling approaches of features, events, and processes are considered in Section 6.4 and are consistent with available data and current scientific understanding, and the results and limitations are considered.

(2) In considering alternative conceptual models for radionuclide release rates and solubility limits, DOE uses appropriate models, tests, and analyses that are sensitive to the processes modeled for both natural and engineering systems. Conceptual model uncertainties are adequately defined and documented, and effects on conclusions regarding performance are properly assessed. For example, in modeling flow and radionuclide release from the drifts, DOE represents significant discrete features, such as fault zones, separately, or demonstrates that their inclusion in the equivalent continuum model produces a conservative effect on calculated performance.

Response: In considering alternative conceptual models for radionuclide release rates and solubility limits (Sections 6.4. and 6.6), the EBS radionuclide transport abstraction uses models and analyses that are sensitive to the processes modeled for both natural and engineering systems. Conceptual model uncertainties are defined and documented, and effects on conclusions regarding performance are assessed. The fundamental relationships, e.g., mass balance and flow equations, upon which the EBS radionuclide transport abstraction is based, are well-established with a long history of use in the scientific community and as such are not subject to significant uncertainty. In addition, the alternative conceptual models have been screened out (Section 6.4), thereby increasing confidence in the selected conceptual model. Other sources of uncertainty involve modeling choices (e.g., assumptions, geometry) that, because of their conservative nature, effectively bound uncertainty.

(3) Consideration of conceptual model uncertainty is consistent with available site characterization data, laboratory experiments, field measurements, natural analog information and process-level modeling studies; and the treatment of conceptual model uncertainty does not result in an under-representation of the risk estimate.

Response: Consideration of conceptual model uncertainty is consistent with available site characterization data, laboratory experiments, field measurements, natural analog information and process-level modeling studies; and the treatment of conceptual model uncertainty does not result in an under-representation of the risk estimate, as discussed throughout Section 6. Section 6.5.2 provides discussions on parameter uncertainty.

(4) The effects of thermal-hydrologic-chemical coupled processes that may occur in the natural setting, or from interactions with engineered materials, or their alteration products, on radionuclide release, are appropriately considered.

Response: The effects of thermal-hydrologic-chemical coupled processes that may occur in the natural setting or from interactions with engineered materials or their alteration products, on radionuclide release, are considered in Section 6. For example, the effect of corrosion products on the transport of radionuclides is provided in Sections 6.3.4, 6.5.1, and 6.5.3.

Acceptance Criterion 5–Model Abstraction Output Is Supported by Objective Comparisons.

(1) The models implemented in this total system performance assessment abstraction provide results consistent with output from detailed process-level models and/or empirical observations (laboratory and field testings and/or natural analogs).

Response: The models implemented in this total system performance assessment abstraction provide results consistent with output from detailed process-level models and/or empirical observations (laboratory testings), as described in Sections 6.3, 6.5, and 7. Section 7 provides comparisons of models developed in this model report with other models and experimental results.

(3) DOE adopts well-documented procedures that have been accepted by the scientific community to construct and test the numerical models, used to simulate coupled thermal-hydrologic-chemical effects on radionuclide release. For example, DOE demonstrates that the numerical models used for high-level radioactive waste degradation and dissolution, and radionuclide release from the engineered barrier system, are adequate representations; include consideration of uncertainties; and are not likely to underestimate radiological exposures to the reasonably maximally exposed individual and releases of radionuclides into the accessible environment.

Response: The EBS radionuclide transport abstraction uses well-documented procedures in Section 6.5 that have been accepted by the scientific community to construct and test the numerical models used to simulate radionuclide release. The abstraction demonstrates that the numerical models used for radionuclide release from the EBS include consideration of uncertainties and are not likely to underestimate radiological exposures to the reasonably maximally exposed individual and releases of radionuclides into the accessible environment.

8.4 RESTRICTIONS FOR SUBSEQUENT USE

This abstraction was developed specifically for application in TSPA-LA. Assumptions and approximations are made in order to integrate with and be consistent with other models and abstractions incorporated in TSPA-LA. Therefore, individual submodels should not be used independently outside of the TSPA-LA framework. This abstraction must be reevaluated if any models that feed into it are modified.

Use of the three preliminary output DTNs: SN0403T0507703.015, SN0409T0507703.017, and SN0503T0503305.001 is restricted to providing traceability in TSPA-LA. For any other application, the final output DTNs: SN0410T0507703.018, MO0506SPAINPAR.000, and SN0508T0503305.003 are to be used. Differences between the preliminary and final DTNs are described in Appendix I.

9. INPUTS AND REFERENCES

The following is a list of references cited in this document. Column 1 represents the unique six-digit identifier numerical identifier (the Document Input Reference System number), which is placed in the text following the reference callout (e.g., BSC 2005 [DIRS 173617]). The purpose of these numbers is to assist in locating a specific reference. Within the reference list, multiple sources by the same author (e.g., BSC 2002) are sorted alphabetically by title.

9.1 DOCUMENTS CITED

173033 Ainsworth, C.C.; Pilon, J.L.; Gassman, P.L.; and Van Der Sluys, W.G. 1994. "Cobalt, Cadmium, and Lead Sorption to Hydrous Iron Oxide: Residence Time Effect." *Soil Science Society America Journal, 58,* 1615-1623. Madison, Wisconsin: Soil Science Society of America. TIC: 257037.

171637 Anderson, M.J. 2004. "Mass for Nickel Gadolinium Neutron Absorber for Commercial Spent Nuclear Fuel (CSNF) Waste Packages--Initial Calculations (Not Yet Approved)." Interoffice memorandum from M.J. Anderson (BSC) to C. Howard, September 14, 2004, 0914043170, with enclosure. ACC: MOL.20040928.0325.

123665 Anderson, M.P. and Woessner, W.W. 1992. *Applied Groundwater Modeling, Simulation of Flow and Advective Transport.* San Diego, California: Academic Press. TIC: 103227.

154430 Archie, G.E. 1942. "The Electrical Resistivity Log as an Aid in Determining Some Reservoir Characteristics." *Petroleum Development and Technology, Transactions of American Institute of Mining and Metallurgical Engineers, 146,* 54-62. New York, New York: American Institute of Mining and Metallurgical Engineers. TIC: 249687.

111464 Atkins, P.W. 1990. *Physical Chemistry.* 4th Edition. New York, New York: W.H. Freeman and Company. TIC: 245483.

174739 Bachmann, J. and van der Ploeg, R.R. 2002. "A Review on Recent Developments in Soil Water Retention Theory: Interfacial Tension and Temperature Effects." *Journal of Plant Nutrition and Soil Science, 165,* 468-478. Weinheim, Germany: Wiley-VCH Verlag. TIC: 257579.

173887 Bachmann, J.; Horton, R.; Grant, S.A.; and van der Ploeg, R.R. 2002. "Temperature Dependence of Water Retention Curves for Wettable and Water-Repellent Soils." *Soil Science Society America Journal, 66,* 44-52. Madison, Wisconsin: Soil Science Society of America. TIC: 257501.

170953 Baker, N.A. and Grisak, G.E. 2004. "Independent Model Validation Technical Review of the EBS-UZ Interface Sub-Model of the Radionuclide Transport Abstraction Model for the Yucca Mountain Project." Memo from N.A. Baker (INTERA) and G.E. Grisak (INTERA) to J. Schreiber and C. Howard, July 27, 2004. ACC: MOL.20040730.0182.

154439 Balsley, S.D.; Brady, P.V.; Krumhansl, J.L.; and Anderson, H.L. 1998. "Anion Scavengers for Low-Level Radioactive Waste Repository Backfills." *Journal of Soil Contamination, 7,* (2), 125-141. Boca Raton, Florida: Lewis Publishers. TIC: 249779.

174702 Barney, G.S. 1984. "Radionuclide Sorption and Desorption Reactions with Interbed Materials from the Columbia River Basalt Formation." In *ACS Symposium Series 246,* Chapter 1 of *Geochemical Behavior of Disposed Radioactive Waste.* Barney, G.S.; Navartil, J.D.; and Schulz, W.W., eds. Washington, D.C.: American Chemical Society. TIC: 206845.

101379 Bear, J. 1988. *Dynamics of Fluids in Porous Media.* New York, New York: Dover Publications. TIC: 217568.

154437 Bethke, C.M. and Brady, P.V. 2000. "How the Kd Approach Undermines Ground Water Cleanup." *Ground Water, 38,* (3), 435-443. Westerville, Ohio: National Ground Water Association. TIC: 249781.

103524 Bird, R.B.; Stewart, W.E.; and Lightfoot, E.N. 1960. *Transport Phenomena.* New York, New York: John Wiley & Sons. TIC: 208957.

173707 Boily, J.F.; Lützenkirchen, J.; Balmès, O.; Beattie, J.; and Sjöberg, S. 2001. "Modeling Proton Binding at the Goethite (α-FeOOH)-Water Interface." *Colloids and Surfaces A: Physicochemical and Engineering Aspects, 179,* 11-27. New York, New York: Elsevier. TIC: 257303.

154421 Brady, P.V.; Spalding, B.P.; Krupka, K.M.; Waters, R.D.; Zhang, P.; Borns, D.J.; and Brady, W.D. 1999. *Site Screening and Technical Guidance for Monitored Natural Attenuation at DOE Sites.* SAND99-0464. Albuquerque, New Mexico: Sandia National Laboratories. TIC: 249720.

161617 Briand, L.E.; Hirt, A.M.; and Wachs, I.E. 2001. "Quantitative Determination of the Number of Surface Active Sites and the Turnover Frequencies for Methanol Oxidation over Metal Oxide Catalysts: Application to Bulk Metal Molybdates and Pure Metal Oxide Catalysts." *Journal of Catalysis, 202,* ([2), 268-278. New York, New York: Academic Press. TIC: 253845.

131479 Brown, R.L. and Richards, J.C. 1970. *Principles of Powder Mechanics, Essays on the Packing and Flow of Powders and Bulk Solids.* Pages 17-20. New York, New York: Pergamon Press. TIC: 245119.

154441 BSC (Bechtel SAIC Company) 2001. *Committed Materials in Repository Drifts.* CAL-GCS-GE-000002 REV 00. Las Vegas, Nevada: Bechtel SAIC Company. ACC: MOL.20010412.0157.

160828 BSC 2001. *Unsaturated Zone and Saturated Zone Transport Properties (U0100).* ANL-NBS-HS-000019 REV 00 ICN 02. Las Vegas, Nevada: Bechtel SAIC Company. ACC: MOL.20020311.0017.

158193 BSC 2002. *Test Plan for: Atlas Breached Waste Package Test and Drip Shield Experiments.* SITP-02-EBS-005 REV 00. Las Vegas, Nevada: Bechtel SAIC Company. ACC: MOL.20020314.0181.

158966 BSC 2002. *The Enhanced Plan for Features, Events, and Processes (FEPs) at Yucca Mountain.* TDR-WIS-PA-000005 REV 00. Las Vegas, Nevada: Bechtel SAIC Company. ACC: MOL.20020417.0385.

163406 BSC 2003. *Atlas Breached Waste Package and Drip Shield Experiments: Breached Drip Shield Tests.* TDR-EBS-MD-000025 REV 00. Las Vegas, Nevada: Bechtel SAIC Company. ACC: DOC.20030619.0001.

165159 BSC 2003. *Design and Engineering, Naval Long Waste Package Configuration.* 000-MW0-DNF0-00103-000-00A. Las Vegas, Nevada: Bechtel SAIC Company. ACC: ENG.20030929.0004.

168796 BSC 2003. *Risk Information to Support Prioritization of Performance Assessment Models.* TDR-WIS-PA-000009 REV 01 ICN 01, with errata. Las Vegas, Nevada: Bechtel SAIC Company. ACC: MOL.20021017.0045; DOC.20031014.0003.

170710 BSC 2004. *21-PWR Waste Package Configuration.* 000-MW0-DSU0-00403-000-00D. Las Vegas, Nevada: Bechtel SAIC Company. ACC: ENG.20040708.0005.

170838 BSC 2004. *44-BWR Waste Package Configuration.* 000-MW0-DSU0-00503-000-00C. Las Vegas, Nevada: Bechtel SAIC Company. ACC: ENG.20040708.0007.

169131 BSC 2004. *Abstraction of Drift Seepage.* MDL-NBS-HS-000019 REV 01. Las Vegas, Nevada: Bechtel SAIC Company. ACC: DOC.20041103.0003.

170026 BSC 2004. *Atmospheric Dispersal and Deposition of Tephra from a Potential Volcanic Eruption at Yucca Mountain, Nevada.* MDL-MGR-GS-000002 REV 01. Las Vegas, Nevada: Bechtel SAIC Company. ACC: DOC.20041025.0003; DOC.20050606.0004.

168030 BSC 2004. *Characterize Framework for Seismicity and Structural Deformation at Yucca Mountain, Nevada.* ANL-CRW-GS-000003 REV 00, with errata. Las Vegas, Nevada: Bechtel SAIC Company. ACC: MOL.20000510.0175; DOC.20040223.0007.

169987 BSC 2004. *CSNF Waste Form Degradation: Summary Abstraction.* ANL-EBS-MD-000015 REV 02. Las Vegas, Nevada: Bechtel SAIC Company. ACC: DOC.20040908.0001.

170559 BSC 2004. *D&E / PA/C IED Emplacement Drift Configuration and Environment.* 800-IED-MGR0-00202-000-00B. Las Vegas, Nevada: Bechtel SAIC Company. ACC: ENG.20040503.0001.

167207 BSC 2004. *D&E/PA/C IED Typical Waste Package Components Assembly [Sheet 2].* 800-IED-WIS0-00202-000-00B. Las Vegas, Nevada: Bechtel SAIC Company. ACC: ENG.20040202.0010.

169472 BSC 2004. *D&E/PA/C IED Typical Waste Package Components Assembly [Sheet 2].* 800-IED-WIS0-00202-000-00C. Las Vegas, Nevada: Bechtel SAIC Company. ACC: ENG.20040517.0008.

169988 BSC 2004. *Defense HLW Glass Degradation Model.* ANL-EBS-MD-000016 REV 02. Las Vegas, Nevada: Bechtel SAIC Company. ACC: DOC.20041020.0015.

166946 BSC 2004. *Design & Engineering, 5 DHLW/DOE SNF - Short Waste Package Configuration.* 000-MW0-DS00-00102-000-00A. Las Vegas, Nevada: Bechtel SAIC Company. ACC: ENG.20040121.0002.

166947 BSC 2004. *Design & Engineering, 5 DHLW/DOE SNF - Short Waste Package Configuration.* 000-MW0-DS00-00103-000-00A. Las Vegas, Nevada: Bechtel SAIC Company. ACC: ENG.20040121.0003.

166953 BSC 2004. *Design and Engineering, 21-PWR Waste Package Configuration.* 000-MW0-DSU0-00402-000-00B. Las Vegas, Nevada: Bechtel SAIC Company. ACC: ENG.20040119.0004.

167394 BSC 2004. *Design and Engineering, 21-PWR Waste Package Configuration.* 000-MW0-DSU0-00403-000-00C. Las Vegas, Nevada: Bechtel SAIC Company. ACC: ENG.20040202.0024.

167555 BSC 2004. *Design and Engineering, 44-BWR Waste Package Configuration.* 000-MW0-DSU0-00503-000-00B. Las Vegas, Nevada: Bechtel SAIC Company. ACC: ENG.20040213.0006.

168326 BSC 2004. *Design and Engineering, Drip Shield Connector Guide.* 000-M00-SSE0-02001-000-00A. Las Vegas, Nevada: Bechtel SAIC Company. ACC: ENG.20040309.0011.

168275 BSC 2004. *Design and Engineering, Interlocking Drip Shield Configuration.* 000-M00-SSE0-00101-000-00B. Las Vegas, Nevada: Bechtel SAIC Company. ACC: ENG.20040305.0020.

168067 BSC 2004. *Design and Engineering, Interlocking Drip Shield Configuration.* 000-M00-SSE0-00102-000-00B. Las Vegas, Nevada: Bechtel SAIC Company. ACC: ENG.20040305.0021.

170028 BSC 2004. *Dike/Drift Interactions.* MDL-MGR-GS-000005 REV 01. Las Vegas, Nevada: Bechtel SAIC Company. ACC: DOC.20041124.0002.

170040 BSC 2004. *Drift-Scale Radionuclide Transport.* MDL-NBS-HS-000016 REV 01. Las Vegas, Nevada: Bechtel SAIC Company. ACC: DOC.20040927.0031.

172453 BSC 2004. *DSNF and Other Waste Form Degradation Abstraction.* ANL-WIS-MD-000004 REV 04. Las Vegas, Nevada: Bechtel SAIC Company. ACC: DOC.20041201.0007.

168138 BSC 2004. *Estimation of Mechanical Properties of Crushed Tuff for Use as Ballast Material in Emplacement Drifts.* 800-CYC-SSE0-00100-000-00A. Las Vegas, Nevada: Bechtel SAIC Company. ACC: ENG.20040309.0023.

169984 BSC 2004. *General Corrosion and Localized Corrosion of Waste Package Outer Barrier.* ANL-EBS-MD-000003 REV 02. Las Vegas, Nevada: Bechtel SAIC Company. ACC: DOC.20041004.0001.

168960 BSC 2004. *Igneous Intrusion Impacts on Waste Packages and Waste Forms.* MDL-EBS-GS-000002 REV 01. Las Vegas, Nevada: Bechtel SAIC Company. ACC: DOC.20040421.0002.

164327 BSC 2004. *In-Drift Natural Convection and Condensation.* MDL-EBS-MD-000001 REV 00. Las Vegas, Nevada: Bechtel SAIC Company. ACC: DOC.20041025.0006; DOC.20050330.0001.

169863 BSC 2004. *In-Drift Precipitates/Salts Model.* ANL-EBS-MD-000045 REV 02. Las Vegas, Nevada: Bechtel SAIC Company. ACC: DOC.20041111.0002.

170022 BSC 2004. *Initial Radionuclide Inventories.* ANL-WIS-MD-000020 REV 01. Las Vegas, Nevada: Bechtel SAIC Company. ACC: DOC.20040921.0003.

170001 BSC 2004. *Number of Waste Packages Hit by Igneous Intrusion.* ANL-MGR-GS-000003 REV 01. Las Vegas, Nevada: Bechtel SAIC Company. ACC: DOC.20041015.0001; DOC.20050602.0001.

170041 BSC 2004. *Particle Tracking Model and Abstraction of Transport Processes.* MDL-NBS-HS-000020 REV 01. Las Vegas, Nevada: Bechtel SAIC Company. ACC: DOC.20041020.0016.

164500 BSC 2004. *Radionuclide Transport Models Under Ambient Conditions.* MDL-NBS-HS-000008 REV 02. Las Vegas, Nevada: Bechtel SAIC Company. ACC: DOC.20041101.0002.

169503 BSC 2004. *Repository Subsurface Emplacement Drifts Steel Invert Structure Plan & Elevation.* 800-SS0-SSE0-00101-000-00B. Las Vegas, Nevada: Bechtel SAIC Company. ACC: ENG.20040520.0004.

169776 BSC 2004. *Repository Subsurface Emplacement Drifts Steel Invert Structure Sect. & Committed Materials.* 800-SS0-SSE0-00102-000-00B. Las Vegas, Nevada: Bechtel SAIC Company. ACC: ENG.20040520.0005.

167652 BSC 2004. *Seepage Model for PA Including Drift Collapse.* MDL-NBS-HS-000002 REV 03. Las Vegas, Nevada: Bechtel SAIC Company. ACC: DOC.20040922.0008.

172203 BSC 2004. *Stress Corrosion Cracking of the Drip Shield, the Waste Package Outer Barrier, and the Stainless Steel Structural Material.* ANL-EBS-MD-000005 REV 02. Las Vegas, Nevada: Bechtel SAIC Company. ACC: DOC.20041028.0008; DOC.20050621.0003.

167083 BSC 2004. *Structural Calculations of Waste Package Exposed to Vibratory Ground Motion.* 000-00C-WIS0-01400-000-00A. Las Vegas, Nevada: Bechtel SAIC Company. ACC: ENG.20040217.0008.

172219 BSC 2004. *Technical Management Review Board (TMRB) Decision Proposal.* TMRB-2004-088. Las Vegas, Nevada: Bechtel SAIC Company. ACC: MOL.20041027.0228.

169861 BSC 2004. *UZ Flow Models and Submodels.* MDL-NBS-HS-000006 REV 02. Las Vegas, Nevada: Bechtel SAIC Company. ACC: DOC.20041101.0004; DOC.20050629.0003.

169996 BSC 2004. *WAPDEG Analysis of Waste Package and Drip Shield Degradation.* ANL-EBS-PA-000001 REV 02. Las Vegas, Nevada: Bechtel SAIC Company. ACC: DOC.20041004.0005.

170025 BSC 2004. *Waste Form and In-Drift Colloids-Associated Radionuclide Concentrations: Abstraction and Summary.* MDL-EBS-PA-000004 REV 01. Las Vegas, Nevada: Bechtel SAIC Company. ACC: DOC.20041028.0007; DOC.20050425.0003.

172895 BSC 2005. *Cladding Degradation Summary for LA.* ANL-WIS-MD-000021 REV 03. Las Vegas, Nevada: Bechtel SAIC Company. ACC: DOC.20050222.0008.

174566 BSC 2005. *Dissolved Concentration Limits of Radioactive Elements.* ANL-WIS-MD-000010 REV 05. Las Vegas, Nevada: Bechtel SAIC Company. ACC: DOC.20050713.0006.

173781 BSC 2005. *Engineered Barrier System Features, Events, and Processes.* ANL-WIS-PA-000002 REV 04. Las Vegas, Nevada: Bechtel SAIC Company. ACC: DOC.20050725.0003.

173727 BSC 2005. *Engineered Barrier System: Physical and Chemical Environment.* ANL-EBS-MD-000033 REV 04. Las Vegas, Nevada: Bechtel SAIC Company. ACC: DOC.20050718.0003.

173303 BSC 2005. *IED Interlocking Drip Shield and Emplacement Pallet [Sheet 1 of 1].* 800-IED-WIS0-00401-000-00E. Las Vegas, Nevada: Bechtel SAIC Company. ACC: ENG.20050301.0007.

173501 BSC 2005. *IED Waste Package Configuration [Sheet 1 of 1].* 800-IED-WIS0-00601-000-00A. Las Vegas, Nevada: Bechtel SAIC Company. ACC: ENG.20050406.0005.

174583 BSC 2005. *In-Package Chemistry Abstraction.* ANL-EBS-MD-000037 REV 04. Las Vegas, Nevada: Bechtel SAIC Company. ACC: DOC.20050714.0003.

173944 BSC 2005. *Multiscale Thermohydrologic Model.* ANL-EBS-MD-000049 REV 03. Las Vegas, Nevada: Bechtel SAIC Company. ACC: DOC.20050711.0001.

174269 BSC 2005. *Q-List.* 000-30R-MGR0-00500-000-002. Las Vegas, Nevada: Bechtel SAIC Company. ACC: ENG.20050805.0006.

173978 BSC 2005. *Screening of Features, Events, and Processes in Drip Shield and Waste Package Degradation.* ANL-EBS-PA-000002 REV 04. Las Vegas, Nevada: Bechtel SAIC Company. ACC: DOC.20050620.0005.

173247 BSC 2005. *Seismic Consequence Abstraction.* MDL-WIS-PA-000003 REV 02E. Las Vegas, Nevada: Bechtel SAIC Company. ACC: MOL.20050718.0011.

174695 BSC 2005. *Technical Management Review Board (TMRB) Decision Proposal.* TMRB-2005-028. Las Vegas, Nevada: Bechtel SAIC Company. ACC: MOL.20050330.0218.

173617 BSC 2005. *Technical Work Plan for: Near-Field Environment and Transport: Engineered Barrier System: Radionuclide Transport Abstraction Model Report Integration.* TWP-MGR-PA-000020 REV 01. Las Vegas, Nevada: Bechtel SAIC Company. ACC: DOC.20050427.0003.

173752 Buerge-Weirich, D.; Hari, R.; Xue, H.; Behra, P.; and Sigg, L. 2002. "Adsorption of Cu, Cd, and Ni on Goethite in the Presence of Natural Groundwater Ligands." *Environmental Science & Technology, 36,* (3), 328-336. New York, New York: American Chemical Society. TIC: 257348.

163817 Campbell, A.N. and Smith, N.O. 1951. *The Phase Rule and its Applications.* 9th Edition. New York, New York: Dover Publications. TIC: 254360.

100565 Campbell, G.S. 1985. *Soil Physics with BASIC Transport Models for Soil-Plant Systems.* Developments in Soil Science 14. Amsterdam, The Netherlands: Elsevier. TIC: 214477.

166275 Canori, G.F. and Leitner, M.M. 2003. *Project Requirements Document.* TER-MGR-MD-000001 REV 02. Las Vegas, Nevada: Bechtel SAIC Company. ACC: DOC.20031222.0006.

138551 Cantrel, L.; Chaouche, R.; and Chopin-Dumas, J. 1997. "Diffusion Coefficients of Molecular Iodine in Aqueous Solutions." *Journal Chemical Engineering Data, 42,* 216-220. Washington, D.C.: American Chemical Society. TIC: 246757.

174705 Chien S.H. and Clayton W.R. 1980. "Application of Elovich Equation to the Kinetics of Phosphate Release and Sorption in Soils." *Soil Science Society of America Journal, 44,* 265-268. Madison, Wisconsin: Soil Science Society of America. TIC: 257577.

161621 Choi, H. and Corapcioglu, M.Y. 1997. "Transport of a Non-volatile Contaminant in Unsaturated Porous Media in the Presence of Colloids." *Journal of Contaminant Hydrology, 25,* (3-4), 299-324. New York, New York: Elsevier. TIC: 253843.

173811 Christl, I. and Kretzschmar R. 1999. "Competitive Sorption of Copper and Lead at the Oxide-Water Interface: Implications for Surface Site Density." *Geochimica et Cosmochimica Acta, 63,* (19/20), 2929-2938. New York, New York: Pergamon. TIC: 257338.

173020 Christophi, C. and Axe, L. 2000. "Competition of Cd, Cu, and Pb Adsorption on Goethite." *Journal of Environmental Engineering, 126,* (1), 66-74. Reston, Virginia: American Society of Civil Engineers. TIC: 257038.

101582 Conca, J.L. and Wright, J. 1990. "Diffusion Coefficients in Gravel Under Unsaturated Conditions." *Water Resources Research, 26,* (5), 1055-1066. Washington, D.C.: American Geophysical Union. TIC: 237421.

100436 Conca, J.L. and Wright, J. 1992. "Diffusion and Flow in Gravel, Soil, and Whole Rock." *Applied Hydrogeology, 1,* 5-24. Hanover, Germany: Verlag Heinz Heise GmbH. TIC: 224081.

170709 Conca, J.L.; Apted, M.; and Arthur, R. 1993. "Aqueous Diffusion in Repository and Backfill Environments." *Scientific Basis for Nuclear Waste Management XVI, Symposium held November 30-December 4, 1992, Boston, Massachusetts.* Interrante, C.G. and Pabalan, R.T., eds. *294,* 395-402. Pittsburgh, Pennsylvania: Materials Research Society. TIC: 208880.

174120 Constantz, J. 1991. "Comparison of Isothermal and Isobaric Water Retention Paths in Nonswelling Porous Materials." *Water Resources Research, 27,* (12), 3165-3170. Washington, D.C.: American Geophysical Union. TIC: 257437.

105761 Corapcioglu, M.Y. and Jiang, S. 1993. "Colloid-Facilitated Groundwater Contaminant Transport." *Water Resources Research, 29,* (7), 2215-2226. Washington, D.C.: American Geophysical Union. TIC: 222362.

167464 Corapcioglu, M.Y. and Wang, S. 1999. "Dual-Porosity Groundwater Contaminant Transport in the Presence of Colloids." *Water Resources Research, 35,* (11), 3261-3273. Washington, D.C.: American Geophysical Union. TIC: 255571.

173864 Cornell, R.M. and Giovanoli R. 1988. "The Influence of Copper on the Transformation of Ferrihydrite ($5Fe_2O_3 \cdot 9H_20$) into Crystalline Products in Alkaline Media." *Polyhedron, 7,* (5), 385-391. New York, New York: Pergamon Press. TIC: 257362.

173037 Cornell, R.M. and Schwertmann, U. 2003. *The Iron Oxides, Structure, Properties, Reactions, Occurrences and Uses.* 2nd Edition. Weinheim, Germany: Wiley-VCH Verlagsgesellschaft. TIC: 257034.

173865 Cornell, R.M.; Schneider, W.; and Giovanoli R. 1989. "Phase Transformations in the Ferrihydrite/Cysteine System." *Polyhedron, 8,* (23), 2829-2836. New York, New York: Pergamon Press. TIC: 257364.

173030 Coughlin, B.R. and Stone, A.T. 1995. "Nonreversible Adsorption of Divalent Metal Ions (Mn^{II}, Co^{II}, Ni^{II}, Cu^{II}, and Pb^{II}) onto Goethite: Effects of Acidification, Fe^{II} Addition, and Picolinic Acid Addition." *Environmental Science Technology, 29,* (9), 2445-2455. Washington, D.C.: American Chemical Society. TIC: 257061.

132164 Coughtrey, P.J.; Jackson, D.; and Thorne, M.C. 1983. *Radionuclide Distribution and Transport in Terrestrial and Aquatic Ecosystems, A Critical Review of Data.* Six volumes. Rotterdam, The Netherlands: A.A. Balkema. TIC: 240299.

102824 CRWMS M&O 1997. *Criticality Evaluation of Degraded Internal Configurations for the PWR AUCF WP Designs.* BBA000000-01717-0200-00056 REV 00. Las Vegas, Nevada: CRWMS M&O. ACC: MOL.19971231.0251.

135968 CRWMS M&O 2000. *Abstraction of Models for Stainless Steel Structural Material Degradation.* ANL-EBS-PA-000005 REV 00. Las Vegas, Nevada: CRWMS M&O. ACC: MOL.20000526.0337.

156680 CRWMS M&O 2000. *The Determination of Diffusion Coefficient of Invert Materials.* TDR-EBS-MD-000002 REV 00. Las Vegas, Nevada: CRWMS M&O. ACC: MOL.20000124.0320.

153246 CRWMS M&O 2000. *Total System Performance Assessment for the Site Recommendation.* TDR-WIS-PA-000001 REV 00 ICN 01. Las Vegas, Nevada: CRWMS M&O. ACC: MOL.20001220.0045.

151566 CRWMS M&O 2000. *WAPDEG Analysis of Waste Package and Drip Shield Degradation.* ANL-EBS-PA-000001 REV 00 ICN 01. Las Vegas, Nevada: CRWMS M&O. ACC: MOL.20001208.0063.

111468 Cussler, E.L. 1997. *Diffusion: Mass Transfer in Fluid Systems.* 2nd Edition. Cambridge, United Kingdom: Cambridge University Press. TIC: 241150.

173743 Davis, A.P. and Upadhyaya, M. 1996. "Desorption of Cadmium from Goethite (α-FeOOH)." *Water Research, 30,* (8), 1894-1904. New York, New York: Pergamon. TIC: 257327.

143280 Davis, J.A. and Kent, D.B. 1990. "Surface Complexation Modeling in Aqueous Geochemistry." *Mineral-Water Interface Geochemistry.* Hochella, M.F., Jr. and White, A.F., eds. Reviews in Mineralogy Volume 23. Pages 177-260. Washington, D.C.: Mineralogical Society of America. TIC: 224085.

125591 Davis, J.A. and Leckie, J.O. 1978. "Surface Ionization and Complexation at the Oxide/Water Interface: II. Surface Properties of Amorphous Iron Oxyhydroxide and Adsorption of Metal Ions." *Journal of Colloid and Interface Science, 67,* (1), 90-107. Orlando, Florida: Academic Press. TIC: 223905.

154436 Davis, J.A.; Coston, J.A.; Kent, D.B.; and Fuller, C.C. 1998. "Application of the Surface Complexation Concept to Complex Mineral Assemblages." *Environmental Science & Technology, 32,* (19), 2820-2828. Washington, D.C.: American Chemical Society. TIC: 249656.

171480 Dillmann, Ph.; Mazaudier, F.; and Hœrlé, S. 2004. "Advances in Understanding Atmospheric Corrosion of Iron. I. Rust Characterisation of Ancient Ferrous Artefacts Exposed to Indoor Atmospheric Corrosion." *Corrosion Science, 46,* 1401 - 1429. New York, New York: Elsevier. TIC: 256483.

102588 DOE (U.S. Department of Energy) 1992. *Characteristics of Potential Repository Wastes.* DOE/RW-0184-R1. Four volumes. Washington, D.C.: U.S. Department of Energy, Office of Civilian Radioactive Waste Management. ACC: HQO.19920827.0001; HQO.19920827.0002; HQO.19920827.0003; HQO.19920827.0004.

123628 DOE 1998. *Deficiency Report VAMO-98-D-132.* Washington, D.C.: U.S. Department of Energy, Office of Civilian Radioactive Waste Management. ACC: MOL.19991029.0063.

153849 DOE 2001. *Yucca Mountain Science and Engineering Report.* DOE/RW-0539. Washington, D.C.: U.S. Department of Energy, Office of Civilian Radioactive Waste Management. ACC: MOL.20010524.0272.

169875 DOE 2004. *Requirements Document for: GoldSim V8.02, Rev. No. 00.* Document ID: 10344-RD-8.02-00. Las Vegas, Nevada: U.S. Department of Energy, Office of Repository Development. ACC: MOL.20040623.0257.

173019 Duc, M.; Lefevre, G.; Fedoroff, M.; Jeanjean, J.; Rouchaud, J.C.; Monteil-Rivera, F.; Dumonceau, J.; and Milonjic, S. 2003. "Sorption of Selenium Anionic Species on Apatites and Iron Oxides from Aqueous Solutions." *Journal of Environmental Radioactivity, 70,* 61-72. New York, New York: Elsevier. TIC: 257072.

174716 Duro, L.; Missana, T.; Ripoll, S.; Grivé, M.; and Bruno, J. 2004. "Modelling of Pu Sorption onto the Surface of Goethite and Magnetite as Steel Corrosion Products." *Scientific Basis for Nuclear Waste Management XXVII, Symposium held June 15-19, 2003, Kalmar, Sweden.* Oversby, V.M. and Weme, L.O., eds. *807,* 659-664. Warrendale, Pennsylvania: Materials Research Society. TIC: 256723.

105483 Dzombak, D.A. and Morel, F.M.M. 1990. *Surface Complexation Modeling, Hydrous Ferric Oxide.* New York, New York: John Wiley & Sons. TIC: 224089.

173878 Eggleton, R.A. and Fitzpatrick, R.W. 1988. "New Data and a Revised Structural Model for Ferrihydrite." *Clays and Clay Minerals, 36,* (2), 111-124. Aurora, Colorado: Clay Minerals Society. TIC: 257392.

174704 Eick, M.J.; Peak, J.D.; Brady, P.V. and Pesek, J.D. 1999. "Kinetics of Lead Adsorption/Desorption on Goethite: Residence Time Effect." *Soil Science, 164,* (1), 28-39. Baltimore, MD: Lippincott Williams & Wilkins. TIC: 257580.

170376 EPA (U.S. Environmental Protection Agency) 1999. *Review of Geochemistry and Available K_d Values for Cadmium, Cesium, Chromium, Lead, Plutonium, Radon, Strontium, Thorium, Tritium (^3H), and Uranium.* Volume II of *Understanding Variation in Partition Coefficient, K_d, Values.* EPA 402-R-99-004B. Washington, D.C.: U.S. Environmental Protection Agency, Office of Radiation and Indoor Air. ACC: MOL.20040628.0034.

172215 EPA 2004. "Review of Geochemistry and Available K_d Values for Americium, Arsenic, Curium, Iodine, Neptunium, Radium, and Technetium." Volume III of *Understanding the Variation in Partition Coefficient, K_d, Values.* EPA 402-R-04-002C. Washington, D.C.: U.S. Environmental Protection Agency. ACC: MOL.20041102.0060.

154149 EPRI (Electric Power Research Institute) 2000. *Evaluation of the Candidate High-Level Radioactive Waste Repository at Yucca Mountain Using Total System Performance Assessment, Phase 5.* 1000802. Palo Alto, California: Electric Power Research Institute. TIC: 249555.

170706 Faruque, M. 1993. *LWR Fuel Assemblies PC Database (VA-M04-20004.015.C032 602465).* Canyon Lake, Texas: Knowledge Dynamics. ACC: MOL.19990816.0229.

173708 Felmy, A.R. and Rustad J.R. 1998. "Molecular Statics Calculations of Proton Binding to Goethite Surfaces: Thermodynamic Modeling of the Surface Charging and Protonation of Goethite in Aqueous Solution." *Geochimica et Cosmochimica Acta, 62,* (1), 25-31. New York, New York: Pergamon. TIC: 257304.

173031 Fendorf, S.; Eick, M.J.; Grossl, P.; and Sparks, D.L. 1997. "Arsenate and Chromate Retention Mechanisms on Goethite. 1. Surface Structure." *Environmental Science & Technology, 31,* (2), 315-320. Washington, D.C.: American Chemical Society. TIC: 257062.

173034 Fendorf, S.E.; Li, G.; and Gunter, M.E. 1996. "Micromorphologies and Stabilities of Chromium (III) Surface Precipitates Elucidated by Scanning Force Microscopy." *Soil Science Society America Journal, 60,* 99-106. Madison, Wisconsin: Soil Science Society America. TIC: 257036.

174727 Ford, R.G.; Bertsch, P.M.; and Farley, K.J. 1997. "Changes in Transition and Heavy Metal Partitioning during Hydrous Iron Oxide Aging." *Environmental Science & Technology, 31,* (7), 2028-2033. Washington, D.C.: American Chemical Society. TIC: 257574.

154365 Freeze, G.A.; Brodsky, N.S.; and Swift, P.N. 2001. *The Development of Information Catalogued in REV00 of the YMP FEP Database.* TDR-WIS-MD-000003 REV 00 ICN 01. Las Vegas, Nevada: Bechtel SAIC Company. ACC: MOL.20010301.0237.

101173 Freeze, R.A. and Cherry, J.A. 1979. *Groundwater.* Englewood Cliffs, New Jersey: Prentice-Hall. TIC: 217571.

130407 Gabriel, U.; Gaudet, J.-P.; Spadini, L.; and Charlet, L. 1998. "Reactive Transport of Uranyl in a Goethite Column: An Experimental and Modelling Study." *Chemical Geology, 151,* p. 107-128. New York, New York: Elsevier. TIC: 246884.

173750 Gao, Y. and Mucci, A. 2001. "Acid Base Reactions, Phosphate and Arsenate Complexation, and Their Competitive Adsorption at the Surface of Goethite in 0.7 M NaCl Solution." *Geochimica et Cosmochimica Acta, 65,* (14), 2361-2378. New York, New York: Pergamon. TIC: 257331.

167466 Gerke, H.H. and van Genuchten, M.Th. 1996. "Macroscopic Representation of Structural Geometry for Simulating Water and Solute Movement in Dual-Porosity Media." *Advances in Water Resources, 19,* (6), 343-357. New York, New York: Elsevier. TIC: 255572.

107880 Gertsch, R.E.; Fjeld, A.; Asbury, B.; and Ozdemir, L. 1993. *Construction Applications for TSw2 TBM Cuttings at Yucca Mountain.* Golden, Colorado: Colorado School of Mines. ACC: NNA.19940317.0013.

160579 GoldSim Technology Group. 2002. *GoldSim Contaminant Transport Module, User's Guide.* Version 1.30. Redmond, Washington: Golder Associates. TIC: 253562.

166226 GoldSim Technology Group. 2003. *User's Guide, GoldSim Probabilistic Simulation Environment.* Version 8.01. Redmond, Washington: Golder Associates. TIC: 255170.

154419 Graf, W.L. 1994. *Plutonium and the Rio Grande, Environmental Change and Contamination in the Nuclear Age.* New York, New York: Oxford University Press. TIC: 249730.

173751 Gräfe, M.; Nachtegaal, M.; and Sparks, D.L. 2004. "Formation of Metal-Arsenate Precipitates at the Goethite-Water Interface." *Environmental Science & Technology, 38,* (24), 6561-6570. Washington, D.C.: American Chemical Society. TIC: 257349.

174738 Grant, S.A. and Salehzadeh, A. 1996. "Calculation of Temperature Effects on Wetting Coefficients of Porous Solids and Their Capillary Pressure Functions." *Water Resources Research, 32,* (2), 261-270. Washington, D.C.: American Geophysical Union. TIC: 252291.

138541 Gray, D.E., ed. 1972. *American Institute of Physics Handbook.* 3rd Edition. New York, New York: McGraw-Hill Book Company. TIC: 247425.

153010 Gregg, S.J. and Sing, K.S.W. 1982. *Adsorption, Surface Area and Porosity.* 2nd Edition. 4th Printing 1997. San Diego, California: Academic Press. TIC: 249076.

173032 Grossl, P.R.; Eick, M.; Sparks, D.L.; Goldberg, S.; and Ainsworth, C.C. 1997. "Arsenate and Chromate Retention Mechanisms on Goethite. 2. Kinetic Evaluation Using a Pressure-Jump Relaxation Technique." *Environmental Science & Technology, 31,* (2), 321-326. Washington, D.C.: American Chemical Society. TIC: 257083.

138643 Haltier, E.; Fourest, B.; and David, F. 1990. "Spectroelectrochemical Study of Uranium and Cerium in Carbonate Media." *Radiochimica Acta, 51,* 107-112. München, Germany: R. Oldenbourg Verlag. TIC: 246868.

173866 Hamzaoui, A.; Mgaidi, A.; Megriche, A.; and El Maaoui, M. 2002. "Kinetic Study of Goethite Formation from Ferrihydrite in Alkaline Medium." *Industrial & Engineering Chemistry Research, 41,* (21), 5226-5231. Washington, D.C.: American Chemical Society. TIC: 257379.

173742 Hansmann, D.D. and Anderson M.A. 1985. "Using Electrophoresis in Modeling Sulfate, Selenite, and Phosphate Absorption onto Goethite." *Environmental Science & Technology, 19,* (6), 544-551. Washington, D.C.: American Chemical Society. TIC: 257350.

174125 Haridasan, M. and Jensen, R.D. 1972. "Effect of Temperature on Pressure Head-Water Content Relationship and Conductivity of Two Soils." *Soil Science Society of America Proceedings, 36,* 703-708. Madison, Wisconsin: Soil Science Society of America. TIC: 257435.

174706 Havlin, J.L.; Westfall D.G.; and Olsen, S.R. 1985. "Mathematical Models for Potassium Release Kinetics in Calcareous Soils." *Soil Science Society of America Journal, 49,* 371-376. Madison, Wisconsin: Soil Science Society of America. TIC: 257578.

173817 Hayes, K.F. and Leckie, J.O. 1987. "Modeling Ionic Strength Effects on Cation Adsorption at Hydrous Oxide/Solution Interfaces." *Journal of Colloid and Interface Science, 115,* (2), 564-572. New York, New York: Academic Press. TIC: 226460.

117358 Hiemenz, P.C. 1986. *Principles of Colloid and Surface Chemistry.* 2nd Edition, Revised and Expanded. Undergraduate Chemistry Volume 9. Lagowski, J.J., ed. New York, New York: Marcel Dekker. TIC: 246392.

173023 Hiemstra, T. and Van Riemsdijk, W.H. 1996. "A Surface Structural Approach to Ion Adsorption: The Charge Distribution (CD) Model." *Journal of Colloid and Interface Science, 179,* 488-508. New York, New York: Academic Press. TIC: 257052.

173783 Hofmann, A.; Pelletier, M.; Michot, L.; Stradner, A.; Schurtenberger, P.; and Kretzschmar, R. 2004. "Characterization of the Pores in Hydrous Ferric Oxide Aggregates Formed by Freezing and Thawing." *Journal of Colloid and Interface Science, 271,* 163-173. New York, New York: Elsevier. TIC: 257504.

173711 Hofmann, A.; van Beinum, W.; Meeussen, J.C.L.; and Kretzschmar, R. 2005. "Sorption Kinetics of Strontium in Porous Hydrous Ferric Oxide Aggregates II. Comparison of Experimental Results and Model Predictions." *Journal of Colloid and Interface Science, 283,* 29-40. New York, New York: Elsevier. TIC: 257308.

154379 Holmes, H.F.; Fuller, E.L., Jr.; and Beh, R.A. 1974. "Adsorption of Argon, Nitrogen, and Water Vapor on Zirconium Oxide." *Journal of Colloid and Interface Science, 47,* (2), 365-371. New York, New York: Academic Press. TIC: 249666.

173754 Hongshao, Z. and Stanforth, R. 2001. "Competitive Adsorption of Phosphate and Arsenate on Goethite." *Environmental Science & Technology, 35,* (24), 4753-4757. Washington, D.C.: American Chemical Society. TIC: 257347.

174122 Hopmans, J.W. and Dane, J.H. 1986. "Temperature Dependence of Soil Hydraulic Properties." *Soil Science Society of America Journal, 50,* 4-9. Madison, Wisconsin: Soil Science Society of America. TIC: 257434.

161516 Howard, C.L. 2002. Breached Waste Package Test and Drip Shield Experiments. Scientific Notebook SN-M&O-SCI-043-V1. ACC: MOL.20021219.0022.

161522 Howard, C.L. 2002. Breached Waste Package Test and Drip Shield Experiments. Scientific Notebook SN-M&O-SCI-043-V2. ACC: MOL.20021219.0023.

161623 Hu, Q.; Kneafsey, T.; Wang, J.S.Y.; Roberts, J.; and Carlson, S. 2001. *Summary Report on Phase I Feasibility Study of In-Drift Diffusion.* LBNL-49063. Berkeley, California: Lawrence Berkeley National Laboratory. ACC: MOL.20030225.0125.

170882 Ibrahim, S.A. and Salazar, W.R. 2000. "Physicochemical Speciation of Americium in Soils from Rocky Flats, Colorado, USA." *Journal of Radioanalytical and Nuclear Chemistry, 243,* (2), 347-351. Dordrecht, The Netherlands: Kluwer Academic Publishers. TIC: 256466.

154381 Jurinak, J.J. 1964. "Interaction of Water with Iron and Titanium Oxide Surfaces: Goethite, Hematite, and Anatase." *Journal of Colloid Science, 19,* 477-487. New York, New York: Academic Press. TIC: 249667.

106313 Keeney-Kennicutt, W.L. and Morse, J.W. 1985. "The Redox Chemistry of $Pu(V)O^{+}_{2}$ Interaction with Common Mineral Surfaces in Dilute Solutions and Seawater." *Geochimica et Cosmochimica Acta, 49,* (12), 2577-2588. New York, New York: Pergamon. TIC: 237000.

111470 Keller, G.V. and Frischknecht, F.C. 1966. *Electrical Methods in Geophysical Prospecting.* Volume 10 of *International Series in Electromagnetic Waves.* Cullen, A.L.; Fock, V.A.; and Wait, J.R., eds. New York, New York: Pergamon Press. TIC: 230941.

103282 Kersting, A.B.; Efurd, D.W.; Finnegan, D.L.; Rokop, D.J.; Smith, D.K.; and Thompson, J.L. 1999. "Migration of Plutonium in Ground Water at the Nevada Test Site." *Nature, 397,* (6714), 56-59. London, England: Macmillan Journals. TIC: 243597.

106733 Knight, B. 1982. "Why Do Some Iron Objects Break Up In Store?" *Conservation of Iron.* Clarke, R.W. and Blackshaw, S.M., eds. Maritime Monographs and Reports 53-1982. Pages 50-51. London, England: National Maritime Museum. TIC: 241006.

173784 Koch, C.J.W. and Møller, P.J. 1987. "Adsorption of Nitrogen and Water Vapour onto Goethite Surfaces." *Thermochimica Acta, 114,* 139-144. Amsterdam, The Netherlands: Elsevier. TIC: 257505.

173819 Kooner, Z.S. 1993. "Comparative Study of Adsorption Behavior of Copper, Lead, and Zinc onto Goethite in Aqueous Systems." *Environmental Geology, 21,* (4), 242-250. New York, New York: Springer-Verlag. TIC: 257356.

155761 Kügler, A. 1991. Special Sheet and Plate - Do the Job All Over the World. Mürzzuschlag, Austria: Bohler Bleche GmbH. TIC: 250553.

107760 Kügler, A. 1996. *Böhler Neutronit A976 Sheet and Plate for Nuclear Engineering.* Mürzzuschlag, Austria: Böhler Bleche GmbH. TIC: 240558.

100051 Langmuir, D. 1997. *Aqueous Environmental Geochemistry.* Upper Saddle River, New Jersey: Prentice Hall. TIC: 237107.

100913 Lee, J.H.; Chambré, P.L.; and Andrews, R.W. 1996. "Mathematical Models for Diffusive Mass Transfer from Waste Package Container with Multiple Perforations." *Proceedings of the 1996 International Conference on Deep Geological Disposal of Radioactive Waste, September 16-19, 1996, Winnipeg, Manitoba, Canada.* Pages 5-61–5-72. Toronto, Ontario, Canada: Canadian Nuclear Society. TIC: 233923.

154380 Lee, S. and Staehle, R.W. 1994. *Report to TRW on Contract No. DX 1456KP2L, Adsorption Studies of Water on Gold, Copper, Nickel and Iron Using the Quartz-Crystal Microbalance Technique.* Minneapolis, Minnesota: University of Minnesota. ACC: NNA.19940428.0129.

104943 Lee, S. and Staehle, R.W. 1997. "Adsorption of Water on Copper, Nickel, and Iron." *Corrosion, 53,* (1), 33-42. Houston, Texas: National Association of Corrosion Engineers. TIC: 244501.

162229 Lide, D.R., ed. 2000. *CRC Handbook of Chemistry and Physics.* 81st Edition. Boca Raton, Florida: CRC Press. TIC: 253056.

160832 Lide, D.R., ed. 2002. *CRC Handbook of Chemistry and Physics.* 83rd Edition. Boca Raton, Florida: CRC Press. TIC: 253582.

161667 Litaor, M.I. and Ibrahim, S.A. 1996. "Plutonium Association with Selected Solid Phases in Soils of Rocky Flats, Colorado, Using Sequential Extraction Technique." *Journal of Environmental Quality, 25,* (5), 1144-1151. Madison, Wisconsin: American Society of Agronomy. TIC: 252783.

105729 Liu, H.H.; Doughty, C.; and Bodvarsson, G.S. 1998. "An Active Fracture Model for Unsaturated Flow and Transport in Fractured Rocks." *Water Resources Research, 34,* (10), 2633-2646. Washington, D.C.: American Geophysical Union. TIC: 243012.

173771 Lövgren, L.; Sjöberg, S.; and Schindler, P.W. 1990. "Acid/Base Reactions and Al(III) Complexation at the Surface of Goethite." *Geochimica et Cosmochimica Acta, 54,* 1301-1306. New York, New York: Pergamon Press. TIC: 257334.

174812 Low, M.J.D. 1960. "Kinetics of Chemisorption of Gases on Solids." *Chemical Reviews, 60,* (3), 267-312. Washington, D.C.: American Chemical Society.

166315 Lu, N.; Conca, J.; Parker, G.R.; Leonard, P.A.; Moore, B.; Strietelmeier, B.; and Triay, I.R. 2000. *Adsorption of Actinides onto Colloids as a Function of Time, Temperature, Ionic Strength, and Colloid Concentration, Waste Form Colloids Report for Yucca Mountain Program (Colloid Data Summary from 1999 to 2000 Research).* LA-UR-00-5121. Los Alamos, New Mexico: Los Alamos National Laboratory. ACC: MOL.20031204.0108.

174714 Lu, N.; Cotter, C.R.; Kitten, H.D.; Bentley, J.; and Triay, I.R. 1998. "Reversibility of Sorption of Plutonium-239 onto Hematite and Goethite Colloids." *Radiochimica Acta, 83,* 167-173. München, Germany: R. Oldenbourg Verlag. TIC: 257572.

100946 Lu, N.; Triay, I.R.; Cotter, C.R.; Kitten, H.D.; and Bentley, J. 1998. *Reversibility of Sorption of Plutonium-239 onto Colloids of Hematite, Goethite, Smectite, and Silica.* LA-UR-98-3057. Los Alamos, New Mexico: Los Alamos National Laboratory. ACC: MOL.19981030.0202.

173757 Lützenkirchen, J.; Boily, J-F.; Lövgren, L.; and Sjöberg, S. 2002. "Limitations of the Potentiometric Titration Technique in Determining the Proton Active Site Density of Goethite Surfaces." *Geochimica et Cosmochimica Acta, 66,* (19), 3389-3396. New York, New York: Pergamon. TIC: 257328.

173758 Machesky, M.L.; Andrade, W.O.; and Rose, A.W. 1991. "Adsorption of Gold(III) and Gold(I)-Thiosulfate Anions by Goethite." *Geochimica et Cosmochimica Acta, 55,* 769-776. Elmsford, New York: Pergamon. TIC: 257329.

174725 Manning, B.A. and Burau, R.G. 1995. "Selenium Immobilization in Evaporation Pond Sediments by In Situ Precipitation of Ferric Oxyhydroxide." *Environmental Science & Technology, 29,* (10), 2639-2646. Washington, D.C.: American Chemical Society. TIC: 257575.

154383 Matsuda, T.; Taguchi, H.; and Nagao, M. 1992. "Energetic Properties of NiO Surface Examined by Heat-of-Adsorption Measurement." *Journal of Thermal Analysis, 38,* 1835-1845. Chichester, England: John Wiley & Sons. TIC: 249669.

154382 McCafferty, E. and Zettlemoyer, A.C. 1970. "Entropy of Adsorption and the Mobility of Water Vapor on Alpha-Fe_2O_3." *Journal of Colloid and Interface Science, 34,* (3), 452-460. New York, New York: Academic Press. TIC: 249668.

154378 McCafferty, E. and Zettlemoyer, A.C. 1971. "Adsorption of Water Vapour on Alpha-Fe_2O_3." *Discussions of the Faraday Society, 52,* 239-263. London, England: Gurney and Jackson. TIC: 249665.

100780 Meijer, A. 1990. *Yucca Mountain Project Far-Field Sorption Studies and Data Needs.* LA-11671-MS. Los Alamos, New Mexico: Los Alamos National Laboratory. ACC: MOL.19980508.1113.

173785 Micale, F.J.; Kiernan, D.; and Zettlemoyer, A.C. 1985. "Characterization of the Surface Properties of Iron Oxides." *Journal of Colloid and Interface Science, 105,* (2), 570-576. New York, New York: Academic Press. TIC: 257514.

138677 Millard, A.R. and Hedges, R.E.M. 1996. "A Diffusion-Adsorption Model of Uranium Uptake by Archaeological Bone." *Geochimica et Cosmochimica Acta, 60,* (12), 2139-2152. New York, New York: Pergamon Press. TIC: 246791.

133392 Mills, R. 1973. "Self-Diffusion in Normal and Heavy Water in the Range 1-45°." *Journal of Physical Chemistry, 77,* (5), 685-688. Washington, D.C.: American Chemical Society. TIC: 246404.

138725 Mills, R. and Lobo, V.M.M. 1989. *Self-Diffusion in Electrolyte Solutions, A Critical Examination of Data Compiled from the Literature.* Physical Sciences Data 36. Pages 314-319. New York, New York: Elsevier. TIC: 248026.

159327 Misawa, T.; Hashimoto, K.; and Shimodaira, S. 1974. "The Mechanism of Formation of Iron Oxide and Oxyhydroxides in Aqueous Solutions at Room Temperature." *Corrosion Science, 14,* 131-149. New York, New York: Pergamon Press. TIC: 212539.

173759 Missana, T.; García-Gutiérrez, M.; and Maffiotte, C. 2003. "Experimental and Modeling Study of the Uranium (VI) Sorption on Goethite." *Journal of Colloid and Interface Science, 260,* 291-301. New York, New York: Academic Press. TIC: 257330.

130419 Mohanty, S.; Cragnolino, G.; Ahn, T.; Dunn, D.S.; Lichtner, P.C.; Manteufel, R.D.; and Sridhar, N. 1996. *Engineered Barrier System Performance Assessment Code: Ebspac Version 1.0B Technical Description and User's Manual.* CNWRA 96-011. San Antonio, Texas: Center for Nuclear Waste Regulatory Analyses. TIC: 233382.

162877 Morimoto, T.; Nagao, M.; and Tokuda, F. 1969. "The Relation Between the Amounts of Chemisorbed and Physisorbed Water on Metal Oxides." *The Journal of Physical Chemistry, 73,* (1), 243 -248. Washington, D.C.: American Chemical Society. TIC: 254165.

174703 Morse, J.W. and Choppin, G.R. 1986. "Laboratory Studies of Plutonium in Marine Systems." *Marine Chemistry, 20,* 73-89. Amsterdam, The Netherlands: Elsevier. TIC: 257581.

173760 Müller, B. and Sigg, L. 1992. "Adsorption of Lead(II) on the Goethite Surface: Voltammetric Evaluation of Surface Complexation Parameters." *Journal of Colloid and Interface Science, 148,* (2), 517-532. New York, New York: Academic Press. TIC: 257336.

162878 Nagao, M.; Kumashiro, R.; Matsuda, T.; and Kuroda, Y. 1995. "Calorimetric Study of Water Two-Dimensionally Condensed on the Homogeneous Surface of a Solid." *Thermochimica Acta, 253,* (1-2), 221-233. New York, New York: Elsevier. TIC: 254099.

174394 National Research Council 2000. *Natural Attenuation for Groundwater Remediation.* Washington, D.C.: National Academy Press. TIC: 257470.

173018 Naveau, A.; Monteil-Rivera, F.; Dumonceau, J.; and Boudesocque, S. 2005. "Sorption of Europium on a Goethite Surface: Influence of Background Electrolyte." *Journal of Contaminant Hydrology, 77,* 1-16. New York, New York: Elsevier. TIC: 257071.

174124 Nimmo, J.R. and Miller, E.E. 1986. "The Temperature Dependence of Isothermal Moisture vs. Potential Characteristics of Soils." *Soil Science Society of America Journal, 50,* 1105-1113. Madison, Wisconsin: Soil Science Society of America. TIC: 257436.

163274 NRC (U.S. Nuclear Regulatory Commission) 2003. *Yucca Mountain Review Plan, Final Report.* NUREG-1804, Rev. 2. Washington, D.C.: U.S. Nuclear Regulatory Commission, Office of Nuclear Material Safety and Safeguards. TIC: 254568.

167377 Nye, P.H. 1979. "Diffusion of Ions and Uncharged Solutes in Soils and Soil Clays." *Advances in Agronomy, 31,* 225-272. New York, New York: Academic Press. TIC: 255345.

154588 Olesen, T.; Moldrup, P.; and Gamst, J. 1999. "Solute Diffusion and Adsorption in Six Soils along a Soil Texture Gradient." *Soil Science Society of America Journal, 63,* (3), 519-524. Madison, Wisconsin: Soil Science Society of America. TIC: 249743.

155700 Olesen, T.; Moldrup, P.; Henriksen, K.; and Petersen, L.W. 1996. "Modeling Diffusion and Reaction in Soils: IV. New Models for Predicting Ion Diffusivity." *Soil Science, 161,* (10), 633-645. Baltimore, Maryland: Williams & Wilkins. TIC: 250477.

173799 Or, D. and Tuller, M. 1999. "Liquid Retention and Interfacial Area in Variability Saturated Porous Media: Upscaling from Single-Pore To Sample-Scale Model." *Water Resources Research, 35,* (12), 3591-3605. Washington, D.C.: American Geophysical Union. TIC: 257326.

174071 Painter, S.; Cvetkovic, V.; Pickett, D.; and Turner, D.R. 2002. "Significance of Kinetics for Sorption of Inorganic Colloids: Modeling and Experiment Interpretation Issues." *Environmental Science & Technology, 36,* (24), 5369-5375. Washington, D.C.: American Chemical Society. TIC: 257438.

174707 Payne, T.E.; Davis, J.A.; and Waite, T.D. 1994. "Uranium Retention by Weathered Schists - The Role of Iron Minerals." *Radiochimica Acta, 66/67,* 297-303. München, Germany: R. Oldenbourg Verlag. TIC: 257571.

138732 Perry, D.L.; Phillips, S.L.; and Chung, J.D. 1988. "Potentiostatic Measurement of the Diffusion Coefficient of UO_2^{2+} in Carbonate Media." *Inorganica Chimica Acta, 149,* 301-304. Lausanne, Switzerland: Elsevier. TIC: 246806.

104946 Perry, R.H. and Chilton, C.H., eds. 1973. *Chemical Engineers' Handbook.* 5th Edition. New York, New York: McGraw-Hill. TIC: 242591.

119529 Perry, R.H.; Chilton, C.H.; and Kirkpatrick, S.D., eds. 1963. *Chemical Engineers' Handbook.* 4th Edition. New York, New York: McGraw-Hill. TIC: 237828.

173762 Persson, P.; Nordin, J.; Rosenqvist, J.; Lövgren, L.; Öhman, L-O.; and Sjöberg, S. 1998. "Comparison of the Adsorption of o-Phthalate on Boehmite (γ-AlOOH), Aged (γ -Al_2O_3, and Goethite (α-Fe-OOH)." *Journal of Colloid and Interface Science, 206,* 252-266. New York, New York: Academic Press. TIC: 257283.

105743 Philip, J.R.; Knight, J.H.; and Watcher, R.T. 1989. "Unsaturated Seepage and Subterranean Holes: Conspectus, and Exclusion Problem for Circular Cylindrical Cavities." *Water Resources Research, 25,* (1), 16-28. Washington, D.C.: American Geophysical Union. TIC: 239117.

111477 Pirson, S.J. 1963. *Handbook of Well Log Analysis for Oil and Gas Formation Evaluation.* Englewood Cliffs, New Jersey: Prentice-Hall. TIC: 245393.

173714 Pivovarov, S. 1997. "Surface Structure and Site Density of the Oxide-Solution Interface." *Journal of Colloid and Interface Science, 196,* 321-323. New York, New York: Academic Press. TIC: 257309.

123115 Porter, L.K.; Kemper, W.D.; Jackson, R.D.; and Stewart, B.A. 1960. "Chloride Diffusion in Soils as Influenced by Moisture Content." *Soil Science Society of America Proceedings, 24,* (5), 460-463. Danville, Illinois: Soil Science Society of America. TIC: 246854.

174726 Powell, B.A.; Fjeld, R.A.; Kaplan, D.I.; Coates, J.T.; and Serkiz, S.M. 2005. "$Pu(V)O_2^+$ Adsorption and Reduction by Synthetic Hematite and Goethite." *Environmental Science & Technology, 39,* (7), 2107-2114. Washington, D.C.: American Chemical Society. TIC: 257576.

173709 Randall, S.R.; Sherman, D.M.; Ragnardottir, K.V.; and Collins, C.R. 1999. "The Mechanism of Cadmium Surface Complexation on Iron Oxyhydroxide Minerals." *Geochimica et Cosmochimica Acta, 63,* (19/20), 2971-2987. New York, New York: Pergamon. TIC: 257307.

154434 Reardon, E.J. 1981. "Kd's — Can They be Used to Describe Reversible Ion Sorption Reactions in Contaminant Migration?" *Ground Water, 19,* (3), 279-286. Worthington, Ohio: Water Well Journal Publishing Company. TIC: 249726.

163008 Reimus, P.W.; Ware, S.D.; Benedict, F.C.; Warren, R.G.; Humphrey, A.; Adams, A.; Wilson, B.; and Gonzales, D. 2002. *Diffusive and Advective Transport of ^{3}H, ^{14}C, and ^{99}Tc in Saturated, Fractured Volcanic Rocks from Pahute Mesa, Nevada.* LA-13891-MS. Los Alamos, New Mexico: Los Alamos National Laboratory. TIC: 253905.

173846 Rhoades, J.D. and Oster, J.D. 1986. "Solute Content." Chapter 42 of *Methods of Soil Analysis, Part 1 Physical and Mineralogical Methods.* Klute, A., ed. 2nd Edition. Madison, Wisconsin: Soil Science Society of America. TIC: 217566.

173835 Rhoades, J.D.; Raats, P.A.C.; and Prather, R.J. 1976. "Effects of Liquid-Phase Electrical Conductivity, Water Content, and Surface Conductivity on Bulk Soil Electrical Conductivity." *Soil Science Society America Journal, 40,* (5), 651-655. Madison, Wisconsin: Soil Science Society of America. TIC: 257324.

101710 Roberts, J.J. and Lin, W. 1997. "Electrical Properties of Partially Saturated Topopah Spring Tuff: Water Distribution as a Function of Saturation." *Water Resources Research, 33,* (4), 577-587. Washington, D.C.: American Geophysical Union. TIC: 239736.

173763 Robertson, A.P. and Leckie, J.O. 1997. "Cation Binding Predictions of Surface Complexation Models: Effects of pH, Ionic Strength, Cation Loading, Surface Complex, and Model Fit." *Journal of Colloid and Interface Science, 188,* 444-472. New York, New York: Academic Press. TIC: 257300.

173710 Rodda, D.P.; Johnson, B.B.; and Wells, J.D. 1996. "Modeling the Effect of Temperature on Adsorption of Lead(II) and Zinc(II) onto Goethite at Constant pH." *Journal of Colloid and Interface Science, 184,* 365-377. New York, New York: Academic Press. TIC: 257312.

174022 Romero E.; Gens, A.; and Lloret, A. 2001. "Temperature Effects on the Hydraulic Behaviour of an Unsaturated Clay." *Geotechnical and Geological Engineering, 19,* 311-332. Amsterdam, The Netherlands: Kluwer Academic Publishers. TIC: 257400.

138739 Rosch, F. and Khalkin, V.A. 1990. "Ion Mobilities of Trivalent f-Elements in Aqueous Electrolytes." *Radiochimica Acta, 51,* 101-106. Munich, Germany: R. Oldenbourg Verlag. TIC: 246710.

168432 Runde, W.; Conradson, S.D.; Efurd, D.W.; Lu, N.P.; VanPelt, C.E.; and Tait, C.D. 2002. "Solubility and Sorption of Redox-Sensitive Radionuclides (Np, Pu) in J-13 Water from the Yucca Mountain Site: Comparison between Experiment and Theory." *Applied Geochemistry, 17,* (6), 837-853. New York, New York: Pergamon. TIC: 254046.

155697 Russo, R.E.; Mao, X.; Borisov, O.V.; and Liu, H. 2000. "Laser Ablation in Atomic Spectroscopy." *Encyclopedia of Analytical Chemistry.* Meyers, R.A., ed. Pages 9485-9506. Chichester, England: John Wiley & Sons. TIC: 250479.

173766 Rustad, J.R.; Felmy, A.R.; and Hay, B.P. 1996. "Molecular Statics Calculations of Proton Binding to Goethite Surfaces: A New Approach to Estimation of Stability Constants for Multisite Surface Complexation Models." *Geochimica et Cosmochimica Acta, 60,* (9), 1563-1576. New York, New York: Pergamon. TIC: 257333.

173812 Sahai, N. and Sverjensky D.A. 1997. "Evaluation of Internally Consistent Parameters for the Triple-Layer Model by the Systematic Analysis of Oxide Surface Titration Data." *Geochimica et Cosmochimica Acta, 61,* (14), 2801-2826. New York, New York: Pergamon. TIC: 257337.

107213 Sanchez, A.L.; Murray, J.W.; and Sibley, T.H. 1985. "The Adsorption of Plutonium IV and V on Goethite." *Geochimica et Cosmochimica Acta, 49,* (11), 2297-2307. New York, New York: Pergamon Press. TIC: 224091.

170923 Santschi, P.H.; Roberts, K.A.; and Guo, L. 2002. "Organic Nature of Colloidal Actinides Transported in Surface Water Environments." *Environmental Science & Technology, 36,* (17), 3711-3719. Washington, D.C.: American Chemical Society. TIC: 256463.

173028 Schultz, M.F.; Benjamin, M.M.; and Ferguson, J.F. 1987. "Adsorption and Desorption of Metals on Ferrihydrite: Reversibility of the Reaction and Sorption Properties of the Regenerated Solid." *Environmental Science Technology, 21,* (9), 863-869. Washington, D.C.: American Chemical Society. TIC: 257057.

144629 Schwertmann, U. and Cornell, R.M. 1991. *Iron Oxides in the Laboratory: Preparation and Characterization.* New York, New York: VCH Publishers. TIC: 237942.

173863 Schwertmann, U.; Friedl, J.; Stanjek, H.; and Schulze, D.G. 2000. "The Effect of Al on Fe Oxides. XIX. Formation of Al-Substituted Hematite from Ferrihydrite at 25°C and pH 4 to 7." *Clays and Clay Minerals, 48,* (2), 159-172. Aurora, Colorado: Clay Minerals Society. TIC: 257393.

173836 Shainberg, I.; Rhoades, J.D.; and Prather, R.J 1980. "Effect of Exchangeable Sodium Percentage, Cation Exchange Capacity, and Soil Solution Concentration on Soil Electrical Conductivity." *Soil Science Society America Journal, 44,* (3), 469-473. Madison, Wisconsin: Soil Science Society of America. TIC: 257317.

167469 Šimunek, J.; Jarvis, N.J.; van Genuchten, M.Th.; and Gardenas, A. 2003. "Review and Comparison of Models for Describing Non-Equilibrium and Preferential Flow and Transport in the Vadose Zone." *Journal of Hydrology, 272,* (1-4), 14-35. New York, New York: Elsevier. TIC: 255570.

161624 Singh, A.K.; Singh, H.; Singh, S.P.; and Sawhney, R.L. 2002. "Numerical Calculation of Psychrometric Properties on a Calculator." *Building and Environment, 37,* (4), 415-419. New York, New York: Elsevier. TIC: 253846.

170588 So, H.B. and Nye, P.H. 1989. "The Effect of Bulk Density, Water Content and Soil Type on the Diffusion of Chloride in Soil." *Journal of Soil Science, 40,* (4), 743-749. Oxford, England: Blackwell Scientific. TIC: 255392.

127253 Sposito, G. 1984. *The Surface Chemistry of Soils.* New York, New York: Oxford University Press. TIC: 217687.

141778 Stumm, W. 1992. *Chemistry of the Solid-Water Interface, Processes at the Mineral-Water and Particle-Water Interface in Natural Systems.* New York, New York: John Wiley & Sons. TIC: 237213.

118706 Tada, H.; Paris, P.C.; and Irwin, G.R. 1973. *The Stress Analysis of Cracks Handbook.* St. Louis, Missouri: Del Research Corporation. TIC: 247050.

161625 Tamura, H.; Tanaka, A.; Mita, K.; and Furuichi, R. 1999. "Surface Hydroxyl Site Densities on Metal Oxides as a Measure for the Ion-Exchange Capacity." *Journal of Colloid and Interface Science, 209,* (1), 225-231. New York, New York: Academic Press. TIC: 253844.

155334 Towe, K.M. and Bradley, W.F. 1967. "Mineralogical Constitution of Colloidal 'Hydrous Ferric Oxides'." *Journal of Colloid and Interface Science, 24,* 384-392. New York, New York: Academic Press. TIC: 250230.

173021 Trivedi, P.; Axe, L.; and Dyer, J. 2001. "Adsorption of Metal Ions onto Goethite: Single-Adsorbate and Competitive Systems." *Colloids and Surfaces, 191,* 107-121. New York, New York: Elsevier. TIC: 257088.

138747 Tsukamoto, M.; Ohe, T.; Fujita, T.; Hesbol, R.; and Hermansson, H-P. 1994. "Diffusion of Neptunium(V) in Loosely Compacted Sodium Bentonite." *Radiochimica Acta, 66/67,* 397-403. München, Germany: R. Oldenbourg Verlag. TIC: 246893.

144702 Van Geen, A.; Robertson, A.P.; and Leckie, J.O. 1994. "Complexation of Carbonate Species at the Goethite Surface: Implications for Adsorption of Metal Ions in Natural Waters." *Geochimica et Cosmochimica Acta, 58,* (9), 2073-2086. New York, New York: Elsevier. TIC: 212000.

100610 van Genuchten, M.T. 1980. "A Closed-Form Equation for Predicting the Hydraulic Conductivity of Unsaturated Soils." *Soil Science Society of America Journal, 44,* (5), 892-898. Madison, Wisconsin: Soil Science Society of America. TIC: 217327.

173017 Villalobos, M.; Trotz, M.A.; and Leckie, J.O. 2003. "Variability in Goethite Surface Site Density: Evidence from Proton and Carbonate Sorption." *Journal of Colloid and Interface Science, 268,* 273-287. New York, New York: Elsevier. TIC: 257076.

124994 Wan, J. and Wilson, J.L. 1994. "Visualization of the Role of the Gas-Water Interface on the Fate and Transport of Colloids in Porous Media." *Water Resources Research, 30,* (1), 11-23. Washington, D.C.: American Geophysical Union. TIC: 246300.

173035 Watson, E.B. 1996. "Surface Enrichment and Trace-Element Uptake during Crystal Growth." *Geochimica et Cosmochimica Acta, 60,* (24), 5013-5020. Tarrytown, New York: Elsevier. TIC: 257077.

100833 Weast, R.C. and Astle, M.J., eds. 1981. *CRC Handbook of Chemistry and Physics.* 62nd Edition. Boca Raton, Florida: CRC Press. TIC: 240722.

111561 Weast, R.C., ed. 1985. *CRC Handbook of Chemistry and Physics.* 66th Edition. Boca Raton, Florida: CRC Press. TIC: 216054.

173713 Xue, Y. and Traina, S.J. 1996. "Cosolvent Effect on Goethite Surface Protonation." *Environmental Science & Technology, 30,* (11), 3161 - 3166. Washington, D.C.: American Chemical Society. TIC: 257272.

104441 YMP (Yucca Mountain Site Characterization Project) 1998. *Disposal Criticality Analysis Methodology Topical Report.* YMP/TR-004Q, Rev. 00. Las Vegas, Nevada: Yucca Mountain Site Characterization Office. ACC: MOL.19990210.0236.

9.2 CODES, STANDARDS, REGULATIONS, AND PROCEDURES

173273 10 CFR 63. 2005 Energy: Disposal of High-Level Radioactive Wastes in a Geologic Repository at Yucca Mountain, Nevada. ACC: MOL.20050405.0118.

AP-2.22Q, Rev. 1, ICN 1. *Classification Analyses and Maintenance of the Q-List.* Washington, D.C.: U.S. Department of Energy, Office of Civilian Radioactive Waste Management. ACC: DOC.20040714.0002.

154085 ASM 1979. *Properties and Selection: Nonferrous Alloys and Pure Metals.* Volume 2 of *Metals Handbook.* 9th Edition. Metals Park, Ohio: American Society for Metals. TIC: 209800.

147578 ASTM A 20/A20M-99a. 1999. *Standard Specification for General Requirements for Steel Plates for Pressure Vessels.* West Conshohocken, Pennsylvania: American Society for Testing and Materials. TIC: 247403.

162724 ASTM A 588/A 588M-01. 2001. *Standard Specification for High-Strength Low-Alloy Structural Steel with 50 ksi [345 MPa] Minimum Yield Point to 4–in. [100–mm] Thick.* West Conshohocken, Pennsylvania: American Society for Testing and Materials. TIC: 253998.

159971 ASTM A 759-00. 2001. *Standard Specification for Carbon Steel Crane Rails.* West Conshohocken, Pennsylvania: American Society for Testing and Materials. TIC: 253176.

168403 ASTM B 932-04. 2004. *Standard Specification for Low-Carbon Nickel-Chromium-Molybdenum-Gadolinium Alloy Plate, Sheet, and Strip.* West Conshohocken, Pennsylvania: American Society for Testing and Materials. TIC: 255846.

103515 ASTM G 1-90 (Reapproved 1999). 1999. *Standard Practice for Preparing, Cleaning, and Evaluating Corrosion Test Specimens.* West Conshohocken, Pennsylvania: American Society for Testing and Materials. TIC: 238771.

LP-2.29Q-BSC, Rev. 0, ICN 1. *Planning for Science Activities.* Washington, D.C.: U.S. Department of Energy, Office of Civilian Radioactive Waste Management. ACC: DOC.20050718.0002.

LP-SI.11Q-BSC, Rev. 0, ICN 01. *Software Management.* Washington, D.C.: U.S. Department of Energy, Office of Civilian Radioactive Waste Management. ACC: DOC.20041005.0008

LP-SIII.2Q-BSC, Rev. 0, ICN 0. *Qualification of Unqualified Data.* Washington, D.C.: U.S. Department of Energy, Office of Civilian Radioactive Waste Management. ACC: DOC.20050119.0002.

LP-SIII.10Q-BSC, Rev. 0, ICN 1. Models. Washington, D.C.: U.S. Department of Energy, Office of Civilian Radioactive Waste Management. ACC: DOC.20050623.0001.

9.3 SOURCE DATA, LISTED BY DATA TRACKING NUMBER

148751 LA0003AM831341.001. Probability Distributions for Sorption Coefficients (Kd's). Submittal date: 03/29/2000.

150272 LA0004NL831352.001. Pu(IV) and Pu(V) Sorption on Hematite and Goethite Colloids with Natural and Synthetic J-13 Water (1997-98 Data). Submittal date: 04/04/2000.

167015 LA0311AM831341.001. Correlation Matrix for Sampling of Sorption Coefficient Probability Distributions. Submittal date: 11/06/2003.

171584 LA0408AM831341.001. Unsaturated Zone Distribution Coefficients (Kds) for U, Np, Pu, Am, Pa, Cs, Sr, Ra, and Th. Submittal date: 08/24/2004.

159525 LB0205REVUZPRP.001. Fracture Properties for UZ Model Layers Developed from Field Data. Submittal date: 05/14/2002.

159672 LB0207REVUZPRP.002. Matrix Properties for UZ Model Layers Developed from Field and Laboratory Data. Submittal date: 07/15/2002.

161788 LB0208UZDSCPLI.002. Drift-Scale Calibrated Property Sets: Lower Infiltration Data Summary. Submittal date: 08/26/2002.

161243 LB0208UZDSCPMI.002. Drift-Scale Calibrated Property Sets: Mean Infiltration Data Summary. Submittal date: 08/26/2002.

162379 LB03013DSSCP3I.001. 3-D Site Scale Calibrated Properties: Data Summaries. Submittal date: 01/27/2003.

161787 LB0302UZDSCPUI.002. Drift-Scale Calibrated Property Sets: Upper Infiltration Data Summary. Submittal date: 02/05/2003.

165451 LB0307FMRADTRN.001. Fracture-Matrix Partitioning Model: Spreadsheet Calculations. Submittal date: 07/31/2003.

153044 MO0003RIB00076.000. Physical and Chemical Characteristics of Type 316N Grade. Submittal date: 03/14/2000.

169973 MO0107TC239753.000. ASME Boiler and Pressure Vessel Code, Sec II B SB-575 Specification for Low-Carbon Nickel-Molybdenum-Chromium, Low-Carbon. Submittal date: 07/23/2004.

169970 MO0107TC240032.000. Standard Specification for Pressure Vessel Plates, Carbon Steel, for Moderate- and-Lower-Temperature Service. Submittal date: 07/19/2001.

163399 MO0207EBSATBWP.021. Atlas Breached Waste Package and Drip Shield Experiments: Initial Tests for Rough Drip Shield Surface. Submittal date: 07/31/2002.

163400 MO0207EBSATBWP.022. Atlas Breached Waste Package and Drip Shield Experiments: Initial Tests for Smooth Drip Shield Surface. Submittal date: 07/31/2002.

163402 MO0207EBSATBWP.023. Atlas Breached Waste Package and Drip Shield Experiments: Single Patch Q(Splash) and Q(Film) Tests on the Smooth Drip Shield Surface. Submittal date: 07/31/2002.

163401 MO0207EBSATBWP.024. Atlas Breached Waste Package and Drip Shield Experiments: Multiple Patch Tests for Smooth Drip Shield Surface. Submittal date: 07/31/2002.

163403 MO0207EBSATBWP.025. Atlas Breached Waste Package and Drip Shield Experiments: Bounding Flow Rate Tests on the Smooth Drip Shield Surface. Submittal date: 07/31/2002.

163404 MO0208EBSATBWP.027. Atlas Breached Waste Package and Drip Shield Experiments: Multiple Patch Tests on the Rough Drip Shield Surface. Submittal date: 08/13/2002.

163405 MO0208EBSATBWP.028. Atlas Breached Waste Package and Drip Shield Experiments: Bounding Flow Rate Tests on the Rough Drip Shield Surface. Submittal date: 08/13/2002.

162871 MO0302UCC034JC.003. Graphical X-Ray Diffractometer Data and Mineral Analysis of Filtered Solids from Effluent Solution During Miniature Waste Package Corrosion. Submittal date: 02/10/2003.

170760 MO0407SEPFEPLA.000. LA FEP List. Submittal date: 07/20/2004.

172097 MO0407SPAPCEML.005. EBS P&CE Model Longevity of Materials Evaluation. Submittal date: 07/02/2004.

172059 MO0409SPAACRWP.000. Aqueous Corrosion Rates For Non-Waste Form Waste Package Materials. Submittal date: 09/16/2004.

164131 SN0306T0504103.006. Revised Sorption Partition Coefficients (Kd Values) for Selected Radionuclides Modeled in the TSPA (Total System Performance Assessment). Submittal date: 06/30/2003.

165540 SN0309T0504103.010. Updated Iron Oxyhydroxide Colloid Concentration Parameters, Specific Surface Area (SA) of Iron Oxyhydroxide Colloids, Target Flux Out Ratio (FRN) and Forward Rate Constant (K) for Pu & Am Sorption to Iron Oxyhydroxide Colloids & Stationary Corrosion. Submittal date: 09/18/2003.

168761 SN0310T0505503.004. Initial Radionuclide Inventories for TSPA-LA. Submittal date: 10/27/2003.

169129 SN0404T0503102.011. Thermal Conductivity of the Potential Repository Horizon Rev 3. Submittal date: 04/27/2004.

9.4 OUTPUT DATA, LISTED BY DATA TRACKING NUMBER

MO0506SPAINPAR.000. Input Parameters for TSPA-LA from ANL-WIS-PA-000001, "Engineered Barrier System: Radionuclide Transport Abstraction." Submittal date: 06/06/2005.

SN0403T0507703.015. Model Inputs Used in Engineered Barrier System (EBS) Radionuclide Transport Abstraction, Version 1. Submittal date: 03/12/2004. (Preliminary developed data).

SN0409T0507703.017. Model Inputs Used in Engineered Barrier System (EBS) Radionuclide Transport Abstraction. Submittal date: 09/27/2004. (Preliminary developed data).

SN0410T0507703.018. Engineered Barrier System (EBS) Radionuclide Transport Abstraction Model Inputs. Submittal date: 11/03/2004.

SN0503T0503305.001. Summary of and Sorption Site Density and Site Characteristics Obtained from Scientific Literature for Goethite and Hydrous Ferric Oxide (HFO). Submittal date: 03/22/2005. (Preliminary developed data).

SN0508T0503305.003. Summary of Sorption Site Density and Site Characteristics Obtained from Scientific Literature for Goethite and Hydrous Ferric Oxide (HFO). Submittal date: 08/18/2005.

9.5 SOFTWARE CODES

166572 Golder Associates. 2003. *Software Code: GoldSim.* V8.01 Service Pack 1. PC, Windows 2000. 10344-8.01 SP1-00.

9.6 UNQUALIFIED OUTPUT DATA, LISTED BY DATA TRACKING NUMBER

MO0508SPAFRAPM.000. Comparison of Results from Fracture-Matrix Partitioning Model with Results from Modified Engineered Barrier System (EBS) Radionuclide Transport Abstraction EBS-UZ Interface Model. Submittal Date: 08/01/2005.

MO0508SPAUZDIF.000. Verification of Dual Invert/Dual UZ Diffusive Flux Bifurcation. Submittal Date: 08/18/2005.

SN0508T0507703.020. Calculations Supporting an Alternative Conceptual Model for Sorption of Pu onto In-Package Corrosion Products, for ANL-WIS-PA-000001 REV 02, EBS Radionuclide Transport Abstraction. Submittal Date: 08/11/2005.

INTENTIONALLY LEFT BLANK

APPENDIX A

MICROSOFT EXCEL SPREADSHEET "MASSES OF MATERIALS"

MICROSOFT EXCEL SPREADSHEET "MASSES OF MATERIALS"

In this spreadsheet, the mass of iron and the equivalent mass of Fe_2O_3 is calculated for four waste packages. The results are reported in Table 6.3-4. The calculation is done: 21-PWR (absorber plate), 44-BWR (absorber plate), 5-DHLW/DOE Short, and Naval Long.

The procedure for determining the equivalent mass of Fe_2O_3 is to calculate the total mass of each type of iron-containing alloy, calculate the mass of iron in all components of each alloy based on the iron content of the alloy, sum the mass of iron in the waste package, and convert the iron mass to Fe_2O_3 mass using the stoichiometry and molecular weights. Only the components within the outer corrosion barrier are included in the calculation; the outer corrosion barrier is considered to be inert.

For a 21-PWR waste package, the mass and number of each component are listed in Figures A-1 and A-2 as shown in Table 4.1-20 (BSC 2004 [DIRS 169472], Table 2). This calculation uses the previous waste package design in which the absorber plates are composed of Neutronit, rather than the current design with Ni-Gd absorber plates (BSC 2004 [DIRS 170710]). The impact of using the previous design is discussed in Section 6.3.4.2.3.1, where it is shown that the differences in absorber plate design should have negligible net effect on radionuclide transport from the EBS. In Column E (Figure A-1), the total mass of the components is computed (e.g., E2=C2*D2). The total mass of all components is summed in Cell E23. The calculation is repeated for a 44-BWR waste package (BSC 2004 [DIRS 169472], Table 3) in Column K (Figure A-1), for a 5–DHLW/DOE Short waste package (BSC 2004 [DIRS 167207], Table 5) in Column Q (Figure A-2), and for a Naval Long waste package (BSC 2004 [DIRS 169472], Table 4) in Column W (Figure A-2). Consistent with the treatment for the 21-PWR waste package, the previous design with Neutronit absorber plates is considered for a 44-BWR waste package rather than the current design (BSC 2004 [DIRS 170838]). For the 5 DHLW/DOE Short waste package, a mass of 1 kg is erroneously used for the Interface Ring (Column O, Row 5 in Figure A-2); the correct mass is 44.6 kg (BSC 2004 [DIRS 167207], Table 5). Also, the 5 DHLW/DOE Short waste package, the mass of the spread ring (Column O, Row 20 in Figure A-2) was increased from 31.9 kg in the earlier design version (BSC 2004 [DIRS 167207], Table 5) to 33.8 kg in the current design (BSC 2005 [DIRS 173501], Table 7). The impact of the design changes and corrections on the mass of corrosion products in the waste packages is summarized in Table A-1.

Table A-1. Summary of Corrosion Product Mass Changes in Waste Packages Resulting from Design Updates and Corrections

Design	21-PWR		44-BWR		5-DHLW/DOE	
	CP Mass, kg	Change from Previous Design, %	CP Mass, kg	Change from Previous Design, %	CP Mass, kg	Change from Previous Design, %
Previous	19,443		22,236		14,233	
Current, corrected	17,474	-10.1	19,463	-12.5	14,324	0.6

NOTE: CP = corrosion products (Fe_2O_3).

	A	B	C	D	E	F	G	H	I	J	K	L
1	21-PWR	Component Name	Mass, kg	Quantity	Total Mass, kg		44-BWR	Component Name	Mass, kg	Quantity	Total Mass, kg	
2	A516 CS	Basket -Side Guide	24.9	16	398.4		A516 CS	Basket -Side Guide	31.5	16	504	
3	A516 CS	Basket -Side Guide Stiffener	0.615	32	19.68		A516 CS	Basket Side Guide Stiffener	0.491	32	15.584	
4	A516 CS	Basket -End Side Guide	32.7	32	1046.4		A516 CS	Basket Corner Guide	43.4	32	1388.8	
5	A516 CS	Basket End Side Guide Stiffener	1.38	64	88.32		A516 CS	Basket Corner Guide Stiffener	2.23	64	142.72	
6	A516 CS	Basket Corner Guide	40.1	16	641.6		A516 CS	Fuel Basket Tube	108	44	4752	
7	A516 CS	Basket Corner Guide Stiffener	2.07	32	66.24		Neutronit A 978	Fuel Basket A - Plate	60.7	4	242.8	
8	A516 CS	Fuel Basket Tube	159	21	3339		Neutronit A 978	Fuel Basket B - Plate	60.7	12	728.4	
9	Neutronit A 978	Fuel Basket A - Plate	86.8	8	694.4		Neutronit A 978	Fuel Basket C - Plate	47.8	16	764.8	
10	Neutronit A 978	Fuel Basket B - Plate	86.8	8	694.4		Neutronit A 978	Fuel Basket D - Plate	60.7	8	485.6	
11	Neutronit A 978	Fuel Basket C - Plate	45.8	16	732.8		Neutronit A 978	Fuel Basket E - Plate	47.8	16	764.8	
12	Al 6061	Fuel Basket D - Plate	27.4	8	219.2		Al 6061	Fuel Basket F - Plate	20.4	8	163.2	
13	Al 6061	Fuel Basket E - Plate	27.4	8	219.2		Al 6061	Fuel Basket G - Plate	20.4	8	163.2	
14	316NG SS	Inner Vessel w/o Gaskets	9920	1	9920		316NG SS	Inner Vessel w/o Gaskets	10200	1	10200	
15	316NG SS	Inner Lid w/ LLF	739	1	739		316NG SS	Inner Lid w/ LLF	776	1	776	
16	316NG SS	Interface Ring	35.6	1	35.6		316NG SS	Interface Ring	36.4	1	36.4	
17	316NG SS	Spread Ring	25.3	1	25.3		316NG SS	Spread Ring	25.9	1	25.9	
18	316NG SS	Total 316 Welds	81	1	81		316NG SS	Total 316 Welds	83	1	83	
19	Alloy 22	OCB with trunnion sleeves	5730	1	5730		Alloy 22	OCB with trunnion sleeves	5890	1	5890	
20	Alloy 22	Middle Lid w/ LLF	226	1	226		Alloy 22	Middle Lid w/ LLF	237	1	237	
21	Alloy 22	Outer Lid w/ LLF	445	1	445		Alloy 22	Outer Lid w/ LLF	467	1	467	
22	Alloy 22	Total Alloy 22 Welds	51.8	1	51.8		Alloy 22	Total Alloy 22 Welds	53	1	53	
23		VP Total			25413.34			VP Total			27884.284	

Figure A-1. Spreadsheet "Masses of Materials;" Calculation of Mass of 21-PWR and 44-BWR Waste Package Components

	L	M	N	O	P	Q	R	S	T	U	V	W
1		5-DHLW	Component Name	Mass, kg	Quantity	Total Mass, kg		Naval SNF	Component Name	Mass, kg	Quantity	Total Mass, kg
2		A516 CS	Divider Plate Assembly	3720	1	3720		316NG SS	Inner Vessel	13300	1	13300
3		316NG SS	Inner Vessel	8860	1	8860		316NG SS	Inner Lid w/ LLF	962	1	962
4		316NG SS	Inner Lid w/ LLF	1170	1	1170		316NG SS	Interface Ring	40.5	1	40.5
5		316NG SS	Interface Ring	1	1	1		316NG SS	Spread Ring	28.9	1	28.9
6		316NG SS	Spread Ring	31.9	1	31.9		316NG SS	Total 316 Welds	92.2	1	92.2
7		316NG SS	Total 316 Welds	102	1	102		Alloy 22	OCB with trunnion sleeves	8960	1	8960
8		Alloy 22	OCB with trunnion sleeves	6540	1	6540		Alloy 22	Middle Lid w/ LLF	290	1	290
9		Alloy 22	Middle Lid w/ LLF	350	1	350		Alloy 22	Outer Lid w/ LLF	573	1	573
10		Alloy 22	Outer Lid w/ LLF	693	1	693		Alloy 22	Total Alloy 22 Welds	58.6	1	58.6
11		Alloy 22	Total Alloy 22 Welds	64.2	1	64.2			VP Total			24385.2
12			VP Total			21532.1						
13								316NG SS	Inner Vessel	13300	1	13300
14		A516 CS	Divider Plate Assembly	3720	1	3720		316NG SS	Inner Lid w/ LLF	962	1	962
15		A516 CS	Total			3720		316NG SS	Interface Ring	40.5	1	40.5
16								316NG SS	Spread Ring	28.9	1	28.9
17		316NG SS	Inner Vessel	8860	1	8860		316NG SS	Total 316 Welds	92.2	1	92.2
18		316NG SS	Inner Lid w/ LLF	1170	1	1170		316NG SS	Total			14423.6
19		316NG SS	Interface Ring	1	1	1						
20		316NG SS	Spread Ring	31.9	1	31.9		Alloy 22	OCB with trunnion sleeves	8960	1	8960
21		316NG SS	Total 316 Welds	102	1	102		Alloy 22	Middle Lid w/ LLF	290	1	290
22		316NG SS	Total			10164.9		Alloy 22	Outer Lid w/ LLF	573	1	573
23								Alloy 22	Total Alloy 22 Welds	58.6	1	58.6
24		Alloy 22	OCB with trunnion sleeves	6540	1	6540		Alloy 22	Total			9881.6
25		Alloy 22	Middle Lid w/ LLF	350	1	350						
26		Alloy 22	Outer Lid w/ LLF	693	1	693						
27		Alloy 22	Total Alloy 22 Welds	64.2	1	64.2						
28		Alloy 22	Total			7647.2						
29												
30												

Figure A-2. Spreadsheet "Masses of Materials;" Calculation of Mass of 5-DHLW and Naval Long Waste Package Components and Materials

In Rows 25-32, the calculation (Figure A-3) is repeated for a 21-PWR waste package for A 516 carbon steel components only. The total mass of carbon steel components is shown in Cell E32. Similarly, the calculation is repeated in Rows 34-37 (Figure A-3) for Neutronit, with the total Neutronit mass shown in Cell E37; in Rows 43-48 for 316 SS, with the total 316 SS mass shown in Cell E48. The masses of Al 6061 and Alloy 22 are also calculated, but this information is not used because the aluminum alloy contains a negligible amount of iron, and the Alloy 22 is considered to be inert. The calculation is repeated for a 44-BWR waste package in Column K (Figure A-3), for a 5-DHLW Short waste package in Column Q (Figure A-2), and for a Naval Long waste package in Column W (Figure A-2).

	A	B	C	D	E	F	G	H	I	J	K	L
24												
25	A516 CS	Bucket -Side Guide	24.9	16	398.4		A516 CS	Bucket -Side Guide	31.5	16	504	
26	A516 CS	Bucket -Side Guide Stiffener	0.615	32	19.68		A516 CS	Bucket Side Guide Stiffener	0.487	32	15.584	
27	A516 CS	Bucket -End Side Guide	32.7	32	1046.4		A516 CS	Bucket Corner Guide	43.4	32	1388.8	
28	A516 CS	Bucket End Side Guide Stiffener	1.38	64	88.32		A516 CS	Bucket Corner Guide Stiffener	2.23	64	142.72	
29	A516 CS	Bucket Corner Guide	40.1	16	641.6		A516 CS	Fuel Bucket Tube	108	44	4752	
30	A516 CS	Bucket Corner Guide Stiffener	2.07	32	66.24		A516 CS	Total			6883.104	
31	A516 CS	Fuel Bucket Tube	159	21	3339							
32	A516 CS	Total			5599.64		Neutronit A 978	Fuel Bucket A - Plate	60.7	4	242.8	
33							Neutronit A 978	Fuel Bucket B - Plate	60.7	12	728.4	
34	Neutronit A 978	Fuel Bucket A - Plate	86.8	8	694.4		Neutronit A 978	Fuel Bucket C - Plate	47.8	16	764.8	
35	Neutronit A 978	Fuel Bucket B - Plate	86.8	8	694.4		Neutronit A 978	Fuel Bucket D - Plate	60.7	8	485.6	
36	Neutronit A 978	Fuel Bucket C - Plate	45.8	16	732.8		Neutronit A 978	Fuel Bucket E - Plate	47.8	16	764.8	
37	Neutronit A 978	Total			2121.6		Neutronit A 978	Total			2986.4	
38												
39	Al 6061	Fuel Bucket D - Plate	27.4	8	219.2		Al 6061	Fuel Bucket F - Plate	20.4	8	163.2	
40	Al 6061	Fuel Bucket E - Plate	27.4	8	219.2		Al 6061	Fuel Bucket G - Plate	20.4	8	163.2	
41	Al 6061	Total			438.4		Al 6061	Total			326.4	
42												
43	316NG SS	Inner Vessel w/o Guides	9520	1	9520							
44	316NG SS	Inner Lid w/ LLF	739	1	739		316NG SS	Inner Vessel w/o Guides	10200	1	10200	
45	316NG SS	Interface Ring	35.6	1	35.6		316NG SS	Inner Lid w/ LLF	776	1	776	
46	316NG SS	Spread Ring	25.3	1	25.3		316NG SS	Interface Ring	36.4	1	36.4	
47	316NG SS	Total 316 Welds	81	1	81		316NG SS	Spread Ring	25.9	1	25.9	
48	316NG SS	Total			10800.9		316NG SS	Total 316 Welds	83	1	83	
49							316NG SS	Total			11121.3	
50	Alloy 22	OCB with trunnion sleeves	5730	1	5730							
51	Alloy 22	Middle Lid w/ LLF	226	1	226		Alloy 22	OCB with trunnion sleeves	5890	1	5890	
52	Alloy 22	Outer Lid w/ LLF	445	1	445		Alloy 22	Middle Lid w/ LLF	237	1	237	
53	Alloy 22	Total Alloy 22 Welds	51.8	1	518		Alloy 22	Outer Lid w/ LLF	467	1	467	
54	Alloy 22	Total			6452.8		Alloy 22	Total Alloy 22 Welds	53	1	53	
55							Alloy 22	Total			6647	
56												
57			Fe content (%)	Total Mass (kg)	Fe Mass (kg)				Fe content (%)	Total Mass (kg)	Fe Mass (kg)	
58		316NG SS	61.935	10801	6690			316NG SS	61.935	11121	6888	
59		A516 CS	98.37	5600	5508			A516 CS	98.37	6883	6692	
60		Neutronit A 978	66.06	2122	1402			Neutronit A 978	66.06	2986	1973	
61				18522	13599	73.4				20911	15553	74.4
62		Equivalent Fe_2O_3 mass (kg)			19443			Equivalent Fe_2O_3 mass (kg)			22236	
63												

Figure A-3. Spreadsheet "Masses of Materials;" Calculation of Mass of 21-PWR and 44-BWR Waste Package Materials and Equivalent Mass of Fe_2O_3

In Row 78, Columns C-E (Figure A-4), the iron content is calculated for the three alloys of interest (316 stainless steel, A 516 carbon steel, and Neutronit A 978, respectively). The iron content of these alloys is specified as "Balance" (see Table 4.1-14). It is calculated by summing the content of all nonferrous components of the alloys (Row 77, Columns C-E) and subtracting from 100%.

	A	B	C	D	E	F
64						
65						
66		Element	316NG Stainless Steel [a]	A 516 Carbon Steel [b]	Neutronit A 978 [c]	
67		Mo	3	0	2.2	
68		Cr	18	0	18.5	
69		Ni	14	0	13	
70		Co	0	0	0.2	
71		Mn	2	1.3	0	
72		C	0.08	0.26	0.04	
73		P	0.045	0.035	0	
74		S	0.03	0.035	0	
75		Si	0.75	0	0	
76		N	0.16	0	0	
77		Total Non-Fe	38.065	1.63	33.94	
78		Fe	61.935	98.37	66.06	
79						
80		[a]DTN: MO0003RIB00076.000.				
81		[b]DTN: MO0107TC240032.000.				
82		[c]Kügler 1991, p. 15.				
83						

DTN: MO0003RIB00076.000 [DIRS 153044]; DTN: MO0107TC240032.000 [DIRS 169970].

Source: Kügler 1991 [DIRS 155761], p.15.

Figure A-4. Spreadsheet "Masses of Materials;" Elemental Weight Percent Compositions used in Calculation of Iron Content in Three Steel Alloys

In Figure A-3, the total masses of 316 SS (from E48), of A 516 CS (from E32), and of Neutronit A 978 (from E37) in all 21-PWR components are listed in Column D, Rows 58-60, respectively. The iron content of all components for each alloy is calculated in Column E (e.g., E58=C58*D58/100). The total iron content in the three alloys is summed in Cell E61. The average iron content of all components constructed of these three alloys is calculated in Cell F61 (F61=E61*100/D61); this information is not used.

The equivalent mass of Fe_2O_3 is computed in Cell E62 (Figure A-3) using the formula shown in Footnote f of Table 6.3-4: E62=E61*0.15969/0.055847/2. The results of these calculations (Rows 58-62, Columns C-F) are presented in Table 6.3-4 for a 21-PWR. These calculations are repeated for a 44-BWR waste package (Rows 58-62, Columns I-L; see Figure A-3), a 5-DHLW waste package (Rows 58-62, Columns O-R; Figure A-5), and for a Naval Long waste package (Rows 58-62, Columns U-X; Figure A-5).

	M	N	O	P	Q	R	S	T	U	V	W	X
56												
57			Fe content (%)	Total Mass (kg)	Fe Mass (kg)				Fe content (%)	Total Mass (kg)	Fe Mass (kg)	
58		316NG SS	61.935	10165	6296			316NG SS	61.935	14424	8933	
59		A516 CS	98.37	3720	3659			A516 CS	98.37	0	0	
60		Neutronit A 978	66.06	0	0			Neutronit A 978	66.06	0	0	
61				13885	9955	71.7				14424	8933	61.9
62		Equivalent Fe_2O_3 mass (kg)			14233			Equivalent Fe_2O_3 mass (kg)			12772	

Figure A-5. Spreadsheet "Masses of Materials;" Calculation of Equivalent Mass of Fe_2O_3 in 5-DHLW and Naval Long Waste Packages

INTENTIONALLY LEFT BLANK

APPENDIX B

IMPLEMENTATION OF RADIONUCLIDE SORPTION ONTO COLLOIDAL AND STATIONARY PHASES WITH FINITE DIFFERENCE SOLUTION

IMPLEMENTATION OF RADIONUCLIDE SORPTION ONTO COLLOIDAL AND STATIONARY PHASES WITH FINITE DIFFERENCE SOLUTION

CONCEPTUAL MODEL

The general colloid model accounts for both reversible and irreversible sorption onto the iron oxyhydroxide (designated FeO) mobile colloids and the immobile FeO corrosion products together with reversible sorption onto both waste form and groundwater (GW) colloids within the engineered barrier system (EBS). Figure B-1 shows the conceptual model of radionuclide sorption onto the iron oxy-hydroxide colloidal and stationary phases. The upstream domain is considered to be degraded fuel rods, including secondary mineral phases, in equilibrium with the aqueous phase at the radionuclide solubility limit predicted by the solubility limits model (BSC 2005 [DIRS 174566]). The radionuclides of concern are the Pu and Am isotopes. Since the material balance equations are written as a mass balance, the equations are valid for any solute species. Certain system parameters, such as solubility, decay rate, and partition coefficients, will be dependent on the species. In this appendix, the species used for subsequent analysis and discussion is Pu.

The colloid model considers the general case where both reversible sorption is modeled with non-zero K_d values, and irreversible sorption is modeled as having "unrestricted access" to sites. As such, the irreversible sorption calculation does not account for limitations on the number of sites available for sorption; it does not account for competition for sorption sites among the radionuclides that can sorb; and it does not account for competition for sorption sites with radionuclides such as Pu and Am that sorb irreversibly, which would reduce the number of sites available for reversible sorption. This more general case is included as an alternative conceptual model (Section 6.6.7).

There is no sorption considered in the upstream domain. Pu at its solubility limit is considered to transport by both advection and diffusion downstream into the corrosion product domain, where it can be involved in six separate reactions:

- Reversible Pu sorption onto FeO colloidal particles
- Reversible Pu sorption onto the stationary phase FeO corrosion products
- Irreversible Pu sorption onto FeO colloidal particles
- Irreversible Pu sorption onto the stationary phase FeO corrosion products
- Reversible Pu sorption onto waste form colloids
- Reversible Pu sorption onto GW colloids.

Denote the concentrations (kg Pu m^{-3} water) for the Pu in the seven possible states as

c_{Pu_aq} = concentration of Pu in aqueous solution

$c_{Pu_FeO_c}$ = concentration of Pu in the FeO colloid state from reversible sorption

$c_{Pu_FeO_CP}$ = concentration of Pu in the stationary FeO corrosion product state from reversible sorption

$c_{Irrv_Pu_FeO_c}$ = concentration of Pu in the FeO colloid state from irreversible sorption

$c_{Irrv_Pu_FeO_CP}$ = concentration of Pu in the stationary FeO corrosion products state from irreversible sorption

$c_{Pu_WF_c}$ = concentration of Pu in the waste form colloid state from reversible sorption

$c_{Pu_GW_c}$ = concentration of Pu in the GW colloid state from reversible sorption

and let

c_s = Pu solubility (concentration at the solubility limit) (kg Pu m^{-3} water).

The concentrations (kg colloid m^{-3} water) of all colloids and stationary corrosion products are:

c_{FeO_c} = concentration of FeO in the colloid state

c_{FeO_CP} = concentration of FeO in the corrosion product state

c_{WF_c} = concentration of waste form in the colloid state

c_{GW_c} = concentration of GW in the colloid state.

As indicated in Figure B-1, the mass in the fluid exiting the corrosion-product domain (reaction mixing cell) is expected to be proportioned such that the mass of Pu sorbed onto FeO colloids is some fraction of the total mass of Pu exiting the system in all forms—aqueous, reversibly sorbed, and irreversibly sorbed. Observations in nature, such as the transport of Pu from the Benham test site (Kersting et al. 1999 [DIRS 103282]), suggest that this fraction is about 95%. This is expressed as:

$$\Omega = \frac{\text{colloid mass flux out}}{\text{total mass flux out}} = 0.95 . \qquad \text{(Eq. B-1)}$$

This value of 95% is uncertain with an uncertainty range of 0.90 to 0.99 associated with it (BSC 2004 [DIRS 170025], Table 6-12, p. 6-72). It also may be a function of time, since the observation time for the Benham test is only about 50 years.

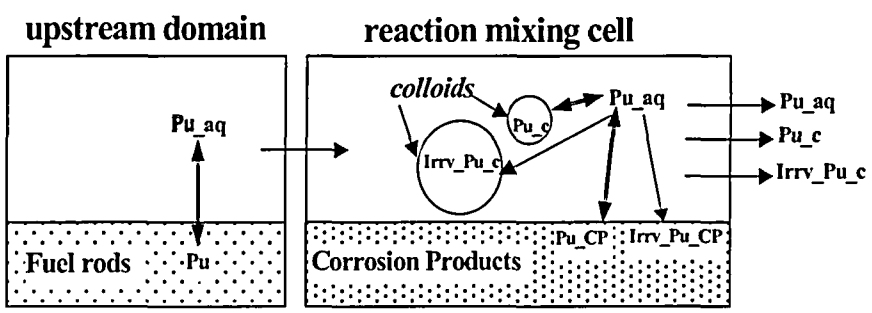

Figure B-1. Conceptual Model Schematic

Also of interest is the ratio of the mass flux leaving the mixing cell to the mass flux entering the mixing cell. This ratio of mass out to mass in is given by:

$$\Psi = \frac{\text{mass flux out}}{\text{mass flux in}}, \qquad \text{(Eq. B-2)}$$

and is a measure of the retardation due to sorption on the stationary corrosion products. The model is set up is such a way that most of the Pu mass entering the mixing cell is expected to be sorbed onto the stationary FeO phase and only a small fraction of it flows downstream to the unsaturated zone.

REACTIONS

The reactions considered in this model are as follows, where R_i, represents the bulk reaction rate of Pu for the ith reaction, in units (kg Pu m^{-3} yr^{-1}):

$$R_1: \quad \text{Pu(aq)} \rightarrow \text{Pu(FeO}_{\text{col}}^{\text{irrev}}\text{)} \qquad \text{(Eq. B-3)}$$

$$R_2: \quad \text{Pu(aq)} \rightarrow \text{Pu(FeO}_{\text{CP}}^{\text{irrev}}\text{)} \qquad \text{(Eq. B-4)}$$

$$R_3: \quad \text{Pu(aq)} \leftrightarrow \text{Pu(FeO}_{\text{col}}^{\text{rev}}\text{)} \qquad \text{(Eq. B-5)}$$

$$R_4: \quad \text{Pu(aq)} \leftrightarrow \text{Pu(FeO}_{\text{CP}}^{\text{rev}}\text{)} \qquad \text{(Eq. B-6)}$$

$$R_5: \quad \text{Pu(aq)} \leftrightarrow \text{Pu(WF}_{\text{col}}^{\text{rev}}\text{)} \qquad \text{(Eq. B-7)}$$

$$R_6: \quad \text{Pu(aq)} \leftrightarrow \text{Pu(GW}_{\text{col}}^{\text{rev}}\text{)} \qquad \text{(Eq. B-8)}$$

Note that the reactions in Equations B-5 through B-8 are reversible equilibrium reactions, therefore their reaction rates are undefined and not included in subsequent mass balance equations. Equilibrium mass-action relationships are imposed instead, for these four reactions.

KINETIC REACTIONS

The ith irreversible reaction rate (where i = 1 or 2), R_i (kg Pu m^{-3} bulk-volume yr^{-1}), is expressed in terms of the ith bulk surface area for the mineral phase involved in the reaction, S_i (m^2 FeO m^{-3} bulk-volume), and the ith intrinsic (or surface) reaction rate, r_i (kg Pu m^{-2} FeO yr^{-1}):

$$R_i = S_i r_i. \qquad \text{(Eq. B-9)}$$

The irreversible reaction of Pu onto FeO colloids is then

$$R_1 = S_{FeO_c} r_1 \qquad \text{(Eq. B-10)}$$

and for the irreversible reaction of Pu onto FeO corrosion products

$$R_2 = S_{FeO_CP} r_2. \qquad \text{(Eq. B-11)}$$

The bulk surface area (m^2 FeO m^{-3} bulk-volume) for FeO colloids and corrosion products are, respectively,

$$S_{FeO_c} = \hat{S}_{FeO_c} c_{FeO_c} \phi S_w \qquad \text{(Eq. B-12)}$$

$$S_{FeO_CP} = \hat{S}_{FeO_CP} c_{FeO_CP} \phi S_w \qquad \text{(Eq. B-13)}$$

where ϕ is the porosity of the FeO matrix, S_w is the water saturation and

$\hat{S}_{FeO_c}$ = specific surface area of FeO colloids (m^2 FeO-colloid kg^{-1} FeO-colloid)

$\hat{S}_{FeO_CP}$ = specific surface area of FeO corrosion products (m^2 FeO-CP kg^{-1} FeO-CP).

The intrinsic or surface reaction rate (i.e., rate per unit mineral surface area) is considered to be the same for the colloidal and stationary phases, i.e., $r_1 = r_2 \equiv r$, and it only has a forward component, since the reaction is irreversible. Further, suppose that the reactions are first order in the solution concentration c_{Pu_aq}:

$$r = k c_{Pu_aq}, \qquad \text{(Eq. B-14)}$$

where

k = forward rate constant, (m^3 water-volume m^{-2} FeO yr^{-1}).

The two irreversible reaction rates on a water volume basis are then

$$\frac{R_1}{\phi S_w} = \hat{S}_{FeO_c} c_{FeO_c} k c_{Pu_aq} = \overline{R}_1 c_{Pu_aq} \qquad \text{(Eq. B-15)}$$

$$\frac{R_2}{\phi S_w} = \hat{S}_{FeO_CP} c_{FeO_CP} k c_{Pu_aq} = \overline{R}_2 c_{Pu_aq}, \qquad \text{(Eq. B-16)}$$

where $\overline{R}_1 = \hat{S}_{FeO_c} c_{FeO_c} k$ and $\overline{R}_2 = \hat{S}_{FeO_CP} c_{FeO_CP} k$ are reaction rate constants (yr^{-1}) for colloids and corrosion products, respectively.

EQUILIBRIUM REACTIONS

The four chemical species, $Pu(FeO_{col}^{rev})$, $Pu(FeO_{CP}^{rev})$, $Pu(WF_{col}^{rev})$ and $Pu(GW_{col}^{rev})$, involved in reversible equilibrium sorption reactions, Equations B-5, B-6, B-7, and B-8, follow the law of mass action according to

$$K_3^{eq} = \frac{[\mathrm{Pu(FeO_{col}^{rev})}]}{[\mathrm{Pu(aq)}]} \qquad \text{(Eq. B-17)}$$

$$K_4^{eq} = \frac{[\mathrm{Pu(FeO_{CP}^{rev})}]}{[\mathrm{Pu(aq)}]} \qquad \text{(Eq. B-18)}$$

$$K_5^{eq} = \frac{[\mathrm{Pu(WF_{col}^{rev})}]}{[\mathrm{Pu(aq)}]} \qquad \text{(Eq. B-19)}$$

$$K_6^{eq} = \frac{[\mathrm{Pu(GW_{col}^{rev})}]}{[\mathrm{Pu(aq)}]} \qquad \text{(Eq. B-20)}$$

where [Pu(j)] represents the thermodynamic activity of Pu in the jth phase (aqueous, colloidal, or corrosion product). Normally, these relationships are expressed for dilute solutions as a simple linear (K_d) (water volume/mass FeO) type of isotherm in terms of concentrations:

$$\hat{c}_{Pu_FeO_c} = K_{d_FeO_c} c_{Pu_aq} \qquad \text{(Eq. B-21)}$$

$$\hat{c}_{Pu_FeO_CP} = K_{d_FeO_CP} c_{Pu_aq} \qquad \text{(Eq. B-22)}$$

$$\hat{c}_{Pu_WF_c} = K_{d_WF_c} c_{Pu_aq} \qquad \text{(Eq. B-23)}$$

$$\hat{c}_{Pu_GW_c} = K_{d_GW_c} c_{Pu_aq} \qquad \text{(Eq. B-24)}$$

where

$\hat{c}_{Pu_FeO_c}$ = mass ratio of Pu sorbed onto FeO colloids (kg Pu kg^{-1} FeO-colloid)

$\hat{c}_{Pu_FeO_CP}$ = mass ratio of Pu sorbed onto FeO corrosion products (kg Pu kg^{-1} FeO-CP)

$\hat{c}_{Pu_WF_c}$ = mass ratio of Pu sorbed onto waste form colloids (kg Pu kg^{-1} WF-colloid)

$\hat{c}_{Pu_GW_c}$ = mass ratio of Pu sorbed onto GW colloids (kg Pu kg^{-1} GW-colloid).

The mass ratio for these reversible sorption reactions can be converted to water volume concentrations by the following:

$$c_{Pu_FeO_c} = c_{FeO_c} \hat{c}_{Pu_FeO_c} \qquad \text{(Eq. B-25)}$$

$$c_{Pu_FeO_CP} = c_{FeO_CP} \hat{c}_{Pu_FeO_CP} \qquad \text{(Eq. B-26)}$$

$$c_{Pu_WF_c} = c_{WF_c} \hat{c}_{Pu_WF_c} \qquad \text{(Eq. B-27)}$$

$$c_{Pu_GW_c} = c_{GW_c} \hat{c}_{Pu_GW_c} \qquad \text{(Eq. B-28)}$$

The reversible Pu equilibrium is expressed by the partition coefficients relating the aqueous state and the two reversible states given by Equations B-25 to B-28 as

$$c_{Pu_FeO_c} = c_{FeO_c} K_{d_FeO_c} c_{Pu_aq} = \overline{K}_{d_FeO_c} c_{Pu_aq} \qquad \text{(Eq. B-29)}$$

$$c_{Pu_FeO_CP} = c_{FeO_CP} K_{d_FeO_CP} c_{Pu_aq} = \overline{K}_{d_FeO_CP} c_{Pu_aq} \quad \text{(Eq. B-30)}$$

$$c_{Pu_WF_c} = c_{WF_c} K_{d_WF_c} c_{Pu_aq} = \overline{K}_{d_WF_c} c_{Pu_aq} \quad \text{(Eq. B-31)}$$

$$c_{Pu_GW_c} = c_{GW_c} K_{d_GW_c} c_{Pu_aq} = \overline{K}_{d_GW_c} c_{Pu_aq} \quad \text{(Eq. B-32)}$$

where $\overline{K}_{d_FeO_c}$, $\overline{K}_{d_FeO_CP}$, $\overline{K}_{d_WF_c}$ and $\overline{K}_{d_GW_c}$ are dimensionless partition coefficients.

QUANTIFICATION OF CORROSION PRODUCTS

The corrosion products are generated from the degradation of the waste packages. It is the corrosion product mass that provides the porous matrix for the transport of radionuclides in the reaction mixing cell. The amount of corrosion products is time dependent. As modeled, the corrosion product density (kg m^{-3} solid) and mass (kg) are known. Let

ρ_{FeO_CP} = corrosion product density

m_{FeO_CP} = mass of corrosion product.

The volume of corrosion products (m^{-3} solid) is then

$$V_{FeO_CP} = \frac{m_{FeO_CP}}{\rho_{FeO_CP}}.$$

If the porosity of the corrosion product mass is specified as

$$\phi = \frac{V_{pore}}{V_{bulk}},$$

then

$$1 - \phi = \frac{V_{FeO_CP}}{V_{bulk}}.$$

The bulk volume is computed from

$$V_{bulk} = \frac{V_{FeO_CP}}{1-\phi}.$$

The pore volume is

$$V_{pore} = \phi V_{bulk} = \frac{\phi}{1-\phi} \frac{m_{FeO_CP}}{\rho_{FeO_CP}},$$

and the water volume is:

$$V_{water} = S_w V_{pore} = \phi S_w V_{bulk}.$$

The stationary corrosion products concentration is defined as

$$c_{FeO_CP} = \frac{m_{FeO_CP}}{V_{water}}.$$

TRANSPORT EQUATIONS

The mass balance equation for the Pu contained in the aqueous state, the reversible colloid state and the reversible corrosion product state with radionuclide decay (neglecting ingrowth) is (see development in Section 6.5.1.2 culminating in Equation 6.5.1.2-46):

$$\begin{aligned}
&\frac{\partial \phi S_w (c_{Pu_aq} + c_{Pu_FeO_c} + c_{Pu_FeO_CP} + c_{Pu_WF_c} + c_{Pu_GW_c})}{\partial t} \\
&+ u \frac{\partial (c_{Pu_aq} + c_{Pu_FeO_c} + c_{Pu_WF_c} + c_{Pu_GW_c})}{\partial x} - \frac{\partial}{\partial x}\left(\phi S_w D_{aq} \frac{\partial c_{Pu_aq}}{\partial x}\right) \\
&- \frac{\partial}{\partial x}\left(\phi S_w D_{colloid} \frac{\partial (c_{Pu_FeO_c} + c_{Pu_WF_c} + c_{Pu_GW_c})}{\partial x}\right) \\
&= -R_1 - R_2 - \lambda \phi S_w (c_{Pu_aq} + c_{Pu_FeO_c} + c_{Pu_FeO_CP} + c_{Pu_WF_c} + c_{Pu_GW_c})
\end{aligned} \qquad \text{(Eq. B-33)}$$

where ϕ is the porosity of the FeO matrix, S_w is the water saturation, u is the Darcy velocity of the water (m yr^{-1}), D_{aq} is the diffusivity (m^2 yr^{-1}) of the Pu in solution, $D_{colloid}$ is the colloid diffusivity (m^2 yr^{-1}), and λ is the radionuclide decay rate (yr^{-1}). Now impose the reversible equilibrium of the Pu mass between the aqueous, colloid and corrosion products (Equations B-29 through B-32) together with representing the irreversible reactions as functions of the aqueous phase Pu concentration (Equations B-15 and B-16). The mass balance (Equation B-33) on a bulk volume basis can be expressed in terms of the concentration in the aqueous state:

$$
\begin{aligned}
&(1+\overline{K}_{d_FeO_c}+\overline{K}_{d_FeO_CP}+\overline{K}_{d_WF_c}+\overline{K}_{d_GW_c})\frac{\partial \phi S_w c_{Pu_aq}}{\partial t} \\
&+u(1+\overline{K}_{d_FeO_c}+\overline{K}_{d_WF_c}+\overline{K}_{d_GW_c})\frac{\partial c_{Pu_aq}}{\partial x} \\
&-\frac{\partial}{\partial x}\left(\phi S_w D_{aq}\frac{\partial c_{Pu_aq}}{\partial x}\right) \\
&-\frac{\partial}{\partial x}\left(\phi S_w D_{colloid}\left(\overline{K}_{d_FeO_c}+\overline{K}_{d_WF_c}+\overline{K}_{d_GW_c}\right)\frac{\partial c_{Pu_aq}}{\partial x}\right) \\
&=-\phi S_w(\overline{R}_1+\overline{R}_2)c_{Pu_aq} \\
&-\lambda\phi S_w(1+\overline{K}_{d_FeO_c}+\overline{K}_{d_FeO_CP}+\overline{K}_{d_WF_c}+\overline{K}_{d_GW_c})c_{Pu_aq}.
\end{aligned}
\qquad \text{(Eq. B-34)}
$$

Based on Equations 6.5.1.2-47 and 6.5.1.2-48, the mass balance equations for the irreversible Pu in the colloid and corrosion product states are, respectively,

$$
\begin{aligned}
&\frac{\partial \phi S_w c_{Irrv_Pu_FeO_c}}{\partial t}+u\frac{\partial c_{Irrv_Pu_FeO_c}}{\partial x}-\frac{\partial}{\partial x}\left(\phi S_w D_{colloid}\frac{\partial c_{Irrv_Pu_FeO_c}}{\partial x}\right) \\
&=\phi S_w \overline{R}_1 c_{Pu_aq}-\lambda\phi S_w c_{Irrv_Pu_FeO_c}
\end{aligned}
\qquad \text{(Eq. B-35)}
$$

and

$$
\frac{\partial \phi S_w c_{Irrv_Pu_FeO_CP}}{\partial t}=\phi S_w \overline{R}_2 c_{Pu_aq}-\lambda\phi S_w c_{Irrv_Pu_FeO_CP}\,. \qquad \text{(Eq. B-36)}
$$

The boundary conditions require the upstream (left boundary cell, if flow is from left to right) conditions

$$
\begin{aligned}
c_{Pu_aq} &= c_s \\
c_{Pu_WF_c} &= \overline{K}_{d_WF_c}c_s
\end{aligned}
\qquad \text{(Eq. B-37)}
$$

$$
c_{Pu_FeO_c}=c_{Pu_FeO_CP}=c_{Irrv_Pu_FeO_c}=c_{Irrv_Pu_FeO_CP}=c_{Pu_GW_c}=0\,, \qquad \text{(Eq. B-38)}
$$

where c_s is the Pu solubility as defined earlier. In this model, no FeO or groundwater colloids exist in the upstream waste form cell. The solubility at the upstream location is dependent on the CO_2 fugacity and pH at the upstream location (BSC 2005 [DIRS 174566], Section 8.1) and in general is time dependent: $c_s = c_s(t)$. The right boundary cell is a free flow boundary with concentrations fixed at zero for the purpose of this appendix. For diffusion calculations it is required to specify down stream diffusion parameters (porosity, diffusivity, diffusive length and diffusive area). The initial conditions within the mixing cell are zero for all Pu concentrations.

Both the colloid and corrosion product concentrations are chosen to be time dependent:

$$
\begin{aligned}
c_{FeO_c} &= c_{FeO_c}(t) \\
c_{FeO_CP} &= c_{FeO_CP}(t) \\
c_{WF_c} &= c_{WF_c}(t) \\
c_{GW_c} &= c_{GW_c}(t)
\end{aligned}
\qquad \text{(Eq. B-39)}
$$

but are independent of the Pu concentrations. This implies that the reaction rates $\overline{R}_1$ and $\overline{R}_2$ are also time dependent.

The mass balance equations are solved numerically by a finite difference method. The calculation sequence for a time step is to solve Equation B-34 for c_{Pu_aq}. Reversible equilibrium Equations B-29 through B-32 then give $c_{Pu_FeO_c}$, $c_{Pu_FeO_CP}$, $c_{Pu_WF_c}$ and $c_{Pu_GW_c}$. With c_{Pu_aq} known the mass balance Equations B-35 and B-36 for the irreversible components are solved.

DIMENSIONLESS FORM OF TRANSPORT EQUATIONS

In order to express the governing equations in dimensionless form, dimensionless length, time and concentration, respectively, are defined:

$$\chi = x / L$$

$$\tau = \frac{ut}{\phi S_w L} = \frac{\overline{u}t}{L}$$

$$\overline{c} = c / c_s,$$

where L is the characteristic length (m) and $\overline{u} = \dfrac{u}{\phi S_w}$ is the average linear advective velocity (m yr^{-1}). The characteristic length would be the interval length or, for a finite difference solution, the grid block cell length. Then the variables are changed to dimensionless space and time in the mass balance equations. If the colloid/corrosion product concentrations are taken to be constant (Equations B-39), then the Pu mass balance equation in the aqueous state is:

$$
\begin{aligned}
&(1+\overline{K}_{d_FeO_c}+\overline{K}_{d_FeO_CP}+\overline{K}_{d_WF_c}+\overline{K}_{d_GW_c})\frac{\partial \overline{c}_{Pu_aq}}{\partial \tau} \\
&+(1+\overline{K}_{d_FeO_c}+\overline{K}_{d_WF_c}+\overline{K}_{d_GW_c})\frac{\partial \overline{c}_{Pu_aq}}{\partial \chi} \\
&-\left[\Delta_{aq}+\Delta_{colloid}\left(\overline{K}_{d_FeO_c}+\overline{K}_{d_WF_c}+\overline{K}_{d_GW_c}\right)\right]\frac{\partial^2 \overline{c}_{Pu_aq}}{\partial \chi^2} \\
&=-(\Theta_1+\Theta_2)\overline{c}_{Pu_aq}-(1+\overline{K}_{d_FeO_c}+\overline{K}_{d_FeO_CP}+\overline{K}_{d_WF_c}+\overline{K}_{d_GW_c})\Lambda\overline{c}_{Pu_aq}
\end{aligned}
\qquad \text{(Eq. B-40)}
$$

where

$$\Delta_{aq} = \frac{\frac{D_{aq}}{L^2}}{\frac{\bar{u}}{L}} = \frac{\text{diffusive rate in water}}{\text{advective rate}}, \qquad \text{(Eq. B-41)}$$

$$\Delta_{collid} = \frac{\frac{D_{colloid}}{L^2}}{\frac{\bar{u}}{L}} = \frac{\text{diffusive rate of colloids}}{\text{advective rate}}, \qquad \text{(Eq. B-42)}$$

$$\Theta_1 = \frac{\bar{R}_1}{\frac{\bar{u}}{L}} = \frac{\text{reaction rate to colloids}}{\text{advective rate}}, \qquad \text{(Eq. B-43)}$$

$$\Theta_2 = \frac{\bar{R}_2}{\frac{\bar{u}}{L}} = \frac{\text{reaction rate to corrosion products}}{\text{advective rate}}, \qquad \text{(Eq. B-44)}$$

$$\Lambda = \frac{\lambda}{\frac{\bar{u}}{L}} = \frac{\text{decay rate}}{\text{advective rate}}. \qquad \text{(Eq. B-45)}$$

The dimensionless form of the mass balance for the irreversible Pu concentrations (Equations B-35 and B-36) are:

$$\frac{\partial \bar{c}_{Irrv_Pu_FeO_c}}{\partial \tau} + \frac{\partial \bar{c}_{Irrv_Pu_FeO_c}}{\partial \chi} - \Delta_{colloid} \frac{\partial^2 \bar{c}_{Irrv_Pu_FeO_c}}{\partial \chi^2} = \Theta_1 \bar{c}_{Pu_aq} - \Lambda \bar{c}_{Irrv_Pu_FeO_c} \qquad \text{(Eq. B-46)}$$

$$\frac{\partial \bar{c}_{Irrv_Pu_FeO_CP}}{\partial \tau} = \Theta_2 \bar{c}_{Pu_aq} - \Lambda \bar{c}_{Irrv_Pu_FeO_CP}. \qquad \text{(Eq. B-47)}$$

DIFFERENCE SOLUTION OF TRANSPORT EQUATIONS

Consider a finite difference approximation of the governing mass balance equations. The discretization uses three spatial cells. The left or first cell represents the upstream boundary conditions. The second cell represents the mixing cell with reactions. The third or right cell represents the down stream boundary conditions. Since cells one and three represent boundary conditions, this discretization is a 0-dimensional or single cell representation of the processes. Let the time step length be Δt. Let superscript n denote the nth time step, for example, $c^n_{Pu_aq}$ denotes the concentration at the nth time step. The discretization uses a first order backward difference approximation for the time derivative and the advective transport term. The diffusive

flux uses a second order approximation. This discretization is consistent with GoldSim (GoldSim Technology Group 2002 [DIRS 160579]). In this model, diffusion of dissolved mass and waste form colloids occurs at the left boundary. At the right boundary, diffusion of both dissolved mass and all colloids occurs. In addition, the porosity and water saturation are time-independent but may vary spatially. If the discretization is fully implicit in concentrations and time dependent velocity, irreversible reactions and solubility, then the discrete form of Equation B-34 for cell 2, in units of mass per unit water volume per unit time, is:

$$\begin{aligned}
&\overline{K}_1 \frac{c_{Pu_aq}^{n+1} - c_{Pu_aq}^{n}}{\Delta t} + \overline{U}^{n+1}\overline{K}_2 c_{Pu_aq}^{n+1} - \overline{U}^{n+1}\left(1+\overline{K}_{d_WF_c}\right)c_s^{n+1} - \overline{D}_{left_aq}\left(c_s^{n+1} - c_{Pu_aq}^{n+1}\right) \\
&\quad + \overline{D}_{right_aq} c_{Pu_aq}^{n+1} - \overline{D}_{left_colloid}\overline{K}_{d_WF_c}\left(c_s^{n+1} - c_{Pu_aq}^{n+1}\right) + \overline{D}_{right_colloid}\overline{K}_3 c_{Pu_aq}^{n+1} \\
&\quad = -\left(\overline{R}_1^{n+1} + \overline{R}_2^{n+1} + \lambda\overline{K}_1\right)c_{Pu_aq}^{n+1}.
\end{aligned}$$

This equation is solved for $c_{Pu_aq}^{n+1}$, resulting in:

$$c_{Pu_aq}^{n+1} = \frac{\overline{K}_1 c_{Pu_aq}^{n} + \left[\overline{U}^{n+1}\left(1+\overline{K}_{d_WF_c}\right) + \overline{D}_{left_aq} + \overline{D}_{left_col}\overline{K}_{d_WF_c}\right]c_s^{n+1}\Delta t}{\overline{K}_1 + \left(\overline{U}^{n+1}\overline{K}_2 + \overline{D}_{left_aq} + \overline{D}_{left_col}\overline{K}_{d_WF_c} + \overline{D}_{right_aq} + \overline{D}_{right_col}\overline{K}_3 + \overline{R}_1^{n+1} + \overline{R}_2^{n+1} + \lambda\overline{K}_1\right)\Delta t}$$

(Eq. B-48)

where

$$\frac{u\Delta t}{\phi S_w L} = \frac{U\Delta t}{V_{water}} = \overline{U}\Delta t$$

is the Courant number (dimensionless), L is the characteristic length (m), V_{water} is the volume of water in the cell (m^3), U is the volumetric water flux ($m^3\ yr^{-1}$), and $\overline{U}$ is the advective rate constant (yr^{-1}). Further,

$$\overline{K}_1 = 1 + \overline{K}_{d_FeO_c} + \overline{K}_{d_FeO_CP} + \overline{K}_{d_WF_c} + \overline{K}_{d_GW_c}$$

$$\overline{K}_2 = 1 + \overline{K}_{d_FeO_c} + \overline{K}_{d_WF_c} + \overline{K}_{d_GW_c}$$

$$\overline{K}_3 = \overline{K}_{d_FeO_c} + \overline{K}_{d_WF_c} + \overline{K}_{d_GW_c}$$

and

$$\overline{D} = \frac{H\left(\frac{\phi S_w D}{L}\right)}{V_{water}} A_s$$

is the diffusive rate constant (yr^{-1}) with respect to either the solution or colloid mass at either the right or left cell interface. Here, A_s is the cross sectional area for diffusion (m^2). For determining the diffusive rate constant for a finite difference approximation to the transport equations, the condition imposed is that the flux across the interface of two adjacent cells be continuous at the interface. The resulting analysis gives the diffusive rate constant between two cells as the harmonic average of $\frac{\phi S_w D}{L}$, or $H\left(\frac{\phi S_w D}{L}\right)$, which guarantees the continuity of the diffusive flux at the cell interface. In general, the harmonic average of two numbers is:

$$H(x_1, x_2) = \frac{2}{\frac{1}{x_1} + \frac{1}{x_2}}.$$

For a finite difference approximation in which the cell lengths are Δx_1 and Δx_2, the harmonic average of $\frac{\phi S_w D}{\Delta x}$ across the Cell 1/Cell 2 interface is:

$$H\left(\left(\frac{\phi S_w D}{\Delta x}\right)_1, \left(\frac{\phi S_w D}{\Delta x}\right)_2\right) = \frac{2}{\frac{\Delta x_1}{\phi_1 S_{w1} D_1} + \frac{\Delta x_2}{\phi_2 S_{w2} D_2}} = \frac{1}{\frac{L_1}{\phi_1 S_{w1} D_1} + \frac{L_2}{\phi_2 S_{w2} D_2}},$$

where L_1 and L_2 are the half-lengths (m) of Cells 1 and 2, respectively. The diffusive rate constant subscript left or right refers to the left or right diffusive boundary conditions, while the subscript *_aq* or *_c* refers to diffusion of the dissolved mass or colloid mass, respectively.

The reversible concentrations are determined from Equations B-29 through B-32

$$c^{n+1}_{Pu_FeO_c} = \overline{K}_{d_FeO_c} c^{n+1}_{Pu_aq} \qquad \text{(Eq. B-49)}$$

$$c^{n+1}_{Pu_FeO_CP} = \overline{K}_{d_FeO_CP} c^{n+1}_{Pu_aq} \qquad \text{(Eq. B-50)}$$

$$c^{n+1}_{Pu_WF_c} = \overline{K}_{d_WF_c} c^{n+1}_{Pu_aq} \qquad \text{(Eq. B-51)}$$

$$c^{n+1}_{Pu_GW_c} = \overline{K}_{d_GW_c} c^{n+1}_{Pu_aq}. \qquad \text{(Eq. B-52)}$$

The discretization of the balance Equation B-35 for irreversible Pu mass on the colloids yields

$$c^{n+1}_{Irrv_Pu_FeO_c} = \frac{c^{n}_{Irrv_Pu_FeO_c} + \overline{R}_1^{n+1}\Delta t c^{n+1}_{Pu_aq}}{1+(\overline{U}^{n+1} + \overline{D}_{right_col} + \lambda)\Delta t} \qquad \text{(Eq. B-53)}$$

and for irreversible Pu mass on the corrosion products, Equation B-36 yields

$$c^{n+1}_{Irrv_Pu_FeO_CP} = \frac{c^{n}_{Irrv_Pu_FeO_CP} + \overline{R}_2^{n+1}\Delta t c^{n+1}_{Pu_aq}}{1+\lambda\Delta t}. \qquad \text{(Eq. B-54)}$$

SAMPLE CALCULATION WITH REPRESENTATIVE PARAMETERS

A sample calculation is performed to demonstrate the solution technique and illustrate the types of behavior that might be expected in this model. Parameter values used in this sample calculation are given in Table B-1. Let the solubility, flow velocity, and irreversible reaction parameters, which are actually time-dependent, be constant over time.

For this set of parameters, the irreversible reactive rates, advective rate, diffusive rates, decay rate and the dimensionless colloids and corrosion product partition coefficients are:

$$\begin{aligned}
\overline{R}_1 &= 0.02000\ \text{yr}^{-1} \\
\overline{R}_2 &= 786\ \text{yr}^{-1} \\
\overline{U} &= 0.04367\ \text{yr}^{-1} \\
\overline{D}_{left_aq} &= 0.09127\ \text{yr}^{-1} \\
\overline{D}_{right_aq} &= 2.229\times10^{-3}\ \text{yr}^{-1} \\
\overline{D}_{right_col} &= 2.229\times10^{-5}\ \text{yr}^{-1} \\
\lambda &= 2.875\times10^{-5}\ \text{yr}^{-1} \\
\overline{K}_{d_FeO_c} &= 0.20 \\
\overline{K}_{d_FeO_CP} &= 1.965\times10^{4} \\
\overline{K}_{d_WF_c} &= 0.60 \\
\overline{K}_{d_GW_c} &= 0.020.
\end{aligned}$$

The simulation for the mixing cell (Cell 2) concentrations over a 1000-year time interval is shown in Figure B-2. The dominant rate constant, by several orders of magnitude, is the irreversible rate constant of the corrosion products, $\overline{R}_2 = 786\ \text{yr}^{-1}$. This is a result of the large mass of corrosion products and results in a relative large concentration of irreversibly sorbed Pu on the corrosion products, $c_{Irrv_Pu_FeO_CP}$. For this simulation, the amount of corrosion product mass is representative of the total mass of corrosion products in a waste package, and all the corrosion products are available at initial time. In the TSPA-LA abstraction model, the corrosion

product mass is time dependent and a function of the corrosion rates for the carbon and stainless steel (see Section 6.5.3.2).

Another large mass of Pu is reversibly sorbed onto the corrosion products. This is a result of the large reversible partition coefficient for the corrosion products, $\overline{K}_{d_FeO_CP} = 19650$, which again is a result of the large corrosion product mass. For this simulation, almost all of the Pu mass is sorbed onto the corrosion products either reversibly or irreversibly. Only a small amount of mass remains in solution or is sorbed onto the colloids. The qualitative behavior of the concentrations in Figure B-2 shows the concentrations approach a limiting value, with the exception of the irreversibly sorbed mass on the corrosion products. This behavior is discussed in the next section, where the concentrations are expressed analytically as solutions of difference equations, and their asymptotic-in-time values are determined.

Table B-1. Representative Parameter Values for Sample Calculation

Parameter	Value	Units	Description
c_s	1.0	mg l^{-1}	Solubility
S_w	1.0	dimensionless	Water saturation
ϕ_1	1.0	dimensionless	Porosity of Cell 1
ϕ_2	0.4	dimensionless	Porosity of Cell 2
ϕ_3	0.3	dimensionless	Porosity of Cell 3
U	0.1	m^3 yr^{-1}	Volumetric water flux
$K_{d_FeO_c}$	1×10^4	ml g^{-1}	Colloid partition coefficient
$K_{d_FeO_CP}$	2.5×10^3	ml g^{-1}	Corrosion product partition coefficient
$K_{d_WF_c}$	2×10^5	ml g^{-1}	Waste form colloids partition coefficient
$K_{d_GW_c}$	2×10^5	ml g^{-1}	Groundwater colloids partition coefficient
$\hat{S}_{FeO_c}$	100	m^2 g^{-1}	Specific surface area of FeO colloids
$\hat{S}_{FeO_CP}$	10	m^2 g^{-1}	Specific surface area of FeO corrosion products
c_{FeO_c}	20	mg l^{-1}	Concentration of FeO colloids
c_{FeO_CP}	7.86×10^6	mg l^{-1}	Concentration of FeO corrosion products
c_{WF_c}	3.0	mg l^{-1}	Concentration of waste form colloids
c_{GW_c}	0.1	mg l^{-1}	Concentration of groundwater colloids
k	0.001	cm yr^{-1}	Forward sorption rate constant
V_{water}	2.290	m^3	Water volume (= pore volume since S_w=1)
A_{s12}	36.0	m^2	Diffusive area between Cell 1 and Cell 2
A_{s23}	1.068	m^2	Diffusive area between Cell 2 and Cell 3

Table B-1. Representative Parameter Values for Sample Calculation (Continued)

Parameter	Value	Units	Description
L_1	0.001	m	Half-length of Cell 1 diffusive path
L_2	5.0	m	Half-length of Cell 2 diffusive path
L_3	0.806	m	Half-length of Cell 3 diffusive path
D_{aq}	2.3×10^{-9}	$m^2\ s^{-1}$	Aqueous diffusivity
$D_{colloid}$	2.3×10^{-11}	$m^2\ s^{-1}$	Colloid diffusivity
λ	2.875×10^{-5}	yr^{-1}	Radionuclide decay rate

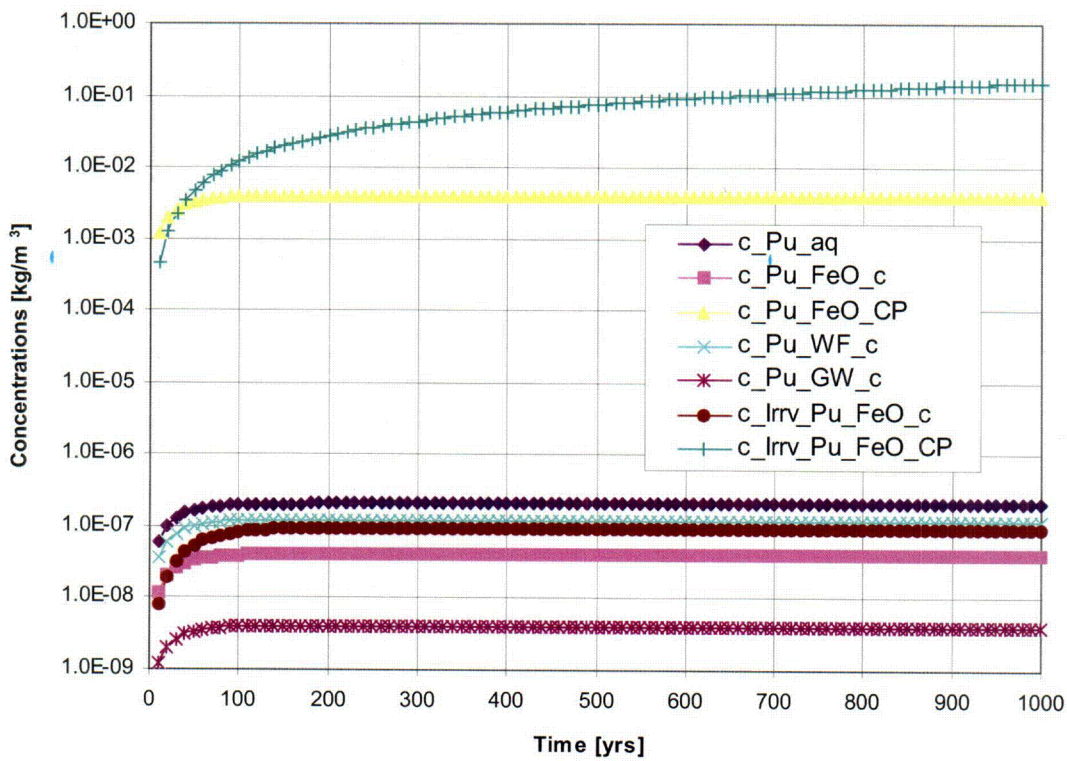

Figure B-2. Concentrations with Respect to Water Volume

CLOSED FORM SOLUTIONS OF THE DIFFERENCE EQUATIONS

If the solubility, advective flux, saturation, and irreversible rates are chosen to be constant over time, then the mass balance equation for the aqueous Pu, Equation B-48, is a first order linear constant coefficient nonhomogeneous difference equation. This equation is of the form

$$c_{Pu_aq}^{n+1} = a_1 c_{Pu_aq}^{n} + a_2 \quad \text{(Eq. B-55)}$$

where

$$a_1 = \frac{\overline{K}_1}{\overline{K}_1 + \left(\overline{U}\,\overline{K}_2 + \overline{D}_{left_aq} + \overline{D}_{left_col}\overline{K}_{d_WF_c} + \overline{D}_{right_aq} + \overline{D}_{right_col}\overline{K}_3 + \overline{R}_1 + \overline{R}_2 + \lambda\overline{K}_1\right)\Delta t}$$

$$a_2 = \frac{\left(\overline{U}(1+\overline{K}_{d_WF_c}) + \overline{D}_{left_aq} + \overline{D}_{left_col}\overline{K}_{d_WF_c}\right)\Delta t c_s}{\overline{K}_1 + \left(\overline{U}\,\overline{K}_2 + \overline{D}_{left_aq} + \overline{D}_{left_col}\overline{K}_{d_WF_c} + \overline{D}_{right_aq} + \overline{D}_{right_col}\overline{K}_3 + \overline{R}_1 + \overline{R}_2 + \lambda\overline{K}_1\right)\Delta t}.$$

The difference equation (Equation B-55) with initial condition of zero concentration has the solution:

$$c^n_{Pu_aq} = \frac{a_2(1-a_1^n)}{1-a_1}, \qquad \text{(Eq. B-56)}$$

where a_1^n is a_1 raised to the nth power (i.e., not a_1 at time step n). Since the condition $0 < a_1 < 1$ is guaranteed (because all terms in the definition are positive, and the denominator is the sum of the numerator plus positive terms), the solution $c^n_{Pu_aq}$ for large time is asymptotic to:

$$\begin{aligned}\lim_{n\to\infty} c^n_{Pu_aq} &= \frac{a_2}{1-a_1} \\ &= \frac{\left(\overline{U}(1+\overline{K}_{d_WF_c}) + \overline{D}_{left_aq} + \overline{D}_{left_col}\overline{K}_{d_WF_c}\right)c_s}{\overline{U}\,\overline{K}_2 + \overline{D}_{left_aq} + \overline{D}_{left_col}\overline{K}_{d_WF_c} + \overline{D}_{right_aq} + \overline{D}_{right_col}\overline{K}_3 + \overline{R}_1 + \overline{R}_2 + \lambda\overline{K}_1}.\end{aligned} \qquad \text{(Eq. B-57)}$$

The terms in this expression represent the effects of advection, diffusion, decay, and reversible and irreversible sorption reactions.

The difference equation for the irreversible colloid concentration (Equation B-53) is first order linear and is written as:

$$c^{n+1}_{Irrv_Pu_FeO_c} = b_1 c^n_{Irrv_Pu_FeO_c} + b_2 c^{n+1}_{Pu_aq} \qquad \text{(Eq. B-58)}$$

where

$$b_1 = \frac{1}{1+\left(\overline{U} + \overline{D}_{right_col} + \lambda\right)\Delta t} \qquad \text{(Eq. B-59)}$$

$$b_2 = \frac{\overline{R}_1 \Delta t}{1+\left(\overline{U} + \overline{D}_{right_col} + \lambda\right)\Delta t} \qquad \text{(Eq. B-60)}$$

and $c^{n+1}_{Pu_aq}$ is given by Equation B-56. The difference Equation B-58 with initial condition zero has solution

$$c^{n}_{Irrv_Pu_FeO_c} = \frac{a_2 b_2}{1-a_1}\left[\frac{1-b_1^{n+1}}{1-b_1} - \frac{a_1^{n+1}-b_1^{n+1}}{a_1-b_1}\right]. \qquad \text{(Eq. B-61)}$$

Since $0 < a_1 < 1$ and $0 < b_1 < 1$, this solution has asymptotic behavior

$$\lim_{n\to\infty} c^{n}_{Irrv_Pu_FeO_c} = \frac{a_2 b_2}{(1-a_1)(1-b_1)}. \qquad \text{(Eq. B-62)}$$

Thus

$$\lim_{n\to\infty} c^{n}_{Irrv_Pu_FeO_c} = \frac{b_2}{1-b_1}\lim_{n\to\infty} c^{n}_{Pu_aq} = \frac{\overline{R}_1}{\overline{U}+\overline{D}_{right_col}+\lambda}\lim_{n\to\infty} c^{n}_{Pu_aq}. \qquad \text{(Eq. B-63)}$$

The difference equation for the concentration of the irreversible mass on the corrosion products is first order linear and is written as

$$c^{n+1}_{Irrv_Pu_FeO_CP} = e_1 c^{n}_{Irrv_Pu_FeO_CP} + e_2 c^{n+1}_{Pu_aq} \qquad \text{(Eq. B-64)}$$

where

$$e_1 = \frac{1}{1+\lambda\Delta t} \qquad \text{(Eq. B-65)}$$

$$e_2 = \frac{\overline{R}_2 \Delta t}{1+\lambda\Delta t}. \qquad \text{(Eq. B-66)}$$

If $\lambda > 0$, Equation B-64 with initial concentration of zero has solution

$$c^{n}_{Irrv_Pu_FeO_CP} = \frac{a_2 e_2}{1-a_1}\left[\frac{1-e_1^{n+1}}{1-e_1} - \frac{a_1^{n+1}-e_1^{n+1}}{a_1-e_1}\right]. \qquad \text{(Eq. B-67)}$$

If $\lambda = 0$, Equation B-64 with initial concentration of zero has solution

$$c^{n}_{Irrv_Pu_FeO_CP} = \frac{a_2 e_2}{1-a_1}\left[n+1-\frac{1-a_1^{n+1}}{1-a_1}\right]. \qquad \text{(Eq. B-68)}$$

The solution Equation B-67 has asymptotic value

$$\lim_{n\to\infty} c^{n}_{Irrv_Pu_FeO_CP} = \frac{e_2}{1-e_1}\lim_{n\to\infty} c^{n}_{Pu_aq} = \frac{\overline{R}_2}{\lambda}\lim_{n\to\infty} c_{Pu_aq}, \qquad \text{(Eq. B-69)}$$

whereas the solution Equation B-68 does not have a limiting value, but is unbounded as a function of the time index n.

BOUNDARY FLUXES

Now consider the two boundary flux conditions given in Equations B-1 and B-2. The left or upstream boundary flux accounts for advection/diffusion of Pu mass in solution (Pu_aq) and Pu mass sorbed to waste form colloids. In this section of the analysis, upstream diffusion of colloids is ignored, although the TSPA-LA implementation does account for upstream colloid diffusion. The mass flux rates (kg yr^{-1}) at the upstream (left) boundary for the nth time step are:

Advective_Pu_aq (kg yr^{-1}) $= \overline{U} V_{water} c_s$

Diffusive_Pu_aq (kg yr^{-1}) $= \overline{D}_{left_aq} V_{water} (c_s - c^n_{Pu_aq})$

Advective_Pu_WF_c (kg yr^{-1}) $= \overline{U} V_{water} \overline{K}_{d_WF_c} c_s$

Diffusive_Pu_WF_c (kg yr^{-1}) $= \overline{D}_{left_col} V_{water} \overline{K}_{d_WF_c} (c_s - c^n_{Pu_aq})$.

The right or downstream boundary flux has contributions from advection/diffusion of Pu in solution and colloid together with advection/diffusion of Irrv_Pu on colloids. There is no advective or diffusive flux associated with the immobile corrosion products. The mass flux rates (kg yr^{-1}) at the right boundary assuming zero downstream concentrations are:

Advective_Pu_aq (kg yr^{-1}) $= \overline{U} V_{water} c^n_{Pu_aq}$

Diffusive_Pu_aq (kg yr^{-1}) $= \overline{D}_{right_aq} V_{water} c^n_{Pu_aq}$

Advective_Pu_FeO_c (kg yr^{-1}) $= \overline{U} V_{water} \overline{K}_{d_FeO_c} c^n_{Pu_aq}$

Diffusive_Pu_FeO_c (kg yr^{-1}) $= \overline{D}_{right_col} V_{water} \overline{K}_{d_FeO_c} c^n_{Pu_aq}$

Advective_Irrv_Pu_FeO_c (kg yr^{-1}) $= \overline{U} V_{water} c^n_{Irrv_Pu_FeO_c}$

Diffusive_Irrv_Pu_FeO_c (kg yr^{-1}) $= \overline{D}_{right_col} V_{water} c^n_{Irrv_Pu_FeO_c}$

Advective_Pu_WF_c (kg yr^{-1}) $= \overline{U} V_{water} \overline{K}_{d_WF_c} c^n_{Pu_aq}$

Diffusive_Pu_WF_c (kg yr^{-1}) $= \overline{D}_{right_col} V_{water} \overline{K}_{d_WF_c} c^n_{Pu_aq}$

Advective_Pu_GW_c (kg yr^{-1}) $= \overline{U} V_{water} \overline{K}_{d_GW_c} c^n_{Pu_aq}$

Diffusive_Pu_GW_c (kg yr^{-1}) $= \overline{D}_{right_col} V_{water} \overline{K}_{d_GW_c} c^n_{Pu_aq}$.

The total flux at the left boundary (upstream) at the nth time step, $F^n_{left_bddy_total}$, is

$$F^n_{left_bddy_total} = \overline{U} V_{water} c_s + \overline{D}_{left_aq} V_{water} (c_s - c^n_{Pu_aq})$$

$$+ \overline{U} V_{water} \overline{K}_{d_WF_c} c_s + \overline{D}_{left_col} V_{water} \overline{K}_{d_WF_c} (c_s - c^n_{Pu_aq}).$$

The condition discussed in Equation B-1 considers the ratio of the colloid mass to total mass flux out the right boundary. The right boundary colloidal flux, $F^n_{right_bddy_colloid}$, due to both reversibly and irreversibly sorbed Pu is:

$$F^n_{right_bddy_colloid} = \overline{U}V_{water}\overline{K}_{d_FeO_c}c^n_{Pu_aq} + \overline{U}V_{water}c^n_{Irrv_Pu_FeO_c}$$

$$+\overline{U}V_{water}\overline{K}_{d_WF_c}c^n_{Pu_aq} + \overline{U}V_{water}\overline{K}_{d_GW_c}c^n_{Pu_aq}$$

$$+\overline{D}_{right_col}V_{water}\overline{K}_{d_FeO_c}c^n_{Pu_aq} + \overline{D}_{right_col}V_{water}c^n_{Irrv_Pu_FeO_c}$$

$$+\overline{D}_{right_col}V_{water}\overline{K}_{d_WF_c}c^n_{Pu_aq} + \overline{D}_{right_col}V_{water}\overline{K}_{d_GW_c}c^n_{Pu_aq}.$$

The total Pu flux at the right boundary, $F^n_{right_bddy_total}$, is

$$F^n_{right_bddy_total} = F^n_{right_bddy_colloid} + \overline{U}V_{water}c^n_{Pu_aq} + \overline{D}_{right_aq}V_{water}c^n_{Pu_aq}.$$

The right boundary ratio of colloid flux out to total flux out at time level n is

$$\Omega_n = \frac{F^n_{right_bddy_colloid}}{F^n_{right_bddy_total}}.$$

Then

$$\Omega_n = \frac{\overline{K}_3 + \dfrac{c^n_{Irrv_Pu_FeO_c}}{c^n_{Pu_aq}}}{\dfrac{\overline{U}\,\overline{K}_2 + \overline{D}_{right_aq} + \overline{D}_{right_col}\overline{K}_3}{\overline{U} + \overline{D}_{right_col}} + \dfrac{c^n_{Irrv_Pu_FeO_c}}{c^n_{Pu_aq}}}.$$

Now from Equation B-63

$$\lim_{n\to\infty}\frac{c^n_{Irrv_Pu_FeO_c}}{c^n_{Pu_aq}} = \frac{\overline{R}_1}{\overline{U} + \overline{D}_{right_col} + \lambda}.$$

The limiting value for the right boundary ratio of colloid flux to total flux is

$$\Omega = \lim_{n\to\infty}\Omega_n = \frac{\overline{K}_3 + \dfrac{\overline{R}_1}{\overline{U} + \overline{D}_{right_col} + \lambda}}{\dfrac{\overline{U}\,\overline{K}_2 + \overline{D}_{right_aq} + \overline{D}_{right_col}\overline{K}_3}{\overline{U} + \overline{D}_{right_col}} + \dfrac{\overline{R}_1}{\overline{U} + \overline{D}_{right_col} + \lambda}}$$

or

$$\Omega = \frac{\overline{K}_3\left(\overline{U} + \overline{D}_{right_col} + \lambda\right) + \overline{R}_1}{\left(\overline{U}\,\overline{K}_2 + \overline{D}_{right_aq} + \overline{D}_{right_col}\overline{K}_3\right)\left(\dfrac{\overline{U} + \overline{D}_{right_col} + \lambda}{\overline{U} + \overline{D}_{right_col}}\right) + \overline{R}_1}. \qquad \text{(Eq. B-70)}$$

This can be written as

$$\Omega = \frac{p_1 + \overline{R}_1}{p_2 + \overline{R}_1} \qquad \text{(Eq. B-71)}$$

where

$$p_1 = \overline{K}_3\left(\overline{U} + \overline{D}_{right_col} + \lambda\right)$$

$$p_2 = \left(\overline{U}\,\overline{K}_2 + \overline{D}_{right_aq} + \overline{D}_{right_col}\overline{K}_3\right)\left(\frac{\overline{U} + \overline{D}_{right_col} + \lambda}{\overline{U} + \overline{D}_{right_col}}\right).$$

Note the limiting flux out ratio Ω satisfies

$$0 < \frac{\overline{K}_3(\overline{U} + \overline{D}_{right_col})}{\overline{U}\,\overline{K}_2 + \overline{D}_{right_aq} + \overline{D}_{right_col}\overline{K}_3} < \Omega < 1,$$

where the lower bound on Ω is obtained when $\overline{R}_1 = 0$. Qualitatively, if the advective, diffusive, and decay rates dominate the reactive rate constant $\overline{R}_1$, then Ω is close to the minimum value. However, if the reactive rate constant dominates, then Ω is close to one. The latter is the expected qualitative behavior of the system as alluded to in the introduction of this appendix. For the parameter values given in Table B-1, the minimum value $\Omega = 0.4384$ is obtained with $\overline{R}_1 = 0$.

The limiting flux out ratio for Table B-1 parameter values ($\overline{R}_1 = 0.02\ \text{yr}^{-1}$) is $\Omega = 0.5487$; in other words, about 55% of the total Pu mass exiting the cell is sorbed onto colloids. Figure B-3 shows the dependence of the flux out ratio Ω on the irreversible linear reaction rate constant *k*, where $\overline{R}_1 = \hat{S}_{FeO_c} c_{FeO_c} k$. The Ω value point obtained with the Table B-1 parameter values is also shown in Figure B-3. An increase of the irreversible linear reaction rate, *k*, of approximately one and a half orders of magnitude would increase the flux out ratio to approximately 95%.

In the expression for irreversible sorption to colloids, $\overline{R}_1 = \hat{S}_{FeO_c} c_{FeO_c} k$, consider the irreversible linear reaction rate k a fitting parameter to match a specified flux out ratio Ω. Then the solution of Equation B-71 for k is:

$$k = \frac{p_2 \Omega - p_1}{(1-\Omega)\hat{S}_{FeO_c} c_{FeO_c}}. \qquad \text{(Eq. B-72)}$$

The result in Equation B-72 provides the fitting parameter, k, given a target flux ratio Ω. From the parameter values in Table B-1 and with $\Omega = 0.95$, the irreversible linear reaction rate is determined from Equation B-72 as $k = 0.04184\,\text{cm yr}^{-1}$. The fitting parameter curve together with this point is shown in Figure B-4.

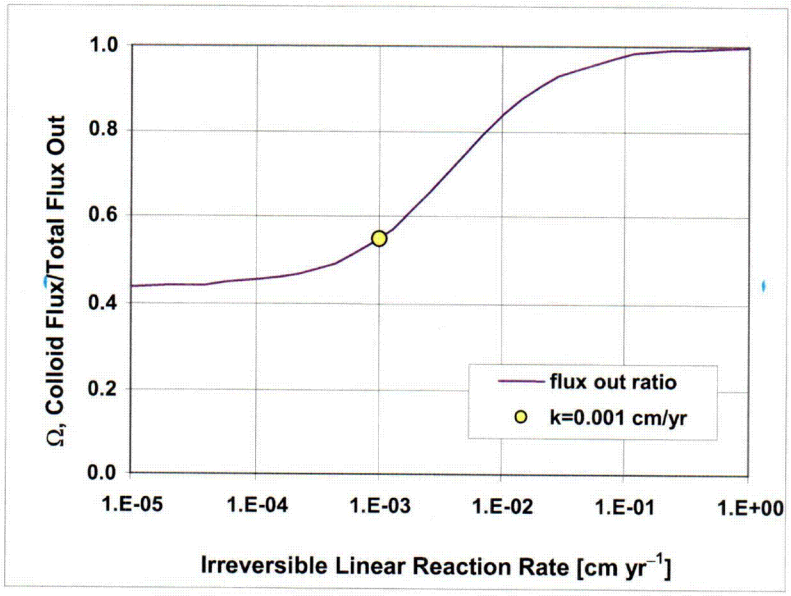

Source: Worksheet: K-surface in Appendix F.

Figure B-3. Limiting Flux Out Ratio, Ω, as a Function of Irreversible Reaction Rate

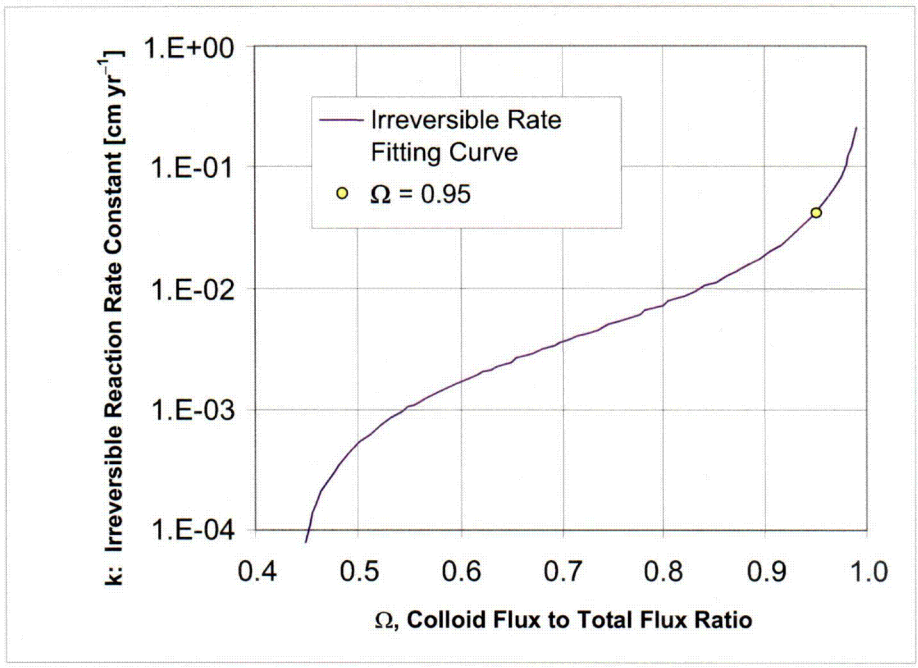

Source: Worksheet: adv_diff_decay in Appendix F.

Figure B-4. Linear Reaction Rate from Colloid to Total Flux Out Ratio, Ω

The ratio of the total flux out (right boundary) to total flux in (left boundary) at time step n is

$$\Psi_n = \frac{\left(\overline{U}\,\overline{K}_2 + \overline{D}_{right_aq} + \overline{D}_{right_col}\overline{K}_3\right)c^n_{Pu_aq} + (\overline{U} + \overline{D}_{right_col})c^n_{Irrv_Pu_FeO_c}}{\left(\overline{U}(1+\overline{K}_{d_WF_c}) + \overline{D}_{left_aq} + \overline{D}_{left_col}\overline{K}_{d_WF_c}\right)c_s - \left(\overline{D}_{left_aq} + \overline{D}_{left_col}\overline{K}_{d_WF_c}\right)c^n_{Pu_aq}}.$$

The numerator and denominator in this expression are divided by $c^n_{Pu_aq}$, and the limit is taken as n goes to infinity. Equation B-63 implies:

$$\lim \frac{c^n_{Irrv_Pu_FeO_c}}{c^n_{Pu_aq}} = \frac{\overline{R}_1}{\overline{U} + \overline{D}_{right_col} + \lambda}.$$

Denote

$$Z = \frac{\overline{U} + \overline{D}_{right_col} + \lambda}{\overline{U} + \overline{D}_{right_col}}$$

and multiply the numerator and denominator of the equation for Ψ_n by Z. The numerator reduces to $p_2 + \overline{R}_1$. Now consider the denominator term multiplied by Z. It follows from Equation B-57 that

$$\left(\overline{U}\left(1+\overline{K}_{d_WF_c}\right)+\overline{D}_{left_aq}+\overline{D}_{left_col}\overline{K}_{d_WF_c}\right)\frac{c_s}{\lim c^n_{Pu_aq}}$$
$$=\overline{UK}_2+\overline{D}_{left_aq}+\overline{D}_{left_col}\overline{K}_{d_WF_c}+\overline{D}_{right_aq}+\overline{D}_{right_col}\overline{K}_3+\overline{R}_1+\overline{R}_2+\lambda\overline{K}_1$$

Therefore, the denominator is calculated as

$$\left[\overline{UK}_2+\overline{D}_{left_aq}+\overline{D}_{left_col}\overline{K}_{d_WF_c}+\overline{D}_{right_aq}+\overline{D}_{right_col}\overline{K}_3+\overline{R}_1+\overline{R}_2+\lambda\overline{K}_1-\left(\overline{D}_{left_aq}+\overline{D}_{left_col}\overline{K}_{d_WF_c}\right)\right]Z$$
$$=\left[\overline{UK}_2+\overline{D}_{right_aq}+\overline{D}_{right_col}\overline{K}_3+\overline{R}_1+\overline{R}_2+\lambda\overline{K}_1\right]Z$$
$$=p_2+\left(\frac{\overline{U}+\overline{D}_{right_col}+\lambda}{\overline{U}+\overline{D}_{right_col}}\right)\left(\overline{R}_1+\overline{R}_2+\lambda\overline{K}_1\right),$$

The limiting flux ratio then has the limiting value:

$$\Psi=\frac{p_2+\overline{R}_1}{p_2+\left(\frac{\overline{U}+\overline{D}_{right_col}+\lambda}{\overline{U}+\overline{D}_{right_col}}\right)\left(\overline{R}_1+\overline{R}_2+\lambda\overline{K}_1\right)}. \qquad \text{(Eq. B-73)}$$

The mass flux ratio Ψ is calculated from Equation B-73 for the Table B-1 parameter values, but with irreversible linear reaction rate k = 0.04184 cm yr^{-1} obtained from the fit to $\Omega = 0.95$. Equation B-73 gives:

$$\Psi = 1.293\times10^{-4},$$

which demonstrates that most of the Pu mass is reacted both reversibly and irreversibly to the corrosion products.

CONVERGENCE ESTIMATES FOR CLOSED FORM SOLUTIONS

Consider the convergence of the concentration in the aqueous state given by Equation B-56:

$$c^n_{Pu_aq}=\frac{a_2}{1-a_1}\left(1-a_1^n\right)$$

with limit value (Equation B-57)

$$\lim_{n\to\infty}c^n_{Pu_aq}=\frac{a_2}{1-a_1}.$$

The relative error estimate with tolerance ε is given by

$$\left|\frac{\lim_{n\to\infty} c^n_{Pu_aq} - c^n_{Pu_aq}}{\lim_{n\to\infty} c^n_{Pu_aq}}\right| < \varepsilon .$$

Then the error estimate is

$$\left|\frac{\frac{a_2}{1-a_1} - \frac{a_2}{1-a_1}\left(1-a_1^n\right)}{\frac{a_2}{1-a_1}}\right| = a_1^n < \varepsilon .$$

The bounds $0 < a_1 < 1$ implies $\log_{10} a_1 < 0$ and the error estimate holds for

$$n > \frac{\log_{10} \varepsilon}{\log_{10} a_1}$$

or

$$\text{time} = n\Delta t > \frac{\log_{10} \varepsilon}{\log_{10} a_1}\Delta t . \qquad \text{(Eq. B-74)}$$

The time to converge to a given relative error tolerance for all reversible sorbed Pu concentrations is the same as the estimate for the aqueous concentration, inequality Equation B-74, since the reversibly sorbed concentration is a constant multiple of the aqueous concentration.

Now consider the convergence of the irreversible Pu concentration on colloids, $c^n_{Irrv_Pu_c}$. An estimate of the relative error is given by

$$\left|\frac{c^n_{Irrv_Pu_c} - \lim_{n\to\infty} c^n_{Irrv_Pu_c}}{\lim_{n\to\infty} c^n_{Irrv_Pu_c}}\right| = \left|\frac{\frac{a_2 b_2}{1-a_1}\left[\frac{1-b_1^{n+1}}{1-b_1} - \frac{a_1^{n+1}-b_1^{n+1}}{a_1-b_1}\right] - \frac{a_2 b_2}{(1-a_1)(1-b_1)}}{\frac{a_2 b_2}{(1-a_1)(1-b_1)}}\right|$$

$$= \left|(1-b_1)\left(\frac{-b_1^{n+1}}{1-b_1} - \frac{a_1^{n+1}-b_1^{n+1}}{a_1-b_1}\right)\right|$$

$$= \left|\frac{(1-a_1)b_1^{n+1}}{a_1-b_1} - \frac{(1-b_1)a_1^{n+1}}{a_1-b_1}\right|$$

$$\le \left|\frac{1-a_1}{a_1-b_1}\right| b_1^{n+1} + \left|\frac{1-b_1}{a_1-b_1}\right| a_1^{n+1} < \varepsilon.$$

This estimate holds if

$$b_1^{n+1} < \left|\frac{a_1 - b_1}{1 - a_1}\right| \frac{\varepsilon}{2} = \delta_1 \text{ and } a_1^{n+1} < \left|\frac{a_1 - b_1}{1 - b_1}\right| \frac{\varepsilon}{2} = \delta_2 .$$

These two estimates are satisfied if

$$n + 1 \geq \text{Integer}\left[\max\left(\frac{\log_{10}\delta_1}{\log_{10} b_1}, \frac{\log_{10}\delta_2}{\log_{10} a_1}\right)\right] + 1$$

or

$$\text{time} = n\Delta t \geq \text{Integer}\left[\max\left(\frac{\log_{10}\delta_1}{\log_{10} b_1}, \frac{\log_{10}\delta_2}{\log_{10} a_1}\right)\right]\Delta t . \qquad \text{(Eq. B-75)}$$

For a relative error tolerance of 1% ($\varepsilon = 0.01$) and the parameter values in Table B-1, Figure B-5 shows the time to converge for time step size 0.1 to 1000 years for both the aqueous Pu concentration and irreversible colloid Pu concentration. For example, if the time step is small, say 10 years, the number of years to converge within the given tolerance for the aqueous phase concentration is 137 years, whereas the time to converge for the irreversible colloid concentration is 240 years. If the time step is increased to 100 years, then the time to converge to the aqueous phase concentration is 286 years (three time steps), whereas the time to converge to the irreversible colloid concentration is 500 years (5 time steps).

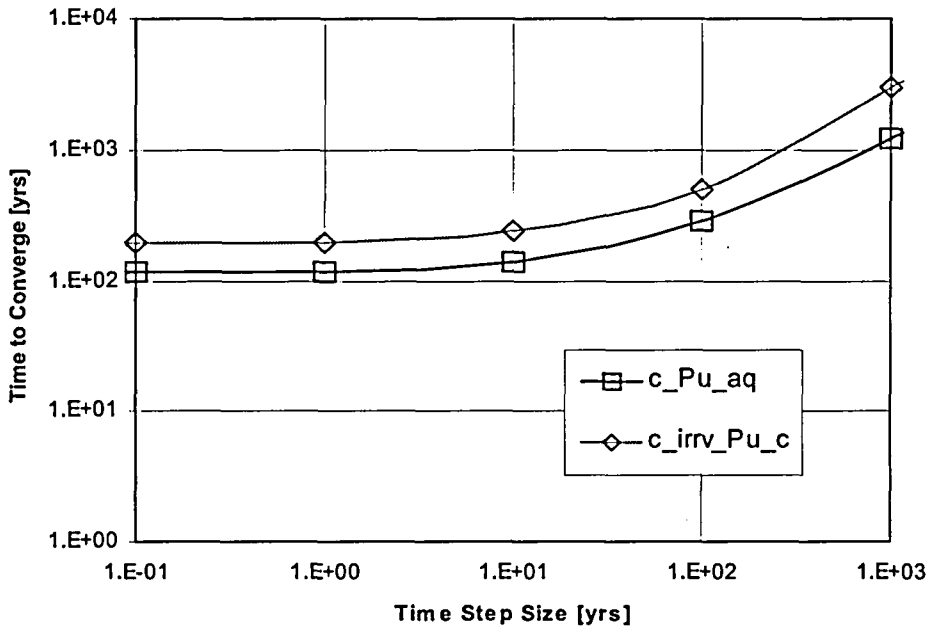

Source: Spreadsheet: time_to_conv.xls, Worksheet: plot_time_to_conv in Appendix F.

Figure B-5. Time for Concentration to Converge with 1% Relative Error Tolerance

Appendix F presents the calculational spreadsheets that implement the equations in this appendix.

APPENDIX C

MICROSOFT EXCEL SPREADSHEET "FLUX SPLIT DRIP SHIELD MODEL"

MICROSOFT EXCEL SPREADSHEET "FLUX SPLIT DRIP SHIELD MODEL"

SPREADSHEET "FLUX SPLIT DRIP SHIELD MODEL" WORKSHEET "F CALCULATIONS"

Breach Flow Fraction Calculation using Smooth Drip Shield Data, On-Crown Tests

Source Data
Calculated results

The spread angles are the mean, 1-sigma, and 1+sigma, calculated on the "Spread Anges" sheet

This cell performs a conditional test, comoparing y to Ya,Yb, Yc, Yd, and l to determine which case applies

DTN: MO0207EBSATBWP.023

For α = 9.8708 degrees

These are the Y values calculated, given x, l, and α, for each measurement. Note that Yb and Yc are different depending on the

	Drip Location (Test Description)	Breach No.	y, Drip Location Relative to Breach Center (cm)	x, Vertical Distance from Crown (drip) to Top of Breach (cm)	l, Patch half-width (cm)	Drip Flux (g)	Flow into Breach (g)	f_meas	x*Tan(α)	Model Case #	Ya	Yb	Yc	Yd	Fraction Case #
9	8 cm right of Patch 4 centerline [Q(film) Test]	4	8	136.5	13.5	178.2	22.02	0.2471	21.3040	2	-39.0180	-7.8040	7.8040	39.0180	5
10	Patch 5 centerline [Q(film) Test]	5	0	86	13.5	163.74	21.12	0.2580	13.4223	1	-31.1363	-0.0777	0.0777	31.1363	4
11	4 cm left of Patch 5 centerline [Q(film) Test]	5	-4	86	13.5	133.79	9.1	0.1360	13.4223	1	-31.1363	-0.0777	0.0777	31.1363	3
12	Patch 4 centerline [Q(film) Test]	4	0	136.5	13.5	188.63	22.25	0.2359	21.3040	2	-39.0180	-7.8040	7.8040	39.0180	4
13	27 cm right of DS center (Multiple Patch	5	-27	86	13.5	276.14	4.49	0.0325	13.4223	1	-31.1363	-0.0777	0.0777	31.1363	2
14	27 cm left of DS center (Multiple patch test)	4	27	136.5	13.5	276.83	2.63	0.0190	21.3040	2	-39.0180	-7.8040	7.8040	39.0180	6
15	81 cm left of DS center (Multiple Patch Test)	4	-27	136.5	13.5	226.22	3.45	0.0305	21.3040	2	-39.0180	-7.8040	7.8040	39.0180	2
16	81 cm right of DS center (Multiple Patch Test)	5	27	86	13.5	221.12	3.54	0.0320	13.4223	1	-31.1363	-0.0777	0.0777	31.1363	6
17	54 cm left of DS center (High Flow Rate Test)	4	0	136.5	13.5	337.72	46.41	0.2748	21.3040	2	-39.0180	-7.8040	7.8040	39.0180	4
18	54 cm left of DS center (Low Flow Rate Test)	4	0	136.5	13.5	88.89	7.88	0.1773	21.3040	2	-39.0180	-7.8040	7.8040	39.0180	4
19	27 cm left of DS center (High Flow Rate Test)	4	27	136.5	13.5	332.69	3.35	0.0201	21.3040	2	-39.0180	-7.8040	7.8040	39.0180	6
20	27 cm left of DS center (Low Flow Rate Test)	4	27	136.5	13.5	100.95	0.65	0.0129	21.3040	2	-39.0180	-7.8040	7.8040	39.0180	6
21	27 cm right of DS center (High Flow Rate	5	-27	86	13.5	378.73	2.45	0.0129	13.4223	1	-31.1363	-0.0777	0.0777	31.1363	2
22	center (Low Flow Rate Test)	5	-27	86	13.5	137.72	4.45	0.0646	13.4223	1	-31.1363	-0.0777	0.0777	31.1363	2

DTN: MO0207EBSATBWP.024

DTN: MO0207EBSATBWP.025

DTN: MO0207EBSATBWP.023 [DIRS 163402]; DTN: MO0207EBSATBWP.024 [DIRS 163401]; DTN: MO0207EBSATBWP.025 [DIRS 163403].

Figure C-1. Spreadsheet "Flux Split Drip Shield Model," Worksheet "f calculations;" Calculation of Experimental Breach Flow Fractions and Model Flow Fractions for Mean Minus One Standard Deviation Rivulet Spread Angle

The purpose of this spreadsheet is to develop the drip shield flux splitting submodel using experimental data from the breached drip shield experiments. The data are analyzed to estimate an average and range of the rivulet spread angle, α. The disparity between measured fraction of dripping flux that enters a breach and the fraction calculated using the model (with the measured range of the rivulet spread angle) is then used to establish a range of uncertainty in the model.

All descriptions for this worksheet (Figures C-1 to C-4) pertain to Rows 9–22. Equations in spreadsheet format are illustrated using Row 9.

Column B: Drip location as indicated for each test in the designated DTN (Figure C-1).

Column C: Breach or patch number most pertinent to this particular test, for which flow is analyzed in this row of the spreadsheet.

Column D: Drip location, y, relative to the center of the breach listed in Column C.

Column E: Distance along the drip shield curved surface, x, from the drip shield crown to the top of the breach.

Column F: Half-width, ℓ, of the breach (13.5 cm), same for all breaches.

Column G: Measured mass of water, F_1, dripped onto the drip shield during the test. It is assumed that half of the water that dripped onto the drip shield, $F_1/2$, flowed down the side that contained the breach.

Column H: Measured mass of water, F_2, that flowed into the breach during the test.

Column I: Fraction of water dripped onto the drip shield that flowed into the breach:

$$f_{expt} = \frac{F_2}{F_1/2} = \frac{2F_2}{F_1}.$$

I9=H9*2/G9

Column J: $x \tan\alpha$, where x is from Column E, and α is the spread angle. For Columns J-X, the value used for α is 8.8708° (Cell $M$7), which is one standard deviation less than the mean measured spread angle for these tests (see Worksheet "Spread angles").

J9=$E9*TAN(RADIANS($M$7))

Column K: Case number as described in Sections 6.5.1.1.2.1 and 6.5.1.1.2.2. For Case 1, $\ell > x\tan\alpha$; for Case 2, $\ell < x\tan\alpha$; x is from Column E, and the half-width of the breach, ℓ, is from Column F.

K9=IF($F9>J9,1,2)

Column L: Value of y_A (Point A) as described in Sections 6.5.1.1.2.1 and 6.5.1.1.2.2, corresponding to the leftmost point from which the edge of the fan from the rivulet can enter the left side of the breach:

$$y_A = -\ell - (x + 2\ell)\tan\alpha$$

L9=-$F9-($E9+2*$F9)*TAN(RADIANS($M$7))

Column M: Value of y_B (Point B) as described in Sections 6.5.1.1.2.1 and 6.5.1.1.2.2, corresponding to the leftmost point from which rivulets will enter the top edge of the breach. The value of y_B depends on the Model Case number (Column K):

$$y_B = -\ell + x\tan\alpha \qquad \text{Case 1.}$$

$$y_B = \ell - x\tan\alpha \qquad \text{Case 2.}$$

```
M9=IF(K9=1,(-$F9+$E9*TAN(RADIANS($M$7))),
($F9-$E9*TAN(RADIANS($M$7))))
```

Column N: Value of y_C (Point C) as described in Sections 6.5.1.1.2.1 and 6.5.1.1.2.2, corresponding to the rightmost point from which rivulets will enter the top edge of the breach. The value of y_C depends on the Model Case number (Column K):

$$y_C = \ell - x\tan\alpha \qquad \text{Case 1.}$$

$$y_C = -\ell + x\tan\alpha \qquad \text{Case 2.}$$

```
N9=IF(K9=1,($F9-$E9*TAN(RADIANS($M$7))),
(-$F9+$E9*TAN(RADIANS($M$7))))
```

Column O: Value of y_D (Point D) as described in Sections 6.5.1.1.2.1 and 6.5.1.1.2.2, corresponding to the rightmost point from which the edge of the fan from the rivulet can enter the right side of the breach:

$$y_D = \ell + (x + 2\ell)\tan\alpha$$

```
O9=$F9+($E9+2*$F9)*TAN(RADIANS($M$7))
```

Column P: Determines which region (designated as Fraction Case #) along the crown where the drip is located:

1. $y \le y_A$
2. $y_A < y \le -\ell$
3. $-\ell < y < y_B$
4. $y_B \le y \le y_C$
5. $y_C < y < \ell$
6. $\ell \le y < y_D$
7. $y \ge y_D$

```
P9=IF(D9<=L9,1,IF(D9<=-F9,2,IF(D9<M9,3,
IF(D9<=N9,4,IF(D9<F9,5,IF(D9<O9,6,IF(D9>=O9,7)))))))
```

Crown Tests

The spread angles are the mean, 1-sigma, and 1+sigma, calculated on the "Spread Anges" sheet

This cell performs a conditional test, comoparing y to Ya,Yb, Yc, Yd, and I to determine which case applies

This cell is the f value determined by the appropriate case of the 7

For α = 8.8708 degrees

These are the Y values calculated, given π, I, and α, for each measurement. Note that Yb and Yc are different depending on the

These are the calculations that represent the 7 different **fraction** cases in the model. Some are constants (1 or 0)

	I	J	K	L	M	N	O	P	Q	R	S	T	U	V	W	X
8	f_{expt}	π*Tan(α)	Model Case #	Ya	Yb	Yc	Yd	Fraction Case #	f_{calc}	f1	f2	f3	f4	f5	f6	f7
9	0.2471	21.3040	2	-39.0180	-7.8040	7.8040	39.0180	5	**0.6291**	0.0000	0.9213	1.0046	0.6337	0.6291	0.6078	0.0000
10	0.2580	13.4223	1	-31.1363	-0.0777	0.0777	31.1363	4	**1.0000**	0.0000	0.8827	1.0029	1.0000	1.0029	0.8827	0.0000
11	0.1360	13.4223	1	-31.1363	-0.0777	0.0777	31.1363	3	**0.8539**	0.0000	0.7693	0.8539	1.0000	1.1519	0.9961	0.0000
12	0.2359	21.3040	2	-39.0180	-7.8040	7.8040	39.0180	4	**0.6337**	0.0000	0.7645	0.8168	0.6337	0.8168	0.7645	0.0000
13	0.0325	13.4223	1	-31.1363	-0.0777	0.0777	31.1363	2	**0.1173**	0.0000	0.1173	-0.0029	1.0000	2.0087	1.6482	0.0000
14	0.0190	21.3040	2	-39.0180	-7.8040	7.8040	39.0180	6	**0.2355**	0.0000	1.2936	1.4505	0.6337	0.1832	0.2355	0.0000
15	0.0305	21.3040	2	-39.0180	-7.8040	7.8040	39.0180	2	**0.2355**	0.0000	0.2355	0.1832	0.6337	1.4505	1.2936	0.0000
16	0.0320	13.4223	1	-31.1363	-0.0777	0.0777	31.1363	6	**0.1173**	0.0000	1.6482	2.0087	1.0000	-0.0029	0.1173	0.0000
17	0.2748	21.3040	2	-39.0180	-7.8040	7.8040	39.0180	4	**0.6337**	0.0000	0.7645	0.8168	0.6337	0.8168	0.7645	0.0000
18	0.1773	21.3040	2	-39.0180	-7.8040	7.8040	39.0180	4	**0.6337**	0.0000	0.7645	0.8168	0.6337	0.8168	0.7645	0.0000
19	0.0201	21.3040	2	-39.0180	-7.8040	7.8040	39.0180	6	**0.2355**	0.0000	1.2936	1.4505	0.6337	0.1832	0.2355	0.0000
20	0.0129	21.3040	2	-39.0180	-7.8040	7.8040	39.0180	6	**0.2355**	0.0000	1.2936	1.4505	0.6337	0.1832	0.2355	0.0000
21	0.0129	13.4223	1	-31.1363	-0.0777	0.0777	31.1363	2	**0.1173**	0.0000	0.1173	-0.0029	1.0000	2.0087	1.6482	0.0000
22	0.0646	13.4223	1	-31.1363	-0.0777	0.0777	31.1363	2	**0.1173**	0.0000	0.1173	-0.0029	1.0000	2.0087	1.6482	0.0000

Figure C-2. Spreadsheet "Flux Split Drip Shield Model," Worksheet "f calculations;" Calculation of Model Flow Fractions for Mean Minus One Standard Deviation Rivulet Spread Angle

Columns R though X (Figure C-2) compute the fraction of dripping flux f_{calc} that is predicted to flow into a breach, assuming the drip location is within each of seven regions along the crown. Although f_{calc} is computed for all seven regions, it is valid in only one of the regions. The correct valid region is determined in Column P (Fraction Case #), and the appropriate value from Columns R through X is entered in Column Q.

Column Q: f_{calc} is the fraction of dripping flux onto the drip shield that is predicted by the drip shield flux splitting submodel, Equations 6.5.1.1.2-2 through 6.5.1.1.2-6 or 6.5.1.1.2-19 through 6.5.1.1.2-23, for Cases 1 and 2, respectively. f_{calc} is intended to be compared with f_{expt} (Column I). The value of f_{calc} is selected from Columns R through X, depending on the appropriate Fraction Case # (Column P).

```
Q9=IF(P9=1,R9,IF(P9=2,S9,IF(P9=3,T9,IF(P9=4,U9,
    IF(P9=5,V9,IF(P9=6,W9,IF(P9=7,X9)))))))
```

Column R: Value of f_{calc} in region 1 ($y \le y_A$), where $f_{calc} = 0$.

R9=0

Column S: Value of f_{calc} in region 2 ($y_A < y \le -\ell$):

$$f_{calc} = \frac{y + \ell + (x + 2\ell)\tan\alpha}{2(x + 2\ell)\tan\alpha}$$

S9=(D9+F9+(E9+2*F9)*TAN(RADIANS($M$7)))/
(2*(E9+2*F9)*TAN(RADIANS($M$7)))

Column T: Value of f_{calc} in region 3 ($-\ell < y < y_B$):

$$f_{calc} = \frac{y + \ell + x\tan\alpha}{2x\tan\alpha}$$

T9=(D9+F9+E9*TAN(RADIANS($M$7)))/(2*E9*TAN(RADIANS($M$7)))

Column U: Value of f_{calc} in region 4 ($y_B \le y \le y_C$):

$$f_{calc} = \frac{2\ell}{2x\tan\alpha}$$

U9=IF(K9=1,1,(2*$F9/(2*$E9*TAN(RADIANS($M$7)))))

Column V: Value of f_{calc} in region 5 ($y_C < y < \ell$):

$$f_{calc} = \frac{-y + \ell + x\tan\alpha}{2x\tan\alpha}$$

V9=(-D9+F9+E9*TAN(RADIANS($M$7)))/(2*E9*TAN(RADIANS($M$7)))

Column W: Value of f_{calc} in region 6 ($\ell \le y < y_D$):

$$f_{calc} = \frac{-y + \ell + (x + 2\ell)\tan\alpha}{2(x + 2\ell)\tan\alpha}$$

W9=(-D9+F9+(E9+2*F9)*TAN(RADIANS($M$7)))/
(2*(E9+2*F9)*TAN(RADIANS($M$7)))

Column X: Value of f_{calc} in region 7 ($y \ge y_D$) where $f_{calc} = 0$:

X9=0

	Y	Z	AA	AB	AC	AD	AE	AF	AG	AH	AI	AJ	AK	AL	AM
1															
2															
3															
4															
5															
6															
7			For α =	13.1527 degrees											
8	E*Tan(α)	Model Case #	Ya	Yb	Yc	Yd	Fraction Case #	f ...	f1	f2	f3	f4	f5	f6	f7
9	31.8968	2	-51.7061	-18.3968	18.3968	51.7061	4	**0.4232**	0.0000	0.7814	0.8370	0.4232	0.5862	0.5720	0.0000
10	20.0962	2	-39.9054	-6.5962	6.5962	39.9054	4	**0.6718**	0.0000	0.7556	0.8359	0.6718	0.8359	0.7556	0.0000
11	20.0962	2	-39.9054	-6.5962	6.5962	39.9054	2	**0.6799**	0.0000	0.6799	0.7364	0.6718	0.9354	0.8314	0.0000
12	31.8968	2	-51.7061	-18.3968	18.3968	51.7061	4	**0.4232**	0.0000	0.6767	0.7116	0.4232	0.7116	0.6767	0.0000
13	20.0962	2	-39.9054	-6.5962	6.5962	39.9054	2	**0.2444**	0.0000	0.2444	0.1641	0.6718	1.5077	1.2669	0.0000
14	31.8968	2	-51.7061	-18.3968	18.3968	51.7061	6	**0.3233**	0.0000	1.0300	1.1349	0.4232	0.2884	0.3233	0.0000
15	31.8968	2	-51.7061	-18.3968	18.3968	51.7061	2	**0.3233**	0.0000	0.3233	0.2884	0.4232	1.1349	1.0300	0.0000
16	20.0962	2	-39.9054	-6.5962	6.5962	39.9054	6	**0.2444**	0.0000	1.2669	1.5077	0.6718	0.1641	0.2444	0.0000
17	31.8968	2	-51.7061	-18.3968	18.3968	51.7061	4	**0.4232**	0.0000	0.6767	0.7116	0.4232	0.7116	0.6767	0.0000
18	31.8968	2	-51.7061	-18.3968	18.3968	51.7061	4	**0.4232**	0.0000	0.6767	0.7116	0.4232	0.7116	0.6767	0.0000
19	31.8968	2	-51.7061	-18.3968	18.3968	51.7061	6	**0.3233**	0.0000	1.0300	1.1349	0.4232	0.2884	0.3233	0.0000
20	31.8968	2	-51.7061	-18.3968	18.3968	51.7061	6	**0.3233**	0.0000	1.0300	1.1349	0.4232	0.2884	0.3233	0.0000
21	20.0962	2	-39.9054	-6.5962	6.5962	39.9054	2	**0.2444**	0.0000	0.2444	0.1641	0.6718	1.5077	1.2669	0.0000
22	20.0962	2	-39.9054	-6.5962	6.5962	39.9054	2	**0.2444**	0.0000	0.2444	0.1641	0.6718	1.5077	1.2669	0.0000

Figure C-3. Spreadsheet "Flux Split Drip Shield Model," Worksheet "f calculations;" Calculation of Model Flow Fractions for Mean Rivulet Spread Angle

Columns Y though AM (Figure C-3) repeat the calculations done in Columns J though X using the mean rivulet spread angle of $\alpha = 13.1527°$ (Cell $AB$7). For Row 9, the spreadsheet equations are as follows:

```
Y9=$E9*TAN(RADIANS($AB$7))

Z9=IF($F9>Y9,1,2)

AA9=-$F9-($E9+2*$F9)*TAN(RADIANS($AB$7))

AB9=IF(Z9=1,(-$F9+$E9*TAN(RADIANS($AB$7))),($F9-$E9*TAN(RADIANS($AB$7))))

AC9=IF(Z9=1,($F9-$E9*TAN(RADIANS($AC$7))),(-$F9+$E9*TAN(RADIANS($AB$7))))

AD9=$F9+($E9+2*$F9)*TAN(RADIANS($AB$7))

AE9=IF(D9<=AA9,1,IF(D9<=-
      U9,2,IF(D9<AB9,3,IF(D9<=AC9,4,IF(D9<U9,5,IF(D9<AD9,6,IF(D9>=AD9,7)))))))

AF9=IF(AE9=1,AG9,IF(AE9=2,AH9,IF(AE9=3,AI9,IF(AE9=4,AJ9,IF(AE9=5,AK9,IF(AE9
      =6,AL9,IF(AE9=7,AM9)))))))
```

```
AG9=0
AH9=(D9+F9+(E9+2*F9)*TAN(RADIANS($AB$7)))/
      (2*(E9+2*F9)*TAN(RADIANS($AB$7)))
AI9=(D9+F9+E9*TAN(RADIANS($AB$7)))/(2*E9*TAN(RADIANS($AB$7)))
AJ9=IF(Z9=1,1,(2*$F9/(2*$E9*TAN(RADIANS($AB$7)))))
AK9=(-D9+F9+E9*TAN(RADIANS($AB$7)))/(2*E9*TAN(RADIANS($AB$7)))
AL9=(-D9+F9+(E9+2*F9)*TAN(RADIANS($AB$7)))/
      (2*(E9+2*F9)*TAN(RADIANS($AB$7)))
AM9=0
```

Columns AN though BB (Figure C-1) repeat the calculations done in Columns J though X using a rivulet spread angle of $\alpha = 17.2903°$ (Cell $AQ$7), which is one standard deviation greater than the mean rivulet spread angle. For Row 9, the spreadsheet equations are as follows:

```
AN9=$E9*TAN(RADIANS($AQ$7))
AO9=IF($F9>AN9,1,2)
AP9=-$F9-($E9+2*$F9)*TAN(RADIANS($AQ$7))
AQ9=IF(AO9=1,(-$F9+$E9*TAN(RADIANS($AQ$7))),($F9-
      $E9*TAN(RADIANS($AQ$7))))
AR9=IF(AO9=1,($F9-$E9*TAN(RADIANS($AQ$7))),
      (-$F9+$E9*TAN(RADIANS($AQ$7))))
AS9=$F9+($E9+2*$F9)*TAN(RADIANS($AQ$7))
AT9=IF(AH9<=AP9,1,IF(AH9<=-AJ9,2,IF(AH9<AQ9,3,IF(AH9<=AR9,4,
      IF(AH9<AJ9,5,IF(AH9<AS9,6,IF(AH9>=AS9,7)))))))
AU9=IF(AT9=1,AV9,IF(AT9=2,AW9,IF(AT9=3,AX9,IF(AT9=4,AY9,IF(AT9=5,AZ9,IF
      (AT9=6,BA9,IF(AT9=7,BB9)))))))
AV9=0
AW9=(D9+F9+(E9+2*F9)*TAN(RADIANS($AQ$7)))/
      (2*(E9+2*F9)*TAN(RADIANS($AQ$7)))
AX9=(D9+F9+E9*TAN(RADIANS($AQ$7)))/(2*E9*TAN(RADIANS($AQ$7)))
AY9=IF(AO9=1,1,(2*$F9/(2*$E9*TAN(RADIANS($AQ$7)))))
AZ9=(-D9+F9+E9*TAN(RADIANS($AQ$7)))/(2*E9*TAN(RADIANS($AQ$7)))
BA9=(-D9+F9+(E9+2*F9)*TAN(RADIANS($AQ$7)))/
      (2*(E9+2*F9)*TAN(RADIANS($AQ$7)))
BB9=0
```

	AN	AO	AP	AQ	AR	AS	AT	AU	AV	AW	AX	AY	AZ	BA	BB
1															
2															
3															
4															
5															
6															
7			For α = ##### degrees												
8	s*tan(α)	Model Case #	Ya	Yb	Yc	Yd	Fraction Case #	f ave	f1	f2	f3	f4	f5	f6	f7
9	42.4896	2	-64.3942	-28.9896	28.9896	64.3942	4	**0.3177**	0.0000	0.7112	0.7530	0.3177	0.5647	0.5540	0.0000
10	26.7700	2	-48.6746	-13.2700	13.2700	48.6746	4	**0.5043**	0.0000	0.6919	0.7521	0.5043	0.7521	0.6919	0.0000
11	26.7700	2	-48.6746	-13.2700	13.2700	48.6746	4	**0.5043**	0.0000	0.6350	0.6774	0.5043	0.8269	0.7488	0.0000
12	42.4896	2	-64.3942	-28.9896	28.9896	64.3942	4	**0.3177**	0.0000	0.6326	0.6589	0.3177	0.6589	0.6326	0.0000
13	26.7700	2	-48.6746	-13.2700	13.2700	48.6746	4	**0.5043**	0.0000	0.3081	0.2479	0.5043	1.2564	1.0757	0.0000
14	42.4896	2	-64.3942	-28.9896	28.9896	64.3942	4	**0.3177**	0.0000	0.8979	0.9766	0.3177	0.3411	0.3674	0.0000
15	42.4896	2	-64.3942	-28.9896	28.9896	64.3942	4	**0.3177**	0.0000	0.3674	0.3411	0.3177	0.9766	0.8979	0.0000
16	26.7700	2	-48.6746	-13.2700	13.2700	48.6746	4	**0.5043**	0.0000	1.0757	1.2564	0.5043	0.2479	0.3081	0.0000
17	42.4896	2	-64.3942	-28.9896	28.9896	64.3942	4	**0.3177**	0.0000	0.6326	0.6589	0.3177	0.6589	0.6326	0.0000
18	42.4896	2	-64.3942	-28.9896	28.9896	64.3942	4	**0.3177**	0.0000	0.6326	0.6589	0.3177	0.6589	0.6326	0.0000
19	42.4896	2	-64.3942	-28.9896	28.9896	64.3942	4	**0.3177**	0.0000	0.8979	0.9766	0.3177	0.3411	0.3674	0.0000
20	42.4896	2	-64.3942	-28.9896	28.9896	64.3942	4	**0.3177**	0.0000	0.8979	0.9766	0.3177	0.3411	0.3674	0.0000
21	26.7700	2	-48.6746	-13.2700	13.2700	48.6746	4	**0.5043**	0.0000	0.3081	0.2479	0.5043	1.2564	1.0757	0.0000
22	26.7700	2	-48.6746	-13.2700	13.2700	48.6746	4	**0.5043**	0.0000	0.3081	0.2479	0.5043	1.2564	1.0757	0.0000

Figure C-4. Spreadsheet "Flux Split Drip Shield Model," Worksheet "f calculations;" Calculation of Model Flow Fractions for Mean Plus One Standard Deviation Rivulet Spread Angle

Rivulet spread measurements are listed in Column D, Rows 6-31 (Figure C-5), for 26 tests described in the indicated DTNs. The sketch to the right shows the relationships between measured rivulet spread ("1/2 spread") and the "1/2 spread angle," α. The average, μ_r, of the 26 spread measurements (Cell D33) is 20.096 cm, with a standard deviation, σ, of 6.674 cm. The uncertainty in the spread angle is incorporated into the drip shield flux splitting submodel by assigning a range for the rivulet spread of $\mu_r \pm 1\sigma$. The mean rivulet spread and $\mu_r \pm 1\sigma$ are shown in Cells K6–K8. The rivulet spread is converted to spread angle in Cells L6-L8 using the relation shown in the sketch that defines α:

$$\alpha = \tan^{-1}\left(\frac{w_r}{x}\right),$$

where w_r is the rivulet "1/2 spread" (cm), and x is the distance from the crown to the spread measurement location (cm). The Microsoft Excel equation for the mean spread angle is:

L6=DEGREES(ATAN(K6/($N$4)))

where $N$4 = x = 86 cm for these tests. The Microsoft Excel function ATAN returns a value in radians, which must be converted to degrees using the DEGREES function.

Also included in this worksheet is a sketch (Figure C-6) showing the dimensions and locations of breaches in the drip shield mockup used in the experiments. The sketch appears in the scientific notebook from the experiments (Howard 2002 [DIRS 161516], p. 14), and is also shown in Figure 4.1-1, Section 4.1.1.

SPREADSHEET "FLUX SPLIT DRIP SHIELD MODEL" WORKSHEET "SPREAD ANGLES"

Experimental Rivulet spread from Drip Impact Point Smooth Surface -- On-Crown Drip)

Source Data
Calculated results

Length from crown to rivulet spread measurement (x): 86 cm

	Measured 1/2 Spread (cm)	
4 cm left of Patch 5 centerline - right side	21.0	(no measurement on left side)
8 cm right of Patch 4 centerline - right side	28.5	
8 cm right of Patch 4 centerline - left side	15.0	
Patch 5 centerline - left side	28.0	(no measurement on right side)
Patch 4 centerline - right side	26.5	
Patch 4 centerline - left side	11.0	
27 cm right of DS center - right side	29.0	DTN: MO0207EBSATBWP.023
27 cm right of DS center - left side	13.0	
27 cm left of DS center - right side	21.5	
27 cm left of DS center - left side	21.0	DTN: MO0207EBSATBWP.024
81 cm left of DS center - right side	23.5	
81 cm left of DS center - left side	17.0	
81 cm right of DS center - right side	18.0	
81 cm right of DS center - left side	20.0	
54 cm left of DS center (High Flow Rate) - right side	32.0	
54 cm left of DS center (High Flow Rate) - left side	22.0	
54 cm left of DS center (Low Flow Rate) - right side	30.0	
54 cm left of DS center (Low Flow Rate) - left side	10.5	
27 cm left of DS center (High Flow Rate) - right side	24.0	
27 cm left of DS center (High Flow Rate) - left side	19.0	DTN: MO0207EBSATBWP.025
27 cm left of DS center (Low Flow Rate) - right side	8.0	
27 cm left of DS center (Low Flow Rate) - left side	10.0	
27 cm right of DS center (High Flow Rate) - right side	16.5	
27 cm right of DS center (High Flow Rate) - left side	24.0	
27 cm right of DS center (Low Flow Rate) - right side	13.5	
27 cm right of DS center (Low Flow Rate) - left side	20.0	
	20.09615385	Average (cm)
	6.673958301	Standard Deviation (cm)

	1/2 Spread (cm)	1/2 Spread Angle (deg)
Mean	20.09615	13.15265
Mean - 1 sigma	13.4223	8.870771
Mean + 1 sigma	26.77001	17.29028

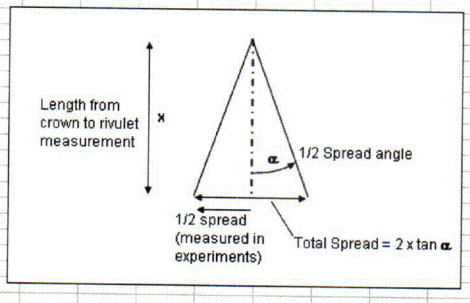

DTN: MO0207EBSATBWP.023 [DIRS 163402]; DTN: MO0207EBSATBWP.024 [DIRS 163401]; DTN: MO0207EBSATBWP.025 [DIRS 163403].

Figure C-5. Spreadsheet "Flux Split Drip Shield Model," Worksheet "Spread angles;" Calculation of Rivulet Spread Angle

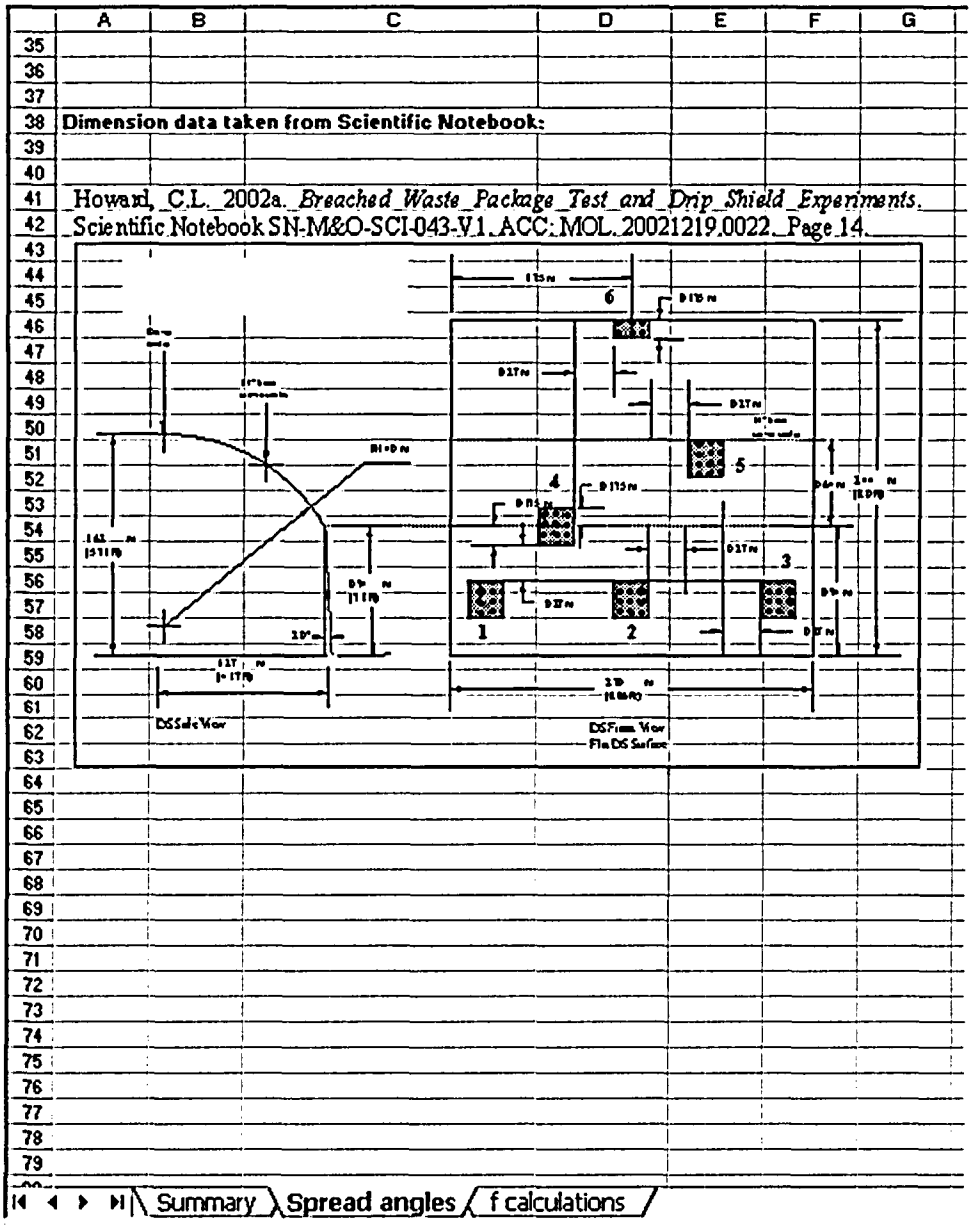

Source: Howard 2002 [DIRS 161516], p. 14.

Figure C-6. Spreadsheet "Flux Split Drip Shield Model," Worksheet "Spread Angles;" Dimensions and Locations of Breaches in Drip Shield Mockup Used in Breached Drip Shield Experiments

SPREADSHEET "FLUX SPLIT DRIP SHIELD MODEL" WORKSHEET "SUMMARY"

	A	B	C	D	E	F	G	H	I	J	K
1											
2		**Drip Shield Model: Comparison of Measured and Modeled Fraction of Drip Seepage Flowing Into a Breach**									
3											
4											
5											
6		This spreadsheet compares results from the "Atlas Breached Waste Package and Drip Shield Experiments: Breached Drip Shield Tests" (documented in TDR-EBS-MD-000025-00 REV 00) with the model developed in the "EBS Radionuclide Transport Abstraction" (ANL-WIS-PA-0000001 REV 02). Test data are taken directly from the TDMS for this comparison.									
7											
8		Methodology:									
9		1. Spreading angles are calculated from the test data in the sheet titled ***Spread angles***									
10		2. Given spread angle and test geometry, seepage fractions are calculated for both the test data and the model in the worksheet ***f calculations***:									
11			a. Geometric data for each measurement (x,y,l) and the spread angle are used to determine which of 7 cases the measurement corresponds to								
12			b. For each test result the appropriate case model is applied to calculate the seepage flow fraction f								
13		3. The seepage fractions calculated from both the test and model are listed and compared in the two tables listed below in this ***Summary*** worksheet									
14											
15		Notes:									
16		Source data DTNs are noted where source data is used									
17		Model equations are provided on the calculational sheets									
18		Data in tables below is linked directly to the calculational worksheets									
19											

Source: BSC 2003 [DIRS 163406].

Figure C-7. Spreadsheet "Flux Split Drip Shield Model," Worksheet "Summary;" Summary of Drip Shield Flux Splitting Submodel

This worksheet, beginning with Figure C-7, summarizes the calculations in worksheets "Spread angles" and "f calculations."

The first table (Figure C-8), "Measured Breach Flow Fractions and Calculated Breach Flow Fractions," Rows 25-43, Columns B-I, is identical to Table 6.5-2. Columns B-E are identical to the same respective columns described earlier for worksheet "f calculations." Column F is identical to Column I in worksheet "f calculations." Columns G-I summarize the calculated fraction of the dripping flux that the flux splitting submodel predicts should flow into the breach, for the minimum, mean, and maximum spread angles. The minimum spread angle is specified to be one standard deviation less than the mean of the measured spread angles. The maximum spread angle is specified to be one standard deviation greater than the mean of the measured spread angles. Column G is identical to Column Q of worksheet "f calculations." Column H is identical to Column AF of worksheet "f calculations." Column I is identical to Column AU of worksheet "f calculations."

Rows 39–43, Columns F–I, show the results of Microsoft Excel functions "AVERAGE," "STDEVA," "MEDIAN," "MIN", and "MAX," respectively, as applied to Rows 25-38.

	A	B	C	D	E	F	G	H	I
19									
20		*Measured Breach Flow Fractions and Calculated Breach Flow Fractions*							
21									
22							f_{calc}		
23							α (deg)	α (deg)	α (deg)
24		Drip Location (Test Description)	Breach No.	y, Drip Location Relative to Breach Center (cm)	z, Vertical Distance from Crown (drip) to Top of Breach (cm)	f_{expt}	8.87	13.15	17.29
25		8 cm right of Patch 4 centerline [Q(film) Test]	4	8	136.5	0.2471	0.6291	0.4232	0.3177
26		Patch 5 centerline [Q(film) Test]	5	0	86.0	0.2580	1.0000	0.6718	0.5043
27		4 cm left of Patch 5 centerline [Q(film) Test]	5	-4	86.0	0.1360	0.8539	0.6799	0.5043
28		Patch 4 centerline [Q(film) Test]	4	0	136.5	0.2359	0.6337	0.4232	0.3177
29		27 cm right of DS center (Multiple Patch Test)	5	-27	86.0	0.0325	0.1173	0.2444	0.5043
30		27 cm left of DS center (Multiple patch test)	4	27	136.5	0.0190	0.2355	0.3233	0.3177
31		81 cm left of DS center (Multiple Patch Test)	4	-27	136.5	0.0305	0.2355	0.3233	0.3177
32		81 cm right of DS center (Multiple Patch Test)	5	27	86.0	0.0320	0.1173	0.2444	0.5043
33		54 cm left of DS center (High Flow Rate Test)	4	0	136.5	0.2748	0.6337	0.4232	0.3177
34		54 cm left of DS center (Low Flow Rate Test)	4	0	136.5	0.1773	0.6337	0.4232	0.3177
35		27 cm left of DS center (High Flow Rate Test)	4	27	136.5	0.0201	0.2355	0.3233	0.3177
36		27 cm left of DS center (Low Flow Rate Test)	4	27	136.5	0.0129	0.2355	0.3233	0.3177
37		27 cm right of DS center (High Flow Rate Test)	5	-27	86.0	0.0129	0.1173	0.2444	0.5043
38		27 cm right of DS center (Low Flow Rate Test)	5	-27	86.0	0.0646	0.1173	0.2444	0.5043
39		Mean				0.1110	0.4139	0.3797	0.3977
40		Std. Dev.				0.1055	0.3048	0.1438	0.0958
41		Median				0.0486	0.2355	0.3233	0.3177
42		Minimum				0.0129	0.1173	0.2444	0.3177
43		Maximum				0.2748	1.0000	0.6799	0.5043
44									

Figure C-8. Spreadsheet "Flux Split Drip Shield Model," Worksheet "Summary;" Summary of Drip Shield Flux Splitting Submodel

The second table (Figure C-9), "Comparison of Measured and Calculated Breach Flows," is identical to Table 6.5-3. Column K is again the drip location. Column L is the fraction of dripping flux that flowed into a breach as measured experimentally; this is identical to Column F of the preceding table, or Column I in worksheet "f calculations." The next three columns (M-O) show the difference between the predicted breach flow fraction, f_{calc}, and the measured fraction, f_{expt}, for the minimum, mean, and maximum rivulet spread angle. Columns P-R show the ratio f_{calc} / f_{expt} for the minimum, mean, and maximum rivulet spread angle.

Rows 39-43, Columns L-R, show the results of Microsoft Excel functions "AVERAGE," "STDEVA," "MEDIAN," "MIN," and "MAX," respectively, as applied to Rows 25-38.

	J	K	L	M	N	O	P	Q	R
19									
20									
21		*Comparison of Measured and Calculated Breach Flows*							
22				$f_{calc} - f_{expt}$			f_{calc} / f_{expt}		
23				α (deg)	α (deg)	α (deg)	α (deg)	α (deg)	α (deg)
24		**Drip Location (Test Description)**	f_{expt}	**8.87**	**13.15**	**17.29**	**8.87**	**13.15**	**17.29**
25		8 cm right of Patch 4 centerline [Q(film) Test]	0.2471	0.3819	0.1761	0.0706	2.5455	1.7126	1.2856
26		Patch 5 centerline [Q(film) Test]	0.2580	0.7420	0.4138	0.2463	3.8764	2.6041	1.9549
27		4 cm left of Patch 5 centerline [Q(film) Test]	0.1360	0.7179	0.5439	0.3683	6.2770	4.9979	3.7071
28		Patch 4 centerline [Q(film) Test]	0.2359	0.3978	0.1873	0.0818	2.6861	1.7941	1.3468
29		27 cm right of DS center (Multiple Patch Test)	0.0325	0.0847	0.2119	0.4718	3.6060	7.5145	15.5074
30		27 cm left of DS center (Multiple patch test)	0.0190	0.2165	0.3043	0.2987	12.3932	17.0164	16.7216
31		81 cm left of DS center (Multiple Patch Test)	0.0305	0.2050	0.2928	0.2872	7.7203	10.6004	10.4168
32		81 cm right of DS center (Multiple Patch Test)	0.0320	0.0852	0.2124	0.4723	3.6624	7.6321	15.7500
33		54 cm left of DS center (High Flow Rate Test)	0.2748	0.3588	0.1484	0.0429	2.3056	1.5399	1.1560
34		54 cm left of DS center (Low Flow Rate Test)	0.1773	0.4564	0.2459	0.1404	3.5741	2.3872	1.7920
35		27 cm left of DS center (High Flow Rate Test)	0.0201	0.2153	0.3032	0.2976	11.6928	16.0548	15.7767
36		27 cm left of DS center (Low Flow Rate Test)	0.0129	0.2226	0.3104	0.3048	18.2860	25.1075	24.6725
37		27 cm right of DS center (High Flow Rate Test)	0.0129	0.1043	0.2314	0.4914	9.0637	18.8879	38.9779
38		27 cm right of DS center (Low Flow Rate Test)	0.0646	0.0526	0.1797	0.4397	1.8146	3.7814	7.8035
39		Mean	0.1110	0.3029	0.2687	0.2867	6.3931	8.6879	11.2049
40		Std. Dev.	0.1055	0.2210	0.1065	0.1550	4.8845	7.6717	11.0326
41		Median	0.0486	0.2195	0.2387	0.2982	3.7694	6.2562	9.1102
42		Minimum	0.0129	0.0526	0.1484	0.0429	1.8146	1.5399	1.1560
43		Maximum	0.2748	0.7420	0.5439	0.4914	18.2860	25.1075	38.9779

Figure C-9. Spreadsheet "Flux Split Drip Shield Model," Worksheet "Summary;" Summary of Drip Shield Flux Splitting Submodel Comparing Measured and Calculated Breach Flows

Finally, a plot in worksheet "Summary" (Figure C-10) compares the calculated f_{calc} with the measured f_{expt} (Column F) for the minimum, mean, and maximum spread angles (Columns G, H, and I, respectively); the f_{expt} and f_{calc} values that are plotted in Figure C-10 are shown in Figure C-8. The diagonal line in the plot represents $f_{calc} = f_{expt}$. All values of f_{calc} lie above the line $f_{calc} = f_{expt}$, indicating that the drip shield flux splitting submodel overestimates the flow into breaches.

	F	G	H	I
Mean	0.1110	0.4139	0.3797	0.3977
Std. Dev.	0.1055	0.3048	0.1438	0.0958
Median	0.0486	0.2355	0.3233	0.3177
Minimum	0.0129	0.1173	0.2444	0.3177
Maximum	0.2748	1.0000	0.6799	0.5043

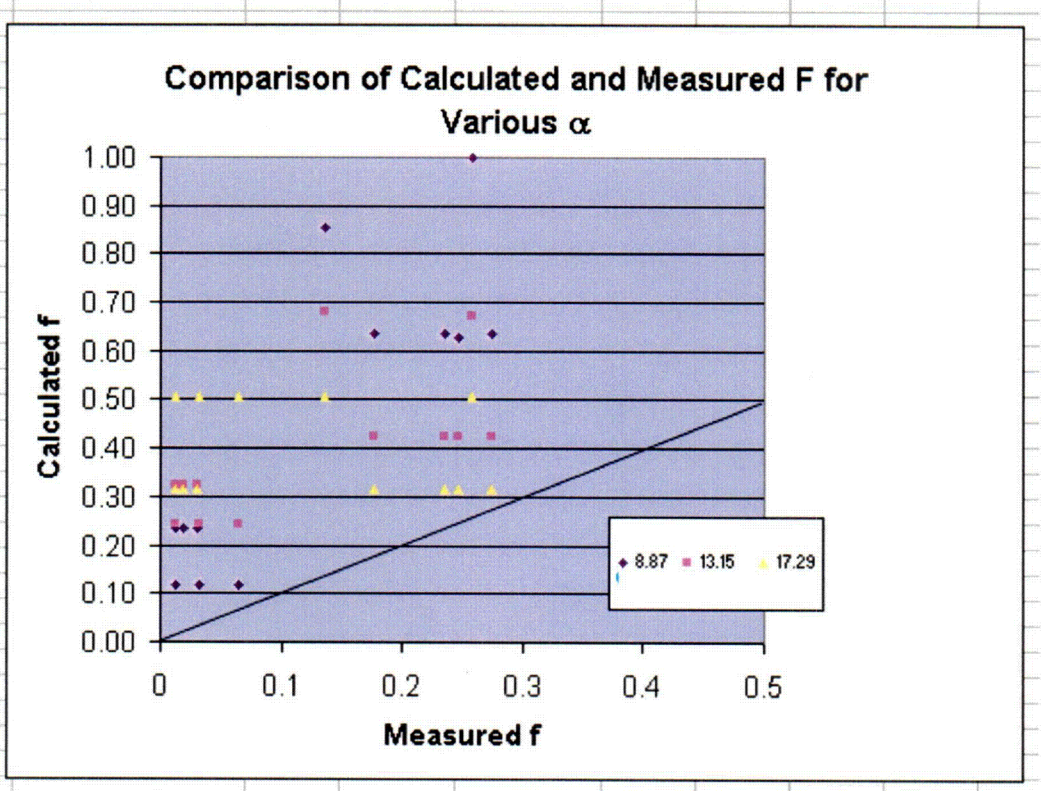

Summary / Spread angles / f calculations

Figure C-10. Spreadsheet "Flux Split Drip Shield Model," Worksheet "Summary;" Comparison of Calculated and Measured Breach Flow Fractions for Drip Shield Flux Splitting Submodel for Minimum (8.87°), Mean (13.15°), and Maximum (17.29°) Rivulet Spread Angles

APPENDIX D

MICROSOFT EXCEL SPREADSHEET "FLUX SPLIT WASTE PACKAGE MODEL"

MICROSOFT EXCEL SPREADSHEET "FLUX SPLIT WASTE PACKAGE MODEL"

SPREADSHEET "FLUX SPLIT WASTE PACKAGE MODEL"–WORKSHEET "F CALCULATIONS"

Breach Flow Fraction Calculation using Smooth Drip Shield Data, Off-Crown Tests

Single Patch Tests (DTN: MO0207EBSATBWP.023)

Source Data
Calculated results

The Model Case depends on whether the breach is wider (case 1) or narrower (case 2) than the spread at the breach. So the patch width is compared to x tan(α).

	Test Type	Test Date	Drip Location (Test Description)	Breach No.	Location of Drip Relative to DS Centerline (cm)	Location of Breach Relative to DS Centerline (cm)	y, Drip Location Relative to Breach Center (cm)	x, Vertical Distance from Drip to Top of Breach (cm)	l, Patch half-width (cm)	Drip Flux (g)	Flow into Breach (g)	f_{expt}	$x^*tan(\alpha)$
9	Q(splash)	5/17/2002	P5, 17.5 cm left of center, 33°	4			-17.5	50.5	13.5	89.77	0	0.0000	4.8659
10	Q(splash)	5/20/2002	P4, center, 33°	4			0.0	50.5	13.5	137.21	109.84	0.8005	4.8659
11	Q(splash)	5/20/2002	P4, 17.5 cm right of center, 33°	4			17.5	50.5	13.5	131.42	8.96	0.0682	4.8659
12	Q(splash)	5/21/2002	P4, 17.5 cm right of center, 16.5°	4			17.5	93.5	13.5	150.76	1.79	0.0119	9.0092
13	Q(splash)	5/21/2002	P4, centerline, 16.5°	4			0.0	93.5	13.5	139.9	84.35	0.6029	9.0092
14	Q(splash)	5/21/2002	P5, 17.5 cm left of center, 16.5°	5			-17.5	43	13.5	187.5	2.66	0.0142	4.1432
15	Q(splash)	5/21/2002	P6, 35.5 cm left of center, 16.5°	4			18.5	93.5	13.5	142.28	0.22	0.0015	9.0092
16	Q(splash)	5/22/2002	P5, centerline, 16.5°	5			0.0	43	13.5	124.74	90.56	0.7260	4.1432
17	Q(splash)	5/22/2002	P6, 36.5 cm left of center, between crown and 16.5°	4			17.5	115	13.5	129.27	6.63	0.0513	11.0808
18	Q(film)	5/31/2002	P4, 8 cm right of center, 16.5°	4			8.0	93.5	13.5	172.38	92.53	0.5368	9.0092
19	Q(film)	5/31/2002	P2, center, 16.5°	4			54.0	93.5	13.5	242.49	151.66	0.6254	9.0092
20	Q(film)	5/31/2002	P2, 15 cm right of center, 16.5°	5			-39.0	43	13.5	177.22	0.39	0.0022	4.1432
21	Q(film)	5/31/2002	P5, 4 cm left of center, 16.5°	5			-4.0	43	13.5	173.17	184.54	1.0657	4.1432
22	Q(film)	6/1/2002	P4, 8 cm right of center, 16.5°	4			8.0	93.5	13.5	137.44	107.38	0.7813	9.0092
23	Bounding	6/18/2002	54 cm left of DS center, 16.5°	4	-54	-54	0.0	93.5	13.5	353.43	169.77	0.4803	9.0092
24	Bounding	6/19/2002	54 cm left of DS center, 16.5°	4	-54	-54	0.0	93.5	13.5	107.01	84.55	0.7901	9.0092
25	Bounding	6/16/2002	27 cm left of DS center, 16.5°	5	-27	54	-81.0	43	13.5	121.76	0.58	0.0048	4.1432
26	Bounding	6/20/2002	27 cm left of DS center, 16.5°	5	-27	54	-81.0	43	13.5	370.41	1.15	0.0031	4.1432
27	Bounding	6/20/2002	27 cm right of DS center, 16.5°	5	27	54	-27.0	43	13.5	339.74	4.24	0.0125	4.1432
28	Bounding	6/20/2002	27 cm right of DS center, 16.5°	5	27	54	-27.0	43	13.5	95.41	0.78	0.0082	4.1432
29	Bounding	6/20/2002	27 cm left of DS center, 33°	4	-27	-54	27.0	50.5	13.5	367.11	0.96	0.0026	4.8659
30	Bounding	6/20/2002	27 cm right of DS center, 33°	4	27	-54	81.0	50.5	13.5	317.6	0.62	0.0020	4.8659
31	Bounding	6/20/2002	54 cm left of DS center, 33°	4	-54	-54	0.0	50.5	13.5	328.85	186.85	0.5682	4.8659
32	Bounding	6/21/2002	54 cm left of DS center, 33°	4	-54	-54	0.0	50.5	13.5	101.13	83.1	0.8217	4.8659
33	Bounding	6/24/2002	27 cm left of DS center, 33°	4	-27	-54	27.0	50.5	13.5	96.21	1.18	0.0123	4.8659
34	Bounding	6/24/2002	27 cm right of DS center, 33°	4	27	-54	81.0	50.5	13.5	95.75	0	0.0000	4.8659

Bounding Flow Rate Tests (DTN: MO0207EBSATBWP.025)

Summary / Spread angles / f calculations

DTN: MO0207EBSATBWP.023 [DIRS 163402]; DTN: MO0207EBSATBWP.025 [DIRS 163403].

Figure D-1. Spreadsheet "Flux Split Waste Package Model," Worksheet "f calculations;" Calculation of Experimental Breach Flow Fractions and Model Flow Fractions for Mean Minus One Standard Deviation Rivulet Spread Angle

The purpose of this spreadsheet is to develop the waste package flux splitting submodel using experimental data from the breached drip shield experiments. The data are analyzed to estimate an average and range of the rivulet spread angle, α. The disparity between measured fraction of dripping flux that enters a breach and the fraction calculated using the model (with the measured range of the rivulet spread angle) is then used to establish a range of uncertainty in the model. Whereas the drip shield submodel is based on data from on-crown drip locations, the waste package submodel uses off-crown drip data, for which the drip location is some distance away from the crown of the drip shield mockup.

All descriptions for this worksheet pertain to Rows 9-34. Equations in spreadsheet format are illustrated using Row 9.

Column B: Test type. The first three columns (B-D) help identify uniquely each test as described in the designated DTN.

Column C: Test date.

Column D: Drip location as indicated for each test in the designated DTN.

Column E: Breach or patch number most pertinent to this particular test, for which flow is analyzed in this row of the spreadsheet.

Column F: Drip location relative to drip shield center. Applies only to Bounding tests, further defining the drip location as specified in the DTN.

Column G: Breach location relative to drip shield center. Applies only to Bounding tests, further defining the breach location as specified in the DTN.

Column H: Drip location, y, relative to the center of the breach listed in Column E.

Column I: Vertical distance, x, from the drip location to the top of the breach.

Column J: Half-width, ℓ, of the breach–13.5 cm, same for all breaches.

Column K: Measured mass of water, F_1, dripped onto the drip shield during the test. For the on-crown drips, it is assumed that half of the water that dripped onto the drip shield, $F_1/2$, flowed down the side that contained the breach. For these off-crown tests, the full dripping flux is assumed to flow down the side where the drip is located.

Column L: Measured mass of water, F_2, that flowed into the breach during the test.

Column M: Fraction of water dripped onto the drip shield that flowed into the breach:

$$f_{expt} = \frac{F_2}{F_1}.$$

M9=L9/K9

Columns N through AB perform calculations that result in f_{calc}, the fraction of dripping flux that is predicted by the model to flow into a breach.

Column N: $x \tan\alpha$, where x is from Column I, and α is the spread angle. For Columns N-AB, the value used for α is 5.5037° (Cell $Q$7), which is one standard deviation less than the mean measured spread angle for these tests (see Worksheet "Spread angles").

N9=$I9*TAN(RADIANS($Q$7))

Column O: Case number as described in Sections 6.5.1.1.2.1 and 6.5.1.1.2.2. For Case 1, $\ell > x \tan\alpha$; for Case 2, $\ell < x \tan\alpha$; x is from Column I, and the half-width of the breach, ℓ, is from Column J.

O9=IF($J9>N9,1,2)

Column P: Value of y_A (Point A) as described in Sections 6.5.1.1.2.1 and 6.5.1.1.2.2, corresponding to the leftmost point from which the edge of the fan from the rivulet can enter the left side of the breach:

$$y_A = -\ell - (x + 2\ell)\tan\alpha$$

P9=-$J9-($I9+2*$J9)*TAN(RADIANS($Q$7))

Column Q: Value of y_B (Point B) as described in Sections 6.5.1.1.2.1 and 6.5.1.1.2.2, corresponding to the leftmost point from which rivulets will enter the top edge of the breach. The value of y_B depends on the Model Case number (Column O):

$$y_B = -\ell + x\tan\alpha \qquad \text{Case 1.}$$
$$y_B = \ell - x\tan\alpha \qquad \text{Case 2.}$$

Q9=IF(O9=1,(-$J9+$I9*TAN(RADIANS($Q$7))),
($J9-$I9*TAN(RADIANS($Q$7))))

Column R: Value of y_C (Point C) as described in Sections 6.5.1.1.2.1 and 6.5.1.1.2.2, corresponding to the rightmost point from which rivulets will enter the top edge of the breach. The value of y_C depends on the Model Case number (Column O):

$$y_C = \ell - x\tan\alpha \qquad \text{Case 1.}$$
$$y_C = -\ell + x\tan\alpha \qquad \text{Case 2.}$$

R9=IF(O9=1,($J9-$I9*TAN(RADIANS($Q$7))),
(-$J9+$I9*TAN(RADIANS($Q$7)))),

Column S: Value of y_D (Point D) as described in Sections 6.5.1.1.2.1 and 6.5.1.1.2.2, corresponding to the rightmost point from which the edge of the fan from the rivulet can enter the right side of the breach:

$$y_D = \ell + (x + 2\ell)\tan\alpha$$

S9=$J9+($I9+2*$J9)*TAN(RADIANS($Q$7))

Column T: Determines which region (designated as Fraction Case #) along the drip shield relative to the center of the breach where the drip is located:

1. $y \le y_A$
2. $y_A < y \le -\ell$
3. $-\ell < y < y_B$
4. $y_B \le y \le y_C$
5. $y_C < y < \ell$
6. $\ell \le y < y_D$
7. $y \ge y_D$

T9=IF($H9<=P9,1,IF($H9<=-$J9,2,IF($H9<Q9,3,
IF($H9<=R9,4,IF($H9<$J9,5,IF($H9<S9,6,IF($H9>=S9,7)))))))

The spread angles are the mean, 1-sigma, and 1+sigma, calculated on the "Spread Anges" sheet

This cell performs a conditional test, comoparing y to Ya,Yb, Yc, Yd, and l to determine which case applies

This cell is the f value determined by the appropriate case of the 7 possible.

For α = 5.5037 degrees

These are the Y values calculated, given x, l, and α, for each measurement. Note that Yb and Yc are different depending on the Model Case #

These are the calculations that represent the 7 different **fraction** cases in the model. Some are constants (1 or 0)

	N	O	P	Q	R	S	T	U	V	W	X	Y	Z	AA	AB
8	x*tan(α)	Model Case #	Ya	Yb	Yc	Yd	Fraction Case #	f_{calc}	f1	f2	f3	f4	f5	f6	f7
9	4.8659	1	-20.9675	-8.6341	8.6341	20.9675	2	**0.2322**	0.0000	0.2322	0.0890	1.0000	3.6854	2.5757	0.0000
10	4.8659	1	-20.9675	-8.6341	8.6341	20.9675	4	**1.0000**	0.0000	1.4039	1.8872	1.0000	1.8872	1.4039	0.0000
11	4.8659	1	-20.9675	-8.6341	8.6341	20.9675	6	**0.2322**	0.0000	2.5757	3.6854	1.0000	0.0890	0.2322	0.0000
12	9.0092	1	-25.1107	-4.4908	4.4908	25.1107	6	**0.3277**	0.0000	1.8350	2.2205	1.0000	0.2780	0.3277	0.0000
13	9.0092	1	-25.1107	-4.4908	4.4908	25.1107	4	**1.0000**	0.0000	1.0814	1.2492	1.0000	1.2492	1.0814	0.0000
14	4.1432	1	-20.2448	-9.3568	9.3568	20.2448	2	**0.2035**	0.0000	0.2035	0.0173	1.0000	4.2410	2.7981	0.0000
15	9.0092	1	-25.1107	-4.4908	4.4908	25.1107	6	**0.2847**	0.0000	1.8780	2.2760	1.0000	0.2225	0.2847	0.0000
16	4.1432	1	-20.2448	-9.3568	9.3568	20.2448	4	**1.0000**	0.0000	1.5008	2.1292	1.0000	2.1292	1.5008	0.0000
17	11.0808	1	-27.1823	-2.4192	2.4192	27.1823	6	**0.3538**	0.0000	1.6328	1.8988	1.0000	0.3195	0.3538	0.0000
18	9.0092	1	-25.1107	-4.4908	4.4908	25.1107	5	**0.8052**	0.0000	1.4259	1.6932	1.0000	0.8052	0.7369	0.0000
19	9.0092	1	-25.1107	-4.4908	4.4908	25.1107	7	**0.0000**	0.0000	3.4068	4.2462	1.0000	-1.7477	-1.2441	0.0000
20	4.1432	1	-20.2448	-9.3568	9.3568	20.2448	1	**0.0000**	0.0000	-1.3903	-2.5773	1.0000	6.8356	4.3919	0.0000
21	4.1432	1	-20.2448	-9.3568	9.3568	20.2448	4	**1.0000**	0.0000	1.2042	1.6464	1.0000	2.6119	1.7973	0.0000
22	9.0092	1	-25.1107	-4.4908	4.4908	25.1107	5	**0.8052**	0.0000	1.4259	1.6932	1.0000	0.8052	0.7369	0.0000
23	9.0092	1	-25.1107	-4.4908	4.4908	25.1107	4	**1.0000**	0.0000	1.0814	1.2492	1.0000	1.2492	1.0814	0.0000
24	9.0092	1	-25.1107	-4.4908	4.4908	25.1107	4	**1.0000**	0.0000	1.0814	1.2492	1.0000	1.2492	1.0814	0.0000
25	4.1432	1	-20.2448	-9.3568	9.3568	20.2448	1	**0.0000**	0.0000	-4.5038	-7.6458	1.0000	11.9041	7.5054	0.0000
26	4.1432	1	-20.2448	-9.3568	9.3568	20.2448	1	**0.0000**	0.0000	-4.5038	-7.6458	1.0000	11.9041	7.5054	0.0000
27	4.1432	1	-20.2448	-9.3568	9.3568	20.2448	1	**0.0000**	0.0000	-0.5008	-1.1292	1.0000	5.3875	3.5023	0.0000
28	4.1432	1	-20.2448	-9.3568	9.3568	20.2448	1	**0.0000**	0.0000	-0.5008	-1.1292	1.0000	5.3875	3.5023	0.0000
29	4.8659	1	-20.9675	-8.6341	8.6341	20.9675	7	**0.0000**	0.0000	3.2118	4.6616	1.0000	-0.8872	-0.4039	0.0000
30	4.8659	1	-20.9675	-8.6341	8.6341	20.9675	7	**0.0000**	0.0000	6.8274	10.2104	1.0000	-6.4360	-4.0196	0.0000
31	4.8659	1	-20.9675	-8.6341	8.6341	20.9675	4	**1.0000**	0.0000	1.4039	1.8872	1.0000	1.8872	1.4039	0.0000
32	4.8659	1	-20.9675	-8.6341	8.6341	20.9675	4	**1.0000**	0.0000	1.4039	1.8872	1.0000	1.8872	1.4039	0.0000
33	4.8659	1	-20.9675	-8.6341	8.6341	20.9675	7	**0.0000**	0.0000	3.2118	4.6616	1.0000	-0.8872	-0.4039	0.0000
34	4.8659	1	-20.9675	-8.6341	8.6341	20.9675	7	**0.0000**	0.0000	6.8274	10.2104	1.0000	-6.4360	-4.0196	0.0000

Figure D-2. Spreadsheet "Flux Split Waste Package Model," Worksheet "f calculations;" Calculation of Model Flow Fractions for Mean Minus One Standard Deviation Rivulet Spread Angle

Columns V though AB compute the fraction of dripping flux f_{calc} that is predicted to flow into a breach, assuming the drip location is within each of seven regions listed above under Column T. Although f_{calc} is computed for all seven regions, it is valid in only one of the regions. The

correct valid region is determined in Column T (Fraction Case #), and the appropriate value from Columns V–AB is entered in Column U.

Column U: f_{calc} is the fraction of dripping flux onto the drip shield that is predicted by the drip shield flux splitting submodel, Equations 6.5.1.1.2-2 through 6.5.1.1.2-6 or 6.5.1.1.2-19 through 6.5.1.1.2-23, for Cases 1 and 2, respectively. f_{calc} is intended to be compared with f_{expt} (Column M). The value of f_{calc} is selected from Columns V through AB, depending on the appropriate Fraction Case # (Column T).

```
U9 =IF(T9=1,V9,IF(T9=2,W9,IF(T9=3,X9,IF(T9=4,Y9,
IF(T9=5,Z9,IF(T9=6,AA9,IF(T9=7,AB9)))))))
```

Column V: Value of f_{calc} in region 1 ($y \le y_A$), where $f_{calc} = 0$.

```
V9=0
```

Column W: Value of f_{calc} in region 2 ($y_A < y \le -\ell$):

$$f_{calc} = \frac{y + \ell + (x + 2\ell)\tan\alpha}{2(x + 2\ell)\tan\alpha}$$

```
W9 =(H9+J9+(I9+2*J9)*TAN(RADIANS($Q$7)))/
(2*(I9+2*J9)*TAN(RADIANS($Q$7)))
```

Column X: Value of f_{calc} in region 3 ($-\ell < y < y_B$):

$$f_{calc} = \frac{y + \ell + x\tan\alpha}{2x\tan\alpha}$$

```
X9=(H9+J9+I9*TAN(RADIANS($Q$7)))/(2*I9*TAN(RADIANS($Q$7)))
```

Column Y: Value of f_{calc} in region 4 ($y_B \le y \le y_C$):

$$f_{calc} = \frac{2\ell}{2x\tan\alpha}$$

```
Y9=IF(O9=1,1,(2*$J9/(2*$I9*TAN(RADIANS($Q$7)))))
```

Column Z: Value of f_{calc} in region 5 ($y_C < y < \ell$):

$$f_{calc} = \frac{-y + \ell + x\tan\alpha}{2x\tan\alpha}$$

```
Z9=(-H9+J9+I9*TAN(RADIANS($Q$7)))/(2*I9*TAN(RADIANS($Q$7)))
```

Column AA: Value of f_{calc} in region 6 ($\ell \le y < y_D$):

$$f_{calc} = \frac{-y + \ell + (x + 2\ell)\tan\alpha}{2(x + 2\ell)\tan\alpha}$$

AA9=(-H9+J9+I9*TAN(RADIANS($Q$7)))/
(2*I9*TAN(RADIANS(AA9$Q$7)))

Column AB: Value of f_{calc} in region 7 ($y \ge y_D$) where $f_{calc} = 0$:

AB9=0

	AC	AD	AE	AF	AG	AH	AI	AJ	AK	AL	AM	AN	AO	AP	AQ
1															
2															
3															
4															
5															
6															
7			For α =	13.7326	degrees										
8	x*tan(α)	Model Case #	Ya	Yb	Yc	Yd	Fraction Case #	f_{calc}	f1	f2	f3	f4	f5	f6	f7
9	12.3410	1	-32.4391	-1.1590	1.1590	32.4391	2	0.3944	0.0000	0.3944	0.3379	1.0000	1.7560	1.3184	0.0000
10	12.3410	1	-32.4391	-1.1590	1.1590	32.4391	4	1.0000	0.0000	0.8564	1.0470	1.0000	1.0470	0.8564	0.0000
11	12.3410	1	-32.4391	-1.1590	1.1590	32.4391	6	0.3944	0.0000	1.3184	1.7560	1.0000	0.3379	0.3944	0.0000
12	22.8491	2	-42.9473	-9.3491	9.3491	42.9473	6	0.4321	0.0000	1.0264	1.1784	0.5908	0.4125	0.4321	0.0000
13	22.8491	2	-42.9473	-9.3491	9.3491	42.9473	4	0.5908	0.0000	0.7292	0.7954	0.5908	0.7954	0.7292	0.0000
14	10.5082	1	-30.6063	-2.9918	2.9918	30.6063	2	0.3831	0.0000	0.3831	0.3097	1.0000	1.9750	1.4061	0.0000
15	22.8491	2	-42.9473	-9.3491	9.3491	42.9473	6	0.4151	0.0000	1.0433	1.2002	0.5908	0.3906	0.4151	0.0000
16	10.5082	1	-30.6063	-2.9918	2.9918	30.6063	4	1.0000	0.0000	0.8946	1.1424	1.0000	1.1424	0.8946	0.0000
17	28.1032	2	-48.2014	-14.6032	14.6032	48.2014	6	0.4424	0.0000	0.9467	1.0515	0.4804	0.4288	0.4424	0.0000
18	22.8491	2	-42.9473	-9.3491	9.3491	42.9473	4	0.5908	0.0000	0.8651	0.9705	0.5908	0.6204	0.5934	0.0000
19	22.8491	2	-42.9473	-9.3491	9.3491	42.9473	7	0.0000	0.0000	1.6461	1.9771	0.5908	-0.3862	-0.1877	0.0000
20	10.5082	1	-30.6063	-2.9918	2.9918	30.6063	1	0.0000	0.0000	-0.2453	-0.7133	1.0000	2.9981	2.0345	0.0000
21	10.5082	1	-30.6063	-2.9918	2.9918	30.6063	3	0.9520	0.0000	0.7777	0.9520	1.0000	1.3327	1.0115	0.0000
22	22.8491	2	-42.9473	-9.3491	9.3491	42.9473	4	0.5908	0.0000	0.8651	0.9705	0.5908	0.6204	0.5934	0.0000
23	22.8491	2	-42.9473	-9.3491	9.3491	42.9473	4	0.5908	0.0000	0.7292	0.7954	0.5908	0.7954	0.7292	0.0000
24	22.8491	2	-42.9473	-9.3491	9.3491	42.9473	4	0.5908	0.0000	0.7292	0.7954	0.5908	0.7954	0.7292	0.0000
25	10.5082	1	-30.6063	-2.9918	2.9918	30.6063	1	0.0000	0.0000	-1.4730	-2.7118	1.0000	4.9965	3.2621	0.0000
26	10.5082	1	-30.6063	-2.9918	2.9918	30.6063	1	0.0000	0.0000	-1.4730	-2.7118	1.0000	4.9965	3.2621	0.0000
27	10.5082	1	-30.6063	-2.9918	2.9918	30.6063	2	0.1054	0.0000	0.1054	-0.1424	1.0000	2.4271	1.6838	0.0000
28	10.5082	1	-30.6063	-2.9918	2.9918	30.6063	2	0.1054	0.0000	0.1054	-0.1424	1.0000	2.4271	1.6838	0.0000
29	12.3410	1	-32.4391	-1.1590	1.1590	32.4391	6	0.1436	0.0000	1.5692	2.1409	1.0000	-0.0470	0.1436	0.0000
30	12.3410	1	-32.4391	-1.1590	1.1590	32.4391	7	0.0000	0.0000	2.9948	4.3287	1.0000	-2.2348	-1.2820	0.0000
31	12.3410	1	-32.4391	-1.1590	1.1590	32.4391	4	1.0000	0.0000	0.8564	1.0470	1.0000	1.0470	0.8564	0.0000
32	12.3410	1	-32.4391	-1.1590	1.1590	32.4391	4	1.0000	0.0000	0.8564	1.0470	1.0000	1.0470	0.8564	0.0000
33	12.3410	1	-32.4391	-1.1590	1.1590	32.4391	6	0.1436	0.0000	1.5692	2.1409	1.0000	-0.0470	0.1436	0.0000
34	12.3410	1	-32.4391	-1.1590	1.1590	32.4391	7	0.0000	0.0000	2.9948	4.3287	1.0000	-2.2348	-1.2820	0.0000

Figure D-3. Spreadsheet "Flux Split Waste Package Model," Worksheet "f calculations;" Calculation of Model Flow Fractions for Mean Rivulet Spread Angle

Columns AC though AQ repeat the calculations done in Columns N though AB using the mean rivulet spread angle of $\alpha = 13.7326°$ (Cell $AF$7). For Row 9, the spreadsheet equations are as follows:

AC9=$I9*TAN(RADIANS($AF$7))

```
AD9=IF($J9>AC9,1,2)

AE9=-$J9-($I9+2*$J9)*TAN(RADIANS($AF$7))

AF9=IF(AD9=1,(-$J9+$I9*TAN(RADIANS($AF$7))),($J9-$I9*TAN(RADIANS($AF$7))))

AG9=IF(AD9=1,($J9-$I9*TAN(RADIANS($AF$7))),(-$J9+$I9*TAN(RADIANS($AF$7))))

AH9=$J9+($I9+2*$J9)*TAN(RADIANS($AF$7))

AI9=IF($H9<=AE9,1,IF($H9<=-$J9,2,IF($H9<AF9,3,
      IF($H9<=AG9,4,IF($H9<$J9,5,IF($H9<AH9,6,IF($H9>=AH9,7)))))))

AJ9=IF(AI9=1,AK9,IF(AI9=2,AL9,IF(AI9=3,AM9,IF(AI9=4,AN9,IF(AI9=5,AO9,IF(AI9=6,A
      P9,IF(AI9=7,AQ9)))))))

AK9=0

AL9=(H9+J9+(I9+2*J9)*TAN(RADIANS($AF$7)))/
      (2*(I9+2*J9)*TAN(RADIANS($AF$7)))

AM9=(H9+J9+I9*TAN(RADIANS($AF$7)))/(2*I9*TAN(RADIANS($AF$7)))

AN9=IF(AD9=1,1,(2*$J9/(2*$I9*TAN(RADIANS($AF$7)))))

AO9=(-H9+J9+I9*TAN(RADIANS($AF$7)))/(2*I9*TAN(RADIANS($AF$7)))

AP9=(-H9+J9+(I9+2*J9)*TAN(RADIANS($AF$7)))/
      (2*(I9+2*J9)*TAN(RADIANS($AF$7)))

AQ9=0
```

Columns AR though BF (next page) repeat the calculations done in Columns N though AB using a rivulet spread angle of $\alpha = 21.9614°$ (Cell $AU$7), which is one standard deviation greater than the mean rivulet spread angle. For Row 9, the spreadsheet equations are as follows:

```
AR9=$I9*TAN(RADIANS($AU$7))

AS9=IF($J9>AR9,1,2)

AT9=-$J9-($I9+2*$J9)*TAN(RADIANS($AU$7))

AU9=IF(AS9=1,(-$J9+$I9*TAN(RADIANS($AU$7))),($J9-$I9*TAN(RADIANS($AU$7))))

AV9=IF(AS9=1,(-$J9+$I9*TAN(AV9RADIANS($AU$7))),($J9-
      $I9*TAN(RADIANS($AU$7))))

AW9=$J9+($I9+2*$J9)*TAN(RADIANS($AU$7))

AX9=IF($H9<=AT9,1,IF($H9<=-$J9,2,IF($H9<AU9,3,IF($H9<=AV9,4,
      IF($H9<$J9,5,IF($H9<AW9,6,IF($H9>=AW9,7)))))))

AY9=IF(AX9=1,AZ9,IF(AX9=2,BA9,IF(AX9=3,BB9,IF(AX9=4,BC9,IF(AX9=5,BD9,IF
      (AX9=6,BE9,IF(AX9=7,BF9)))))))

AZ9=0
```

BA9=(H9+J9+(I9+2*J9)*TAN(RADIANS($AU$7)))/
(2*(I9+2*J9)*TAN(RADIANS($AU$7)))

BB9=(H9+J9+I9*TAN(RADIANS($AU$7)))/(2*I9*TAN(RADIANS($AU$7)))

BC9=IF(AS9=1,1,(2*$J9/(2*$I9*TAN(RADIANS($AU$7)))))

BD9=(-H9+J9+I9*TAN(RADIANS($AU$7)))/(2*I9*TAN(RADIANS($AU$7)))

BE9=(-H9+J9+(I9+2*J9)*TAN(RADIANS($AU$7)))/
(2*(I9+2*J9)*TAN(RADIANS($AU$7)))

BF9=0

	AR	AS	AT	AU	AV	AW	AX	AY	AZ	BA	BB	BC	BD	BE	BF
1															
2															
3															
4															
5															
6															
7			For α =	21.9614	degrees										
8	x*tan(α)	Model Case #	Ya	Yb	Yc	Yd	Fraction Case #	f_{calc}	f1	f2	f3	f4	f5	f6	f7
9	20.3638	2	-44.7513	-6.8638	6.8638	44.7513	2	**0.4360**	0.0000	0.4360	0.4018	0.6629	1.2612	0.9960	0.0000
10	20.3638	2	-44.7513	-6.8638	6.8638	44.7513	4	**0.6629**	0.0000	0.7160	0.8315	0.6629	0.8315	0.7160	0.0000
11	20.3638	2	-44.7513	-6.8638	6.8638	44.7513	6	**0.4360**	0.0000	0.9960	1.2612	0.6629	0.4018	0.4360	0.0000
12	37.7032	2	-62.0907	-24.2032	24.2032	62.0907	4	**0.3581**	0.0000	0.8190	0.9111	0.3581	0.4470	0.4588	0.0000
13	37.7032	2	-62.0907	-24.2032	24.2032	62.0907	4	**0.3581**	0.0000	0.6389	0.6790	0.3581	0.6790	0.6389	0.0000
14	17.3394	2	-41.7270	-3.8394	3.8394	41.7270	2	**0.4291**	0.0000	0.4291	0.3847	0.7786	1.3939	1.0491	0.0000
15	37.7032	2	-62.0907	-24.2032	24.2032	62.0907	4	**0.3581**	0.0000	0.8293	0.9244	0.3581	0.4337	0.4485	0.0000
16	17.3394	2	-41.7270	-3.8394	3.8394	41.7270	4	**0.7786**	0.0000	0.7391	0.8893	0.7786	0.8893	0.7391	0.0000
17	46.3729	2	-70.7605	-32.8729	32.8729	70.7605	4	**0.2911**	0.0000	0.7707	0.8342	0.2911	0.4569	0.4651	0.0000
18	37.7032	2	-62.0907	-24.2032	24.2032	62.0907	4	**0.3581**	0.0000	0.7212	0.7851	0.3581	0.5729	0.5566	0.0000
19	37.7032	2	-62.0907	-24.2032	24.2032	62.0907	6	**0.0833**	0.0000	1.1946	1.3951	0.3581	-0.0371	0.0833	0.0000
20	17.3394	2	-41.7270	-3.8394	3.8394	41.7270	2	**0.0483**	0.0000	0.0483	-0.2353	0.7786	2.0139	1.4300	0.0000
21	17.3394	2	-41.7270	-3.8394	3.8394	41.7270	3	**0.7739**	0.0000	0.6683	0.7739	0.7786	1.0046	0.8100	0.0000
22	37.7032	2	-62.0907	-24.2032	24.2032	62.0907	4	**0.3581**	0.0000	0.7212	0.7851	0.3581	0.5729	0.5566	0.0000
23	37.7032	2	-62.0907	-24.2032	24.2032	62.0907	4	**0.3581**	0.0000	0.6389	0.6790	0.3581	0.6790	0.6389	0.0000
24	37.7032	2	-62.0907	-24.2032	24.2032	62.0907	4	**0.3581**	0.0000	0.6389	0.6790	0.3581	0.6790	0.6389	0.0000
25	17.3394	2	-41.7270	-3.8394	3.8394	41.7270	1	**0.0000**	0.0000	-0.6957	-1.4464	0.7786	3.2250	2.1739	0.0000
26	17.3394	2	-41.7270	-3.8394	3.8394	41.7270	1	**0.0000**	0.0000	-0.6957	-1.4464	0.7786	3.2250	2.1739	0.0000
27	17.3394	2	-41.7270	-3.8394	3.8394	41.7270	2	**0.2609**	0.0000	0.2609	0.1107	0.7786	1.6679	1.2174	0.0000
28	17.3394	2	-41.7270	-3.8394	3.8394	41.7270	2	**0.2609**	0.0000	0.2609	0.1107	0.7786	1.6679	1.2174	0.0000
29	20.3638	2	-44.7513	-6.8638	6.8638	44.7513	6	**0.2840**	0.0000	1.1480	1.4944	0.6629	0.1685	0.2840	0.0000
30	20.3638	2	-44.7513	-6.8638	6.8638	44.7513	7	**0.0000**	0.0000	2.0119	2.8203	0.6629	-1.1574	-0.5800	0.0000
31	20.3638	2	-44.7513	-6.8638	6.8638	44.7513	4	**0.6629**	0.0000	0.7160	0.8315	0.6629	0.8315	0.7160	0.0000
32	20.3638	2	-44.7513	-6.8638	6.8638	44.7513	4	**0.6629**	0.0000	0.7160	0.8315	0.6629	0.8315	0.7160	0.0000
33	20.3638	2	-44.7513	-6.8638	6.8638	44.7513	6	**0.2840**	0.0000	1.1480	1.4944	0.6629	0.1685	0.2840	0.0000
34	20.3638	2	-44.7513	-6.8638	6.8638	44.7513	7	**0.0000**	0.0000	2.0119	2.8203	0.6629	-1.1574	-0.5800	0.0000

Figure D-4. Spreadsheet "Flux Split Waste Package Model," Worksheet "f calculations;" Calculation of Model Flow Fractions for Mean Plus One Standard Deviation Rivulet Spread Angle

SPREADSHEET "FLUX SPLIT WASTE PACKAGE MODEL"–WORKSHEET "SPREAD ANGLES"

	A	B	C	D	E	F	G	H	I	J	K
1		Rivulet spread measurements for WP model: Drips at 16.5° and 33°, measurements at 33° and transition Smooth Drip Shield)									
2											
3					Source Data						
4					Calculated results						
5											
6					Rivulet Spread Measurements						
7					At 33°			At Transition			
8		Q(film) (DTN: MO0207EBSATBWP.023)		Drop Location	x (distance from drop, cm)	Right (cm)	Left (cm)	x (distance from drop, cm)	Right (cm)	Left (cm)	
9		5/31/2002	P4, 8 cm right of center, 16.5°	16.5°	43	5.5	3.5	107.0	13.5		
10		5/31/2002	P2, center, 16.5°	16.5°	43	7.5	4.5	107.0	19.5	22.0	
11		5/31/2002	P2, 15 cm right of center, 16.5°	16.5°	43	11.5	9.0	107.0	18.0	15.0	
12		5/31/2002	P5, 4 cm left of center, 16.5°	16.5°	43	8.5	8.5	107.0			
13											
14		Bounding (DTN: MO0207EBSATBWP.025)									
15		6/18/2002	54 cm left of DS center, 16.5°	16.5°	43	31.0	46.0	107.0	35.0	46.0	
16		6/19/2002	54 cm left of DS center, 16.5°	16.5°	43	8.5	10.0	107.0	19.0	27.0	
17		6/16/2002	27 cm left of DS center, 16.5°	16.5°	43	6.0	8.0	107.0	17.0	16.0	
18		6/20/2002	27 cm left of DS center, 16.5°	16.5°	43	18.0	24.0	107.0	22.0	19.0	
19		6/20/2002	27 cm right of DS center, 16.5°	16.5°	43	13.0	27.0	107.0	14.0	23.0	
20		6/20/2002	27 cm right of DS center, 16.5°	16.5°	43	12.0	17.0	107.0	16.0	19.0	
21		6/20/2002	27 cm left of DS center, 33°	33°				64.0	11.0	17.0	
22		6/20/2002	27 cm right of DS center, 33°	33°				64.0	15.0	17.0	
23		6/20/2002	54 cm left of DS center, 33°	33°				64.0	17.0	17.0	
24		6/24/2002	27 cm left of DS center, 33°	33°				64.0	9.0	9.5	
25		6/24/2002	27 cm right of DS center, 33°	33°				64.0	8.5	10.0	
26											

DTN: MO0207EBSATBWP.023 [DIRS 163402]; DTN: MO0207EBSATBWP.025 [DIRS 163403].

Figure D-5. Spreadsheet "Flux Split Waste Package Model," Worksheet "Spread angles;" Calculation of Rivulet Spread Angle

In this worksheet, the mean and range of the rivulet spread angle α is determined from spread measurements. The drip locations are off-crown, at the 16.5° and 33° positions on the drip shield mockup. These angles are the angular distances from the crown about the center of curvature of the drip shield; thus, the crown is at 0°, and the transition from the curved top surface to the vertical side of the drip shield is located about 60° from vertical. The actual distance (arc length) from the crown to the 16.5° line is 43 cm; from the crown to the 33° line the distance is 86 cm; and from the crown to the transition line the distance is 150 cm. The distance x from the drip location to the spread measurement location (the 33° line or the transition line) is shown in Columns E and H, respectively.

Columns B and C identify the pertinent tests as described in the designated DTNs. In each test, the spread of rivulets to the right and to the left of the drip location was measured. The spread distance measured at the 33° line is listed in Columns F and G. The spread distance measured at the transition line is listed in Columns I and J. For drips at the 33° location, no rivulet spread was measured, although splattering upslope may have resulted in some rivulets appearing at the drip location.

The sketch below from the scientific notebook for the experiments (Howard 2002 [DIRS 161516], p. 14) indicates the dimensions and locations of breaches on the drip shield mockup used in the tests. This sketch is also shown in Figure 4.1-1, Section 4.1.1.

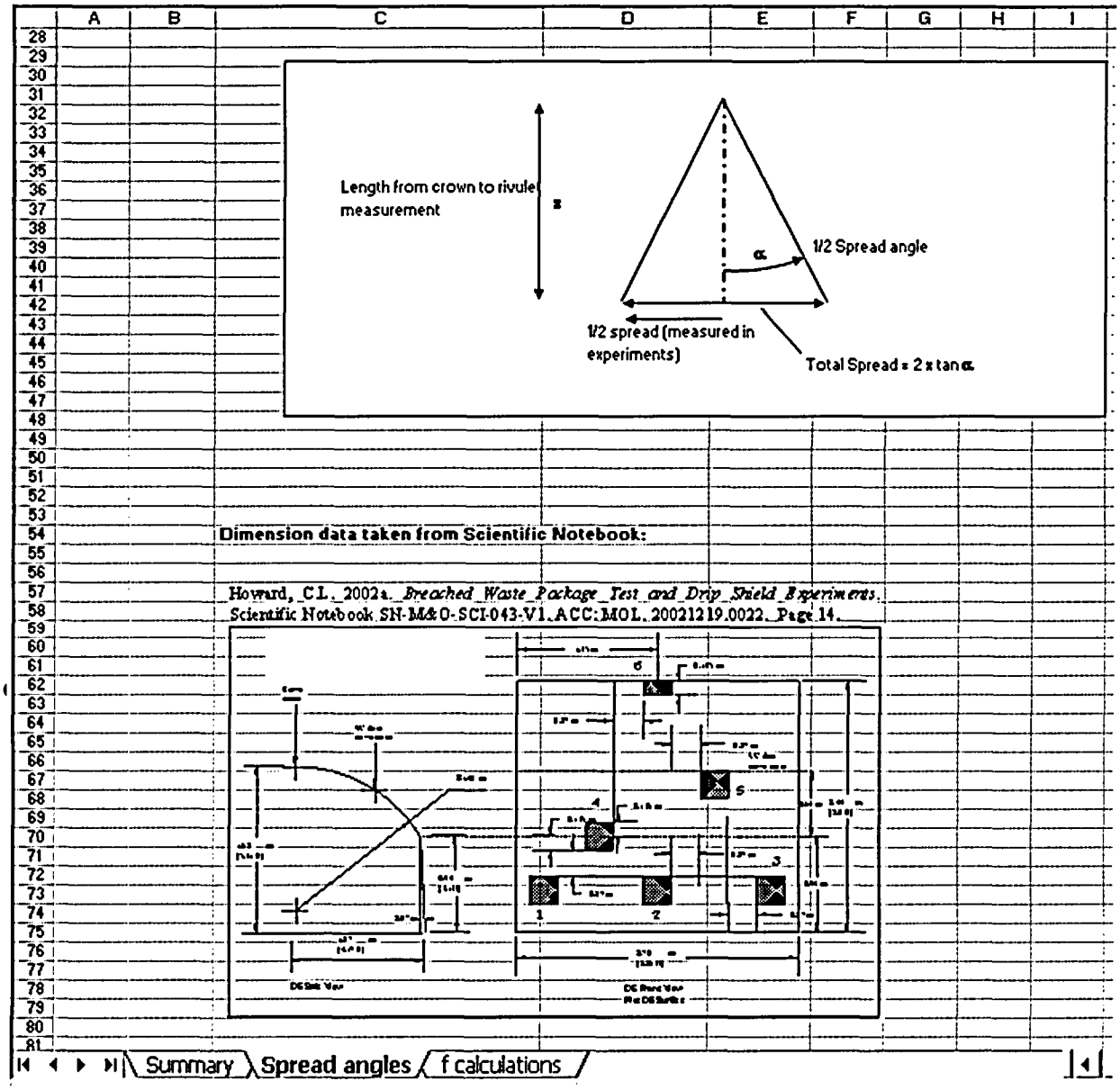

Source: Howard 2002 [DIRS 161516], p. 14.

Figure D-6. Spreadsheet "Flux Split Waste Package Model," Worksheet "Spread angles;" Dimensions and Locations of Breaches in Drip Shield Mockup Used in Breached Drip Shield Experiments

	L	M	N	O	P	Q	R	S	T	U
1										
2										
3										
4										
5										
6										
7										
8		**Measurement (cm)**	**x (distance from drop to measure ment.**	**Spread angle (degrees)**						
9		5.5	43	7.2890						
10		7.5	43	9.8939						
11		11.5	43	14.9729						
12		8.5	43	11.1818						
13		3.5	43	4.6534						
14		4.5	43	5.9743						
15		9.0	43	11.8215						
16		8.5	43	11.1818		**Drip at 16.5°.**			**All Measurements**	
17		31.0	43	35.7890		Spread Angle			Spread Angle	
18		8.5	43	11.1818		No. of mea	20		No. of meas.	47
19		6.0	43	7.9435		Mean	17.0218		Mean	13.7326
20		18.0	43	22.7144		Std. Dev.	11.17224		Std. Dev.	8.228837
21		13.0	43	16.8214					Mean - 1σ	5.5037
22		12.0	43	15.5928					Mean +1σ	21.9614
23		46.0	43	46.9306						
24		10.0	43	13.0919						
25		8.0	43	10.5392						
26		24.0	43	29.1676						
27		27.0	43	32.1250						
28		17.0	43	21.5713						
29										

Figure D-7. Spreadsheet "Flux Split Waste Package Model," Worksheet "Spread angles;" Calculation of Rivulet Spread Angles and Statistical Measures

In Column M, Rows 9–28 (Figure D-7), all of the spread measurements (right and left) at the 33° line are listed for the 16.5° drip location from the Q(film) and Bounding tests. In Rows 31-47 (Figure D-7), the spread from 16.5° drips measured at the transition are listed for the Q(film) and Bounding tests. In Rows 50–59, the spread from 33° drips measured at the transition are listed for the Bounding tests. In Column N, the distance, x, from the drip location to the measurement location is listed. In Column O, the spread angle, α, is computed from the rivulet spread, w_r (cm):

$$\alpha = \tan^{-1}\left(\frac{w_r}{x}\right),$$

The spreadsheet equation for Row 9 is:

O9=DEGREES(ATAN(M9/N9))

In Column R (Figures D-7 and D-8), the mean spread angle and standard deviation are shown for comparison for three groups of data–drip location at 16.5° measured at 33°, drip location at 16.5° measured at the transition line, and drip location at 33° measured at the transition line. The statistics for all measurements are computed in Column U. The mean rivulet spread angle (Cell U19) and the bounds on the range for spread angle as defined by the mean minus one standard deviation (Cell U21) and the mean minus one standard deviation (Cell U22) are used in Worksheet "f calculations" as the basis of the waste package flux splitting submodel to compute the predicted fraction of dripping flux that flows into a breach, f_{calc}.

	L	M	N	O	P	Q	R	S	T	U
29										
30										
31		13.5	107	7.1909						
32		19.5	107	10.3284						
33		18.0	107	9.5491						
34		22.0	107	11.6185						
35		15.0	107	7.9801						
36		35.0	107	18.1131						
37		19.0	107	10.0691		**Drip at 16.5°.**				
38		17.0	107	9.0276		Spread Angle				
39		22.0	107	11.6185		No. of mea	17			
40		14.0	107	7.4543		Mean	11.1561			
41		16.0	107	8.5046		Std. Dev.	4.110299			
42		46.0	107	23.2632						
43		27.0	107	14.1622						
44		16.0	107	8.5046						
45		19.0	107	10.0691						
46		23.0	107	12.1313						
47		19.0	107	10.0691						
48										
49										
50		11.0	64	9.7524						
51		15.0	64	13.1906						
52		17.0	64	14.8757		**Drip at 33°.**				
53		9.0	64	8.0047		Spread Angle				
54		8.5	64	7.5653		No. of mea	10			
55		17.0	64	14.8757		Mean	11.5340			
56		17.0	64	14.8757		Std. Dev.	3.255512			
57		17.0	64	14.8757						
58		9.5	64	8.4432						
59		10.0	64	8.8807						

Figure D-8. Spreadsheet "Flux Split Waste Package Model," Worksheet "Spread angles;" Calculation of Rivulet Spread Angles

SPREADSHEET "FLUX SPLIT WASTE PACKAGE MODEL"–WORKSHEET "SUMMARY"

	A	B	C	D	E	F	G	H	I	J	K
1											
2											
3											
4		**Waste Package Model: Comparison of Measured and Modeled Fraction of Drip Seepage Flowing into a Breach**									
5											
6		This spreadsheet compares results from the "Atlas Breached Waste Package and Drip Shield Experiments: Breached Drip Shield Tests" (documented in TDR-EBS-MD-000025-00 REV 00) with the model developed in the "EBS Radionuclide Transport Abstraction" (ANL-WIS-PA-0000001 REV 02). Test data are taken directly from the TDMS for this comparison.									
7											
8		Methodology:									
9		1. Spreading angles are calculated from the test data in the sheet titled ***Spread angles***									
10		2. Given spread angle and test geometry, seepage fractions are calculated for both the test data and the model in the worksheet ***f calculations***:									
11			a. Geometric data for each measurement (x,y,l) and the spread angle are used to determine which of 7 cases the measurement corresponds to								
12			b. For each test result the appropriate case model is applied to calculate the seepage flow fraction f								
13		3. The seepage fractions calculated from both the test and model are listed and compared in the two tables listed below in this ***Summary*** worksheet									
14		Notes:									
15		Source data DTNs are noted where source data is used									
16		Model equations are provided on the calculational sheets									
17		Data in tables below is linked directly to the calculational worksheets									
18											
19											

Source: BSC 2003 [DIRS 163406].

Figure D-9. Spreadsheet "Flux Split Waste Package Model," Worksheet "Summary;" Summary of Waste Package Flux Splitting Submodel

This worksheet, beginning with Figure D-9, summarizes the calculations in Worksheets "Spread angles" and "f calculations."

In the first table (Figure D-10), "Measured Breach Flow Fractions and Calculated Breach Flow Fractions," Columns B, C, D, and E are identical to Columns D, E, H, and I described earlier for Worksheet "f calculations." Column F (f_{expt}) is identical to Column M in Worksheet "f calculations." Columns G–I summarize the calculated fraction of the dripping flux that the flux splitting submodel predicts should flow into the breach, for the minimum, mean, and maximum spread angles. The minimum spread angle is specified to be one standard deviation less than the mean of the measured spread angles. The maximum spread angle is specified to be one standard deviation greater than the mean of the measured spread angles. Column G is identical to Column U of Worksheet "f calculations." Column H is identical to Column AJ of Worksheet "f calculations." Column I is identical to Column AY of Worksheet "f calculations."

Rows 50–54, Columns F–I, show the results of Microsoft Excel functions "AVERAGE," "STDEVA," "MEDIAN," "MIN," and "MAX," respectively, as applied to Rows 25-49.

	A	B	C	D	E	F	G	H	I
19									
20		*Measured Breach Flow Fractions and Calculated Breach Flow Fractions*							
21									
22				y, Drip Location Relative to Breach Center (cm)	x, Vertical Distance from Drip to Top of Breach (cm)		f_{calc}		
23							α (deg)	α (deg)	α (deg)
24		Drip Location (Test Description)	Breach No.			f_{expt}	5.50	13.73	21.96
25		P5, 17.5 cm left of center, 33°	4	-17.5	50.5	0.0000	0.2322	0.3944	0.4360
26		P4, center, 33°	4	0	50.5	0.8005	1.0000	1.0000	0.6629
27		P4, 17.5 cm right of center, 33°	4	17.5	50.5	0.0682	0.2322	0.3944	0.4360
28		P4, 17.5 cm right of center, 16.5°	4	17.5	93.5	0.0119	0.3277	0.4321	0.3581
29		P4, centerline, 16.5°	4	0	93.5	0.6029	1.0000	0.5908	0.3581
30		P5, 17.5 cm left of center, 16.5°	5	-17.5	43.0	0.0142	0.2035	0.3831	0.4291
31		P6, 35.5 cm left of center, 16.5°	4	18.5	93.5	0.0015	0.2847	0.4151	0.3581
32		P5, centerline, 16.5°	5	0	43.0	0.7260	1.0000	1.0000	0.7786
33		P6, 36.5 cm left of center, between crown and 16.5°	4	17.5	115.0	0.0513	0.3538	0.4424	0.2911
34		P4, 8 cm right of center, 16.5°	4	8	93.5	0.5368	0.8052	0.5908	0.3581
35		P2, 15 cm right of center, 16.5°	5	-39	43.0	0.0022	0.0000	0.0000	0.0483
36		P5, 4 cm left of center, 16.5°	5	-4	43.0	1.0657	1.0000	0.9520	0.7739
37		P4, 8 cm right of center, 16.5°	4	8	93.5	0.7813	0.8052	0.5908	0.3581
38		54 cm left of DS center, 16.5°	4	0	93.5	0.4803	1.0000	0.5908	0.3581
39		54 cm left of DS center, 16.5°	4	0	93.5	0.7901	1.0000	0.5908	0.3581
40		27 cm left of DS center, 16.5°	5	-81	43.0	0.0048	0.0000	0.0000	0.0000
41		27 cm left of DS center, 16.5°	5	-81	43.0	0.0031	0.0000	0.0000	0.0000
42		27 cm right of DS center, 16.5°	5	-27	43.0	0.0125	0.0000	0.1054	0.2609
43		27 cm right of DS center, 16.5°	5	-27	43.0	0.0082	0.0000	0.1054	0.2609
44		27 cm left of DS center, 33°	4	27	50.5	0.0026	0.0000	0.1436	0.2840
45		27 cm right of DS center, 33°	4	81	50.5	0.0020	0.0000	0.0000	0.0000
46		54 cm left of DS center, 33°	4	0	50.5	0.5682	1.0000	1.0000	0.6629
47		54 cm left of DS center, 33°	4	0	50.5	0.8217	1.0000	1.0000	0.6629
48		27 cm left of DS center, 33°	4	27	50.5	0.0123	0.0000	0.1436	0.2840
49		27 cm right of DS center, 33°	4	81	50.5	0.0000	0.0000	0.0000	0.0000
50		Mean				0.2947	0.4498	0.4346	0.3511
51		Std Dev.				0.3683	0.4426	0.3539	0.2316
52		Median				0.0142	0.2847	0.4151	0.3581
53		Minimum				0.0000	0.0000	0.0000	0.0000
54		Maximum				1.0657	1.0000	1.0000	0.7786
55									

Summary / Spread angles / f calculations

Figure D-10. Spreadsheet "Flux Split Waste Package Model," Worksheet "Summary;" Summary of Waste Package Flux Splitting Submodel

In the second table (Figure D-11), "Comparison of Measured and Calculated Breach Flows," Column K is again the drip location. Column L is the fraction of dripping flux (f_{expt}) that flowed into a breach as measured experimentally; this is identical to Column F of the preceding table, or Column M in Worksheet "f calculations." The next three columns (M-O) show the difference between the predicted breach flow fraction, f_{calc}, and the measured fraction, f_{expt}, for the minimum, mean, and maximum rivulet spread angle. Columns P-R show the ratio f_{calc} / f_{expt} for the minimum, mean, and maximum rivulet spread angle.

Rows 50-54, Columns L-R, show the results of Microsoft Excel functions "AVERAGE," "STDEVA," "MEDIAN," "MIN," and "MAX," respectively, as applied to Rows 25-49.

	J	K	L	M	N	O	P	Q	R
19									
20		*Comparison of Measured and Calculated Breach Flow*							
21									
22				*f calc - f meas*			*f calc / f meas*		
23				α (deg)	α (deg)	α (deg)	α (deg)	α (deg)	α (deg)
24		Drip Location (Test Description)	*f meas*	5.50	13.73	21.96	5.50	13.73	21.96
25		P5, 17.5 cm left of center, 33°	0.0000	0.2322	0.3944	0.4360			
26		P4, center, 33°	0.8005	0.1995	0.1995	-0.1376	1.2492	1.2492	0.8281
27		P4, 17.5 cm right of center, 33°	0.0682	0.1640	0.3262	0.3678	3.4054	5.7848	6.3950
28		P4, 17.5 cm right of center, 16.5°	0.0119	0.3159	0.4202	0.3462	27.6039	36.3914	30.1570
29		P4, centerline, 16.5°	0.6029	0.3971	-0.0121	-0.2449	1.6586	0.9799	0.5939
30		P5, 17.5 cm left of center, 16.5°	0.0142	0.1893	0.3689	0.4150	14.3428	27.0031	30.2499
31		P6, 35.5 cm left of center, 16.5°	0.0015	0.2831	0.4136	0.3565	184.1115	268.4581	231.5671
32		P5, centerline, 16.5°	0.7260	0.2740	0.2740	0.0526	1.3774	1.3774	1.0724
33		P6, 36.5 cm left of center, between crown and 16.5°	0.0513	0.3025	0.3911	0.2398	6.8988	8.6251	5.6761
34		P4, 8 cm right of center, 16.5°	0.5368	0.2685	0.0541	-0.1787	1.5001	1.1007	0.6671
35		P2, 15 cm right of center, 16.5°	0.0022	-0.0022	-0.0022	0.0461	0.0000	0.0000	21.9501
36		P5, 4 cm left of center, 16.5°	1.0657	-0.0657	-0.1136	-0.2917	0.9384	0.8934	0.7263
37		P4, 8 cm right of center, 16.5°	0.7813	0.0240	-0.1905	-0.4232	1.0307	0.7562	0.4583
38		54 cm left of DS center, 16.5°	0.4803	0.5197	0.1105	-0.1223	2.0818	1.2300	0.7454
39		54 cm left of DS center, 16.5°	0.7901	0.2099	-0.1993	-0.4321	1.2656	0.7478	0.4532
40		27 cm left of DS center, 16.5°	0.0048	-0.0048	-0.0048	-0.0048	0.0000	0.0000	0.0000
41		27 cm left of DS center, 16.5°	0.0031	-0.0031	-0.0031	-0.0031	0.0000	0.0000	0.0000
42		27 cm right of DS center, 16.5°	0.0125	-0.0125	0.0929	0.2484	0.0000	8.4461	20.9026
43		27 cm right of DS center, 16.5°	0.0082	-0.0082	0.0972	0.2527	0.0000	12.8936	31.9094
44		27 cm left of DS center, 33°	0.0026	-0.0026	0.1410	0.2814	0.0000	54.9116	108.6068
45		27 cm right of DS center, 33°	0.0020	-0.0020	-0.0020	-0.0020	0.0000	0.0000	0.0000
46		54 cm left of DS center, 33°	0.5682	0.4318	0.4318	0.0948	1.7600	1.7600	1.1668
47		54 cm left of DS center, 33°	0.8217	0.1783	0.1783	-0.1588	1.2170	1.2170	0.8068
48		27 cm left of DS center, 33°	0.0123	-0.0123	0.1313	0.2717	0.0000	11.7079	23.1564
49		27 cm right of DS center, 33°	0.0000	0.0000	0.0000	0.0000			
50		Mean	0.2947	0.1551	0.1399	0.0564	10.8887	19.3710	22.5256
51		Std. Dev.	0.3683	0.1670	0.1938	0.2596	38.2681	56.0050	51.4010
52		Median	0.0142	0.1783	0.1105	0.0461	1.2492	1.2492	1.0724
53		Minimum	0.0000	-0.0657	-0.1993	-0.4321	0.0000	0.0000	0.0000
54		Maximum	1.0657	0.5197	0.4318	0.4360	184.1115	268.4581	231.5671
55									

Summary / Spread angles / f calculations

Figure D-11. Spreadsheet "Flux Split Waste Package Model," Worksheet "Summary;" Summary of Waste Package Flux Splitting Submodel Comparing Measured and Calculated Breach Flows

Lastly, a plot in Worksheet "Summary" (Figure D-12) compares the calculated f_{calc} with the measured f_{expt} for the minimum, mean, and maximum spread angles; the f_{expt} and f_{calc} values that are plotted in Figure D-12 are shown in Figure D-10. The diagonal line in the plot represents $f_{calc} = f_{expt}$. Most values of f_{calc} lie above the line $f_{calc} = f_{expt}$, indicating that the waste package flux splitting submodel tends to overestimate the flow into breaches.

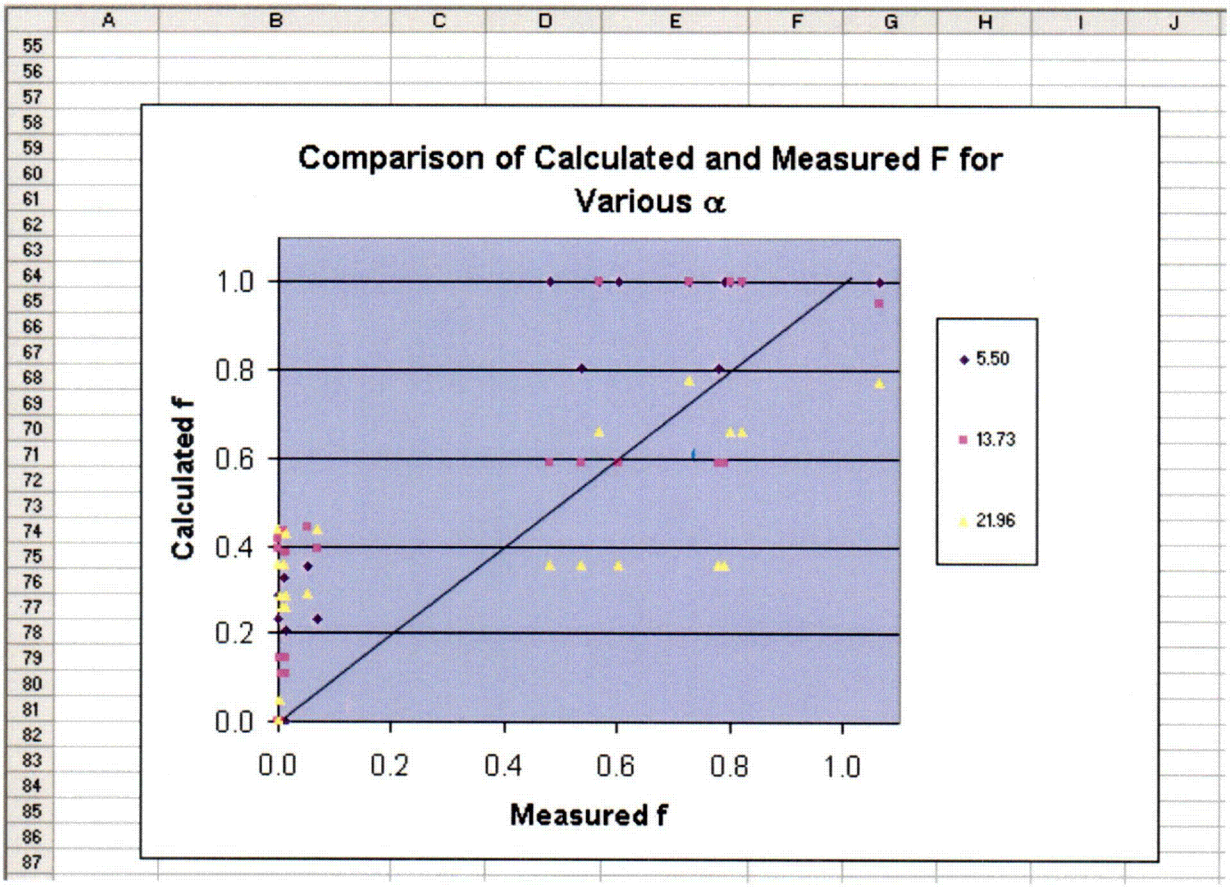

Figure D-12. Spreadsheet "Flux Waste Package Shield Model," Worksheet "Summary;" Comparison of Calculated and Measured Breach Flow Fractions for Waste Package Flux Splitting Submodel for Minimum (5.50°), Mean (13.73°), and Maximum (21.96°) Rivulet Spread Angles

APPENDIX E

MICROSOFT EXCEL SPREADSHEET "FLUX SPLITTING VALIDATION"

MICROSOFT EXCEL SPREADSHEET "FLUX SPLITTING VALIDATION"

SPREADSHEET "FLUX SPLITTING VALIDATION"–WORKSHEET "SPLASH RAD VS NUMBER"

Correlation of Splash Radius and Number of Drips

	Left	Right	No. of Drips	Inner (I) Fringe or Outer (O) Cluster
6	2	2	10	I
7	15	25.5	10	O
8	5	4	21	I
9	15	42.5	21	O
10	18	22	60	I
11	72.5	75.5	60	O
12	35	48	143	I
13	54	82.5	143	O
14	35	48	203	I
15	79.5	106.5	203	O
16	3.5	4	21	I
17	37.5	7	21	O
18	10.5	19	82	I
19	63	32	82	O
20	31.5	30	149	I
21	45	40	207	I
22	7.5	9	30	I
23	19	17.5	82	I
24	28	27.5	137	I
25	29	28	205	I
26	605.5	670.5		
27	30.275	33.525	31.9	
28	22.9085568	27.92493462	25.26429527	
29	28.5	27.75		

Mean	31.9
Std. Dev.	25.2643
Median	28

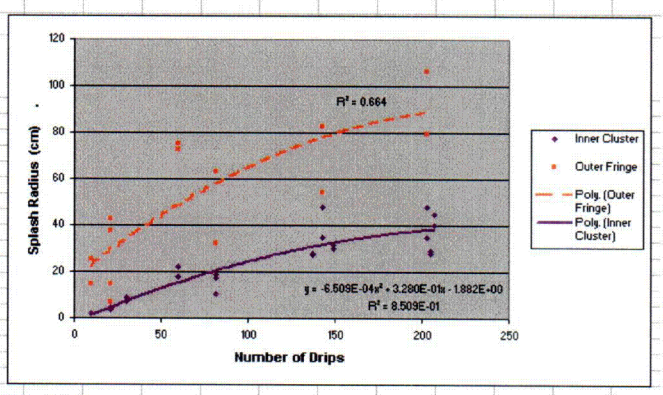

Data for this plot organized in bottom table (same data as table to the left, but organized for plotting by Inner Cluster (I) or Outer Fringe (O)

Figure E-1. Spreadsheet "Flux Splitting Validation"–Worksheet "Splash Rad vs Number;" Effect of Number of Drips on Splash Radius

In this worksheet (Figures E-1 to E-3), the effect of the number of drips on the splash radius is analyzed using data from dripping on the crown in the rough drip shield tests. This analysis is used for validation of the drip shield flux splitting submodel. The splash distance or radius (cm) to the left and to the right of the drip location are listed in Columns A and B, respectively. The number of drips in each test is given in Column C. The type of measurement–inner cluster (I) or outer fringe (O)–is indicated in Column D. These data and the DTN from which they were obtained (MO0207EBSATBWP.021 [DIRS 163399]) are also presented in Table 7.1-1. In Row 26, the sum of the splash radii is shown. Rows 27, 28, and 29 give the mean, standard deviation, and median for each column. The mean, standard deviation, and median for all 40 splash radius measurements are listed in Column G, Rows 11, 12, and 13, respectively.

The plot to the right in Figure E-1, which is reproduced as Figure 7.1-1, shows the dependence of splash radius on the number of drips. As indicated beneath the figure, the data are the same as in the table, but organized by type of measurement further down in this worksheet. The Trendline tool in Microsoft Excel is used to fit a quadratic curve to the inner cluster and outer fringe data. The correlation coefficient is shown for each curve, and the correlation equation is shown for the inner cluster curve. A second degree polynomial was chosen for the Trendline in order to display the expected behavior–the splash radius should increase with the number of drips, but eventually reach a maximum. A functional form such as $y = y_{\max}\left(1 - e^{-ax}\right)$ may be more appropriate, but because this is nonlinear in the fitting parameter a, a simple linear least squares fit using Trendline is not possible. Since the object is simply to demonstrate a correlation, a more accurate fit to the data is not necessary.

In Figure E-2, the experimental data from the top of the worksheet are reorganized by type of measurement and, in Figure E-3, all left and right measurements are consolidated for plotting in the plot at the top of the worksheet (shown in Figure E-1).

	A	B	C	D
25	29	28	205	I
26	605.5	670.5		
27	30.275	33.525	31.9	
28	22.9085568	27.92493462	25.26429527	
29	28.5	27.75		
30	*Inner Cluster Data Only (from table at top of sheet)*			
31	**Left**	**Right**	**No. of Drips**	**Inner (I) Fringe or Outer (O) Cluster**
32	2	2	10	I
33	5	4	21	I
34	18	22	60	I
35	35	48	143	I
36	35	48	203	I
37	3.5	4	21	I
38	10.5	19	82	I
39	31.5	30	149	I
40	45	40	207	I
41	7.5	9	30	I
42	19	17.5	82	I
43	28	27.5	137	I
44	29	28	205	I
45				
46				
47	*Outer Cluster Data Only (from table at top of sheet)*			
48	**Left**	**Right**	**No. of Drips**	**Inner Fringe (I) or Outer (O) Cluster**
49	15	25.5	10	O
50	15	42.5	21	O
51	72.5	75.5	60	O
52	54	82.5	143	O
53	79.5	106.5	203	O
54	37.5	7	21	O

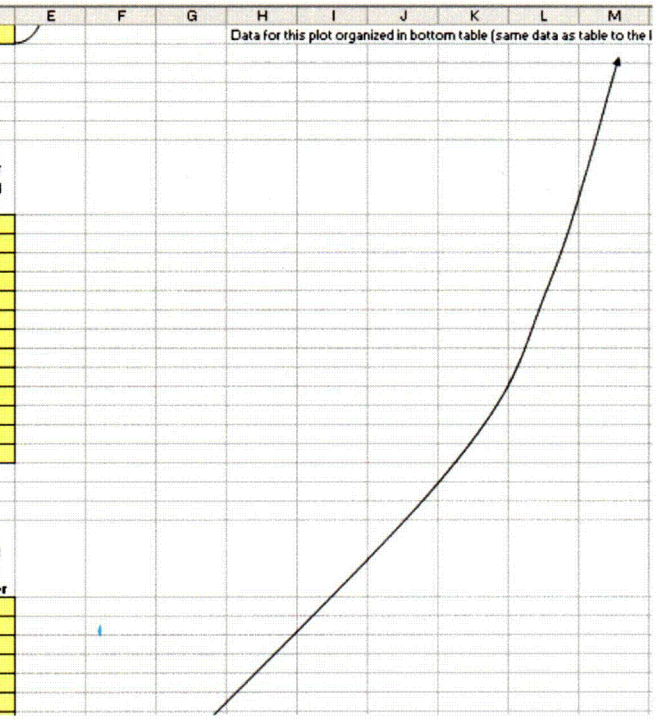

Figure E-2. Spreadsheet "Flux Splitting Validation"–Worksheet "Splash Rad vs Number;" Effect of Number of Drips on Splash Radius; Data Organized by Type of Measurement

Reordered List for Plotting (data from table at top of sheet)

Inner Cluster		Outer Fringe	
# of Drips	Radius cm	# of Drips	Radius cm
10	2	10	15
21	5	21	15
60	18	60	72.5
143	35	143	54
203	35	203	79.5
21	3.5	21	37.5
82	10.5	82	63
149	31.5	10	25.5
207	45	21	42.5
30	7.5	60	75.5
82	19	143	82.5
137	28	203	106.5
205	29	21	7
10	2	82	32
21	4		
60	22		
143	48		
203	48		
21	4		
82	19		
149	30		
207	40		
30	9		
82	17.5		
137	27.5		
205	28		

Figure E-3. Spreadsheet "Flux Splitting Validation"–Worksheet "Splash Rad vs Number;" Effect of Number of Drips on Splash Radius; All Left and Right Measurements Are Consolidated

SPREADSHEET "FLUX SPLITTING VALIDATION"–WORKSHEET "SPLASH RADIUS"

For validation of the drip shield and waste package flux splitting submodels, splash radius data are analyzed for measurements on the rough drip shield surface, with dripping on the crown and at off-crown locations. Data for crown drip locations are used for the drip shield submodel validation, and off-crown drip locations are used for the waste package submodel validation. The statistics (mean, standard deviation, median, mean plus one standard deviation, and mean minus one standard deviation) are shown in Column I, Rows 19–23 for crown drip locations, and in Rows 37-41 for off-crown locations. The data actually used in the model validation are the minimum and maximum values for more than 20 drips, Cells H11 and I9, respectively, for crown locations, and Cells H31 and I36, respectively, for off-crown locations.

Splash Radius Determination, Rough Drip Shield Surface, Dripping on Crown

Source Data
Calculated results

	# Drips	Left (cm)	Right (cm)
Splash Radius Test #1 - Rough DS Surface - Crown	10	2.0	2.0
	21	5.0	4.0
	60	18.0	22.0
	143	35.0	48.0
	203	35.0	48.0
Splash Radius Test #2 - Rough DS Surface - Crown	21	3.5	4.0
	82	10.5	19.0
	149	31.5	30.0
	207	45.0	40.0
Splash Radius Test #3 - Rough DS Surface - Crown	30	7.5	9.0
	82	19.0	17.5
	137	28.0	27.5
	205	29.0	28.0
		Mean	21.8
		Std. Dev.	14.8228
		Median	20.5
		Mean-SD	7.023354
		Mean+SD	36.66895

Splash Radius Determination, Rough Drip Shield Surface, Dripping off Crown

Source Data
Calculated results

	# Drips	Left (cm)	Right (cm)
Splash Radius Test #4 - Rough DS Surface - 33 degrees	31	3	3.5
	82	5.5	6
	158	6.5	6.5
Splash Radius Test #5 - Rough DS Surface - 16.5 degrees	22	9	10
	82	13	14.5
	156	14	15
		Mean	8.875
		Std. Dev.	4.349112
		Median	7.75
		Mean-SD	4.525888
		Mean+SD	13.22411

DTN: MO0207EBSATBWP.021

Splash Rad vs Number | Splash Radius | Rough DS | Rough off crown WP model

DTN: MO0207EBSATBWP.021 [DIRS 163399].

Figure E-4. Spreadsheet "Flux Splitting Validation"–Worksheet "Splash Radius;" Splash Radius Determination

SPREADSHEET "FLUX SPLITTING VALIDATION"–WORKSHEET "ROUGH DS"

This worksheet provides calculations for validation of the drip shield flux splitting submodel based on data from rough drip shield surface tests. An overall view of the worksheet is shown in Figure E-5 to show the layout of the worksheet, and individual tables are then presented more legibly and described in detail on following pages.

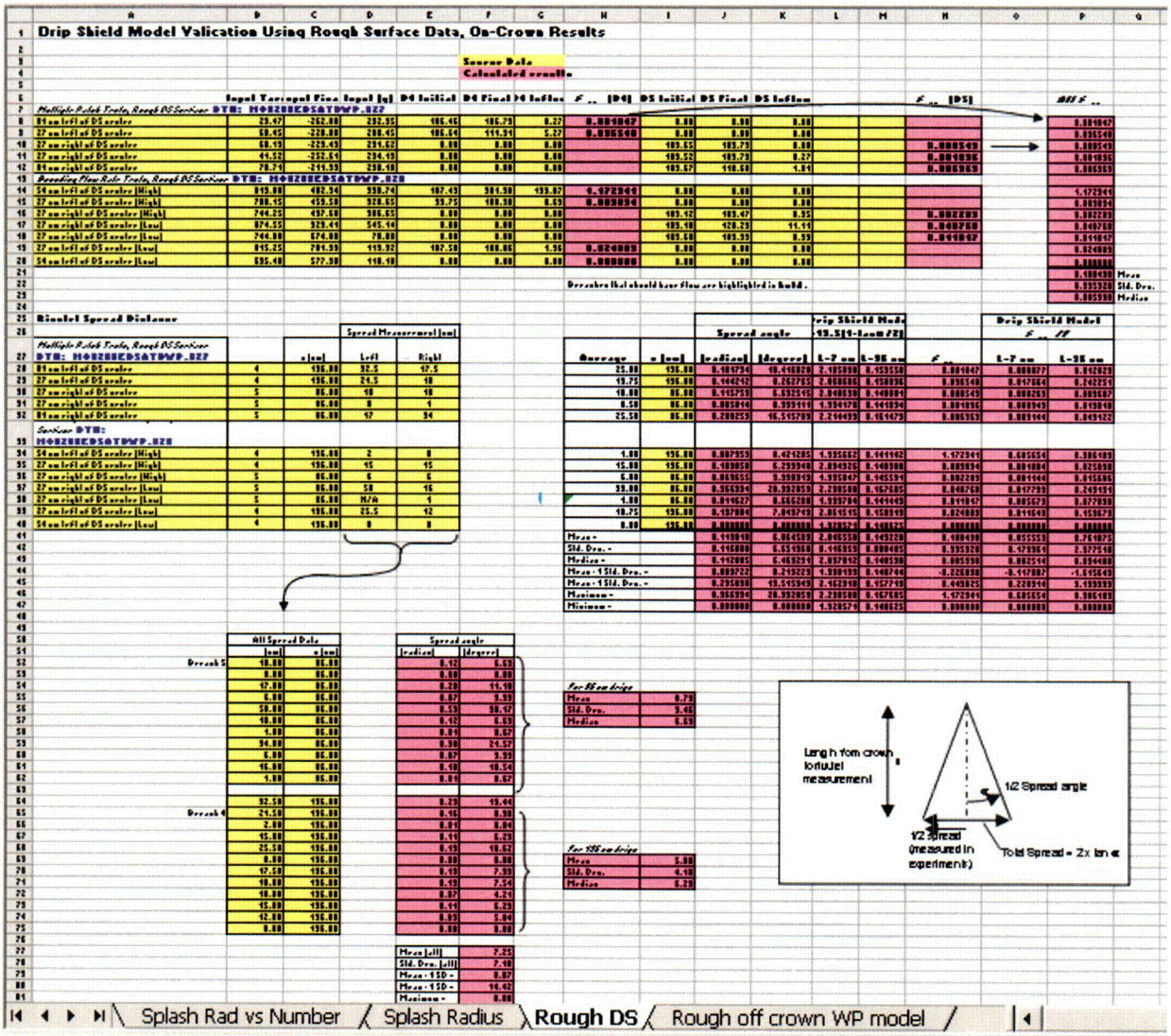

DTN: MO0208EBSATBWP.027 [DIRS 163404]; DTN: MO0208EBSATBWP.028 [DIRS 163405].

Figure E-5. Spreadsheet "Flux Splitting Validation"–Worksheet "Rough DS;" Worksheet Overview

	A	B	C	D	E	F	G	H
1	**Drip Shield Model Valication Using Rough Surface Data, On-Crown Results**							
2								
3						**Source Data**		
4						**Calculated results**		
5								
6		**Input Tare**	**Input Final**	**Input (g)**	**B4 Initial**	**B4 Final**	**B4 Inflow**	f_{expt} **(B4)**
7	*Multiple Patch Tests, Rough DS Surface* **DTN: MO0208EBSATBWP.027**							
8	81 cm left of DS center	29.47	-262.88	292.35	106.46	106.73	0.27	**0.001847**
9	27 cm left of DS center	68.45	-220.00	288.45	106.64	111.91	5.27	**0.036540**
10	27 cm right of DS center	68.19	-223.43	291.62	0.00	0.00	0.00	
11	27 cm right of DS center	41.52	-252.61	294.13	0.00	0.00	0.00	
12	81 cm right of DS center	78.71	-211.39	290.10	0.00	0.00	0.00	
13	*Bounding Flow Rate Tests, Rough DS Surface* **DTN: MO0208EBSATBWP.028**							
14	54 cm left of DS center (High)	813.08	482.34	330.74	107.43	301.30	193.87	**1.172341**
15	27 cm left of DS center (High)	788.15	459.50	328.65	99.75	100.38	0.63	**0.003834**
16	27 cm right of DS center (High)	744.25	437.60	306.65	0.00	0.00	0.00	
17	27 cm right of DS center (Low)	874.55	329.41	545.14	0.00	0.00	0.00	
18	27 cm right of DS center (Low)	744.80	674.00	70.80	0.00	0.00	0.00	
19	27 cm left of DS center (Low)	815.25	701.93	113.32	107.50	108.86	1.36	**0.024003**
20	54 cm left of DS center (Low)	695.48	577.38	118.10	0.00	0.00	0.00	**0.000000**
21								
22								Breaches that sho
23								

DTN: MO0208EBSATBWP.027 [DIRS 163404]; DTN: MO0208EBSATBWP.028 [DIRS 163405].

Figure E-6. Spreadsheet "Flux Splitting Validation"–Worksheet "Rough DS;" Calculation of Experimental Breach Flow Fractions

	H	I	J	K	L	M	N	O	P	Q
1										
2										
3										
4										
5										
6	f_{expt} **(B4)**	**B5 Initial**	**B5 Final**	**B5 Inflow**			f_{expt} **(B5)**		***All*** f_{expt}	
7										
8	**0.001847**	0.00	0.00	0.00					0.001847	
9	**0.036540**	0.00	0.00	0.00					0.036540	
10		109.65	109.73	0.08			**0.000549**	→	0.000549	
11		109.52	109.79	0.27			**0.001836**		0.001836	
12		109.67	110.68	1.01			**0.006963**		0.006963	
13										
14	**1.172341**	0.00	0.00	0.00					1.172341	
15	**0.003834**	0.00	0.00	0.00					0.003834	
16		109.12	109.47	0.35			**0.002283**		0.002283	
17		109.18	120.29	11.11			**0.040760**		0.040760	
18		109.60	109.99	0.39			**0.011017**		0.011017	
19	**0.024003**	0.00	0.00	0.00					0.024003	
20	**0.000000**	0.00	0.00	0.00					0.000000	
21									0.108498	Mean
22	Breaches that should have flow are highlighted in **bold**.								0.335328	Std. Dev.
23									0.005398	Median

Figure E-7. Spreadsheet "Flux Splitting Validation"–Worksheet "Rough DS;" Summary of Experimental Breach Flow Fractions

Tests are identified in Figure E-6 in Column A. Columns B and C are raw data–the initial and final water mass in the input water container. Column D is the difference between Columns B and C (e.g., D8=B8-C8), giving the mass of water dripped onto the drip shield. Columns E and F are the initial and final masses of water in the Breach B4 collection vessel. The difference, in Column G (e.g., G8=F8-E8), is the mass of water that flowed into B4. In Column H (Figure E-7), the fraction of the dripping flux that flowed into B4, f_{expt} (B4), is calculated for tests in which the flow into B4 was greater than zero (e.g., H8=2*G8/D8). Because the dripping was onto the crown, it is assumed that only half of the total input (i.e., D8/2) flowed down the side of the drip shield where B4 was located.

Columns I and J are the initial and final masses of water in the Breach B5 collection vessel. The difference, in Column G (e.g., K8=J8-I8), is the mass of water that flowed into B5. In Column N, the fraction of the dripping flux that flowed into B5, f_{expt} (B5), is calculated for tests in which the flow into B5 was greater than zero (e.g., N10=2*K10/D10). Because the drip location was the crown, it is assumed that only half of the total input (i.e., D10/2) flowed down the side of the drip shield where B5 was located.

The input water mass and flows into Breaches B4 and B5 are summarized in Table 7.1-3.

In Column P, all values of f_{expt} are consolidated. The mean, standard deviation, and median for the 12 data values are given in Rows 21, 22, and 23, respectively. The values of f_{expt} are listed in Table 7.1-4.

24									
25	**Rivulet Spread Distance**								
26				Spread Measurement (cm)				Spread angle	
27	*Multiple Patch Tests, Rough DS Surface* **DTN: MO0208EBSATBWP.027**		x (cm)	Left	Right	Average	x (cm)	(radian)	(degree)
28	81 cm left of DS center	4	136.00	32.5	17.5	25.00	136.00	0.181794	10.416028
29	27 cm left of DS center	4	136.00	21.5	18	19.75	136.00	0.144212	8.262765
30	27 cm right of DS center	5	86.00	10	10	10.00	86.00	0.115759	6.632515
31	27 cm right of DS center	5	86.00	0	1	0.50	86.00	0.005814	0.333111
32	81 cm right of DS center	5	86.00	17	34	25.50	86.00	0.288253	16.515703
33	*Bounding Flow Rate Tests, Rough DS Surface* **DTN: MO0208EBSATBWP.028**								
34	54 cm left of DS center (High)	4	136.00	2	0	1.00	136.00	0.007353	0.421285
35	27 cm left of DS center (High)	4	136.00	15	15	15.00	136.00	0.109850	6.293948
36	27 cm right of DS center (High)	5	86.00	6	6	6.00	86.00	0.069655	3.990913
37	27 cm right of DS center (Low)	5	86.00	50	16	33.00	86.00	0.366394	20.992853
38	27 cm right of DS center (Low)	5	86.00	N/A	1	1.00	86.00	0.011627	0.666200
39	27 cm left of DS center (Low)	4	136.00	25.5	12	18.75	136.00	0.137004	7.849749
40	54 cm left of DS center (Low)	4	136.00	0	0	0.00	136.00	0.000000	0.000000
41									
42						Mean =		0.119810	6.864589
43						Std. Dev. =		0.116088	6.651360
44						Median =		0.112805	6.463231
45						Mean - 1 Std. Dev. =		0.003722	0.213229
46						Mean + 1 Std. Dev. =		0.235898	13.515949
47						Maximum =		0.366394	20.992853
48						Minimum =		0.000000	0.000000
49									
50		All Spread Data			Spread angle				

DTN: MO0208EBSATBWP.027 [DIRS 163404]; DTN: MO0208EBSATBWP.028 [DIRS 163405].

Figure E-8. Spreadsheet "Flux Splitting Validation"–Worksheet "Rough DS;" Rivulet Spread Distances

Rivulet spread distances for each test are listed in Figure E-8, Columns D and E, Rows 28-40, for drips originating on the crown of the rough drip shield surface. The spread data are reorganized in Column B, starting in Row 52 (see Figure E-9). All spread data measured 86 cm from the drip

location are listed first, followed by all data measured 136 cm from the drip location. The corresponding x-distance is listed in Column C, starting in Row 52. In Column E, the spread distances, w_r, are converted to spread angles using the formula:

$$\alpha = \tan^{-1}\left(\frac{w_r}{x}\right).$$

In Cell E52, for example, the Microsoft Excel equation is: E52=ATAN(B52/C52). The result is the spread angle in radians, which is converted to degrees in Column F (e.g., F52=DEGREES(E52)). The mean spread angle for 86-cm drips is given in Cell I55 (I55=AVERAGE(F52:F63)) and for 136-cm drips in Cell I69 (I69=AVERAGE(F65:F75)). Statistics are computed for all individual spread angle data in Column F, Rows 77-82:

F77=AVERAGE(F52:F75)

F78=STDEVA(F52:F75)

F79=F77-F78

F80=F77+F78

F81=MIN(F52:F75)

F82=MAX(F52:F75)

As shown in F79 and F80, the range for the spread angle is zero (rounding down) to 14.4°.

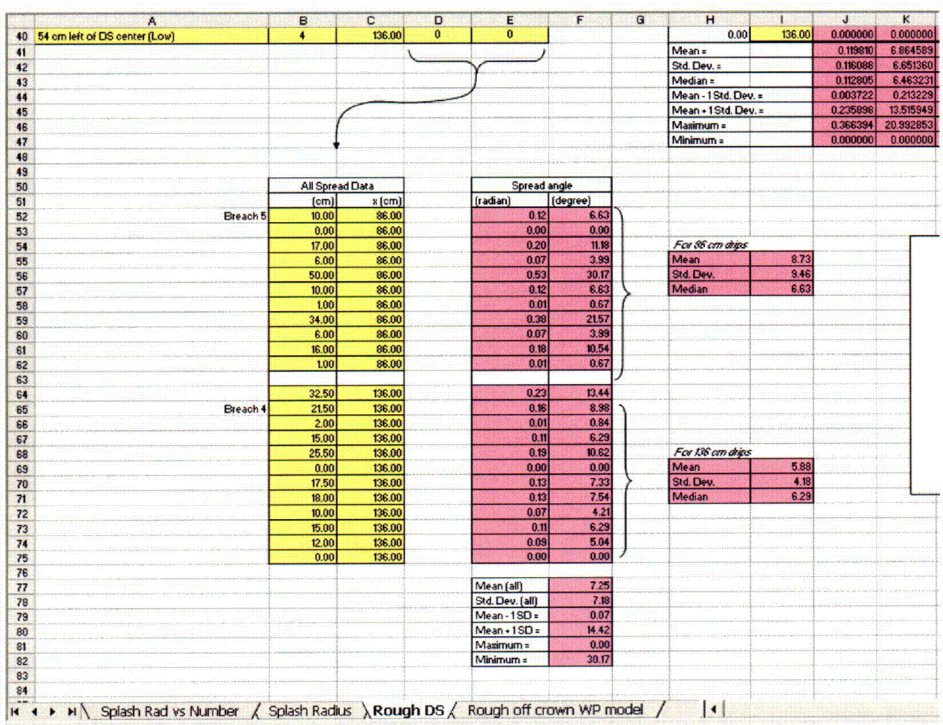

	A	B	C	D	E	F	G	H	I	J	K
40	54 cm left of DS center (Low)	4	136.00	0	0			0.00	136.00	0.000000	0.000000
41								Mean =		0.119810	6.864589
42								Std. Dev. =		0.116088	6.651360
43								Median =		0.112905	6.463231
44								Mean - 1 Std. Dev. =		0.003722	0.213229
45								Mean + 1 Std. Dev. =		0.235898	13.515949
46								Maximum =		0.366394	20.992853
47								Minimum =		0.000000	0.000000
48											
49											
50		All Spread Data			Spread angle						
51		(cm)	x (cm)		(radian)	(degree)					
52	Breach 5	10.00	86.00		0.12	6.63					
53		0.00	86.00		0.00	0.00					
54		17.00	86.00		0.20	11.18		For 86 cm drips			
55		6.00	86.00		0.07	3.99		Mean	8.73		
56		50.00	86.00		0.53	30.17		Std. Dev.	9.46		
57		10.00	86.00		0.12	6.63		Median	6.63		
58		1.00	86.00		0.01	0.67					
59		34.00	86.00		0.38	21.57					
60		6.00	86.00		0.07	3.99					
61		16.00	86.00		0.18	10.54					
62		1.00	86.00		0.01	0.67					
63											
64		32.50	136.00		0.23	13.44					
65	Breach 4	21.50	136.00		0.16	8.98					
66		2.00	136.00		0.01	0.84					
67		15.00	136.00		0.11	6.29					
68		25.50	136.00		0.19	10.62		For 136 cm drips			
69		0.00	136.00		0.00	0.00		Mean	5.88		
70		17.50	136.00		0.13	7.33		Std. Dev.	4.18		
71		18.00	136.00		0.13	7.54		Median	6.29		
72		10.00	136.00		0.07	4.21					
73		15.00	136.00		0.11	6.29					
74		12.00	136.00		0.09	5.04					
75		0.00	136.00		0.00	0.00					
76											
77					Mean (all)	7.25					
78					Std. Dev. (all)	7.18					
79					Mean - 1 SD =	0.07					
80					Mean + 1 SD =	14.42					
81					Maximum =	0.00					
82					Minimum =	30.17					
83											
84											

Splash Rad vs Number / Splash Radius / Rough DS / Rough off crown WP model

Figure E-9. Spreadsheet "Flux Splitting Validation"–Worksheet "Rough DS;" Rivulet Spread Data Reorganized

	G	H	I	J	K	L	M	N	O	P	Q
24											
25						Drip Shield Mode			Drip Shield Model		
26				Spread angle		F=13.5(1+tanα/2)/l			f_{crept} /F		
27		Average	z (cm)	(radian)	(degree)	L=7 cm	L=96 cm	f_{crept}	L=7 cm	L=96 cm	
28		25.00	136.00	0.181794	10.416028	2.105830	0.153550	0.001847	0.000877	0.012029	
29		19.75	136.00	0.144212	8.262765	2.068606	0.150836	0.036540	0.017664	0.242251	
30		10.00	86.00	0.115759	6.632515	2.040698	0.148801	0.000549	0.000269	0.003687	
31		0.50	86.00	0.005814	0.333111	1.934178	0.141034	0.001836	0.000949	0.013018	
32		25.50	86.00	0.288253	16.515703	2.214493	0.161473	0.006963	0.003144	0.043122	
33											
34		1.00	136.00	0.007353	0.421285	1.935662	0.141142	1.172341	0.605654	8.306109	
35		15.00	136.00	0.109850	6.293948	2.034926	0.148380	0.003834	0.001884	0.025838	
36		6.00	86.00	0.069655	3.990913	1.995847	0.145531	0.002283	0.001144	0.015686	
37		33.00	86.00	0.366394	20.992853	2.298588	0.167605	0.040760	0.017733	0.243191	
38		1.00	86.00	0.011627	0.666200	1.939784	0.141443	0.011017	0.005679	0.077890	
39		18.75	136.00	0.137004	7.849749	2.061515	0.150319	0.024003	0.011643	0.159679	
40		0.00	136.00	0.000000	0.000000	1.928571	0.140625	0.000000	0.000000	0.000000	
41		Mean =		0.119810	6.864589	2.046558	0.149228	0.108498	0.055553	0.761875	
42		Std. Dev. =		0.116088	6.651360	0.116359	0.008485	0.335328	0.173361	2.377518	
43		Median =		0.112805	6.463231	2.037812	0.148590	0.005398	0.002514	0.034480	
44		Mean - 1 Std. Dev. =		0.003722	0.213229	1.930199	0.140744	-0.226830	-0.117807	-1.615643	
45		Mean + 1 Std. Dev. =		0.235898	13.515949	2.162918	0.157713	0.443825	0.228914	3.139393	
46		Maximum =		0.366394	20.992853	2.298588	0.167605	1.172341	0.605654	8.306109	
47		Minimum =		0.000000	0.000000	1.928571	0.140625	0.000000	0.000000	0.000000	
48											
49											
50											
51											
52											
53											
54		*For 86 cm drips*									
55		Mean	8.73								
56		Std. Dev.	9.46								
57		Median	6.63								
58											
59											
60											
61											
62											
63											
64											
65											
66											
67											
68		*For 136 cm drips*									
69		Mean	5.88								
70		Std. Dev.	4.18								
71		Median	6.29								
72											
73											
74											

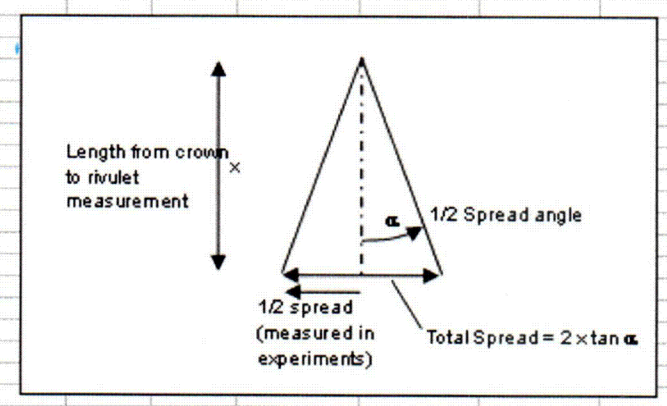

Splash Rad vs Number | Splash Radius | **Rough DS** | Rough off crown WP model

Figure E-10. Spreadsheet "Flux Splitting Validation"–Worksheet "Rough DS;" Calculation of Rivulet Spread Angles

In Column H, Rows 28-40 (see Figure E-10), the average rivulet spread is computed for each experiment (e.g., H28=(D28+E28)/2). Column I is the distance from the crown to the point where the rivulet spread was measured (identical to Column C). The spread angle is computed in Column J, Rows 28-40, (e.g., J28=ATAN(H28/I28)). In Column K, Rows 28-40, the

average spread angle in radians is converted to degrees (e.g., K28=DEGREES(J28)). In Worksheet "Splash Rad vs Number," the minimum splash radius for tests using 20 or more drips was 3.5 cm, for a total splash distance of 7 cm. This is used as the effective drip shield length in Column L, where f_{calc} is obtained using the formula

$$f_{calc} = \frac{\ell}{L}\left(1+\frac{\tan\alpha}{2}\right)$$
$$= \frac{13.5}{7}\left(1+\frac{\tan\alpha}{2}\right)$$

L28=13.5*(1+TAN(J28)/2)/7

The maximum splash radius tests using 20 or more drips was 48 cm in Worksheet "Splash Rad vs. Number," giving a total splash distance of 96 cm. This is used as the effective drip shield length in Column M:

$$f_{calc} = \frac{\ell}{L}\left(1+\frac{\tan\alpha}{2}\right)$$
$$= \frac{13.5}{96}\left(1+\frac{\tan\alpha}{2}\right)$$

M28=13.5*(1+TAN(J28)/2)/96

The values of f_{calc} in Columns L and M are similar to F/f_{VD} in Table 7.1-5, the only difference being the values used for spread angle. Table 7.1-5 uses the rounded values for spread angle obtained from Figure E-9, zero to 14.4°, whereas in Columns L and M in Figure E-10, f_{calc} is calculated from a different average spread angle.. As shown in the statistics (Rows 46–47), f_{calc} or F/f_{VD} ranges from 0.141 to 2.30, based on minimum and maximum average spread angles. Using the mean plus or minus one standard deviation for the spread angle, f_{calc} ranges from 0.141 to 2.16 (Rows 44-45, Columns L and M), close to the values reported in Table 7.1-5 (0.141 to 2.17).

In Column N, Rows 28–40, the values of f_{expt} are transferred from Column P, Rows 9–20. In Column O, the ratio f_{expt}/f_{calc} is computed (e.g., O28=N28/L28) for the minimum effective drip shield length of 7 cm. In Column P, the ratio f_{expt}/f_{calc} is computed (e.g., P28=N28/M28) for the maximum effective drip shield length of 96 cm. This ratio is identical to the uncertainty factor f_{VD} in Equation 7.1.1.1-2. As shown in the statistics (Rows 46–47), F/f_{VD} for the experimental data ranges from 0.0 to 8.306

SPREADSHEET "FLUX SPLITTING VALIDATION"–WORKSHEET "ROUGH OFF CROWN WP MODEL"

This worksheet provides calculations for validation of the waste package flux splitting submodel based on data from the rough drip shield surface tests. An overall view of the worksheet is shown in Figure E-11, and individual tables are then described in detail.

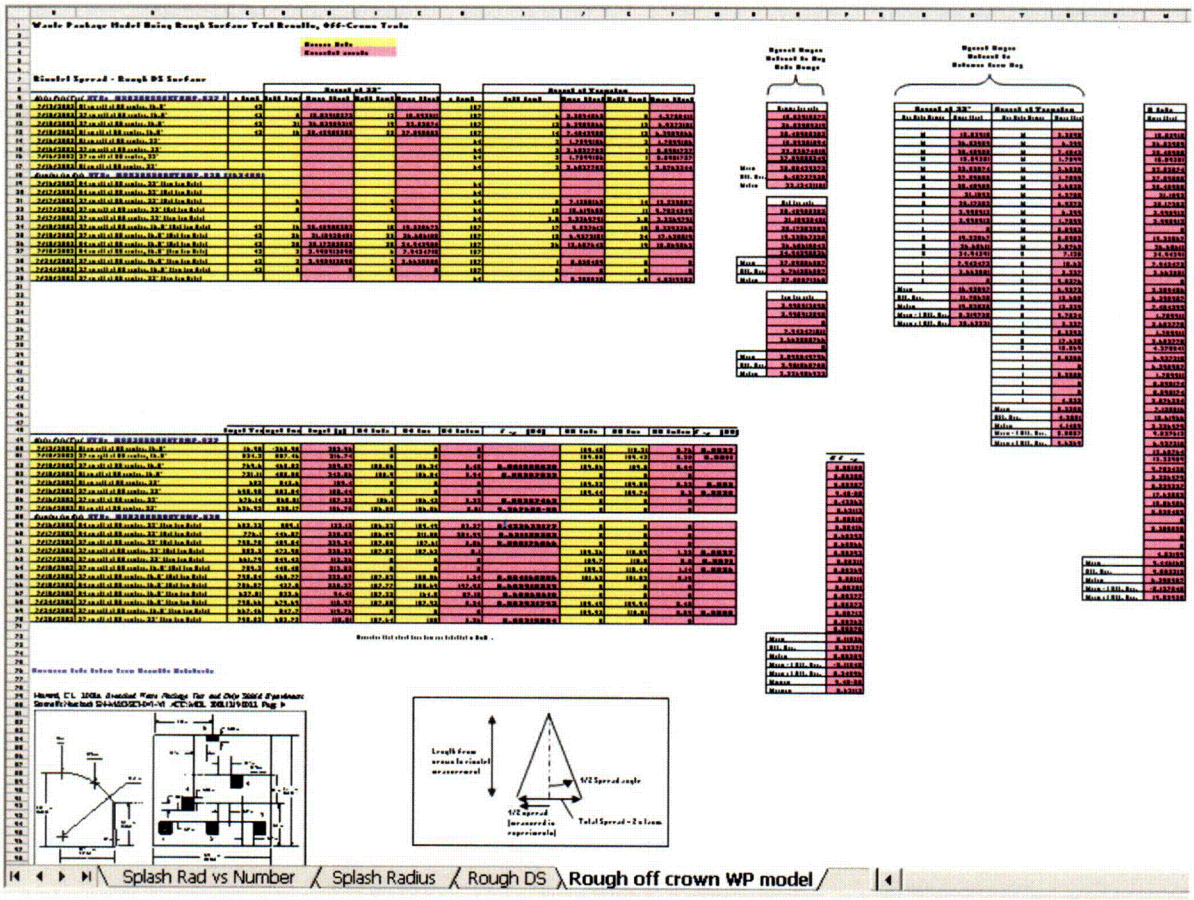

Figure E-11. Spreadsheet "Flux Splitting Validation"–Worksheet "Rough off crown WP model;" Worksheet Overview

	A	B	C	D	E	F	G	H	I	J	K	L
1	Waste Package Model Using Rough Surface Test Results, Off-Crown Tests											
2												
3					Source Data							
4					Calculated results							
5												
6												
7	Rivulet Spread - Rough DS Surface											
8				Spread at 33°					Spread at Transition			
9	*Multiple Patch Test* DTN: MO0208EBSATBWP.027		x (cm)	Left (cm)	Angle (deg)	Right (cm)	Angle (deg)	x (cm)	Left (cm)	Angle (deg)	Right (cm)	Angle (deg)
10	7/12/2002	81 cm right of DS center, 16.5°	43					107				
11	7/15/2002	27 cm right of DS center, 16.5°	43	8	10.53918373	12	15.59281094	107	6	3.209486318	8	4.275841113
12	7/15/2002	27 cm left of DS center, 16.5°	43	21	26.02959219	19	23.83874018	107	12	6.398956627	13	6.927218126
13	7/15/2002	81 cm left of DS center, 16.5°	43	16	20.40988283	22	27.09555249	107	14	7.454298613	12	6.398956627
14	7/16/2002	81 cm right of DS center, 33°						64	2	1.789910608	2	1.789910608
15	7/16/2002	27 cm right of DS center, 33°						64	3	2.683775159	1	0.89517371
16	7/16/2002	27 cm left of DS center, 33°						64	2	1.789910608	1	0.89517371
17	7/16/2002	81 cm left of DS center, 33°						64	3	2.683775159	4	3.576334375
18	*Bounding Flow Rate* DTN: MO0208EBSATBWP.028											
19	7/16/2002	54 cm left of DS center, 33° (Low Flow Rate)						64				
20	7/17/2002	54 cm left of DS center, 33° (High Flow Rate)						64				
21	7/17/2002	27 cm left of DS center, 33° (High Flow Rate)		6		9		64	8	7.125016349	14	12.33908728
22	7/17/2002	27 cm right of DS center, 33° (High Flow Rate)		5		3		64	12	10.61965528	11	9.752424942
23	7/17/2002	27 cm right of DS center, 33° (Low Flow Rate)						64	2.5	2.236979063	2.5	2.236979063
24	7/18/2002	27 cm right of DS center, 16.5° (High Flow Rate)	43	16	20.40988283	15	19.23067238	107	17	9.027612951	10	5.339236804
25	7/18/2002	27 cm left of DS center, 16.5° (High Flow Rate)	43	26	31.15930451	32	36.65610842	107	13	6.927218126	34	17.62801937
26	7/18/2002	54 cm left of DS center, 16.5° (High Flow Rate)	43	25	30.17352003	20	24.94390526	107	26	13.65764251	19	10.0690627
27	7/18/2002	54 cm left of DS center, 16.5° (Low Flow Rate)	43	3	3.990913098	6	7.943471811	107				
28	7/24/2002	27 cm left of DS center, 16.5° (Low Flow Rate)	43	3	3.990913098	2	2.663000766	107	1	0.535458986	0	0
29	7/24/2002	27 cm right of DS center, 16.5° (Low Flow Rate)	43	0	0	0	0	107	0	0	0	0
30	7/25/2002	27 cm left of DS center, 33° (Low Flow Rate)						64	6	5.355825043	4.5	4.021990177
31												

DTN: MO0208EBSATBWP.027 [DIRS 163404]; DTN: MO0208EBSATBWP.028 [DIRS 163405].

Figure E-12. Spreadsheet "Flux Splitting Validation"–Worksheet "Rough off crown WP model;" Calculation of Rivulet Spread Angles

In Figure E-12, Columns A and B, Rows 10–30, identify the tests reported in indicated DTNs. In Columns C and H, the value of x, the distance from the drip location to the measurement point, is listed. Rivulet spread measured to the left and right of the drip location is shown in Columns D and F, respectively, for measurements at the 33° line. Measurements at the transition line are listed in Columns I and K. Portions of this table are reproduced in Table 7.1-8.

The spread distance, w_r, is converted to spread angle, α, in Columns E, G, J, and L:

$$\alpha = \tan^{-1}\left(\frac{w_r}{x}\right).$$

An example of the Microsoft Excel equation used for this calculation is:

E11=DEGREES(ATAN(D11/C11))

where the DEGREES function converts the result of the inverse tangent function ATAN from radians to degrees.

In Figure E-13, Column O, Rows 11–38, the spread angles measured at the 33° line are ordered by drip rate. The "nominal" drip rate is that used in the Multiple Patch tests, and the high and low drip rates were used in the Bounding Flow Rate tests. The mean, standard deviation, and median are computed for each of the three drip rates.

In Column S, the spread angles from Column O are repeated, and statistics (mean, standard deviation, median, and mean plus or minus one standard deviation) are computed for the entire set in Rows 31–35. The drip rate is indicated in Column R, where "M" indicates the nominal drip rate.

In Column U, the spread angles from Columns J and L are consolidated for measurements at the transition line. The drip rate used in each test is indicated in Column T. (The values in this column are currently incorrect, since they are just copies of the incorrect results in Column L and incorrectly recalculated values from Column J, where the actual Column J values are correct.)

All 50 spread angle measurements are compiled in Column W, with statistics (mean, standard deviation, median, and mean plus or minus one standard deviation) computed for the entire set in Rows 63-67 (Figure E-14). The mean plus or minus one standard deviation are used as the spread angle range in Section 7.1.1.2 for determination of the uncertainty in the waste package flux splitting submodel validation.

Spread Angles Ordered by Drip Rate Range

	Nominal drip rate
	10.53918373
	26.02959219
	20.40988283
	15.59281094
	23.83874018
	27.09555249
Mean	20.58429373
Std. Dev.	6.45737938
Median	22.12431151

	High drip rate
	20.40988283
	31.15930451
	30.17352003
	19.23067238
	36.65610842
	24.94390526
Mean	27.09556557
Std. Dev.	6.761306057
Median	27.55871265

	Low drip rate
	3.990913098
	3.990913098
	0
	7.943471811
	2.663000766
	0
Mean	3.098049796
Std. Dev.	2.981865758
Median	3.326956932

Spread Angles Ordered by Distance from Drip

Spread at 33°		Spread at Transition		All data
Drip Rate Range	Angle (deg)	Drip Rate Range	Angle (deg)	Angle (deg)
M	10.5391837	M	3.20949	10.5391837
M	26.0295922	M	6.39896	26.0295922
M	20.4098828	M	7.4543	20.4098828
M	15.5928109	M	1.78991	15.5928109
M	23.8387402	M	2.68378	23.8387402
M	27.0955525	M	1.78991	27.0955525
H	20.4098828	M	2.68378	20.4098828
H	31.1593045	M	4.27584	31.1593045
H	30.17352	M	6.92722	30.17352
L	3.9909131	M	6.39896	3.9909131
L	3.9909131	M	1.78991	3.9909131
L	0	M	0.89517	0
H	19.2306724	M	0.89517	19.2306724
H	36.6561084	M	3.57633	36.6561084
H	24.9439053	H	7.12502	24.9439053
L	7.94347181	H	10.6197	7.94347181
L	2.66300077	L	2.23698	2.66300077
L	0	H	9.02761	0
Mean	16.9259697	H	6.92722	3.20948632
Std. Dev.	11.7062451	H	13.6576	6.39895663
Median	19.8202776	H	12.3391	7.45429881
Mean - 1 Std. Dev.	5.21972461	H	9.75242	1.78991061
Mean + 1 Std. Dev.	28.6322148	L	2.23698	2.68377516
		H	5.33924	1.78991061
		H	17.628	2.68377516
		H	10.0691	4.27584111
		L	0.53546	6.92721813
		L	0	6.39895663
		L	5.35583	1.78991061
		L	0	0.89517371
		L	0	0.89517371
		L	4.02199	3.57633437
		Mean	5.23878	7.12501635
		Std. Dev.	4.38812	10.6196553
		Median	4.14892	2.23697906
		Mean - 1 Std. Dev.	0.85066	9.02761295
		Mean + 1 Std. Dev.	9.6269	6.92721813
				13.6576425
				12.3390873
				9.75242494

f_{root} (B5)	
0.0026859	
0.001105	

All f_{root}: 0.0015505

Splash Rad vs Number / Splash Radius / Rough DS / **Rough off crown WP model**

Figure E-13. Spreadsheet "Flux Splitting Validation"–Worksheet "Rough off crown WP model;" Additional Calculations of Rivulet Spread Angles

	S	T	U	V	W
45		Mean	5.23878		7.12501635
46		Std. Dev.	4.38812		10.6196553
47		Median	4.14892		2.23697906
48		Mean - 1 Std. Dev.	0.85066		9.02761295
49		Mean + 1 Std. Dev.	9.6269		6.92721813
50					13.6576425
51					12.3390873
52					9.75242494
53					2.23697906
54					5.3392368
55					17.6280194
56					10.0690627
57					0.53545899
58					0
59					5.35582504
60					0
61					0
62					4.02199018
63				Mean	9.4461677
64				Std. Dev.	9.58321235
65				Median	6.39895663
66				Mean - 1 Std. Dev.	-0.1370447
67				Mean + 1 Std. Dev.	19.02938

Figure E-14. Spreadsheet "Flux Splitting Validation"–Worksheet "Rough off crown WP model;" Statistics of Rivulet Spread Angles

	A	B	C	D	E	F	G	H	I
47									
48			Input Tare	Input Final	Input (g)	B4 Initial	B4 Final	B4 Inflow	f_{expt} (B4)
49	*Multiple Patch Test*	**DTN: MO0208EBSATBWP.027**							
50	7/12/2002	81 cm right of DS center, 16.5'	16.98	-265.98	282.96	0	0	0	
51	7/15/2002	27 cm right of DS center, 16.5'	824.2	507.46	316.74	0	0	0	
52	7/15/2002	27 cm left of DS center, 16.5'	769.6	460.03	309.57	105.86	106.34	0.48	**0.001550538**
53	7/15/2002	81 cm left of DS center, 16.5'	731.11	488.55	242.56	105.9	106.84	0.94	**0.00387533**
54	7/16/2002	81 cm right of DS center, 33'	652	542.6	109.4	0	0	0	
55	7/16/2002	27 cm right of DS center, 33'	690.98	582.54	108.44	0	0	0	
56	7/16/2002	27 cm left of DS center, 33'	676.14	568.81	107.33	106.1	106.43	0.33	**0.00307463**
57	7/16/2002	81 cm left of DS center, 33'	636.92	530.17	106.75	106.05	106.06	0.01	**9.36768E-05**
58	*Bounding Flow Rate*	**DTN: MO0208EBSATBWP.028**							
59	7/16/2002	54 cm left of DS center, 33' (Low Flow Rate)	682.23	559.1	123.13	106.22	159.49	53.27	**0.432632177**
60	7/17/2002	54 cm left of DS center, 33' (High Flow Rate)	776.1	446.07	330.03	106.09	311.08	204.99	**0.621125352**
61	7/17/2002	27 cm left of DS center, 33' (High Flow Rate)	798.78	459.54	339.24	107.55	107.61	0.06	**0.000176866**
62	7/17/2002	27 cm right of DS center, 33' (High Flow Rate)	803.2	472.98	330.22	107.52	107.62	0.1	
63	7/17/2002	27 cm right of DS center, 33' (Low Flow Rate)	661.79	549.43	112.36	0	0	0	
64	7/18/2002	27 cm right of DS center, 16.5' (High Flow Rate)	759.3	445.48	313.82	0	0	0	
65	7/18/2002	27 cm left of DS center, 16.5' (High Flow Rate)	790.84	468.77	322.07	107.52	108.86	1.34	**0.004160586**
66	7/18/2002	54 cm left of DS center, 16.5' (High Flow Rate)	756.07	427.8	328.27	107.77	305.69	197.92	**0.602918329**
67	7/18/2002	54 cm left of DS center, 16.5' (Low Flow Rate)	627.01	532.6	94.41	107.32	164.5	57.18	**0.60565618**
68	7/24/2002	27 cm left of DS center, 16.5' (Low Flow Rate)	795.66	679.69	115.97	107.58	107.92	0.34	**0.002931793**
69	7/24/2002	27 cm right of DS center, 16.5' (Low Flow Rate)	667.46	547.7	119.76	0	0	0	
70	7/25/2002	27 cm left of DS center, 33' (Low Flow Rate)	798.53	682.72	115.81	107.64	108	0.36	**0.00310854**
71									
72						Breaches that should have flow are highlighted in **bold**.			

DTN: MO0208EBSATBWP.027 [DIRS 163404]; DTN: MO0208EBSATBWP.028 [DIRS 163405].

Figure E-15. Spreadsheet "Flux Splitting Validation"–Worksheet "Rough off crown WP model;" Calculation of Experimental Breach Flow Fractions

For the tests identified in Columns A and B, Rows 50–70 (Figure E-15), the initial and final water mass in the input water container are listed in Columns C and D, and the amount of water dripped onto the drip shield is calculated in Column E (e.g., E50=C50-D50). The initial and final mass of water in the Breach B4 collection vessel is listed in Columns F and G, respectively, and the amount of water collected from flow into Breach B4 is calculated in Column H (e.g., H52=G52-F52). The fraction of water dripped onto the drip shield that flowed into Breach B4, f_{expt} (B4), is computed in Column I for the tests in which the inflow was greater than zero (e.g., I52=H52/E52).

	J	K	L	M	N	O	P
47							
48	**B5 Initial**	**B5 Final**	**B5 Inflow**	**f_{expt} (B5)**			
49							
50	109.45	110.21	0.76	**0.00268589**			
51	109.08	109.43	0.35	**0.00110501**			***All f_{expt}***
52	109.06	109.5	0.44				0.001550538
53	0	0	0				0.00387533
54	109.33	109.55	0.22	**0.00201097**			0.00307463
55	109.44	109.74	0.3	**0.00276651**			9.36768E-05
56	0	0	0				0.432632177
57	0	0	0				0.621125352
58							0.000176866
59	0	0	0				0.004160586
60	0	0	0				0.602918329
61	0	0	0				0.60565618
62	109.36	110.59	1.23	**0.00372479**			0.002931793
63	109.7	110.5	0.8	**0.00711997**			0.00310854
64	109.3	110.44	1.14	**0.00363266**			0.002685892
65	101.63	101.82	0.19				0.001105007
66	0	0	0				0.002010969
67	0	0	0				0.002766507
68	109.49	109.94	0.45				0.00372479
69	109.92	110.01	0.09	**0.0007515**			0.007119972
70	0	0	0				0.003632656
71							0.000751503
72						Mean	0.115255065
73						Std. Dev.	0.233709623
74						Median	0.003091585
75						Mean - 1 Std. Dev.	-0.11845456
76						Mean + 1 Std. Dev.	0.348964688
77						Minimum	9.36768E-05
78						Maximum	0.621125352

Figure E-16. Spreadsheet "Flux Splitting Validation"–Worksheet "Rough Off Crown WP Model;" Summary of Experimental Breach Flow Fractions

The initial and final mass of water in the Breach B5 collection vessel is listed in Figure E-16, Columns I and J, respectively, and the amount of water collected from flow into Breach B5 is calculated in Column L (e.g., L50=K50-J50). The fraction of water dripped onto the drip shield that flowed into Breach B5, f_{expt} (B5), is computed in Column M for the tests in which the inflow was greater than zero (e.g., M50=L50/E50).

The 20 values of f_{expt} are compiled in Column P, with statistics (mean, standard deviation, median, and mean plus or minus one standard deviation) presented in Rows 73-76.

The input water, breach inflows, and f_{expt} for each breach are reproduced in Table 7.1-10.

INTENTIONALLY LEFT BLANK

APPENDIX F

MICROSOFT EXCEL SPREADSHEETS "TRANSPORT_CALC_ALL_COLLOIDS," "FLUX_OUT_RATIO.XLS," AND "TIME_TO_CONV.XLS"

MICROSOFT EXCEL SPREADSHEETS "TRANSPORT_CALC_ALL_COLLOIDS," "FLUX_OUT_RATIO.XLS," AND "TIME_TO_CONV.XLS"

SPREADSHEET "TRANSPORT_CALC_ALL_COLLOIDS.XLS"

The purpose of this spreadsheet is to implement the colloid model that represents the sorption of radionuclides onto the oxy-hydroxide (designated FeO) corrosion material within the engineered barrier system (EBS). The model accounts for both reversible and irreversible sorption onto the FeO mobile colloids and the immobile corrosion products together with reversible sorption onto both waste form and groundwater (GW) colloids. This description refers to equations in Appendix B, "Implementation of Radionuclide Sorption onto Colloidal and Stationary Phases with Finite Difference Solution."

Description of Input Values

The first 29 rows of the worksheet (see Figure F-1 for an image of the worksheet) contain parameter input values. Column D contains the typical values input from the GoldSim model. Column B contains values from Column D that are scaled appropriately for the current calculations.

Row 2: c_s [kg/m^3],

c_s = Pu solubility

$B$2=$D$2/1000

Row 3: phi_1

ϕ_cell1, $\phi = \frac{V_{pore}}{V_{bulk}}$, porosity of the upstream boundary

$B$3=$D$3

Row 4: phi_2

ϕ_cell2, $\phi = \frac{V_{pore}}{V_{bulk}}$, porosity of the corrosion product mass

$B$4=$D$4

Row 5: phi_3

ϕ_cell3, $\phi = \frac{V_{pore}}{V_{bulk}}$, porosity of the downstream boundary

$B$5=$D$5

Row 6: u [m^3/yr]

volumetric water flux, U Table B-1

$B$6=$D$6

Row 7: Kd_FeO_c [m^3/kg]

partition coefficient in the FeO colloid state

$B$7=$D$7/1000

Row 8: Kd_FeO_CP [m^3/kg]

partition coefficient in the stationary FeO corrosion product state

$B$8=$D$8/1000

Row 9: Kd_WF_c [m^3/kg]

partition coefficient in the waste form colloid state

$B$9=$D$9/1000

	A	B	C	D
1	Input for Excel sreadsheet		Input from GoldSim	
2	c_s [kg/m^3]	0.001	**c_s [mg/L]**	1
3	phi_1	1	**phi_1**	1
4	phi_2	0.4	**phi_2**	0.4
5	phi_3	0.3	**phi_3**	0.3
6	u [m^3/yr]	0.1	**u [m^3/yr]**	0.1
7	Kd_FeO_c [m^3/kg]	1.00000E+01	**Kd_FeO_c [ml/g]**	1.00000E+04
8	Kd_FeO_CP [m^3/kg]	2.50000E+00	**Kd_FeO_CP [ml/g]**	2.50000E+03
9	Kd_WF_c [m^3/kg]	2.00000E+02	**Kd_WF_c [ml/g]**	2.00000E+05
10	Kd_GW_c [m^3/kg]	2.00000E+02	**Kd_GW_c [ml/g]**	2.00000E+05
11	mass_FeO_CP [kg]	1.80000E+04	**mass_FeO_CP [g]**	1.80000E+07
12	V_pore [m^3]	2.29008E+00	**V_pore [L]**	2.29008E+03
13	c_FeO_c [kg/m^3]	2.00000E-02	**c_FeO_c [mg/L]**	2.00000E+01
14	c_FeO_CP [kg/m^3]	7.86000E+03	**c_FeO_CP [mg/L]**	7.86000E+06
15	c_WF_c [kg/m^3]	3.00000E-03	**c_WF_c [mg/L]**	3.00000E+00
16	c_GW_c [kg/m^3]	1.00000E-04	**c_GW_c [mg/L]**	1.00000E-01
17	rate [m/yr]	1.00000E-05	**rate [cm/yr]**	1.00000E-03
18	S_FeO_c [m^2/kg]	1.00000E+05	**S_FeO_c[m^2/g]**	1.00000E+02
19	S_FeO_CP [m^2/kg]	1.00000E+04	**S_FeO_CP [m^2/g]**	1.00000E+01
20	d_FeO [kg/m^3]	5.24000E+03	**den FeO [kg/m^3]**	5.24000E+03
21	diffus_aq [m^2/yr]	7.25834E-02	**diffus_aq [m^2/s]**	2.30000E-09
22	diffus_colloid [m^2/yr]	7.25834E-04	**diffus_colloid [m^2/**	2.30000E-11
23	diff_length_1 [m]	1.00000E-03	**diff_length_1 [m]**	1.00000E-03
24	diff_length_2 [m]	5.00000E+00	**diff_length_2 [m]**	5.00000E+00
25	diff_length_3 [m]	8.06000E-01	**diff_length_3 [m]**	8.06000E-01
26	diff_area_1_2 [m^2]	3.60000E+01	**diff_area_1_2 [m^2]**	3.60000E+01
27	diff_area_2_3 [m^2]	1.06800E+00	**diff_area_2_3 [m^2]**	1.06800E+00
28	decay [1/yr]	2.87494E-05	**decay [1/yr]**	2.87494E-05
29	delt [yr]	10	**delt [yr]**	10

Figure F-1. Spreadsheet "Transport_Calc_all_colloids.xls;" Summary of Inputs

Row 10: Kd_GW_c [m^3/kg]

partition coefficient in the GW colloid state

$B$10=$D$10/1000

Row 11: mass_FeO_CP [kg]

m_{FeO_CP} = mass of corrosion product

$B$11=$D$11/1000

Row 12: V_pore [m^3]

$V_{pore} = \phi V_{bulk} = \frac{\phi}{1-\phi}\frac{m_{FeO_CP}}{\rho_{FeO_CP}}$, pore volume

$B$12=$D$12/1000

Row 13: c_FeO_c [kg/m^3]

$c_{Pu_FeO_c}$, concentration of Pu in the FeO colloid state from reversible sorption

$B$13=$D$13/1000

Row 14: c_FeO_CP [kg/m^3]

$c_{Pu_FeO_CP}$, concentration of Pu in the stationary FeO corrosion product state from reversible sorption

$B$14=$D$14/1000

Row 15: c_WF_c [kg/m^3]

$c_{Pu_WF_c}$, concentration of Pu in the waste form colloid state from reversible sorption

$B$15=$D$15/1000

Row 16: c_GW_c [kg/m^3]

$c_{Pu_GW_c}$, concentration of Pu in the GW colloid state from reversible sorption

$B$16=$D$16/1000

Row 17: rate [m/yr]

k, forward rate constant (m^3 water m^{-2} FeO yr^{-1})

$B$17=$D$17/100

Row 18: S_FeO_c [m^2/kg]

$\hat{S}_{FeO}$ = specific surface area of FeO ($m^2\ kg^{-1}$) in the colloid state

$B$18=$D$18*1000

Row 19: S_FeO_CP [m^2/kg]

$\hat{S}_{FeO}$ = specific surface area of FeO ($m^2\ kg^{-1}$) in the corrosion product state

$B$19=$D$19*1000

Row 20: d_FeO [kg/m^3]

ρ_{FeO_CP} = corrosion product (FeO) density ($kg\ m^{-3}$)

$B$20=$D$20

Row 21: diffus_aq [m^2/yr]

D_{aq} = aqueous diffusivity ($m^2\ yr^{-1}$)

$B$21=$D$21*31558000

Row 22: diffus_colloid [m^2/yr]

$D_{colloid}$ = colloid diffusivity ($m^2\ yr^{-1}$)

$B$22=$D$22*31558000

Row 23: diff_length_1 [m]

L_1 = diffusive length for cell_1

$B$23=$D$23

Row 24: diff_length_2 [m]

L_2 = diffusive length for cell_2

$B$24=$D$24

Row 25: diff_length_3 [m]

L_3 = diffusive length for cell_3

$B$25=$D$25

Row 26: diff_area_1_2 [m^2]

A_{s12} = diffusive area at cell_1 and cell_2 interface

$B$26=$D$26

Row 27: diff_area_2_3 [m^2]

A_{s23} = diffusive area at cell_2 and cell_3 interface

$B$27=$D$27

Row 28: decay [1/yr]

λ, decay rate (yr^{-1})

$B$28=$D$28

Row 29: delt [yr]

Δt, time step length

$B$29=$D$29

Rows 30 through 53 contain additional derived parameters for the mixing cell colloid model.

	A	B	C	D	E	F	G
30	R_bar_1 [1/yr]	2.00000E-02					
31	R_bar_2 [1/yr]	7.86000E+02					
32	U_bar [1/yr]	4.36667E-02					
33	Kd_bar_FeO_c	2.00000E-01					
34	Kd_bar_FeO_CP	1.96500E+04					
35	Kd_bar_WF_c	6.00000E-01					
36	Kd_bar_GW_c	2.00000E-02					
37	K_bar_1	1.96518E+04					
38	K_bar_2	1.82000E+00					
39	K_bar_3	8.20000E-01					
40	Diff_left_aq	9.12736E-02					
41	Diff_left_c	9.12736E-04					
42	Diff_right_aq	2.22893E-03		limiting values			
43	Diff_right_colloid	2.22893E-05		p_1	3.58485E-02		
44	denom_a_1_2	2.75194E+04		p_2	8.17743E-02	tolerence =	1.00000E-02
45	a_1	7.14108E-01		lim c_Pu_aq	2.05511E-07	Pu_aq time [yr]	137
46	a_2	5.87541E-08		lim c_irr_c	9.40175E-08	delta_1	3.2004E-04
47	b_1	6.95808E-01		lim c_rev_c	4.11023E-08	delta_2	3.0078E-04
48	b_2	1.39162E-01		lim c_irr_CP	5.61862E+00	t_1	22
49	e_1	9.99713E-01		lim c_rev_CP	4.03830E-03	t_2	24
50	e_2	7.85774E+03		flux out ratio	5.48749E-01	irrv_Pu_c time [yr]	240
51	Omega	9.5000E-01		flux out/flux in	1.29289E-04		
52	k_fit_Omega [cm/yr]	4.1837E-02		irrv_col/rev_col	5.57903E-01		
53	p1/p2	4.3838E-01					
54							
55							

Figure F-2. Spreadsheet "Transport_Calc_all_colloids.xls;" Additional Derived Parameters

Row 30: R_bar_1 [1/yr]

$\overline{R}_1 = \hat{S}_{FeO_c} c_{FeO_c} k$, reaction rate for colloids

$B$30=$B$18*$B$13*$B$17

Row 31: R_bar_2 [1/yr]

$\overline{R}_2 = \hat{S}_{FeO_CP} c_{FeO_CP} k$, reaction rate constants for corrosion products

$B$31=$B$19*$B$14*$B$17

Row 32: U_bar [1/yr]

$\overline{U}$ is the advective rate constant

$B$32=$B$6/$B$12

Row 33: Kd_bar_FeO_c

advective dimensionless partition coefficient in the FeO colloid state

$B$33=$B$13*$B$7

Row 34: Kd_bar_FeO_CP

advective dimensionless partition coefficient in the FeO corrosion product state

$B$34=$B$14*$B$8

Row 35: Kd_bar_WF_c

advective dimensionless partition coefficient in the waste form colloid state

$B$35=$B$15*$B$9

Row 36: Kd_bar_GW_c

advective dimensionless partition coefficient in the GW colloid state

$B$36=$B$16*$B$10

Row 37: K_bar_1

$\overline{K}_1 = 1 + \overline{K}_{d_FeO_c} + \overline{K}_{d_FeO_CP} + \overline{K}_{d_WF_c} + \overline{K}_{d_GW_c}$, combination of dimensionless partition coefficients

$B$37=1+$B$33+$B$34+$B$35+$B$36

Row 38: K_bar_2

$\overline{K}_2 = 1 + \overline{K}_{d_FeO_c} + \overline{K}_{d_WF_c} + \overline{K}_{d_GW_c}$, combination of dimensionless partition coefficients

$B$38=1+$B$33+$B$35+$B$36

Row 39: K_bar_3

$\overline{K}_3 = \overline{K}_{d_FeO_c} + \overline{K}_{d_WF_c} + \overline{K}_{d_GW_c}$, combination of dimensionless partition coefficients

$B$39=$B$33+$B$35+$B$36

Row 40: Diff_left_aq

aqueous diffusive rate constant for left diffusive boundary condition

$B$40=($B$26/($B$23/($B$3*$B$21)+$B$24/($B$4*$B$21)))/$B$12

Row 41: Diff_left_c

colloid diffusive rate constant for left diffusive boundary condition

$B$41=($B$26/($B$23/($B$3*$B$22)+$B$24/($B$4*$B$22)))/$B$12

Row 42: Diff_right_aq

aqueous diffusive rate constant for right diffusive boundary condition

$B$42=($B$27/($B$24/($B$4*$B$21)+$B$25/($B$5*$B$21)))/$B$12

Row 43: Diff_right_colloid

colloid diffusive rate constant for right diffusive boundary condition

$B$43=($B$27/($B$24/($B$4*$B$22)+$B$25/($B$5*$B$22)))/$B$12

Row 44: denom_a_1_2

denominator of a_1 in Equation B-55 (see Row 45)

$B$44=$B$37+($B$32*$B$38+$B$40+$B$41*$B$35+$B$42+$B$43*$B$39
+$B$30+$B$31+$B$28*$B$37)*$B$29

Row 45: a_1

first order linear constant coefficient for Equation B-55,

$$a_1 = \frac{\overline{K}_1}{\overline{K}_1 + \left(\overline{UK}_2 + \overline{D}_{left_aq} + \overline{D}_{left_col}\overline{K}_{d_WF_c} + \overline{D}_{right_aq} + \overline{D}_{right_col}\overline{K}_3 + \overline{R}_1 + \overline{R}_2 + \lambda\overline{K}_1\right)\Delta t}$$

B$45=$B$37/$B$44

Row 46: a_2

first order linear constant coefficient for Equation B-55,

$$a_2 = \frac{\left(\overline{U}(1+\overline{K}_{d_WF_c}) + \overline{D}_{left_aq} + \overline{D}_{left_col}\overline{K}_{d_WF_c}\right)\Delta t c_s}{\overline{K}_1 + \left(\overline{UK}_2 + \overline{D}_{left_aq} + \overline{D}_{left_col}\overline{K}_{d_WF_c} + \overline{D}_{right_aq} + \overline{D}_{right_col}\overline{K}_3 + \overline{R}_1 + \overline{R}_2 + \lambda\overline{K}_1\right)\Delta t}$$

$B$46=(($B$32*(1+$B$35)+$B$40+$B$41*$B$35)*$B$29*$B$2)/$B$44

Row 47: b_1

irreversible colloid coefficient (Equation B-59) for Equation B-58,

$$b_1 = \frac{1}{1+\left(\overline{U}+\overline{D}_{right_col}+\lambda\right)\Delta t}$$

$B$47=1/(1+($B$32+$B$43+$B$28)*$B$29)

Row 48: b_2

irreversible colloid coefficient (Equation B-60) for Equation B-58,

$$b_2 = \frac{\overline{R}_1\Delta t}{1+\left(\overline{U}+\overline{D}_{right_col}+\lambda\right)\Delta t}$$

$B$48=($B$30*$B$29)*$B$47

Row 49: e_1

irreversible corrosion products coefficient (Equation B-65) for Equation B-64,

$$e_1 = \frac{1}{1+\lambda\Delta t}$$

$B$49=1/(1+$B$28*$B$29)

Row 50: e_2

irreversible corrosion products coefficient (Equation B-66) for Equation B-64,

$$e_2 = \frac{\overline{R}_2\Delta t}{1+\lambda\Delta t}$$

$B$50=($B$31*$B$29)*$B$49

Row 51: Omega

$$\Omega = \frac{\text{colloid mass flux out}}{\text{total mass flux out}} = 0.95 \text{ (Equation B-1)}$$

$B$51=0.95

Row 52: k_fit_Omega [cm/yr]

$k = \dfrac{p_2\Omega - p_1}{(1-\Omega)\hat{S}_{FeO_c}c_{FeO_c}}$, fitting parameter, k, given a target flux ratio Ω, Equation B-72

$B$52=100*($E$44*$B$51-$E$43)/((1-$B$51)*$B$18*$B$13)

Row 53: p1/p2

$$\Omega = \frac{p_1 + \overline{R}_1}{p_2 + \overline{R}_1} \qquad \text{(Equation B-71)}$$

$B$53=$E$43/$E$44

The values of parameters in Column E & G Rows 43 through 52 under the heading "limiting values" pertain to the equations and discussion in Section "Boundary Fluxes" in Appendix B.

Row 43, Column E: p_1

$$p_1 = \overline{K}_3\left(\overline{U} + \overline{D}_{right_col} + \lambda\right)$$

$E$43=$B$39*($B$32+$B$43+$B$28)

Row 44, Column E: p_2

$$p_2 = \left(\overline{UK}_2 + \overline{D}_{right_aq} + \overline{D}_{right_col}\overline{K}_3\right)\left(\frac{\overline{U} + \overline{D}_{right_col} + \lambda}{\overline{U} + \overline{D}_{right_col}}\right)$$

$E$44=($B$32*$B$38+$B$42+$B$43*$B$39)*($B$32+$B$43+$B$28)/($B$32+$B$43)

Row 45, Column E: lim c_Pu_aq

$$\lim_{n\to\infty} c^n_{Pu_aq} = \frac{a_2}{1-a_1}$$

$E$45=$B$46/(1-$B$45)

Row 46, Column E: lim c_irr_c

$$\lim_{n\to\infty} c^n_{Irrv_Pu_FeO_c} = \frac{a_2 b_2}{(1-a_1)(1-b_1)}$$

$E$46=($B$30*$E$45)/($B$32+$B$43+$B$28)

Row 47, Column E: lim c_rev_c

$$\lim_{n\to\infty} c^n_{Pu_FeO_c} = \overline{K}_{d_FeO_c} \lim_{n\to\infty} c^n_{Pu_aq}$$

$E$47=$B$33*$E$45

Row 48, Column E: lim c_irr_CP

$$\lim_{n\to\infty} c^n_{Irrv_Pu_FeO_CP} = \frac{e_2}{1-e_1} \lim_{n\to\infty} c^n_{Pu_aq} = \frac{\overline{R}_2}{\lambda} \lim_{n\to\infty} c^n_{Pu_aq}$$

$E$48=$E$45*$B$31/$B$28

Row 49, Column E: lim c_rev_CP

$$\lim_{n\to\infty} c^n_{Pu_FeO_CP} = \overline{K}_{d_FeO_CP} \lim_{n\to\infty} c^n_{Pu_aq}$$

$E$49=$B$34*$E$45

Row 50, Column E: flux out ratio

$$\Omega = \frac{p_1 + \overline{R}_1}{p_2 + \overline{R}_1}$$

$E$50=($E$43+$B$30)/($E$44+$B$30)

Row 51, Column E: flux out/flux in

$$\Psi = \frac{p_2 + \overline{R}_1}{p_2 + \left(\frac{\overline{U} + \overline{D}_{right_col} + \lambda}{\overline{U} + \overline{D}_{right_col}}\right)\left(\overline{R}_1 + \overline{R}_2 + \lambda \overline{K}_1\right)}$$

$E$51=($E$44+$B$30)/($E$44+($B$32+$B$43+$B$28)*($B$30+$B$31+$B$28*$B$37)/($B$32+$B$43))

Row 52, Column E: irrv_col/rev_col

$$0 < \frac{\overline{K}_3(\overline{U} + \overline{D}_{right_col})}{\overline{U}\overline{K}_2 + \overline{D}_{right_aq} + \overline{D}_{right_col}\overline{K}_3} < \Omega < 1$$

$E$52=($B$32+$B$43)*$E$46/(($B$32+$B$43)*$B$39*$E$45)

Row 44, Column G: tolerance

relative error estimate with tolerance ε

$G$44 =G44

Row 45, Column G: Pu_aq time [yr]

$$time = n\Delta t > \frac{\log_{10} \varepsilon}{\log_{10} a_1} \Delta t \quad \text{(Equation B-74)}$$

$G$45 =$B$29*LOG10($G$44)/LOG10($B$45)

Row 46, Column G: delta_1

$$b_1^{n+1} < \left|\frac{a_1 - b_1}{1 - a_1}\right| \frac{\varepsilon}{2} = \delta_1$$

$G$46 =0.5*$G$44*ABS(($B$47-$B$45)/(1-$B$45))

Row 47, Column G: delta_2

$$a_1^{n+1} < \left|\frac{a_1 - b_1}{1 - b_1}\right| \frac{\varepsilon}{2} = \delta_2$$

$G$47 =0.5*$G$44*ABS(($B$47-$B$45)/(1-$B$47))

Row 48, Column G: t_1

$$\frac{\log_{10} \delta_1}{\log_{10} b_1}$$

$G$48 =LOG10($G$46)/LOG10($B$47)

Row 49, Column G: t_2

$$\frac{\log_{10} \delta_2}{\log_{10} a_1}$$

$G$49 =LOG10($G$47)/LOG10($B$45)

Row 50, Column G: irrv_Pu_c time [yr]

time to converge to a given relative error tolerance,

$$time = n\Delta t > \frac{\log_{10} \varepsilon}{\log_{10} a_1} \Delta t$$

$G$50 =INT(MAX($G$48,$G$49))*$B$29

Rows 58 thru 158 and Columns A through AC contain calculated solutions and equation terms, iterated in time, for the mixing cell colloid model. Images of this section of the spreadsheet are included at the end of this appendix (Figures F-3 through F-14).

A58 through A158 are the model times, time(n+1) = time(n)+delt, $A$59=$A58+$B$29

Column B: c_Pu_aq

B$59=$B$45*$B58+$B$46

Column C: c_Pu_FeO_c

C$59 =$B$33*$B59

Column D: c_Pu_FeO_CP

D$59 =$B$34*$B59

Column E: c_Pu_WF_c

E$59 =$B$35*$B59

Column F: c_Pu_GW_c

F$59 =$B$36*$B59

Column G: c_irrv_Pu FeO_c

G$59 =$B$47*$G58+$B$48*$B59

Column H: c_irrv_Pu FeO_CP

H$59 =$B$49*$H58+$B$50*$B59

Column I: c_Pu_Fluid1 [mg/L]

I$59 =1000*($B59+$C59+$E59+$F59)

Column J: c_Pu_FeO_c [g/kg]

J$59 =1000*$C59/$B$13

Column K: c_Pu_FeO_CP [g/kg]

K$59 =1000*$D59/$B$14

Column L: c_PU_WF_c [g/kg]

L$59 =1000*$E59/$B$15

Column M: c_Pu_GW_c [g/kg]

M$59 =1000*$F59/$B$16

Column N: c_Irrv_Pu_c [g/kg]

N$59 =1000*$G59/$B$13

Column O: c_Irrv_Pu_CP [g/kg]

O$59 =1000*$H59/$B$14

Column P: time

P$59 =$A59

Column Q: left_bddy_flux [kg]

$$F^n_{left_bddy_total} = \overline{U}V_{pore}c_s + \overline{D}_{left_aq}V_{pore}(c_s - c^n_{Pu_aq})$$
$$+\overline{U}V_{pore}\overline{K}_{d_WF_c}c_s + \overline{D}_{left_col}V_{pore}\overline{K}_{d_WF_c}(c_s - c^n_{Pu_aq})$$

Q$59=($B$32*(1+$B$35)*$B$2+($B$40+$B$41*$B$35)*($B$2-$B59))*$B$12*$B$29

Column R: right_bddy colloid flux [kg]

$$F^n_{right_bddy_colloid} = \overline{U}V_{pore}\overline{K}_{d_FeO_c}c^n_{Pu_aq} + \overline{U}V_{pore}c^n_{Irrv_Pu_FeO_c}$$
$$\overline{U}V_{pore}\overline{K}_{d_WF_c}c^n_{Pu_aq} + \overline{U}V_{pore}\overline{K}_{d_GW_c}c^n_{Pu_aq}$$
$$+\overline{D}_{right_col}V_{pore}\overline{K}_{d_FeO_c}c^n_{Pu_aq} + \overline{D}_{right_col}V_{pore}c^n_{Irrv_Pu_FeO_c}$$
$$\overline{D}_{right_col}V_{pore}\overline{K}_{d_WF_c}c^n_{Pu_aq} + \overline{D}_{right_col}V_{pore}\overline{K}_{d_GW_c}c^n_{Pu_aq}$$

R$59 =($B$32+$B$43)*($B$39*$B59+$G59)*$B$12*$B$29

Column S: right bddy total flux [kg]

$$F^n_{right_bddy_total} = F^n_{right_bddy_colloid} + \overline{U}V_{pore}c^n_{Pu_aq} + \overline{D}_{right_aq}V_{pore}c^n_{Pu_aq}$$

S$59 =$R59+($B$32+$B$42)*$B59*$B$12*$B$29

Column T: col_out/total_out

$$\Omega_n = \frac{F^n_{right_bddy_colloid}}{F^n_{right_bddy_total}}$$

T$59 =$R59/$S59

Column U: flux_out/flux_in

U$59 =$S59/$Q59

Column V: change mass [kg]

V$59 =(($B59-$B58)+($C59-$C58)+($D59-$D58)+($E59-$E58)+($F59-$F58))*$B$12

Column W: in - out [kg]

W$59=$Q59-(($B$32+$B$43)*$B$39+$B$32+$B$42)*$B59*$B$12*$B$29

Column X: react/decay [kg]

X$59 =-($B$30+$B$31+$B$28*$B$37)*$B$12*$B$29*$B59

Column Y: PU mass balance

Y$59 =$V59-$W59-$X59

Column Z: change mass [kg]

Z$59 =(($G59-$G58)+($H59-$H58))*$B$12

Column AA: in-out [kg]

AA$59 =-($B$32+$B$43)*$G59*$B$12*$B$29

Column AB: react/decay [kg]

AB$59 =(($B$30+$B$31)*$B59-$B$28*($G59+$H59))*$B$12*$B$29

Column AC: Irrv_Pu mass balance

AC$59 =$Z59-$AA59-$AB59

	A	B	C	D	E	F	G	H	I
56		concentration are Pu mass per pore volume [kg/m^3]							
57	time	c_Pu_aq	c_Pu_FeO_c	c_Pu_FeO_CP	c_Pu_WF_c	c_Pu_GW_c	c_irrv_Pu FeO_c	c_irrv_Pu FeO_CP	c_Pu_Fluid1 [mg/L]
58	0.00	0	0	0	0	0	0	0	0
59	10.00	5.87541E-08	1.17508E-08	1.15452E-03	3.52525E-08	1.17508E-09	8.17633E-09	4.61675E-04	1.0693E-04
60	20.00	1.00711E-07	2.01422E-08	1.97897E-03	6.04266E-08	2.01422E-09	1.97043E-08	1.25290E-03	1.8329E-04
61	30.00	1.30673E-07	2.61345E-08	2.56772E-03	7.84036E-08	2.61345E-09	3.18950E-08	2.27933E-03	2.3782E-04
62	40.00	1.52068E-07	3.04137E-08	2.98814E-03	9.12411E-08	3.04137E-09	4.33549E-08	3.47359E-03	2.7676E-04
63	50.00	1.67347E-07	3.34695E-08	3.28838E-03	1.00408E-07	3.34695E-09	5.34551E-08	4.78757E-03	3.0457E-04
64	60.00	1.78258E-07	3.56516E-08	3.50277E-03	1.06955E-07	3.56516E-09	6.20012E-08	6.18690E-03	3.2443E-04
65	70.00	1.86050E-07	3.72099E-08	3.65588E-03	1.11630E-07	3.72099E-09	6.90320E-08	7.64705E-03	3.3861E-04
66	80.00	1.91614E-07	3.83227E-08	3.76521E-03	1.14968E-07	3.83227E-09	7.46983E-08	9.15050E-03	3.4874E-04
67	90.00	1.95587E-07	3.91174E-08	3.84328E-03	1.17352E-07	3.91174E-09	7.91939E-08	1.06847E-02	3.5597E-04
68	100.00	1.98424E-07	3.96849E-08	3.89904E-03	1.19055E-07	3.96849E-09	8.27169E-08	1.22408E-02	3.6113E-04
69	110.00	2.00450E-07	4.00901E-08	3.93885E-03	1.20270E-07	4.00901E-09	8.54501E-08	1.38124E-02	3.6482E-04
70	120.00	2.01897E-07	4.03795E-08	3.96728E-03	1.21138E-07	4.03795E-09	8.75533E-08	1.53949E-02	3.6745E-04
71	130.00	2.02931E-07	4.05861E-08	3.98759E-03	1.21758E-07	4.05861E-09	8.91605E-08	1.69850E-02	3.6933E-04
72	140.00	2.03668E-07	4.07337E-08	4.00208E-03	1.22201E-07	4.07337E-09	9.03815E-08	1.85805E-02	3.7068E-04
73	150.00	2.04195E-07	4.08391E-08	4.01244E-03	1.22517E-07	4.08391E-09	9.13044E-08	2.01797E-02	3.7164E-04
74	160.00	2.04572E-07	4.09143E-08	4.01983E-03	1.22743E-07	4.09143E-09	9.19989E-08	2.17814E-02	3.7232E-04
75	170.00	2.04840E-07	4.09681E-08	4.02511E-03	1.22904E-07	4.09681E-09	9.25195E-08	2.33847E-02	3.7281E-04
76	180.00	2.05032E-07	4.10064E-08	4.02888E-03	1.23019E-07	4.10064E-09	9.29085E-08	2.49891E-02	3.7316E-04
77	190.00	2.05169E-07	4.10338E-08	4.03157E-03	1.23102E-07	4.10338E-09	9.31982E-08	2.65941E-02	3.7341E-04
78	200.00	2.05267E-07	4.10534E-08	4.03350E-03	1.23160E-07	4.10534E-09	9.34134E-08	2.81994E-02	3.7359E-04
79	210.00	2.05337E-07	4.10674E-08	4.03487E-03	1.23202E-07	4.10674E-09	9.35729E-08	2.98047E-02	3.7371E-04
80	220.00	2.05387E-07	4.10774E-08	4.03585E-03	1.23232E-07	4.10774E-09	9.36908E-08	3.14100E-02	3.7380E-04
81	230.00	2.05422E-07	4.10845E-08	4.03655E-03	1.23253E-07	4.10845E-09	9.37778E-08	3.30152E-02	3.7387E-04
82	240.00	2.05448E-07	4.10896E-08	4.03705E-03	1.23269E-07	4.10896E-09	9.38419E-08	3.46200E-02	3.7392E-04
83	250.00	2.05466E-07	4.10932E-08	4.03741E-03	1.23280E-07	4.10932E-09	9.38890E-08	3.62246E-02	3.7395E-04
84	260.00	2.05479E-07	4.10958E-08	4.03766E-03	1.23287E-07	4.10958E-09	9.39236E-08	3.78288E-02	3.7397E-04
85	270.00	2.05488E-07	4.10977E-08	4.03785E-03	1.23293E-07	4.10977E-09	9.39489E-08	3.94326E-02	3.7399E-04
86	280.00	2.05495E-07	4.10990E-08	4.03798E-03	1.23297E-07	4.10990E-09	9.39675E-08	4.10360E-02	3.7400E-04
87	290.00	2.05500E-07	4.10999E-08	4.03807E-03	1.23300E-07	4.10999E-09	9.39810E-08	4.26389E-02	3.7401E-04

conc_plot / conc_plot_porevol / implicit_FD

Figure F-3. Spreadsheet "Transport_Calc_all_colloids.xls;" Calculated Solutions and Equation Terms, Iterated in Time, for Mixing Cell Colloid Model, Time 0 – 290 Years

	J	K	L	M	N	O	P	Q	R	S	T
56											
57	c_Pu_FeO_c [g/kg]	c_Pu_FeO_CP [g/kg]	c_PU_WF_c [g/kg]	c_Pu_GW_c [g/kg]	c_Irrv_Pu_c [g/kg]	c_Irrv_Pu_CP [g/kg]	time	left_bddy_flux [kg]	right_bddy colloid flux [kg]	right bddy total flux [kg]	col_out/total_out
58	0	0			0	0					
59	5.8754E-04	1.4689E-04	1.1751E-02	1.1751E-02	4.0882E-04	5.8737E-05	10.00	3.70265E-03	5.63835E-08	1.18137E-07	4.77273E-01
60	1.0071E-03	2.5178E-04	2.0142E-02	2.0142E-02	9.8521E-04	1.5940E-04	20.00	3.70256E-03	1.02339E-07	2.06191E-07	4.91565E-01
61	1.3067E-03	3.2668E-04	2.6135E-02	2.6135E-02	1.5948E-03	2.8999E-04	30.00	3.70250E-03	1.39118E-07	2.76460E-07	5.03210E-01
62	1.5207E-03	3.8017E-04	3.0414E-02	3.0414E-02	2.1677E-03	4.4193E-04	40.00	3.70246E-03	1.68137E-07	3.27967E-07	5.12663E-01
63	1.6735E-03	4.1837E-04	3.3469E-02	3.3469E-02	2.6726E-03	6.0911E-04	50.00	3.70242E-03	1.90777E-07	3.66667E-07	5.20301E-01
64	1.7826E-03	4.4565E-04	3.5652E-02	3.5652E-02	3.1001E-03	7.8714E-04	60.00	3.70240E-03	2.08279E-07	3.95636E-07	5.26441E-01
65	1.8605E-03	4.6512E-04	3.7210E-02	3.7210E-02	3.4516E-03	9.7291E-04	70.00	3.70238E-03	2.21706E-07	4.17252E-07	5.31347E-01
66	1.9161E-03	4.7903E-04	3.8323E-02	3.8323E-02	3.7349E-03	1.1642E-03	80.00	3.70237E-03	2.31940E-07	4.33334E-07	5.35245E-01
67	1.9559E-03	4.8897E-04	3.9117E-02	3.9117E-02	3.9597E-03	1.3594E-03	90.00	3.70236E-03	2.39697E-07	4.45268E-07	5.38322E-01
68	1.9842E-03	4.9606E-04	3.9685E-02	3.9685E-02	4.1358E-03	1.5574E-03	100.00	3.70236E-03	2.45550E-07	4.54103E-07	5.40737E-01
69	2.0045E-03	5.0113E-04	4.0090E-02	4.0090E-02	4.2725E-03	1.7573E-03	110.00	3.70235E-03	2.49947E-07	4.60629E-07	5.42621E-01
70	2.0190E-03	5.0474E-04	4.0379E-02	4.0379E-02	4.3777E-03	1.9586E-03	120.00	3.70235E-03	2.53238E-07	4.65441E-07	5.44062E-01
71	2.0293E-03	5.0733E-04	4.0586E-02	4.0586E-02	4.4580E-03	2.1609E-03	130.00	3.70235E-03	2.55694E-07	4.68983E-07	5.45210E-01
72	2.0367E-03	5.0917E-04	4.0734E-02	4.0734E-02	4.5191E-03	2.3639E-03	140.00	3.70235E-03	2.57521E-07	4.71586E-07	5.46075E-01
73	2.0420E-03	5.1049E-04	4.0839E-02	4.0839E-02	4.5652E-03	2.5674E-03	150.00	3.70235E-03	2.58877E-07	4.73495E-07	5.46736E-01
74	2.0457E-03	5.1143E-04	4.0914E-02	4.0914E-02	4.5999E-03	2.7712E-03	160.00	3.70235E-03	2.59880E-07	4.74894E-07	5.47238E-01
75	2.0484E-03	5.1210E-04	4.0968E-02	4.0968E-02	4.6260E-03	2.9752E-03	170.00	3.70235E-03	2.60622E-07	4.75918E-07	5.47619E-01
76	2.0503E-03	5.1258E-04	4.1006E-02	4.1006E-02	4.6454E-03	3.1793E-03	180.00	3.70234E-03	2.61168E-07	4.76666E-07	5.47906E-01
77	2.0517E-03	5.1292E-04	4.1034E-02	4.1034E-02	4.6599E-03	3.3835E-03	190.00	3.70234E-03	2.61570E-07	4.77212E-07	5.48122E-01
78	2.0527E-03	5.1317E-04	4.1053E-02	4.1053E-02	4.6707E-03	3.5877E-03	200.00	3.70234E-03	2.61866E-07	4.77611E-07	5.48283E-01
79	2.0534E-03	5.1334E-04	4.1067E-02	4.1067E-02	4.6786E-03	3.7920E-03	210.00	3.70234E-03	2.62083E-07	4.77901E-07	5.48404E-01
80	2.0539E-03	5.1347E-04	4.1077E-02	4.1077E-02	4.6845E-03	3.9962E-03	220.00	3.70234E-03	2.62242E-07	4.78112E-07	5.48494E-01
81	2.0542E-03	5.1356E-04	4.1084E-02	4.1084E-02	4.6889E-03	4.2004E-03	230.00	3.70234E-03	2.62358E-07	4.78266E-07	5.48561E-01
82	2.0545E-03	5.1362E-04	4.1090E-02	4.1090E-02	4.6921E-03	4.4046E-03	240.00	3.70234E-03	2.62443E-07	4.78378E-07	5.48610E-01
83	2.0547E-03	5.1367E-04	4.1093E-02	4.1093E-02	4.6944E-03	4.6087E-03	250.00	3.70234E-03	2.62505E-07	4.78459E-07	5.48647E-01
84	2.0548E-03	5.1370E-04	4.1096E-02	4.1096E-02	4.6962E-03	4.8128E-03	260.00	3.70234E-03	2.62550E-07	4.78518E-07	5.48674E-01
85	2.0549E-03	5.1372E-04	4.1098E-02	4.1098E-02	4.6974E-03	5.0169E-03	270.00	3.70234E-03	2.62583E-07	4.78561E-07	5.48694E-01
86	2.0549E-03	5.1374E-04	4.1099E-02	4.1099E-02	4.6984E-03	5.2209E-03	280.00	3.70234E-03	2.62607E-07	4.78592E-07	5.48709E-01
87	2.0550E-03	5.1375E-04	4.1100E-02	4.1100E-02	4.6991E-03	5.4248E-03	290.00	3.70234E-03	2.62625E-07	4.78614E-07	5.48719E-01

conc_plot / conc_plot_porevol / implicit_FD

Figure F-4. Spreadsheet "Transport_Calc_all_colloids.xls;" Additional Calculated Solutions and Equation Terms, Iterated in Time, for Mixing Cell Colloid Model, Time 0 – 290 Years

	U	V	W	X	Y	Z	AA	AB	AC
56		Pu mass balance				Irreversible Pu mass balance			
57	flux_out/flux_in	change mass [kg]	in - out [kg]	react/decay [kg]	PU mass balance	change mass [kg]	in-out [kg]	react/decay [kg]	Irrv_Pu mass balance
58									
59	3.19060E-05	2.64418E-03	3.70254E-03	-1.05836E-03	0.00000E+00	1.05729E-03	-8.18050E-09	1.05730E-03	0.00000E+00
60	5.62289E-05	1.88823E-03	3.70238E-03	-1.81415E-03	0.00000E+00	1.81200E-03	-1.97143E-08	1.81202E-03	0.00000E+00
61	7.46685E-05	1.34840E-03	3.70226E-03	-2.35386E-03	0.00000E+00	2.35063E-03	-3.19113E-08	2.35067E-03	0.00000E+00
62	8.85810E-05	9.62903E-04	3.70217E-03	-2.73927E-03	0.00000E+00	2.73497E-03	-4.33771E-08	2.73501E-03	0.00000E+00
63	9.90342E-05	6.87616E-04	3.70211E-03	-3.01449E-03	0.00000E+00	3.00912E-03	-5.34824E-08	3.00918E-03	0.00000E+00
64	1.06859E-04	4.91032E-04	3.70207E-03	-3.21104E-03	0.00000E+00	3.20459E-03	-6.20329E-08	3.20466E-03	0.00000E+00
65	1.12698E-04	3.50650E-04	3.70204E-03	-3.35139E-03	0.00000E+00	3.34388E-03	-6.90672E-08	3.34394E-03	0.00000E+00
66	1.17042E-04	2.50402E-04	3.70201E-03	-3.45161E-03	0.00000E+00	3.44303E-03	-7.47364E-08	3.44311E-03	0.00000E+00
67	1.20266E-04	1.78814E-04	3.70200E-03	-3.52318E-03	0.00000E+00	3.51354E-03	-7.92343E-08	3.51362E-03	4.33681E-18
68	1.22652E-04	1.27692E-04	3.70199E-03	-3.57430E-03	0.00000E+00	3.56359E-03	-8.27591E-08	3.56367E-03	0.00000E+00
69	1.24415E-04	9.11861E-05	3.70198E-03	-3.61079E-03	0.00000E+00	3.59902E-03	-8.54937E-08	3.59911E-03	4.77049E-18
70	1.25715E-04	6.51167E-05	3.70197E-03	-3.63686E-03	0.00000E+00	3.62402E-03	-8.75980E-08	3.62411E-03	0.00000E+00
71	1.26672E-04	4.65003E-05	3.70197E-03	-3.65547E-03	0.00000E+00	3.64157E-03	-8.92060E-08	3.64166E-03	0.00000E+00
72	1.27375E-04	3.32062E-05	3.70197E-03	-3.66876E-03	0.00000E+00	3.65380E-03	-9.04276E-08	3.65389E-03	1.04083E-17
73	1.27890E-04	2.37126E-05	3.70196E-03	-3.67825E-03	0.00000E+00	3.66223E-03	-9.13510E-08	3.66232E-03	6.07153E-18
74	1.28268E-04	1.69335E-05	3.70196E-03	-3.68503E-03	0.00000E+00	3.66795E-03	-9.20458E-08	3.66804E-03	0.00000E+00
75	1.28545E-04	1.20924E-05	3.70196E-03	-3.68987E-03	0.00000E+00	3.67173E-03	-9.25668E-08	3.67182E-03	1.08420E-17
76	1.28747E-04	8.63525E-06	3.70196E-03	-3.69333E-03	0.00000E+00	3.67413E-03	-9.29559E-08	3.67422E-03	7.80626E-18
77	1.28895E-04	6.16650E-06	3.70196E-03	-3.69579E-03	0.00000E+00	3.67554E-03	-9.32458E-08	3.67563E-03	0.00000E+00
78	1.29002E-04	4.40354E-06	3.70196E-03	-3.69756E-03	0.00000E+00	3.67624E-03	-9.34611E-08	3.67633E-03	3.90313E-18
79	1.29081E-04	3.14460E-06	3.70196E-03	-3.69882E-03	0.00000E+00	3.67644E-03	-9.36207E-08	3.67654E-03	1.21431E-17
80	1.29138E-04	2.24559E-06	3.70196E-03	-3.69971E-03	0.00000E+00	3.67628E-03	-9.37386E-08	3.67638E-03	8.67362E-18
81	1.29179E-04	1.60359E-06	3.70196E-03	-3.70036E-03	0.00000E+00	3.67587E-03	-9.38257E-08	3.67596E-03	5.20417E-18
82	1.29209E-04	1.14514E-06	3.70196E-03	-3.70081E-03	0.00000E+00	3.67527E-03	-9.38898E-08	3.67536E-03	0.00000E+00
83	1.29231E-04	8.17751E-07	3.70196E-03	-3.70114E-03	0.00000E+00	3.67454E-03	-9.39369E-08	3.67463E-03	3.46945E-18
84	1.29247E-04	5.83962E-07	3.70196E-03	-3.70138E-03	0.00000E+00	3.67372E-03	-9.39715E-08	3.67381E-03	9.54098E-18
85	1.29259E-04	4.17012E-07	3.70196E-03	-3.70154E-03	0.00000E+00	3.67283E-03	-9.39969E-08	3.67292E-03	1.34441E-17
86	1.29267E-04	2.97791E-07	3.70196E-03	-3.70166E-03	0.00000E+00	3.67189E-03	-9.40154E-08	3.67199E-03	0.00000E+00
87	1.29273E-04	2.12655E-07	3.70196E-03	-3.70175E-03	0.00000E+00	3.67092E-03	-9.40290E-08	3.67102E-03	0.00000E+00

conc_plot / conc_plot_porevol / implicit_FD

Figure F-5. Spreadsheet "Transport_Calc_all_colloids.xls;" Final Calculated Solutions and Equation Terms, Iterated in Time, for Mixing Cell Colloid Model, Time 0 – 290 Years

	A	B	C	D	E	F	G	H	I
88	300.00	2.05503E-07	4.11006E-08	4.03813E-03	1.23302E-07	4.11006E-09	9.39910E-08	4.42415E-02	3.7402E-04
89	310.00	2.05505E-07	4.11011E-08	4.03818E-03	1.23303E-07	4.11011E-09	9.39982E-08	4.58436E-02	3.7402E-04
90	320.00	2.05507E-07	4.11014E-08	4.03822E-03	1.23304E-07	4.11014E-09	9.40035E-08	4.74452E-02	3.7402E-04
91	330.00	2.05508E-07	4.11017E-08	4.03824E-03	1.23305E-07	4.11017E-09	9.40073E-08	4.90464E-02	3.7403E-04
92	340.00	2.05509E-07	4.11019E-08	4.03826E-03	1.23306E-07	4.11019E-09	9.40101E-08	5.06472E-02	3.7403E-04
93	350.00	2.05510E-07	4.11020E-08	4.03827E-03	1.23306E-07	4.11020E-09	9.40121E-08	5.22474E-02	3.7403E-04
94	360.00	2.05510E-07	4.11021E-08	4.03828E-03	1.23306E-07	4.11021E-09	9.40136E-08	5.38473E-02	3.7403E-04
95	370.00	2.05511E-07	4.11021E-08	4.03828E-03	1.23306E-07	4.11021E-09	9.40147E-08	5.54466E-02	3.7403E-04
96	380.00	2.05511E-07	4.11022E-08	4.03829E-03	1.23307E-07	4.11022E-09	9.40155E-08	5.70456E-02	3.7403E-04
97	390.00	2.05511E-07	4.11022E-08	4.03829E-03	1.23307E-07	4.11022E-09	9.40160E-08	5.86440E-02	3.7403E-04
98	400.00	2.05511E-07	4.11022E-08	4.03829E-03	1.23307E-07	4.11022E-09	9.40164E-08	6.02420E-02	3.7403E-04
99	410.00	2.05511E-07	4.11022E-08	4.03830E-03	1.23307E-07	4.11022E-09	9.40167E-08	6.18396E-02	3.7403E-04
100	420.00	2.05511E-07	4.11023E-08	4.03830E-03	1.23307E-07	4.11023E-09	9.40169E-08	6.34366E-02	3.7403E-04
101	430.00	2.05511E-07	4.11023E-08	4.03830E-03	1.23307E-07	4.11023E-09	9.40171E-08	6.50333E-02	3.7403E-04
102	440.00	2.05511E-07	4.11023E-08	4.03830E-03	1.23307E-07	4.11023E-09	9.40172E-08	6.66294E-02	3.7403E-04
103	450.00	2.05511E-07	4.11023E-08	4.03830E-03	1.23307E-07	4.11023E-09	9.40173E-08	6.82251E-02	3.7403E-04
104	460.00	2.05511E-07	4.11023E-08	4.03830E-03	1.23307E-07	4.11023E-09	9.40173E-08	6.98204E-02	3.7403E-04
105	470.00	2.05511E-07	4.11023E-08	4.03830E-03	1.23307E-07	4.11023E-09	9.40174E-08	7.14152E-02	3.7403E-04
106	480.00	2.05511E-07	4.11023E-08	4.03830E-03	1.23307E-07	4.11023E-09	9.40174E-08	7.30095E-02	3.7403E-04
107	490.00	2.05511E-07	4.11023E-08	4.03830E-03	1.23307E-07	4.11023E-09	9.40174E-08	7.46034E-02	3.7403E-04
108	500.00	2.05511E-07	4.11023E-08	4.03830E-03	1.23307E-07	4.11023E-09	9.40175E-08	7.61968E-02	3.7403E-04
109	510.00	2.05511E-07	4.11023E-08	4.03830E-03	1.23307E-07	4.11023E-09	9.40175E-08	7.77897E-02	3.7403E-04
110	520.00	2.05511E-07	4.11023E-08	4.03830E-03	1.23307E-07	4.11023E-09	9.40175E-08	7.93822E-02	3.7403E-04
111	530.00	2.05511E-07	4.11023E-08	4.03830E-03	1.23307E-07	4.11023E-09	9.40175E-08	8.09743E-02	3.7403E-04
112	540.00	2.05511E-07	4.11023E-08	4.03830E-03	1.23307E-07	4.11023E-09	9.40175E-08	8.25659E-02	3.7403E-04
113	550.00	2.05511E-07	4.11023E-08	4.03830E-03	1.23307E-07	4.11023E-09	9.40175E-08	8.41570E-02	3.7403E-04
114	560.00	2.05511E-07	4.11023E-08	4.03830E-03	1.23307E-07	4.11023E-09	9.40175E-08	8.57476E-02	3.7403E-04
115	570.00	2.05511E-07	4.11023E-08	4.03830E-03	1.23307E-07	4.11023E-09	9.40175E-08	8.73379E-02	3.7403E-04
116	580.00	2.05511E-07	4.11023E-08	4.03830E-03	1.23307E-07	4.11023E-09	9.40175E-08	8.89276E-02	3.7403E-04
117	590.00	2.05511E-07	4.11023E-08	4.03830E-03	1.23307E-07	4.11023E-09	9.40175E-08	9.05169E-02	3.7403E-04
118	600.00	2.05511E-07	4.11023E-08	4.03830E-03	1.23307E-07	4.11023E-09	9.40175E-08	9.21057E-02	3.7403E-04
119	610.00	2.05511E-07	4.11023E-08	4.03830E-03	1.23307E-07	4.11023E-09	9.40175E-08	9.36941E-02	3.7403E-04
120	620.00	2.05511E-07	4.11023E-08	4.03830E-03	1.23307E-07	4.11023E-09	9.40175E-08	9.52621E-02	3.7403E-04
121	630.00	2.05511E-07	4.11023E-08	4.03830E-03	1.23307E-07	4.11023E-09	9.40175E-08	9.68695E-02	3.7403E-04

conc_plot / conc_plot_porevol / Implicit_FD

Figure F-6. Spreadsheet "Transport_Calc_all_colloids.xls;" Calculated Solutions and Equation Terms, Iterated in Time, for Mixing Cell Colloid Model, Time 300 – 630 Years

	J	K	L	M	N	O	P	Q	R	S	T
88	2.0550E-03	5.1376E-04	4.1101E-02	4.1101E-02	4.6995E-03	5.6287E-03	300.00	3.70234E-03	2.62637E-07	4.78630E-07	5.48727E-01
89	2.0551E-03	5.1376E-04	4.1101E-02	4.1101E-02	4.6999E-03	5.8325E-03	310.00	3.70234E-03	2.62647E-07	4.78642E-07	5.48733E-01
90	2.0551E-03	5.1377E-04	4.1101E-02	4.1101E-02	4.7002E-03	6.0363E-03	320.00	3.70234E-03	2.62653E-07	4.78650E-07	5.48737E-01
91	2.0551E-03	5.1377E-04	4.1102E-02	4.1102E-02	4.7004E-03	6.2400E-03	330.00	3.70234E-03	2.62658E-07	4.78657E-07	5.48740E-01
92	2.0551E-03	5.1377E-04	4.1102E-02	4.1102E-02	4.7005E-03	6.4437E-03	340.00	3.70234E-03	2.62662E-07	4.78661E-07	5.48743E-01
93	2.0551E-03	5.1377E-04	4.1102E-02	4.1102E-02	4.7006E-03	6.6473E-03	350.00	3.70234E-03	2.62664E-07	4.78664E-07	5.48744E-01
94	2.0551E-03	5.1378E-04	4.1102E-02	4.1102E-02	4.7007E-03	6.8508E-03	360.00	3.70234E-03	2.62666E-07	4.78667E-07	5.48745E-01
95	2.0551E-03	5.1378E-04	4.1102E-02	4.1102E-02	4.7007E-03	7.0543E-03	370.00	3.70234E-03	2.62667E-07	4.78668E-07	5.48746E-01
96	2.0551E-03	5.1378E-04	4.1102E-02	4.1102E-02	4.7008E-03	7.2577E-03	380.00	3.70234E-03	2.62668E-07	4.78669E-07	5.48747E-01
97	2.0551E-03	5.1378E-04	4.1102E-02	4.1102E-02	4.7008E-03	7.4611E-03	390.00	3.70234E-03	2.62669E-07	4.78670E-07	5.48747E-01
98	2.0551E-03	5.1378E-04	4.1102E-02	4.1102E-02	4.7008E-03	7.6644E-03	400.00	3.70234E-03	2.62670E-07	4.78671E-07	5.48748E-01
99	2.0551E-03	5.1378E-04	4.1102E-02	4.1102E-02	4.7008E-03	7.8676E-03	410.00	3.70234E-03	2.62670E-07	4.78671E-07	5.48748E-01
100	2.0551E-03	5.1378E-04	4.1102E-02	4.1102E-02	4.7008E-03	8.0708E-03	420.00	3.70234E-03	2.62670E-07	4.78672E-07	5.48748E-01
101	2.0551E-03	5.1378E-04	4.1102E-02	4.1102E-02	4.7009E-03	8.2740E-03	430.00	3.70234E-03	2.62670E-07	4.78672E-07	5.48748E-01
102	2.0551E-03	5.1378E-04	4.1102E-02	4.1102E-02	4.7009E-03	8.4770E-03	440.00	3.70234E-03	2.62671E-07	4.78672E-07	5.48748E-01
103	2.0551E-03	5.1378E-04	4.1102E-02	4.1102E-02	4.7009E-03	8.6800E-03	450.00	3.70234E-03	2.62671E-07	4.78672E-07	5.48748E-01
104	2.0551E-03	5.1378E-04	4.1102E-02	4.1102E-02	4.7009E-03	8.8830E-03	460.00	3.70234E-03	2.62671E-07	4.78672E-07	5.48749E-01
105	2.0551E-03	5.1378E-04	4.1102E-02	4.1102E-02	4.7009E-03	9.0859E-03	470.00	3.70234E-03	2.62671E-07	4.78672E-07	5.48749E-01
106	2.0551E-03	5.1378E-04	4.1102E-02	4.1102E-02	4.7009E-03	9.2887E-03	480.00	3.70234E-03	2.62671E-07	4.78672E-07	5.48749E-01
107	2.0551E-03	5.1378E-04	4.1102E-02	4.1102E-02	4.7009E-03	9.4915E-03	490.00	3.70234E-03	2.62671E-07	4.78672E-07	5.48749E-01
108	2.0551E-03	5.1378E-04	4.1102E-02	4.1102E-02	4.7009E-03	9.6942E-03	500.00	3.70234E-03	2.62671E-07	4.78672E-07	5.48749E-01
109	2.0551E-03	5.1378E-04	4.1102E-02	4.1102E-02	4.7009E-03	9.8969E-03	510.00	3.70234E-03	2.62671E-07	4.78672E-07	5.48749E-01
110	2.0551E-03	5.1378E-04	4.1102E-02	4.1102E-02	4.7009E-03	1.0100E-02	520.00	3.70234E-03	2.62671E-07	4.78672E-07	5.48749E-01
111	2.0551E-03	5.1378E-04	4.1102E-02	4.1102E-02	4.7009E-03	1.0302E-02	530.00	3.70234E-03	2.62671E-07	4.78672E-07	5.48749E-01
112	2.0551E-03	5.1378E-04	4.1102E-02	4.1102E-02	4.7009E-03	1.0505E-02	540.00	3.70234E-03	2.62671E-07	4.78673E-07	5.48749E-01
113	2.0551E-03	5.1378E-04	4.1102E-02	4.1102E-02	4.7009E-03	1.0707E-02	550.00	3.70234E-03	2.62671E-07	4.78673E-07	5.48749E-01
114	2.0551E-03	5.1378E-04	4.1102E-02	4.1102E-02	4.7009E-03	1.0909E-02	560.00	3.70234E-03	2.62671E-07	4.78673E-07	5.48749E-01
115	2.0551E-03	5.1378E-04	4.1102E-02	4.1102E-02	4.7009E-03	1.1112E-02	570.00	3.70234E-03	2.62671E-07	4.78673E-07	5.48749E-01
116	2.0551E-03	5.1378E-04	4.1102E-02	4.1102E-02	4.7009E-03	1.1314E-02	580.00	3.70234E-03	2.62671E-07	4.78673E-07	5.48749E-01
117	2.0551E-03	5.1378E-04	4.1102E-02	4.1102E-02	4.7009E-03	1.1516E-02	590.00	3.70234E-03	2.62671E-07	4.78673E-07	5.48749E-01
118	2.0551E-03	5.1378E-04	4.1102E-02	4.1102E-02	4.7009E-03	1.1718E-02	600.00	3.70234E-03	2.62671E-07	4.78673E-07	5.48749E-01
119	2.0551E-03	5.1378E-04	4.1102E-02	4.1102E-02	4.7009E-03	1.1920E-02	610.00	3.70234E-03	2.62671E-07	4.78673E-07	5.48749E-01
120	2.0551E-03	5.1378E-04	4.1102E-02	4.1102E-02	4.7009E-03	1.2122E-02	620.00	3.70234E-03	2.62671E-07	4.78673E-07	5.48749E-01
121	2.0551E-03	5.1378E-04	4.1102E-02	4.1102E-02	4.7009E-03	1.2324E-02	630.00	3.70234E-03	2.62671E-07	4.78673E-07	5.48749E-01

conc_plot / conc_plot_porevol / Implicit_FD

Figure F-7. Spreadsheet "Transport_Calc_all_colloids.xls;" Additional Calculated Solutions and Equation Terms, Iterated in Time, for Mixing Cell Colloid Model, Time 300 – 630 Years

	U	V	W	X	Y	Z	AA	AB	AC
88	1.29278E-04	1.51859E-07	3.70196E-03	-3.70181E-03	0.00000E+00	3.66993E-03	-9.40389E-08	3.67002E-03	0.00000E+00
89	1.29281E-04	1.08443E-07	3.70196E-03	-3.70185E-03	0.00000E+00	3.66892E-03	-9.40462E-08	3.66901E-03	8.23994E-18
90	1.29283E-04	7.74403E-08	3.70196E-03	-3.70188E-03	0.00000E+00	3.66789E-03	-9.40515E-08	3.66799E-03	1.60462E-17
91	1.29285E-04	5.53007E-08	3.70196E-03	-3.70190E-03	0.00000E+00	3.66686E-03	-9.40553E-08	3.66695E-03	9.97466E-18
92	1.29286E-04	3.94907E-08	3.70196E-03	-3.70192E-03	0.00000E+00	3.66582E-03	-9.40581E-08	3.66592E-03	1.47451E-17
93	1.29287E-04	2.82006E-08	3.70196E-03	-3.70193E-03	0.00000E+00	3.66478E-03	-9.40601E-08	3.66487E-03	9.97466E-18
94	1.29287E-04	2.01383E-08	3.70196E-03	-3.70194E-03	0.00000E+00	3.66373E-03	-9.40616E-08	3.66383E-03	2.03830E-17
95	1.29288E-04	1.43809E-08	3.70196E-03	-3.70194E-03	0.00000E+00	3.66269E-03	-9.40627E-08	3.66278E-03	6.07153E-18
96	1.29288E-04	1.02695E-08	3.70196E-03	-3.70195E-03	0.00000E+00	3.66164E-03	-9.40634E-08	3.66173E-03	1.43115E-17
97	1.29288E-04	7.33353E-09	3.70196E-03	-3.70195E-03	0.00000E+00	3.66059E-03	-9.40640E-08	3.66068E-03	1.64799E-17
98	1.29289E-04	5.23693E-09	3.70196E-03	-3.70195E-03	0.00000E+00	3.65954E-03	-9.40644E-08	3.65963E-03	1.73472E-17
99	1.29289E-04	3.73973E-09	3.70196E-03	-3.70196E-03	0.00000E+00	3.65849E-03	-9.40647E-08	3.65858E-03	6.93889E-18
100	1.29289E-04	2.67057E-09	3.70196E-03	-3.70196E-03	0.00000E+00	3.65744E-03	-9.40649E-08	3.65753E-03	0.00000E+00
101	1.29289E-04	1.90708E-09	3.70196E-03	-3.70196E-03	0.00000E+00	3.65639E-03	-9.40651E-08	3.65648E-03	7.37257E-18
102	1.29289E-04	1.36186E-09	3.70196E-03	-3.70196E-03	0.00000E+00	3.65534E-03	-9.40652E-08	3.65543E-03	-8.23994E-18
103	1.29289E-04	9.72513E-10	3.70196E-03	-3.70196E-03	0.00000E+00	3.65429E-03	-9.40653E-08	3.65438E-03	2.90566E-17
104	1.29289E-04	6.94479E-10	3.70196E-03	-3.70196E-03	0.00000E+00	3.65324E-03	-9.40653E-08	3.65333E-03	5.63785E-18
105	1.29289E-04	4.95933E-10	3.70196E-03	-3.70196E-03	0.00000E+00	3.65219E-03	-9.40654E-08	3.65228E-03	0.00000E+00
106	1.29289E-04	3.54150E-10	3.70196E-03	-3.70196E-03	0.00000E+00	3.65114E-03	-9.40654E-08	3.65123E-03	-4.77049E-18
107	1.29289E-04	2.52901E-10	3.70196E-03	-3.70196E-03	0.00000E+00	3.65009E-03	-9.40654E-08	3.65018E-03	5.20417E-18
108	1.29289E-04	1.80599E-10	3.70196E-03	-3.70196E-03	0.00000E+00	3.64904E-03	-9.40654E-08	3.64913E-03	2.16840E-17
109	1.29289E-04	1.28967E-10	3.70196E-03	-3.70196E-03	0.00000E+00	3.64799E-03	-9.40655E-08	3.64808E-03	1.25767E-17
110	1.29289E-04	9.20962E-11	3.70196E-03	-3.70196E-03	0.00000E+00	3.64694E-03	-9.40655E-08	3.64704E-03	1.56125E-17
111	1.29289E-04	6.57666E-11	3.70196E-03	-3.70196E-03	0.00000E+00	3.64589E-03	-9.40655E-08	3.64599E-03	3.20924E-17
112	1.29289E-04	4.69644E-11	3.70196E-03	-3.70196E-03	0.00000E+00	3.64485E-03	-9.40655E-08	3.64494E-03	3.90313E-18
113	1.29289E-04	3.35377E-11	3.70196E-03	-3.70196E-03	0.00000E+00	3.64380E-03	-9.40655E-08	3.64389E-03	3.07913E-17
114	1.29289E-04	2.39495E-11	3.70196E-03	-3.70196E-03	0.00000E+00	3.64275E-03	-9.40655E-08	3.64285E-03	-4.77049E-18
115	1.29289E-04	1.71025E-11	3.70196E-03	-3.70196E-03	0.00000E+00	3.64170E-03	-9.40655E-08	3.64180E-03	1.30104E-17
116	1.29289E-04	1.22130E-11	3.70196E-03	-3.70196E-03	0.00000E+00	3.64066E-03	-9.40655E-08	3.64075E-03	3.20924E-17
117	1.29289E-04	8.72143E-12	3.70196E-03	-3.70196E-03	0.00000E+00	3.63961E-03	-9.40655E-08	3.63971E-03	4.42354E-17
118	1.29289E-04	6.22804E-12	3.70196E-03	-3.70196E-03	0.00000E+00	3.63857E-03	-9.40655E-08	3.63866E-03	1.30104E-17
119	1.29289E-04	4.44749E-12	3.70196E-03	-3.70196E-03	0.00000E+00	3.63752E-03	-9.40655E-08	3.63761E-03	7.37257E-18
120	1.29289E-04	3.17599E-12	3.70196E-03	-3.70196E-03	0.00000E+00	3.63647E-03	-9.40655E-08	3.63657E-03	0.00000E+00
121	1.29289E-04	2.26800E-12	3.70196E-03	-3.70196E-03	0.00000E+00	3.63543E-03	-9.40655E-08	3.63552E-03	1.82146E-17

conc_plot / conc_plot_porevol / implicit_FD

Figure F-8. Spreadsheet "Transport_Calc_all_colloids.xls;" Final Calculated Solutions and Equation Terms, Iterated in Time, for Mixing Cell Colloid Model, Time 300 – 630 Years

	A	B	C	D	E	F	G	H	I
122	640.00	2.05511E-07	4.11023E-08	4.03830E-03	1.23307E-07	4.11023E-09	9.40175E-08	9.84565E-02	3.7403E-04
123	650.00	2.05511E-07	4.11023E-08	4.03830E-03	1.23307E-07	4.11023E-09	9.40175E-08	1.00043E-01	3.7403E-04
124	660.00	2.05511E-07	4.11023E-08	4.03830E-03	1.23307E-07	4.11023E-09	9.40175E-08	1.01629E-01	3.7403E-04
125	670.00	2.05511E-07	4.11023E-08	4.03830E-03	1.23307E-07	4.11023E-09	9.40175E-08	1.03215E-01	3.7403E-04
126	680.00	2.05511E-07	4.11023E-08	4.03830E-03	1.23307E-07	4.11023E-09	9.40175E-08	1.04800E-01	3.7403E-04
127	690.00	2.05511E-07	4.11023E-08	4.03830E-03	1.23307E-07	4.11023E-09	9.40175E-08	1.06385E-01	3.7403E-04
128	700.00	2.05511E-07	4.11023E-08	4.03830E-03	1.23307E-07	4.11023E-09	9.40175E-08	1.07969E-01	3.7403E-04
129	710.00	2.05511E-07	4.11023E-08	4.03830E-03	1.23307E-07	4.11023E-09	9.40175E-08	1.09553E-01	3.7403E-04
130	720.00	2.05511E-07	4.11023E-08	4.03830E-03	1.23307E-07	4.11023E-09	9.40175E-08	1.11136E-01	3.7403E-04
131	730.00	2.05511E-07	4.11023E-08	4.03830E-03	1.23307E-07	4.11023E-09	9.40175E-08	1.12719E-01	3.7403E-04
132	740.00	2.05511E-07	4.11023E-08	4.03830E-03	1.23307E-07	4.11023E-09	9.40175E-08	1.14302E-01	3.7403E-04
133	750.00	2.05511E-07	4.11023E-08	4.03830E-03	1.23307E-07	4.11023E-09	9.40175E-08	1.15884E-01	3.7403E-04
134	760.00	2.05511E-07	4.11023E-08	4.03830E-03	1.23307E-07	4.11023E-09	9.40175E-08	1.17465E-01	3.7403E-04
135	770.00	2.05511E-07	4.11023E-08	4.03830E-03	1.23307E-07	4.11023E-09	9.40175E-08	1.19046E-01	3.7403E-04
136	780.00	2.05511E-07	4.11023E-08	4.03830E-03	1.23307E-07	4.11023E-09	9.40175E-08	1.20627E-01	3.7403E-04
137	790.00	2.05511E-07	4.11023E-08	4.03830E-03	1.23307E-07	4.11023E-09	9.40175E-08	1.22207E-01	3.7403E-04
138	800.00	2.05511E-07	4.11023E-08	4.03830E-03	1.23307E-07	4.11023E-09	9.40175E-08	1.23787E-01	3.7403E-04
139	810.00	2.05511E-07	4.11023E-08	4.03830E-03	1.23307E-07	4.11023E-09	9.40175E-08	1.25366E-01	3.7403E-04
140	820.00	2.05511E-07	4.11023E-08	4.03830E-03	1.23307E-07	4.11023E-09	9.40175E-08	1.26945E-01	3.7403E-04
141	830.00	2.05511E-07	4.11023E-08	4.03830E-03	1.23307E-07	4.11023E-09	9.40175E-08	1.28523E-01	3.7403E-04
142	840.00	2.05511E-07	4.11023E-08	4.03830E-03	1.23307E-07	4.11023E-09	9.40175E-08	1.30101E-01	3.7403E-04
143	850.00	2.05511E-07	4.11023E-08	4.03830E-03	1.23307E-07	4.11023E-09	9.40175E-08	1.31679E-01	3.7403E-04
144	860.00	2.05511E-07	4.11023E-08	4.03830E-03	1.23307E-07	4.11023E-09	9.40175E-08	1.33256E-01	3.7403E-04
145	870.00	2.05511E-07	4.11023E-08	4.03830E-03	1.23307E-07	4.11023E-09	9.40175E-08	1.34832E-01	3.7403E-04
146	880.00	2.05511E-07	4.11023E-08	4.03830E-03	1.23307E-07	4.11023E-09	9.40175E-08	1.36408E-01	3.7403E-04
147	890.00	2.05511E-07	4.11023E-08	4.03830E-03	1.23307E-07	4.11023E-09	9.40175E-08	1.37984E-01	3.7403E-04
148	900.00	2.05511E-07	4.11023E-08	4.03830E-03	1.23307E-07	4.11023E-09	9.40175E-08	1.39559E-01	3.7403E-04
149	910.00	2.05511E-07	4.11023E-08	4.03830E-03	1.23307E-07	4.11023E-09	9.40175E-08	1.41134E-01	3.7403E-04
150	920.00	2.05511E-07	4.11023E-08	4.03830E-03	1.23307E-07	4.11023E-09	9.40175E-08	1.42708E-01	3.7403E-04
151	930.00	2.05511E-07	4.11023E-08	4.03830E-03	1.23307E-07	4.11023E-09	9.40175E-08	1.44282E-01	3.7403E-04
152	940.00	2.05511E-07	4.11023E-08	4.03830E-03	1.23307E-07	4.11023E-09	9.40175E-08	1.45855E-01	3.7403E-04
153	950.00	2.05511E-07	4.11023E-08	4.03830E-03	1.23307E-07	4.11023E-09	9.40175E-08	1.47428E-01	3.7403E-04
154	960.00	2.05511E-07	4.11023E-08	4.03830E-03	1.23307E-07	4.11023E-09	9.40175E-08	1.49001E-01	3.7403E-04
155	970.00	2.05511E-07	4.11023E-08	4.03830E-03	1.23307E-07	4.11023E-09	9.40175E-08	1.50573E-01	3.7403E-04

conc_plot / conc_plot_porevol / implicit_FD

Figure F-9. Spreadsheet "Transport_Calc_all_colloids.xls;" Calculated Solutions and Equation Terms, Iterated in Time, for Mixing Cell Colloid Model, Time 640 – 970 Years

	J	K	L	M	N	O	P	Q	R	S	T
122	2.0551E-03	5.1378E-04	4.1102E-02	4.1102E-02	4.7009E-03	1.2526E-02	640.00	3.70234E-03	2.62671E-07	4.78673E-07	5.48749E-01
123	2.0551E-03	5.1378E-04	4.1102E-02	4.1102E-02	4.7009E-03	1.2728E-02	650.00	3.70234E-03	2.62671E-07	4.78673E-07	5.48749E-01
124	2.0551E-03	5.1378E-04	4.1102E-02	4.1102E-02	4.7009E-03	1.2930E-02	660.00	3.70234E-03	2.62671E-07	4.78673E-07	5.48749E-01
125	2.0551E-03	5.1378E-04	4.1102E-02	4.1102E-02	4.7009E-03	1.3132E-02	670.00	3.70234E-03	2.62671E-07	4.78673E-07	5.48749E-01
126	2.0551E-03	5.1378E-04	4.1102E-02	4.1102E-02	4.7009E-03	1.3333E-02	680.00	3.70234E-03	2.62671E-07	4.78673E-07	5.48749E-01
127	2.0551E-03	5.1378E-04	4.1102E-02	4.1102E-02	4.7009E-03	1.3535E-02	690.00	3.70234E-03	2.62671E-07	4.78673E-07	5.48749E-01
128	2.0551E-03	5.1378E-04	4.1102E-02	4.1102E-02	4.7009E-03	1.3737E-02	700.00	3.70234E-03	2.62671E-07	4.78673E-07	5.48749E-01
129	2.0551E-03	5.1378E-04	4.1102E-02	4.1102E-02	4.7009E-03	1.3938E-02	710.00	3.70234E-03	2.62671E-07	4.78673E-07	5.48749E-01
130	2.0551E-03	5.1378E-04	4.1102E-02	4.1102E-02	4.7009E-03	1.4139E-02	720.00	3.70234E-03	2.62671E-07	4.78673E-07	5.48749E-01
131	2.0551E-03	5.1378E-04	4.1102E-02	4.1102E-02	4.7009E-03	1.4341E-02	730.00	3.70234E-03	2.62671E-07	4.78673E-07	5.48749E-01
132	2.0551E-03	5.1378E-04	4.1102E-02	4.1102E-02	4.7009E-03	1.4542E-02	740.00	3.70234E-03	2.62671E-07	4.78673E-07	5.48749E-01
133	2.0551E-03	5.1378E-04	4.1102E-02	4.1102E-02	4.7009E-03	1.4743E-02	750.00	3.70234E-03	2.62671E-07	4.78673E-07	5.48749E-01
134	2.0551E-03	5.1378E-04	4.1102E-02	4.1102E-02	4.7009E-03	1.4945E-02	760.00	3.70234E-03	2.62671E-07	4.78673E-07	5.48749E-01
135	2.0551E-03	5.1378E-04	4.1102E-02	4.1102E-02	4.7009E-03	1.5146E-02	770.00	3.70234E-03	2.62671E-07	4.78673E-07	5.48749E-01
136	2.0551E-03	5.1378E-04	4.1102E-02	4.1102E-02	4.7009E-03	1.5347E-02	780.00	3.70234E-03	2.62671E-07	4.78673E-07	5.48749E-01
137	2.0551E-03	5.1378E-04	4.1102E-02	4.1102E-02	4.7009E-03	1.5548E-02	790.00	3.70234E-03	2.62671E-07	4.78673E-07	5.48749E-01
138	2.0551E-03	5.1378E-04	4.1102E-02	4.1102E-02	4.7009E-03	1.5749E-02	800.00	3.70234E-03	2.62671E-07	4.78673E-07	5.48749E-01
139	2.0551E-03	5.1378E-04	4.1102E-02	4.1102E-02	4.7009E-03	1.5950E-02	810.00	3.70234E-03	2.62671E-07	4.78673E-07	5.48749E-01
140	2.0551E-03	5.1378E-04	4.1102E-02	4.1102E-02	4.7009E-03	1.6151E-02	820.00	3.70234E-03	2.62671E-07	4.78673E-07	5.48749E-01
141	2.0551E-03	5.1378E-04	4.1102E-02	4.1102E-02	4.7009E-03	1.6352E-02	830.00	3.70234E-03	2.62671E-07	4.78673E-07	5.48749E-01
142	2.0551E-03	5.1378E-04	4.1102E-02	4.1102E-02	4.7009E-03	1.6552E-02	840.00	3.70234E-03	2.62671E-07	4.78673E-07	5.48749E-01
143	2.0551E-03	5.1378E-04	4.1102E-02	4.1102E-02	4.7009E-03	1.6753E-02	850.00	3.70234E-03	2.62671E-07	4.78673E-07	5.48749E-01
144	2.0551E-03	5.1378E-04	4.1102E-02	4.1102E-02	4.7009E-03	1.6954E-02	860.00	3.70234E-03	2.62671E-07	4.78673E-07	5.48749E-01
145	2.0551E-03	5.1378E-04	4.1102E-02	4.1102E-02	4.7009E-03	1.7154E-02	870.00	3.70234E-03	2.62671E-07	4.78673E-07	5.48749E-01
146	2.0551E-03	5.1378E-04	4.1102E-02	4.1102E-02	4.7009E-03	1.7355E-02	880.00	3.70234E-03	2.62671E-07	4.78673E-07	5.48749E-01
147	2.0551E-03	5.1378E-04	4.1102E-02	4.1102E-02	4.7009E-03	1.7555E-02	890.00	3.70234E-03	2.62671E-07	4.78673E-07	5.48749E-01
148	2.0551E-03	5.1378E-04	4.1102E-02	4.1102E-02	4.7009E-03	1.7756E-02	900.00	3.70234E-03	2.62671E-07	4.78673E-07	5.48749E-01
149	2.0551E-03	5.1378E-04	4.1102E-02	4.1102E-02	4.7009E-03	1.7956E-02	910.00	3.70234E-03	2.62671E-07	4.78673E-07	5.48749E-01
150	2.0551E-03	5.1378E-04	4.1102E-02	4.1102E-02	4.7009E-03	1.8156E-02	920.00	3.70234E-03	2.62671E-07	4.78673E-07	5.48749E-01
151	2.0551E-03	5.1378E-04	4.1102E-02	4.1102E-02	4.7009E-03	1.8356E-02	930.00	3.70234E-03	2.62671E-07	4.78673E-07	5.48749E-01
152	2.0551E-03	5.1378E-04	4.1102E-02	4.1102E-02	4.7009E-03	1.8557E-02	940.00	3.70234E-03	2.62671E-07	4.78673E-07	5.48749E-01
153	2.0551E-03	5.1378E-04	4.1102E-02	4.1102E-02	4.7009E-03	1.8757E-02	950.00	3.70234E-03	2.62671E-07	4.78673E-07	5.48749E-01
154	2.0551E-03	5.1378E-04	4.1102E-02	4.1102E-02	4.7009E-03	1.8957E-02	960.00	3.70234E-03	2.62671E-07	4.78673E-07	5.48749E-01
155	2.0551E-03	5.1378E-04	4.1102E-02	4.1102E-02	4.7009E-03	1.9157E-02	970.00	3.70234E-03	2.62671E-07	4.78673E-07	5.48749E-01

conc_plot / conc_plot_porevol / implicit_FD

Figure F-10. Spreadsheet "Transport_Calc_all_colloids.xls;" Additional Calculated Solutions and Equation Terms, Iterated in Time, for Mixing Cell Colloid Model, Time 640 – 970 Years

	U	V	W	X	Y	Z	AA	AB	AC
122	1.29289E-04	1.61959E-12	3.70196E-03	-3.70196E-03	0.00000E+00	3.63438E-03	-9.40655E-08	3.63448E-03	1.12757E-17
123	1.29289E-04	1.15657E-12	3.70196E-03	-3.70196E-03	0.00000E+00	3.63334E-03	-9.40655E-08	3.63343E-03	7.37257E-18
124	1.29289E-04	8.25913E-13	3.70196E-03	-3.70196E-03	0.00000E+00	3.63230E-03	-9.40655E-08	3.63239E-03	-5.20417E-18
125	1.29289E-04	5.89790E-13	3.70196E-03	-3.70196E-03	0.00000E+00	3.63125E-03	-9.40655E-08	3.63135E-03	2.08167E-17
126	1.29289E-04	4.21174E-13	3.70196E-03	-3.70196E-03	0.00000E+00	3.63021E-03	-9.40655E-08	3.63030E-03	2.55872E-17
127	1.29289E-04	3.00763E-13	3.70196E-03	-3.70196E-03	0.00000E+00	3.62916E-03	-9.40655E-08	3.62926E-03	1.99493E-17
128	1.29289E-04	2.14777E-13	3.70196E-03	-3.70196E-03	0.00000E+00	3.62812E-03	-9.40655E-08	3.62822E-03	3.98986E-17
129	1.29289E-04	1.53374E-13	3.70196E-03	-3.70196E-03	0.00000E+00	3.62708E-03	-9.40655E-08	3.62717E-03	0.00000E+00
130	1.29289E-04	1.09526E-13	3.70196E-03	-3.70196E-03	0.00000E+00	3.62604E-03	-9.40655E-08	3.62613E-03	-4.77049E-18
131	1.29289E-04	7.82128E-14	3.70196E-03	-3.70196E-03	0.00000E+00	3.62499E-03	-9.40655E-08	3.62509E-03	8.67362E-18
132	1.29289E-04	5.58527E-14	3.70196E-03	-3.70196E-03	0.00000E+00	3.62395E-03	-9.40655E-08	3.62405E-03	6.93889E-18
133	1.29289E-04	3.98851E-14	3.70196E-03	-3.70196E-03	0.00000E+00	3.62291E-03	-9.40655E-08	3.62300E-03	2.38524E-17
134	1.29289E-04	2.84826E-14	3.70196E-03	-3.70196E-03	0.00000E+00	3.62187E-03	-9.40655E-08	3.62196E-03	1.77809E-17
135	1.29289E-04	2.03379E-14	3.70196E-03	-3.70196E-03	0.00000E+00	3.62083E-03	-9.40655E-08	3.62092E-03	2.21177E-17
136	1.29289E-04	1.45254E-14	3.70196E-03	-3.70196E-03	0.00000E+00	3.61979E-03	-9.40655E-08	3.61988E-03	4.20670E-17
137	1.29289E-04	1.03735E-14	3.70196E-03	-3.70196E-03	0.00000E+00	3.61875E-03	-9.40655E-08	3.61884E-03	5.63785E-18
138	1.29289E-04	7.40570E-15	3.70196E-03	-3.70196E-03	0.00000E+00	3.61771E-03	-9.40655E-08	3.61780E-03	3.90313E-17
139	1.29289E-04	5.28809E-15	3.70196E-03	-3.70196E-03	0.00000E+00	3.61667E-03	-9.40655E-08	3.61676E-03	2.73219E-17
140	1.29289E-04	3.77834E-15	3.70196E-03	-3.70196E-03	0.00000E+00	3.61563E-03	-9.40655E-08	3.61572E-03	2.47198E-17
141	1.29289E-04	2.69569E-15	3.70196E-03	-3.70196E-03	0.00000E+00	3.61459E-03	-9.40655E-08	3.61468E-03	3.64292E-17
142	1.29289E-04	1.92691E-15	3.70196E-03	-3.70196E-03	0.00000E+00	3.61355E-03	-9.40655E-08	3.61364E-03	2.55872E-17
143	1.29289E-04	1.37665E-15	3.70196E-03	-3.70196E-03	0.00000E+00	3.61251E-03	-9.40655E-08	3.61261E-03	6.46184E-17
144	1.29289E-04	9.81335E-16	3.70196E-03	-3.70196E-03	0.00000E+00	3.61147E-03	-9.40655E-08	3.61157E-03	3.33934E-17
145	1.29289E-04	7.01238E-16	3.70196E-03	-3.70196E-03	0.00000E+00	3.61043E-03	-9.40655E-08	3.61053E-03	-3.90313E-18
146	1.29289E-04	5.00600E-16	3.70196E-03	-3.70196E-03	0.00000E+00	3.60940E-03	-9.40655E-08	3.60949E-03	7.37257E-18
147	1.29289E-04	3.57572E-16	3.70196E-03	-3.70196E-03	0.00000E+00	3.60836E-03	-9.40655E-08	3.60845E-03	3.94650E-17
148	1.29289E-04	2.56260E-16	3.70196E-03	-3.70196E-03	0.00000E+00	3.60732E-03	-9.40655E-08	3.60742E-03	4.77049E-17
149	1.29289E-04	1.82759E-16	3.70196E-03	-3.70196E-03	0.00000E+00	3.60629E-03	-9.40655E-08	3.60638E-03	3.33934E-17
150	1.29289E-04	1.29123E-16	3.70196E-03	-3.70196E-03	0.00000E+00	3.60525E-03	-9.40655E-08	3.60534E-03	3.72966E-17
151	1.29289E-04	9.33659E-17	3.70196E-03	-3.70196E-03	0.00000E+00	3.60421E-03	-9.40655E-08	3.60431E-03	7.97973E-17
152	1.29289E-04	6.55549E-17	3.70196E-03	-3.70196E-03	0.00000E+00	3.60318E-03	-9.40655E-08	3.60327E-03	2.99240E-17
153	1.29289E-04	4.76762E-17	3.70196E-03	-3.70196E-03	0.00000E+00	3.60214E-03	-9.40655E-08	3.60224E-03	-1.43115E-17
154	1.29289E-04	3.37706E-17	3.70196E-03	-3.70196E-03	0.00000E+00	3.60111E-03	-9.40655E-08	3.60120E-03	2.60209E-17
155	1.29289E-04	2.38381E-17	3.70196E-03	-3.70196E-03	0.00000E+00	3.60007E-03	-9.40655E-08	3.60017E-03	1.38778E-17

conc_plot / conc_plot_porevol / implicit_FD

Figure F-11. Spreadsheet "Transport_Calc_all_colloids.xls;" Final Calculated Solutions and Equation Terms, Iterated in Time, for Mixing Cell Colloid Model, Time 640 – 970 Years

	A	B	C	D	E	F	G	H	I
156	980.00	2.05511E-07	4.11023E-08	4.03830E-03	1.23307E-07	4.11023E-09	9.40175E-08	1.52144E-01	3.7403E-04
157	990.00	2.05511E-07	4.11023E-08	4.03830E-03	1.23307E-07	4.11023E-09	9.40175E-08	1.53716E-01	3.7403E-04
158	1000.00	2.05511E-07	4.11023E-08	4.03830E-03	1.23307E-07	4.11023E-09	9.40175E-08	1.55286E-01	3.7403E-04
159									

Figure F-12. Spreadsheet "Transport_Calc_all_colloids.xls;" Calculated Solutions and Equation Terms, Iterated in Time, for Mixing Cell Colloid Model, Time 980 – 1000 Years

	J	K	L	M	N	O	P	Q	R	S	T
156	2.0551E-03	5.1378E-04	4.1102E-02	4.1102E-02	4.7009E-03	1.9357E-02	980.00	3.70234E-03	2.62671E-07	4.78673E-07	5.48749E-01
157	2.0551E-03	5.1378E-04	4.1102E-02	4.1102E-02	4.7009E-03	1.9557E-02	990.00	3.70234E-03	2.62671E-07	4.78673E-07	5.48749E-01
158	2.0551E-03	5.1378E-04	4.1102E-02	4.1102E-02	4.7009E-03	1.9757E-02	1000.00	3.70234E-03	2.62671E-07	4.78673E-07	5.48749E-01
159											

Figure F-13. Spreadsheet "Transport_Calc_all_colloids.xls;" Additional Calculated Solutions and Equation Terms, Iterated in Time, for Mixing Cell Colloid Model, Time 980 – 1000 Years

	U	V	W	X	Y	Z	AA	AB	AC
156	1.29289E-04	1.78786E-17	3.70196E-03	-3.70196E-03	0.00000E+00	3.59904E-03	-9.40655E-08	3.59913E-03	3.94650E-17
157	1.29289E-04	1.19191E-17	3.70196E-03	-3.70196E-03	0.00000E+00	3.59800E-03	-9.40655E-08	3.59810E-03	4.25007E-17
158	1.29289E-04	9.93245E-18	3.70196E-03	-3.70196E-03	0.00000E+00	3.59697E-03	-9.40655E-08	3.59706E-03	3.90313E-18
159									

Figure F-14. Spreadsheet "Transport_Calc_all_colloids.xls;" Final Calculated Solutions and Equation Terms, Iterated in Time, for Mixing Cell Colloid Model, Time 980 – 1000 Years

SPREADSHEET "FLUX_OUT_RATIO.XLS"

The purpose of this spreadsheet is to demonstrate the use of the irreversible linear reaction rate constant to fit a specified flux out ratio. The spreadsheet calculates and plots the figures "Limiting Flux Out Ratio as a function of Irreversible Reaction Rate" and "Linear reaction rate from colloid to total flux out ratio."

The calculations for flux out ratio as a function of k, linear irreversible reaction rate, are done in Worksheet "adv_diff_decay." The calculations for k as a function of flux out ratio are done in Worksheet "K-surface." This description refers to equations from Appendix B, "Implementation of Radionuclide Sorption onto Colloidal and Stationary Phases with Finite Difference Solution."

Description of Input Values

The first 29 rows of the worksheet contain the input data values with the exception of Row 12, where pore volume is computed. Column D contains typical input values . Column B contains values from Column D that are scaled for unit conversion of mass (kg), length (m), and time (yr). An image of the first 31 rows of the Microsoft Excel spreadsheet is shown in Figure F-15.

Row 2: c_s [kg/m^3]

c_s (mg L^{-1}) = Pu solubility

$B$2=$D$2/1000

Row 3: phi_1

ϕ_1, porosity of the waste form cell_1

$B$3=$D$3

Row 4: phi_2

ϕ_2, porosity of the corrosion product mass in waste form cell_2

$B$4=$D$4

Row 5: phi_3

ϕ_3, porosity of the invert

$B$5=$D$5

Row 6: u [m^3/yr]

u, volumetric water flux

$B$6=$D$6

	A	B	C	D
1				
2	c_s [kg/m^3]	0.001	c_s[mg/l]	1
3	phi_1	1	phi_1	1
4	phi_2	0.4	phi_2	0.4
5	phi_3	0.3	phi_3	0.3
6	u [m^3/yr]	0.1	u[m^3/yr]	0.1
7	Kd_FeO_c [m^3/kg]	1.0000E+01	Kd_FeO_c[ml/g]	1.00000E+04
8	Kd_FeO_CP [m^3/kg]	2.5000E+00	Kd_FeO_CP[ml/g]	2.50000E+03
9	Kd_WF_c [ml/g]	2.0000E+02	Kd_WF_c[ml/g]	2.00000E+05
10	Kd_GW_c [mg/g]	2.0000E+02	Kd_GW_c[mg/g]	2.00000E+05
11	mass_FeO_CP [kg]	1.80000E+04	mass_FeO_CP [g]	1.80000E+07
12	V_pore [m^3]	2.29008E+00	V_pore [L]	2.29008E+03
13	c_FeO_c [kg/m^3]	2.00000E-02	c_FeO_c [mg/L]	2.00000E+01
14	c_FeO_CP [kg/m^3]	7.86000E+03	c_FeO_CP [mg/L]	7.86000E+06
15	c_WF_c [kg/m^3]	3.0000E-03	c_WF_c[kg/m^3]	3.00000E+00
16	c_GW_c [kg/m^3]	1.0000E-04	c_GW_c[kg/m^3]	1.00000E-01
17	rate [m/yr]	4.1837E-04	rate[cm/yr]	4.18370E-02
18	S_FeO_c [m^2/kg]	1.0000E+05	S_FeO_c[m^2/g]	1.00000E+02
19	S_FeO_CP [m^2/kg]	1.0000E+04	S_FeO_CP[m^2/g]	1.00000E+01
20	d_FeO [kg/m^3]	5.2400E+03	den_FeO[kg/m^3]	5.24000E+03
21	diffus_aq [m^2/yr]	7.2583E-02	diffus_aq[m^2/s]	2.30000E-09
22	diffus_colloid [m^2/yr]	7.2583E-04	diffus_colloid[m^2/s]	2.30000E-11
23	diff_length_1 [m]	1.0000E-03	diff_length_1[m]	1.00000E-03
24	diff_length_2 [m]	5.0000E+00	diff_length_2[m]	5.00000E+00
25	diff_length_3 [m]	8.0600E-01	diff_length_3[m]	8.06000E-01
26	diff_area_1_2 [m^2]	3.6000E+01	diff_area_1_2[m^2]	3.60000E+01
27	diff_area_2_3 [m^2]	1.0680E+00	diff_area_2_3[m^2]	1.06800E+00
28	decay [1/yr]	2.8749E-05	decay[1/yr]	2.87494E-05
29	delt [yr]	10	delt[yr]	10
30	R_bar_1 [1/yr]	8.36740E-01		
31	R_bar_2 [1/yr]	3.28839E+04		

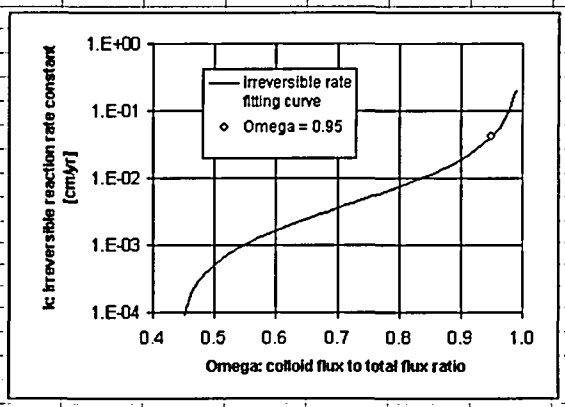

K-surface / adv_diff_decay

Figure F-15. Spreadsheet "flux_out_ratio.xls," Worksheet "K-surface;" Summary of Inputs

Row 7: Kd_FeO_c [m^3/kg]

$K_{d_FeO_c}$, partition coefficient in the FeO colloid state

$B$7=$D$7/1000

Row 8: Kd_FeO_CP [m^3/kg]

$K_{d_FeO_CP}$, partition coefficient in the stationary FeO corrosion product state

$B$8=$D$8/1000

Row 9: Kd_WF_c [m^3/kg]

$K_{d_WF_c}$, partition coefficient in the waste form colloid state

$B$9=$D$9/1000

Row 10: Kd_GW_c [m^3/kg]

$K_{d_GW_c}$, partition coefficient in the GW colloid state

$B$10=$D$10/1000

Row 11: mass_FeO_CP [kg]

m_{FeO_CP}, mass of corrosion products

$B$11=$D$11/1000

Row 12: V_pore [m^3]

$V_{pore} = \phi V_{bulk} = \frac{\phi}{1-\phi}\frac{m_{FeO_CP}}{\rho_{FeO_CP}}$, pore volume

$B$12=$D$12/1000

$D$12=$D$4*$D$11/($D$20*(1-$D$4))

Row 13: c_FeO_c [kg/m^3]

$c_{Pu_FeO_c}$, concentration of FeO colloids

$B$13=$D$13/1000

Row 14: c_FeO_CP [kg/m^3]

$c_{Pu_FeO_CP}$, concentration of FeO corrosion product

$B$14=$D$14/1000

Row 15: c_WF_c [kg/m^3]

$c_{Pu_WF_c}$, concentration of waste form colloids

$B$15=$D$15/1000

Row 16: c_GW_c [kg/m^3]

$c_{Pu_GW_c}$, concentration of GW colloid state

$B$16=$D$16/1000

Row 17: k [m/yr]

k, intrinsic or surface reaction rate ($m^3\ m^{-2}\ yr^{-1}$)

$B$17=$D$17/100

Row 18: S_FeO_c [m^2/kg]

$\hat{S}_{FeO_c}$ = specific surface area of FeO colloids ($m^2\ kg^{-1}$)

$B$18=$D$18*1000

Row 19: S_FeO_CP [m^2/kg]

$\hat{S}_{FeO_CP}$ = specific surface area of FeO corrosion products ($m^2\ kg^{-1}$)

$B$19=$D$19*1000

Row 20: d_FeO [kg/m^3]

ρ_{FeO_CP} = density of FeO

$B$20=$D$20

Row 21: diffus_aq [m^2/yr]

D_{aq} = aqueous diffusivity

$B$21=$D$21*31558000

Row 22: diffus_colloid [m^2/yr]

$D_{colloid}$ = colloid diffusivity

$B$22=$D$22*31558000

Row 23: diff_length_1 [m]

L_1 = diffusive length for cell_1

$B$23=$D$23

Row 24: diff_length_2 [m]

L_2 = diffusive length for cell_2

$B$24=$D$24

Row 25: diff_length_3 [m]

L_3 = diffusive length for cell_3

$B$25=$D$25

Row 26: diff_area_1_2 [m^2]

A_{s12} = diffusive area at cell_1 and cell_2 interface

$B$26=$D$26

Row 27: diff_area_2_3 [m^2]

A_{s23} = diffusive area at cell_2 and cell_3 interface

$B$27=$D$27

Row 28: decay [1/yr]

λ, decay rate

$B$28=$D$28

Row 29: delt [yr]

Δt, time step length

$B$29=$D$29

Rows 30 through 51 contain additional derived parameters for the colloid model. Images of Rows 32 through 100 are shown at the end of the description of this spreadsheet.

Row 30: R_bar_1 [1/yr]

$\overline{R}_1 = \hat{S}_{FeO_c} c_{FeO_c} k$, reaction rate constant for colloids

$B$30=$B$18*$B$13*$B$17

Row 31: R_bar_2 [1/yr]

$\overline{R}_2 = \hat{S}_{FeO_CP} c_{FeO_CP} k$, reaction rate constant for corrosion products

$B$31=$B$19*$B$14*$B$17

Row 32: U_bar [1/yr]

$\overline{U}$ = advective rate constant

$B$32=$B$6/$B$12

Row 33: Kd_bar_FeO_c

dimensionless partition coefficient in the FeO colloid state

$B$33=$B$13*$B$7

Row 34: Kd_bar_FeO_CP

dimensionless partition coefficient in the FeO corrosion product state

$B$34=$B$14*$B$8

Row 35: Kd_bar_WF_c

dimensionless partition coefficient in the waste form colloid state

$B$35=$B$15*$B$9

Row 36: Kd_bar_GW_c

dimensionless partition coefficient in the GW colloid state

$B$36=$B$16*$B$10

Row 37: K_bar_1

$\overline{K}_1 = 1 + \overline{K}_{d_FeO_c} + \overline{K}_{d_FeO_CP} + \overline{K}_{d_WF_c} + \overline{K}_{d_GW_c}$, combination of dimensionless partition coefficients

$B$37=1+$B$33+$B$34+$B$35+$B$36

Row 38: K_bar_2

$\overline{K}_2 = 1 + \overline{K}_{d_FeO_c} + \overline{K}_{d_WF_c} + \overline{K}_{d_GW_c}$, combination of dimensionless partition coefficients

$B$38=1+$B$33+$B$35+$B$36

Row 39: K_bar_3

$\overline{K}_3 = \overline{K}_{d_FeO_c} + \overline{K}_{d_WF_c} + \overline{K}_{d_GW_c}$, combination of dimensionless partition coefficients

$B$39=$B$33+$B$35+$B$36

Row 40: Diff_left_aq [1/yr]

diffusive rate constant, left interface in water

$B$40=($B$26/($B$23/($B$3*$B$21)+$B$24/($B$4*$B$21)))/$B$12

Row 41: Diff_right_aq

diffusive rate constant, right interface in water

$B$41=($B$27/($B$24/($B$4*$B$21)+$B$25/($B$5*$B$21)))/$B$12

Row 42: Diff_right_colloid

diffusive rate constant, right interface colloids

$B$42=($B$27/($B$24/($B$4*$B$22)+$B$25/($B$5*$B$22)))/$B$12

Row 43: Omega

$$\Omega = \frac{\text{colloid mass flux out}}{\text{total mass flux out}}$$

$B$43=($B$44+$B$30)/($B$45+$B$30)

Row 44: p_1

$$p_1 = \overline{K}_3\left(\overline{U} + \overline{D}_{right_col} + \lambda\right)$$

$B$44=$B$39*($B$32+$B$42+$B$28)

Row 45: p_2

$$p_2 = \left(\overline{UK}_2 + \overline{D}_{right_aq} + \overline{D}_{right_col}\overline{K}_3\right)\left(\frac{\overline{U} + \overline{D}_{right_col} + \lambda}{\overline{U} + \overline{D}_{right_col}}\right)$$

$B$45=($B$32*$B$38+$B$41+$B$42*$B$39)*($B$32+$B$42+$B$28)/($B$32+$B$42)

Row 46: delta

scale value for $k = 2.0$

Row 47: comments

Rows 48 through 81 are values for the flux out ratio calculated as a function of the irreversible forward reaction rate, Equation B-71. Column A contains the values of k, and Column B contains the corresponding values of flux out ratio.

$A$48=0
$A$49=1.E-5
$A50 = $B$46*$A49

Row 50 is dragged down through Row 81.

Then in Column B the flux out ratio, $\Omega = \frac{\text{colloid mass flux out}}{\text{total mass flux out}}$, is calculated as a function of the irreversible reaction rate value:

$B48 = ($B$44+$B$18*$B$13*$A48*0.01)/($B$45+$B$18*$B$13*$A48*0.01)

The factor 0.01 converts the irreversible reaction rate constant from units of cm yr^{-1} to m yr^{-1}. The above expression is then dragged down through Row 81.

Figure B-3 in Appendix B, "Limiting Flux Out Ratio as a Function of Irreversible Reaction Rate," is plotted, where:

x-axis: $A$49:$A$73
y-axis: $B$49:$B$73

The point $k = 0.001$ cm yr^{-1} is

x-axis: $D$17:$D$17
y-axis: $B$43:$B$43

In Worksheet "K-surface," Rows 1 through 46 are the same as for Worksheet "adv_diff_decay." In Worksheet "K-surface," Rows 48 through 100 (Figure F-16), values for the irreversible forward reaction rate, k, are calculated as a function of the flux out ratio, Ω, Equation B-72. Column A contains the values of flux out ratio, and Column B contains the corresponding values of k.

$A$48: minimum flux out ratio when k = 0, $\Omega = \frac{p_1}{p_2}$

$A$48 = $B$44/$B$45

$A49 to $A100: uniform spacing of omega values between the minimum and 1.
$A49 = $A48+(1-$A$48)/53.

$A49 is dragged down to row 100.

$B48 to $B101: irreversible reaction rate. $k = \frac{p_2\Omega - p_1}{(1-\Omega)\hat{S}_{FeO_c}c_{FeO_c}}$

$B48 = 100*($B$35*$A48-$B$44)/((1-$A48)*$B$18*$B$13)

(The factor of 100 is a conversion from meters to cm.)

$B$48 is dragged down through $B$100

Figure B-4 in Appendix B, "Linear Reaction Rate from Colloid to Total Flux Out Ratio," is the plot in Worksheet "K-surface," where

x-axis: $A$49:$A$100
y-axis: $B$49:$B$100

The point labeled "Omega = 0.95" is

x-axis: $B$43:$B$43
y-axis: $D$17:$D$17

	A	B	C
32	U_bar [1/yr]	4.36667E-02	
33	Kd_FeO_c_bar	2.00000E-01	
34	Kd_FeO_CP_bar	1.96500E+04	
35	Kd_WF_c_bar	6.00000E-01	
36	Kd_GW_c_bar	2.00000E-02	
37	K_1	1.96518E+04	
38	K_2	1.82000E+00	
39	K_3	8.20000E-01	
40	Diff_left_aq	9.12736E-02	
41	Diff_right_aq	2.22893E-03	
42	Diff_right_colloid	2.22893E-05	
43	Omega	9.50000E-01	
44	p_1	3.58485E-02	
45	p_2	8.17743E-02	
46	delta	2.00E+00	
47	Omega	k	
48	0.4384	0.0000E+00	
49	0.4490	7.8629E-05	
50	0.4596	1.6034E-04	
51	0.4702	2.4532E-04	
52	0.4808	3.3377E-04	
53	0.4914	4.2591E-04	
54	0.5020	5.2196E-04	
55	0.5126	6.2220E-04	
56	0.5232	7.2688E-04	
57	0.5338	8.3633E-04	
58	0.5443	9.5086E-04	
59	0.5549	1.0709E-03	
60	0.5655	1.1967E-03	
61	0.5761	1.3288E-03	
62	0.5867	1.4677E-03	
63	0.5973	1.6140E-03	
64	0.6079	1.7681E-03	
65	0.6185	1.9308E-03	

K-surface / adv_diff_decay

	A	B
66	0.6291	2.1028E-03
67	0.6397	2.2849E-03
68	0.6503	2.4780E-03
69	0.6609	2.6832E-03
70	0.6715	2.9017E-03
71	0.6821	3.1347E-03
72	0.6927	3.3838E-03
73	0.7033	3.6506E-03
74	0.7139	3.9373E-03
75	0.7245	4.2460E-03
76	0.7351	4.5794E-03
77	0.7457	4.9405E-03
78	0.7563	5.3331E-03
79	0.7669	5.7614E-03
80	0.7775	6.2304E-03
81	0.7881	6.7464E-03
82	0.7987	7.3166E-03
83	0.8093	7.9503E-03
84	0.8199	8.6585E-03
85	0.8305	9.4552E-03
86	0.8411	1.0358E-02
87	0.8516	1.1390E-02
88	0.8622	1.2581E-02
89	0.8728	1.3970E-02
90	0.8834	1.5611E-02
91	0.8940	1.7581E-02
92	0.9046	1.9989E-02
93	0.9152	2.2999E-02
94	0.9258	2.6869E-02
95	0.9364	3.2028E-02
96	0.9470	3.9252E-02
97	0.9576	5.0087E-02
98	0.9682	6.8145E-02
99	0.9788	1.0426E-01

K-surface / adv_diff_decay

	A	B
100	0.9894	2.1261E-01
101		

Figure F-16. Spreadsheet "flux_out_ratio.xls," Worksheet "K-surface;" Calculation of Irreversible Forward Reaction Rate, k, as Function of Flux Out Ratio, Ω

SPREADSHEET "TIME_TO_CONV.XLS"

The purpose of this spreadsheet is to demonstrate the time to converge for the Pu concentration in solution and the irreversible Pu concentration on colloids. The spreadsheet verifies the convergence estimate discussed in Section "Convergence Estimates For Closed Form Solutions" in Appendix B.

The calculations are done in Worksheet "time_to_conv," while the plot is in Worksheet "plot_time_to_conv." This description will refer to equations from Appendix B, "Implementation of Radionuclide Sorption onto Colloidal and Stationary Phases with Finite Difference Solution."

Description of Input Values

The first 29 rows of each worksheet contain the input data values, with the exception of Row 12, where pore volume is computed. Column D contains input values. Column B contains values from column D that are scaled for unit conversion of mass (kg), length (m), time (yr). An image of Rows 1 through 33 is shown on the next page.

Row 2: c_s [kg/m^3]

c_s (mg L^{-1}) = Pu solubility

$B$2=$D$2/1000

Row 3: phi_1

ϕ_1, porosity of the waste form cell_1

$B$3=$D$3

Row 4: phi_2

ϕ_2, porosity of the corrosion product mass in waste form cell_2

$B$4=$D$4

Row 5: phi_3

ϕ_3, porosity of the invert

$B$5=$D$5

Row 6: u [m^3/yr]

u = volumetric water flux (m^3 yr^{-1})

$B$6=$D$6

Row 7: Kd_FeO_c [m^3/kg]

$K_{d_FeO_c}$, partition coefficient in the FeO colloid state

$B$7=$D$7/1000

	A	B	C	D
1	Input for Excel sreadsheet		Input from GoldSim	
2	c_s [kg/m^3]	0.001	c_s[mg/L]	1
3	phi_1	1	phi_1	1
4	phi_2	0.4	phi_2	0.4
5	phi_3	0.3	phi_3	0.3
6	u [m^3/yr]	0.1	u[m^3/yr]	0.1
7	Kd_FeO_c [m^3/kg]	1.00000E+01	Kd_FeO_c [ml/g]	1.00000E+04
8	Kd_FeO_CP [m^3/kg]	2.50000E+00	Kd_FeO_CP [ml/g]	2.50000E+03
9	Kd_WF_c [m^3/kg]	2.00000E+02	Kd_WF_c [ml/g]	2.00000E+05
10	Kd_GW_c [m^3/kg]	2.00000E+02	Kd_GW_c [ml/g]	2.00000E+05
11	mass_FeO_CP [kg]	1.80000E+04	mass_FeO_CP [g]	1.80000E+07
12	V_pore [m^3]	2.29008E+00	V_pore [L]	2.29008E+03
13	c_FeO_c [kg/m^3]	2.00000E-02	c_FeO_c [mg/L]	2.00000E+01
14	c_FeO_CP [kg/m^3]	7.86000E+03	c_FeO_CP [mg/L]	7.86000E+06
15	c_WF_c [kg/m^3]	3.00000E-03	c_WF_c [mg/L]	3.00000E+00
16	c_GW_c [kg/m^3]	1.00000E-04	c_GW_c [mg/L]	1.00000E-01
17	rate [m/yr]	1.00000E-05	rate [cm/yr]	1.00000E-03
18	S_FeO_c [m^2/kg]	1.00000E+05	S_FeO_c[m^2/g]	1.00000E+02
19	S_FeO_CP [m^2/kg]	1.00000E+04	S_FeO_CP [m^2/g]	1.00000E+01
20	d_FeO [kg/m^3]	5.24000E+03	den FeO [kg/m^3]	5.24000E+03
21	diffus_aq [m^2/yr]	7.25834E-02	diffus_aq [m^2/s]	2.30000E-09
22	diffus_colloid [m^2/yr]	7.25834E-04	diffus_colloid [m^2/	2.30000E-11
23	diff_length_1 [m]	1.00000E-03	diff_length_1 [m]	1.00000E-03
24	diff_length_2 [m]	5.00000E+00	diff_length_2 [m]	5.00000E+00
25	diff_length_3 [m]	8.06000E-01	diff_length_3 [m]	8.06000E-01
26	diff_area_1_2 [m^2]	3.60000E+01	diff_area_1_2 [m^2]	3.60000E+01
27	diff_area_2_3 [m^2]	1.06800E+00	diff_area_2_3 [m^2]	1.06800E+00
28	decay [1/yr]	2.87494E-05	decay [1/yr]	2.87494E-05
29	delt [yr]	1.00000E+01	delt [yr]	10
30	R_bar_1 [1/yr]	2.00000E-02		
31	R_bar_2 [1/yr]	7.86000E+02		
32	U_bar [1/yr]	4.36667E-02		
33	Kd_bar_FeO_c	2.00000E-01		
34	Kd_bar_FeO_CP	1.06500E+04		

plot_time_to_conv | time_to_conv

Figure F-17. Spreadsheet "time_to_conv.xls," Worksheet "time_to_conv;" Summary of Inputs

Row 8: Kd_FeO_CP [m^3/kg]

$K_{d_FeO_CP}$, partition coefficient in the stationary FeO corrosion product state

$B$8=$D$8/1000

Row 9: Kd_WF_c [m^3/kg]

$K_{d_WF_c}$, partition coefficient in the waste form colloid state

$B$9=$D$9/1000

Row 10: Kd_GW_c [m^3/kg]

$K_{d_GW_c}$, partition coefficient in the GW colloid state

$B$10=$D$10/1000

Row 11: mass_FeO_CP [kg]

m_{FeO_CP} mass of corrosion products

$B$11=$D$11/1000

Row 12: V_pore [m^3]

$V_{pore} = \phi V_{bulk} = \frac{\phi}{1-\phi} \frac{m_{FeO_CP}}{\rho_{FeO_CP}}$, pore volume

$B$12=$D$12/1000

$D$12=$D$4*$D$11/($D$20*(1-$D$4))

Row 13: c_FeO_c [kg/m^3]

$c_{Pu_FeO_c}$, concentration of FeO colloids

$B$13=$D$13/1000

Row 14: c_FeO_CP [kg/m^3]

$c_{Pu_FeO_CP}$, concentration of FeO corrosion product

$B$14=$D$14/1000

Row 15: c_WF_c [kg/m^3]

$c_{Pu_WF_c}$, concentration of waste form colloids

$B$15=$D$15/1000

Row 16: c_GW_c [kg/m^3]

$c_{Pu_GW_c}$, concentration of GW colloid state

$B$16=$D$16/1000

Row 17: k [m/yr]

k, intrinsic or surface reaction rate (pore-vol/area-FeO/time)

$B$17=$D$17/100

Row 18: S_FeO_c [m^2/kg]

$\hat{S}_{FeO_c}$ = specific surface area of FeO colloids ($m^2\ kg^{-1}$)

$B$18=$D$18*1000

Row 19: S_FeO_CP [m^2/kg]

$\hat{S}_{FeO_CP}$ = specific surface area of FeO corrosion products ($m^2\ kg^{-1}$)

$B$19=$D$19*1000

Row 20: d_FeO [kg/m^3]

ρ_{FeO_CP} = density of FeO

$B$20=$D$20

Row 21: diffus_aq [m^2/yr]

D_{aq} = aqueous diffusivity

$B$21=$D$21*31558000

Row 22: diffus_colloid [m^2/yr]

$D_{colloid}$ = colloid diffusivity

$B$22=$D$22*31558000

Row 23: diff_length_1 [m]

L_1 = diffusive length for cell_1

$B$23=$D$23

Row 24: diff_length_2 [m]

L_2 = diffusive length for cell_2

$B$24=$D$24

Row 25: diff_length_3 [m]

L_3 = diffusive length for cell_3

$B$25=$D$25

Row 26: diff_area_1_2 [m^2]

A_{s12} = diffusive area at cell_1 and cell_2 interface

$B$26=$D$26

Row 27: diff_area_2_3 [m^2]

A_{s23} = diffusive area at cell_2 and cell_3 interface

$B$27=$D$27

Row 28: decay [1/yr]

λ, decay rate

$B$28=$D$28

Row 29: delt [yr]

Δt, time step length

$B$29=$D$29

Rows 30 through 51 contains additional derived parameters for the colloid model. An image of Rows 34 through 61 is shown in Figure F-18.

	A	B	C	D	E	F	G	H	I	J
34	Kd_bar_FeO_CP	1.96500E+04								
35	Kd_bar_WF_c	6.00000E-01								
36	Kd_bar_GW_c	2.00000E-02								
37	K_bar_1	1.96518E+04								
38	K_bar_2	1.82000E+00								
39	K_bar_3	8.20000E-01								
40	Diff_left_aq	9.12736E-02								
41	Diff_left_c	9.12736E-04								
42	Diff_right_aq	2.22893E-03								
43	Diff_right_colloid	2.22893E-05								
44	denom_a_1_2	2.75194E+04								
45	a_1	7.14108E-01								
46	a_2	5.87541E-08								
47	b_1	6.95808E-01								
48	b_2	1.39162E-01								
49	e_1	9.99713E-01								
50	e_2	7.85774E+03								
51	tolerance	1.00000E-02								
52										
53	*delt_time*	*denom_a_1_2*	*a_1*	*time Pu_aq [yrs]*	*b_1*	*delta_1*	*delta_2*	*t_1*	*t_2*	*time [yrs]*
54	1.0E-03	1.9653E+04	9.9996E-01	115	9.9996E-01	4.5993E-04	4.2119E-04	1.7578E+05	1.9415E+05	194
55	1.0E-02	1.9660E+04	9.9960E-01	115	9.9956E-01	4.5975E-04	4.2104E-04	1.7582E+04	1.9419E+04	194
56	1.0E-01	1.9730E+04	9.9601E-01	115	9.9565E-01	4.5795E-04	4.1952E-04	1.7626E+03	1.9463E+03	195
57	1.0E+00	2.0439E+04	9.6151E-01	117	9.5811E-01	4.4068E-04	4.0499E-04	1.8059E+02	1.9900E+02	199
58	1.0E+01	2.7519E+04	7.1411E-01	137	6.9581E-01	3.2004E-04	3.0078E-04	2.2188E+01	2.4083E+01	240
59	1.0E+02	9.8328E+04	1.9986E-01	286	1.8616E-01	8.5624E-05	8.4182E-05	5.5709E+00	5.8272E+00	500
60	1.0E+03	8.0641E+05	2.4370E-02	1240	2.2363E-02	1.0286E-05	1.0265E-05	3.0220E+00	3.0925E+00	3000
61	1.0E+04	7.8872E+06	2.4916E-03	7682	2.2822E-03	1.0497E-06	1.0495E-06	2.2633E+00	2.2965E+00	20000

Figure F-18. Spreadsheet "time_to_conv.xls," Worksheet "time_to_conv;" Additional Derived Parameters and Results for Colloid Model

Row 30: R_bar_1 [1/yr]

$\overline{R}_1 = \hat{S}_{FeO_c} c_{FeO_c} k$, reaction rate constant for colloids

$B$30=$B$18*$B$13*$B$17

Row 31: R_bar_2 [1/yr]

$\overline{R}_2 = \hat{S}_{FeO_CP} c_{FeO_CP} k$, reaction rate constant for corrosion products

$B$31=$B$19*$B$14*$B$17

Row 32: U_bar [1/yr]

$\overline{U}$ advective rate constant

$B$32=$B$6/$B$12

Row 33: Kd_bar_FeO_c

dimensionless partition coefficient in the FeO colloid state

$B$33=$B$13*$B$7

Row 34: Kd_bar_FeO_CP

dimensionless partition coefficient in the FeO corrosion product state

$B$34=$B$14*$B$8

Row 35: Kd_bar_WF_c

dimensionless partition coefficient in the waste form colloid state

$B$35=$B$15*$B$9

Row 36: Kd_bar_GW_c

dimensionless partition coefficient in the GW colloid state

$B$36=$B$16*$B$10

Row 37: K_bar_1

$\overline{K}_1 = 1 + \overline{K}_{d_FeO_c} + \overline{K}_{d_FeO_CP} + \overline{K}_{d_WF_c} + \overline{K}_{d_GW_c}$, combination of dimensionless partition coefficients

$B$37=1+$B$33+$B$34+$B$35+$B$36

Row 38: K_bar_2

$\overline{K}_2 = 1 + \overline{K}_{d_FeO_c} + \overline{K}_{d_WF_c} + \overline{K}_{d_GW_c}$, combination of dimensionless partition coefficients

$B$38=1+$B$33+$B$35+$B$36

Row 39: K_bar_3

$\overline{K}_3 = \overline{K}_{d_FeO_c} + \overline{K}_{d_WF_c} + \overline{K}_{d_GW_c}$, combination of dimensionless partition coefficients

$B$39=$B$33+$B$35+$B$36

Row 40: Diff_left_aq [1/yr]

diffusive rate constant, left interface in water

$B$40=($B$26/($B$23/($B$3*$B$21)+$B$24/($B$4*$B$21)))/$B$12

Row 41: Diff_left_colloid [1/yr]

diffusive rate constant, left interface colloids

$B$41=($B$26/($B$23/($B$3*$B$22)+$B$24/($B$4*$B$22)))/$B$12

Row 42: Diff_right_aq [1/yr]

diffusive rate constant, right interface in water

$B$41=($B$27/($B$24/($B$4*$B$21)+$B$25/($B$5*$B$21)))/$B$12

Row 43: Diff_right_colloid [1/yr]

diffusive rate constant, right interface colloids

$B$42=($B$27/($B$24/($B$4*$B$22)+$B$25/($B$5*$B$22)))/$B$12

Row 44: denom_a_1_2

denominator of Equation B-48

$B$44=$B$37+($B$32*$B$38+$B$40+$B$41*$B$35+$B$42+$B$43*$B$39
+$B$30+$B$31+$B$28*$B$37)*$B$29

Row 45: a_1

first coefficient for Equation B-55,

$$a_1 = \frac{\overline{K}_1}{\overline{K}_1 + \left(\overline{UK}_2 + \overline{D}_{left_aq} + \overline{D}_{left_col}\overline{K}_{d_WF_c} + \overline{D}_{right_aq} + \overline{D}_{right_col}\overline{K}_3 + \overline{R}_1 + \overline{R}_2 + \lambda\overline{K}_1\right)\Delta t}$$

$B$45=$B$37/$B$44

Row 46: a_2

second coefficient for Equation B-55,

$$a_2 = \frac{\left(\overline{U}(1+\overline{K}_{d_WF_c}) + \overline{D}_{left_aq} + \overline{D}_{left_col}\overline{K}_{d_WF_c}\right)\Delta t c_s}{\overline{K}_1 + \left(\overline{UK}_2 + \overline{D}_{left_aq} + \overline{D}_{left_col}\overline{K}_{d_WF_c} + \overline{D}_{right_aq} + \overline{D}_{right_col}\overline{K}_3 + \overline{R}_1 + \overline{R}_2 + \lambda\overline{K}_1\right)\Delta t}$$

$B$46=(($B$32*(1+$B$35)+$B$40+$B$41*$B$35)*$B$29*$B$2)/$B$44

Row 47: b_1

first coefficient for Equation B-58, $b_1 = \dfrac{1}{1+\left(\overline{U} + \overline{D}_{right_col} + \lambda\right)\Delta t}$

$B$47=1/(1+($B$32+$B$43+$B$28)*$B$29)

Row 48: b_2

second coefficient for Equation B-58, $b_2 = \dfrac{\overline{R}_1\Delta t}{1+\left(\overline{U} + \overline{D}_{right_col} + \lambda\right)\Delta t}$

$B$48=($B$30*$B$29)*$B$47

Row 49: e_1

first coefficient for Equation B-64, $e_1 = \dfrac{1}{1+\lambda\Delta t}$

$B$49=1/(1+$B$28*$B$29)

Row 50: e_2

second coefficient for Equation B-64, $e_2 = \dfrac{\overline{R}_2\Delta t}{1+\lambda\Delta t}$

$B$50=($B$31*$B$29)*$B$49

Row 51: convergence relative error tolerance 1% = 0.01.

Rows 54 through 61 calculates the times to converge to limit value for Pu_aq concentration and Irrv_Pu_c concentration as a function of time step size. The time step size (yr) varies by order of magnitude increments from 1×10^{-3} to 1×10^{4}.

Column A: delt_time

Row 54: assign time step value 1×10^{-3}

Rows 55: $A55 = 10*$A54

This value is dragged down through Row 61

Column B: denom_a_1_2

denominator in the calculation for a_1 and a_2 coefficients.

$B54=$B$37+($B$32*$B$38+$B$40+$B$41*$B$35+$B$42+$B$43*$B$39+ $B$30+$B$31+$B$28*$B$37)*$A54

This value is dragged down through Row 61

Column C: a_1

coefficient in Pu_aq concentration Equation B-56.

Row 54: $C54 = $B$37/$B54

This result is dragged down through Row 61

Column D: time Pu_aq [yrs]

time for Pu_aq concentration to converge, estimate Equation B-74.

Row 54: $D54 = $A54*LOG10($B$51)/LOG10($C54)

This result is dragged down through Row 61

Column E: b_1

coefficient in Irrv_Pu_c concentration, Equation B-59.

Row 54: $E54 = 1/(1+($B$32+$B$43+$B$28)*$A54)

This result is dragged down through Row 61

Column F: delta_1

intermediate tolerance δ_1 in estimate for Irrv_Pu_c concentration convergence.

Row 54: $F54 = 0.5*$B$51*ABS(($E54-$C54)/(1-$C54))

This result is dragged down through Row 61

Column G:delta_2

intermediate tolerance δ_2 in estimate for Irrv_Pu_c concentration convergence.

Row 54: $G54 = 0.5*$B$51*ABS(($E54-$C54)/(1-$E54))

This result is dragged down through Row 61

Column H:t_1

intermediate result $\frac{\log_{10}(\delta_1)}{\log_{10}(b_1)}$ Equation B-75.

Row 54: $H54 = LOG10($F54)/LOG10($E54)

This result is dragged down through row 61

Column I: t_2

intermediate result $\frac{\log_{10}(\delta_2)}{\log_{10}(a_1)}$ Equation B-75.

Row 54: $G54 = LOG10($G54)/LOG10($C54)

This result is dragged down through Row 61

Column J: time [yrs]

time for Irrv_Pu_c concentration to converge to given tolerance, Equation B-75.

Row 54: $J54
=$A54*INT(MAX(LOG10($F54)/LOG10($E54),LOG10($G54)/LOG10($C54)))

This result is dragged down through Row 61.

The plot of the time to converge (shown in Figure F-19) is in Worksheet "plot_time_to_conv" and is Figure B-5 of Appendix B.

Time to converge for Pu_aq concentration is

x-axis: $A$54:$A$61
y-axis: $D$54:$D$61

Time to converge for Irrv_Pu_colloids is

x-axis: $A$54:$A$61
y-axis: $J$54:$J$61

Note that the *x*-axis scale is from 1×10^{-3} to 1×10^{3} years, so only Rows 54 through 60 are shown in the figure.

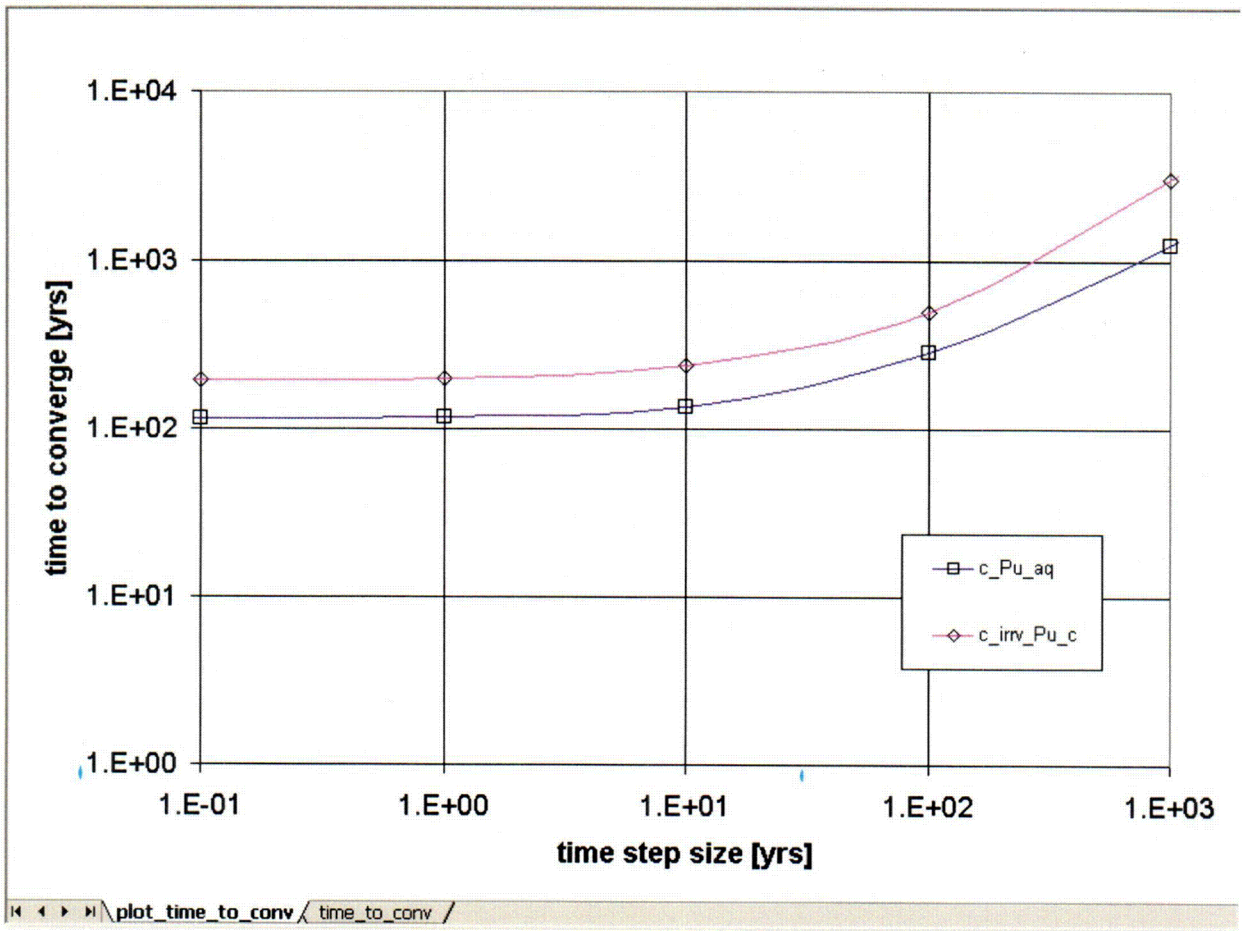

Figure F-19. Spreadsheet "time_to_conv.xls," Worksheet "plot_time_to_conv;" Plot of Colloid Model Results

INTENTIONALLY LEFT BLANK

APPENDIX G

MICROSOFT EXCEL SPREADSHEET "INVERT DIFFUSION COEFFICIENT"

MICROSOFT EXCEL SPREADSHEET "INVERT DIFFUSION COEFFICIENT"

SPREADSHEET "INVERT DIFFUSION COEFFICIENT" WORKSHEET "MODEL"

The purpose of this spreadsheet is to perform a statistical analysis of the dependence of effective invert diffusion coefficients, D_I ($cm^2\ s^{-1}$), on volumetric moisture content, θ (percent, 100 m^3 water m^{-3} bulk volume), as described in Section 6.3.4.1.1. The diffusion data are fit to an equation of the form

$$\phi S_w D_I = D_0 \left(\frac{\theta}{100} \right)^n , \qquad \text{(Eq. G-1)}$$

where ϕ is the porosity (m^3 void volume m^{-3} bulk volume), S_w is the water saturation (m^3 water m^{-3} void volume) ($100\phi S_w = \theta$), D_0 is the self-diffusion coefficient of water (2.299×10^{-5} $cm^2\ s^{-1}$) (Mills 1973 [DIRS 133392], Table III), and the fitting parameter is the exponent, n. To perform a least squares fit of the data, this equation is linearized in terms of n:

$$\log_{10}\left(\frac{\phi S_w D_I}{D_0} \right) = n \log_{10}\left(\frac{\theta}{100} \right). \qquad \text{(Eq. G-2)}$$

Column A, Rows 1 through 125, of the spreadsheet, shown in Figures G-1 through G-4, contains the moisture content values, θ (percent) (Conca and Wright 1992 [DIRS 100436]; Conca et al. 1993 [DIRS 170709]), that are listed in Table 4.1-17. The corresponding diffusion coefficient values ($\phi S_w D_I$) listed in Table 4.1-17 are in Column B, Rows 1 through 125 (where they are labeled D, which represents the effective diffusion coefficient, $\phi S_w D_I$, used in Section 6.3.4.1.1). In Column C, the quantity $\theta/100$ is computed (e.g., C3=A3/100], and $\phi S_w D_I / D_0$ is computed in Column D (e.g., D3=B3/0.00002299). The log term on the right hand side of Equation G-2, containing the moisture content, is computed Column E (e.g., E3=LOG10(A3)-2). In Column F, the left-hand side of Equation G-2 is calculated (e.g., D3=LOG10(D3)).

The least squares fit of the data is done using the Microsoft Excel Trendline tool. In Figure G-5, the results in Column F are plotted on the y-axis against the corresponding values in Column E on the x-axis in the plot located between Rows 132 and 154 of the worksheet. The type of regression is linear. The Trendline features, "Set intercept = 0," "Display equation on chart," and "Display R-squared value on chart" are clicked on. In particular, the "Set intercept = 0" feature results in a fit to Equation G-2, in which the intercept is constrained to be zero.

As shown on the charts, the fitting parameter, n, has a value of 1.863. The correlation coefficient, R^2, is 0.915, indicating a strong correlation between the diffusion coefficient and the volumetric moisture content. The regression equation is:

$$\phi S_w D_I = D_0 \left(\frac{\theta}{100} \right)^{1.863} , \qquad \text{(Eq. G-3)}$$

In Column G, the error, or deviation of each data point from the fitted equation, is calculated (e.g., G3=F3-1.862899*E3)); i.e., for data point i, the calculation in Column G is the deviation ε_i

$$\varepsilon_i = \log_{10}\left(\frac{\phi S_w D_I}{D_0}\right) - 1.863\log_{10}\left(\frac{\theta}{100}\right). \qquad \text{(Eq. G-4)}$$

In Cell G128, the average of the 125 values of ε_i is computed: G128=AVERAGE(G3:G127). The standard deviation of the ε_i, Cell G129 is computed: G129=STDEV(G3:G127).

	A	B	C	D	E	F	G
1	Water Content, θ	Diffusion Coefficient, D	θ/100	D/D_0	$\log_{10}\theta$ - 2	$\log_{10}(D/D_0)$	Error = [$\log_{10}(D/D_0)$
2	(%)	(cm^2/s)					- 1.863 ($\log_{10}\theta$ - 2)]
3	1.50	1.39E-08	0.0150	6.046E-04	-1.824	-3.219	0.1792
4	1.70	6.60E-09	0.0170	2.871E-04	-1.770	-3.542	-0.2455
5	1.90	8.60E-09	0.0190	3.741E-04	-1.721	-3.427	-0.2205
6	2.17	2.77E-08	0.0217	1.205E-03	-1.664	-2.919	0.1799
7	2.20	3.63E-08	0.0220	1.579E-03	-1.658	-2.802	0.2863
8	2.29	1.09E-08	0.0229	4.741E-04	-1.640	-3.324	-0.2687
9	2.50	2.50E-08	0.0250	1.087E-03	-1.602	-2.964	0.0209
10	3.10	3.30E-08	0.0310	1.435E-03	-1.509	-2.843	-0.0326
11	3.14	3.06E-08	0.0314	1.331E-03	-1.503	-2.876	-0.0757
12	3.20	1.35E-08	0.0320	5.872E-04	-1.495	-3.231	-0.4465
13	3.27	2.79E-08	0.0327	1.214E-03	-1.485	-2.916	-0.1487
14	3.33	6.35E-08	0.0333	2.762E-03	-1.478	-2.559	0.1938
15	3.34	2.60E-08	0.0334	1.131E-03	-1.476	-2.947	-0.1965
16	3.57	3.37E-08	0.0357	1.466E-03	-1.447	-2.834	-0.1377
17	3.70	3.70E-08	0.0370	1.609E-03	-1.432	-2.793	-0.1260
18	3.70	6.60E-08	0.0370	2.871E-03	-1.432	-2.542	0.1253
19	4.00	5.22E-08	0.0400	2.271E-03	-1.398	-2.644	-0.0396
20	4.20	5.94E-08	0.0420	2.584E-03	-1.377	-2.588	-0.0230
21	4.60	6.21E-08	0.0460	2.701E-03	-1.337	-2.568	-0.0773
22	4.90	7.20E-08	0.0490	3.132E-03	-1.310	-2.504	-0.0642
23	5.10	1.32E-07	0.0510	5.742E-03	-1.292	-2.241	0.1667
24	5.30	2.40E-08	0.0530	1.044E-03	-1.276	-2.981	-0.6048
25	5.40	7.60E-08	0.0540	3.306E-03	-1.268	-2.481	-0.1193
26	5.51	7.68E-08	0.0551	3.341E-03	-1.259	-2.476	-0.1311
27	5.83	1.23E-07	0.0583	5.350E-03	-1.234	-2.272	0.0278
28	5.90	9.30E-08	0.0590	4.045E-03	-1.229	-2.393	-0.1033
29	6.00	8.92E-08	0.0600	3.880E-03	-1.222	-2.411	-0.1350
30	6.30	1.06E-07	0.0630	4.611E-03	-1.201	-2.336	-0.0995
31	6.90	6.00E-08	0.0690	2.610E-03	-1.161	-2.583	-0.4203
32	6.93	1.50E-07	0.0693	6.525E-03	-1.159	-2.185	-0.0259

Model / Validation / Sheet3

Figure G-1. Spreadsheet "Invert Diffusion Coefficient," Worksheet "Model;" Invert Diffusion Coefficient Input Data (Water Content 1.50 to 6.93%)

	A	B	C	D	E	F	G
33	7.30	1.60E-07	0.0730	6.960E-03	-1.137	-2.157	-0.0399
34	7.40	2.50E-07	0.0740	1.087E-02	-1.131	-1.964	0.1429
35	7.60	2.60E-07	0.0760	1.131E-02	-1.119	-1.947	0.1384
36	7.60	1.10E-07	0.0760	4.785E-03	-1.119	-2.320	-0.2352
37	7.60	2.69E-07	0.0760	1.170E-02	-1.119	-1.932	0.1531
38	7.70	1.10E-07	0.0770	4.785E-03	-1.114	-2.320	-0.2458
39	8.00	1.98E-07	0.0800	8.612E-03	-1.097	-2.065	-0.0214
40	8.10	1.70E-07	0.0810	7.395E-03	-1.092	-2.131	-0.0977
41	8.32	4.10E-07	0.0832	1.783E-02	-1.080	-1.749	0.2629
42	8.35	2.15E-07	0.0835	9.352E-03	-1.078	-2.029	-0.0203
43	8.60	3.20E-07	0.0860	1.392E-02	-1.066	-1.856	0.1285
44	8.80	2.30E-07	0.0880	1.000E-02	-1.056	-2.000	-0.0335
45	9.24	2.55E-07	0.0924	1.109E-02	-1.034	-1.955	-0.0282
46	9.24	2.55E-07	0.0924	1.109E-02	-1.034	-1.955	-0.0282
47	9.56	3.00E-07	0.0956	1.305E-02	-1.020	-1.884	0.0149
48	9.64	3.07E-07	0.0964	1.335E-02	-1.016	-1.874	0.0182
49	9.75	3.20E-07	0.0975	1.392E-02	-1.011	-1.856	0.0270
50	10.10	3.51E-07	0.1010	1.527E-02	-0.996	-1.816	0.0386
51	10.10	3.62E-07	0.1010	1.575E-02	-0.996	-1.803	0.0520
52	10.20	3.54E-07	0.1020	1.540E-02	-0.991	-1.813	0.0343
53	10.20	3.30E-07	0.1020	1.435E-02	-0.991	-1.843	0.0039
54	10.30	3.34E-07	0.1030	1.453E-02	-0.987	-1.838	0.0012
55	10.30	2.10E-07	0.1030	9.134E-03	-0.987	-2.039	-0.2003
56	10.40	3.40E-07	0.1040	1.479E-02	-0.983	-1.830	0.0011
57	10.90	3.62E-07	0.1090	1.575E-02	-0.963	-1.803	-0.0097
58	11.10	3.72E-07	0.1110	1.618E-02	-0.955	-1.791	-0.0125
59	11.10	4.22E-07	0.1110	1.836E-02	-0.955	-1.736	0.0422
60	11.10	4.27E-07	0.1110	1.857E-02	-0.955	-1.731	0.0474
61	11.20	4.19E-07	0.1120	1.823E-02	-0.951	-1.739	0.0319
62	11.20	5.48E-07	0.1120	2.384E-02	-0.951	-1.623	0.1485
63	11.40	4.27E-07	0.1140	1.857E-02	-0.943	-1.731	0.0258
64	11.40	4.12E-07	0.1140	1.792E-02	-0.943	-1.747	0.0102
65	11.60	5.40E-07	0.1160	2.349E-02	-0.936	-1.629	0.1137

Model / Validation / Sheet3

Figure G-2. Spreadsheet "Invert Diffusion Coefficient," Worksheet "Model;" Invert Diffusion Coefficient Input Data (Water Content 7.30 to 11.60%)

	A	B	C	D	E	F	G
65	11.60	5.40E-07	0.1160	2.349E-02	-0.936	-1.629	0.1137
66	11.70	2.60E-07	0.1170	1.131E-02	-0.932	-1.947	-0.2107
67	11.80	4.80E-07	0.1180	2.088E-02	-0.928	-1.680	0.0487
68	12.00	2.40E-07	0.1200	1.044E-02	-0.921	-1.981	-0.2659
69	12.00	4.47E-07	0.1200	1.944E-02	-0.921	-1.711	0.0042
70	12.20	4.09E-07	0.1220	1.779E-02	-0.914	-1.750	-0.0478
71	12.30	5.05E-07	0.1230	2.197E-02	-0.910	-1.658	0.0372
72	12.30	4.40E-07	0.1230	1.914E-02	-0.910	-1.718	-0.0227
73	12.30	3.60E-07	0.1230	1.566E-02	-0.910	-1.805	-0.1098
74	12.30	4.50E-07	0.1230	1.957E-02	-0.910	-1.708	-0.0129
75	12.50	2.90E-07	0.1250	1.261E-02	-0.903	-1.899	-0.2168
76	12.70	4.37E-07	0.1270	1.901E-02	-0.896	-1.721	-0.0515
77	12.70	4.90E-07	0.1270	2.131E-02	-0.896	-1.671	-0.0018
78	12.70	5.32E-07	0.1270	2.314E-02	-0.896	-1.636	0.0339
79	13.10	4.77E-07	0.1310	2.075E-02	-0.883	-1.683	-0.0386
80	13.90	5.39E-07	0.1390	2.344E-02	-0.857	-1.630	-0.0335
81	13.90	7.80E-07	0.1390	3.393E-02	-0.857	-1.469	0.1270
82	14.10	5.12E-07	0.1410	2.227E-02	-0.851	-1.652	-0.0674
83	14.20	5.52E-07	0.1420	2.401E-02	-0.848	-1.620	-0.0404
84	14.40	4.50E-07	0.1440	1.957E-02	-0.842	-1.708	-0.1404
85	14.40	5.20E-07	0.1440	2.262E-02	-0.842	-1.646	-0.0776
86	14.40	4.50E-07	0.1440	1.957E-02	-0.842	-1.708	-0.1404
87	14.60	6.82E-07	0.1460	2.967E-02	-0.836	-1.528	0.0290
88	14.70	9.00E-07	0.1470	3.915E-02	-0.833	-1.407	0.1439
89	14.80	6.54E-07	0.1480	2.845E-02	-0.830	-1.546	-0.0002
90	16.00	1.47E-06	0.1600	6.394E-02	-0.796	-1.194	0.2884
91	16.10	6.82E-07	0.1610	2.967E-02	-0.793	-1.528	-0.0502
92	16.50	5.45E-07	0.1650	2.371E-02	-0.783	-1.625	-0.1674
93	16.70	6.60E-07	0.1670	2.871E-02	-0.777	-1.542	-0.0940
94	17.00	1.20E-06	0.1700	5.220E-02	-0.770	-1.282	0.1512
95	17.10	8.20E-07	0.1710	3.567E-02	-0.767	-1.448	-0.0189
96	17.30	1.76E-06	0.1730	7.656E-02	-0.762	-1.116	0.3034
97	17.50	1.10E-06	0.1750	4.785E-02	-0.757	-1.320	0.0900

Model / Validation / Sheet3

Figure G-3. Spreadsheet "Invert Diffusion Coefficient," Worksheet "Model;" Invert Diffusion Coefficient Input Data (Water Content 11.60 to 17.50%)

	A	B	C	D	E	F	G	H	I
97	17.50	1.10E-06	0.1750	4.785E-02	-0.757	-1.320	0.0900		
98	18.80	1.60E-06	0.1880	6.960E-02	-0.726	-1.157	0.1948		
99	18.90	8.19E-07	0.1890	3.562E-02	-0.724	-1.448	-0.1004		
100	19.40	9.89E-07	0.1940	4.302E-02	-0.712	-1.366	-0.0396		
101	20.40	4.19E-06	0.2040	1.823E-01	-0.690	-0.739	0.5468		
102	20.80	3.58E-06	0.2080	1.557E-01	-0.682	-0.808	0.4627		
103	21.00	2.34E-06	0.2100	1.018E-01	-0.678	-0.992	0.2703		
104	21.50	1.23E-06	0.2150	5.350E-02	-0.668	-1.272	-0.0280		
105	21.60	1.29E-06	0.2160	5.611E-02	-0.666	-1.251	-0.0111		
106	23.10	2.40E-06	0.2310	1.044E-01	-0.636	-0.981	0.2042		
107	23.10	1.90E-06	0.2310	8.264E-02	-0.636	-1.083	0.1027		
108	24.00	2.90E-06	0.2400	1.261E-01	-0.620	-0.899	0.2555		
109	25.30	5.82E-06	0.2530	2.532E-01	-0.597	-0.597	0.5153		
110	25.40	2.50E-06	0.2540	1.087E-01	-0.595	-0.964	0.1451		
111	25.70	9.26E-06	0.2570	4.028E-01	-0.590	-0.395	0.7043		
112	28.20	3.50E-06	0.2820	1.522E-01	-0.550	-0.817	0.2067		
113	28.50	1.00E-06	0.2850	4.350E-02	-0.545	-1.362	-0.3460		
114	30.90	1.51E-06	0.3090	6.568E-02	-0.510	-1.183	-0.2324		
115	31.70	1.23E-05	0.3170	5.350E-01	-0.499	-0.272	0.6578		
116	32.30	4.60E-06	0.3230	2.001E-01	-0.491	-0.699	0.2155		
117	33.80	1.34E-05	0.3380	5.829E-01	-0.471	-0.234	0.6431		
118	35.80	1.57E-05	0.3580	6.829E-01	-0.446	-0.166	0.6654		
119	38.50	4.33E-06	0.3850	1.883E-01	-0.415	-0.725	0.0472		
120	39.30	1.36E-05	0.3930	5.916E-01	-0.406	-0.228	0.5276		
121	39.50	1.13E-05	0.3950	4.915E-01	-0.403	-0.308	0.4430		
122	40.00	6.90E-06	0.4000	3.001E-01	-0.398	-0.523	0.2186		
123	42.00	5.80E-06	0.4200	2.523E-01	-0.377	-0.598	0.1037		
124	42.50	3.22E-06	0.4250	1.401E-01	-0.372	-0.854	-0.1614		
125	43.40	1.02E-05	0.4340	4.437E-01	-0.363	-0.353	0.3224		
126	49.00	6.09E-06	0.4900	2.649E-01	-0.310	-0.577	0.0002		
127	66.30	1.83E-05	0.6630	7.960E-01	-0.178	-0.099	0.2334		
128							0.0329	Average	
129							0.2181	Standard Deviation	

Model / Validation / Sheet3

Figure G-4. Spreadsheet "Invert Diffusion Coefficient," Worksheet "Model;" Invert Diffusion Coefficient Input Data (Water Content 17.50 to 66.30%)

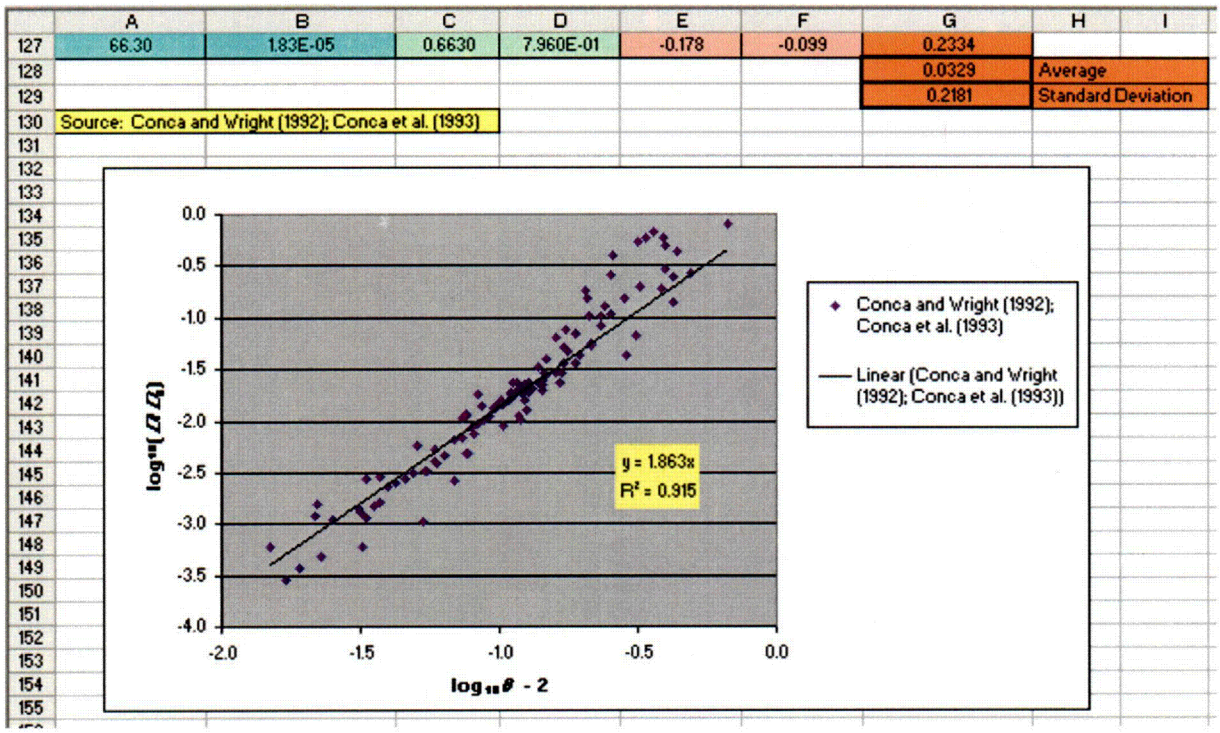

Source: Conca and Wright 1992 [DIRS 100436]; Conca et al. 1993 [DIRS 170709].

Figure G-5. Spreadsheet "Invert Diffusion Coefficient," Worksheet "Model;" Plot of Fitted Invert Diffusion Coefficient Data

In the plot in Figure G-6 between Rows 169 and 191, the lines for the mean and for the mean plus or minus three standard deviations are added to the plot shown earlier. The lines are drawn over the range of the data, i.e., for $\theta/100$ from 0.015 to 0.663 (Column C, Rows 159 to 166). The y-values for the Trendline fit are computed as $\phi S_w D_I / D_0 = (\theta/100)^{1.863}$ (e.g., D159=(C159^1.863)), and the values plotted are $\log_{10}(\phi S_w D_I / D_0)$ (e.g., G159=LOG10(D159)). For the mean curve, the y-values are computed as $\phi S_w D_I / D_0 = (\theta/100)^{1.863} 10^{0.033}$ (e.g., D163=(C163^1.863)*10^(0.033)), and the values plotted are again $\log_{10}(\phi S_w D_I / D_0)$ (e.g., G163=LOG10(D163)). For the mean plus three standard deviations curve, the y-values are computed as $\phi S_w D_I / D_0 = (\theta/100)^{1.863} 10^{0.033+3(0.218)}$ (e.g., G161=(C161^1.863)*10^(0.033+3*0.218)), and the values plotted are again $\log_{10}(\phi S_w D_I / D_0)$ (e.g., G161=LOG10(D161)). The mean minus three standard deviations curve is done similarly. This plot is shown as Figure 6.3-4 in Section 6.3.4.1.1.

Lines for plot at ± 3 standard deviations

log10(q/100)	θ/100	$D/D_0=(\theta/100)^{1.863x}$		$\log_{10}(D/D_0)$
-1.8239	0.015	4.000E-04	Trendline	-3.3979
-0.1785	0.663	4.650E-01	Trendline	-0.3325
-1.8239	0.015	1.946E-03	mean + 3 std dev	-2.7109
-0.1785	0.663	2.262E+00	mean + 3 std dev	0.3545
-1.8239	0.015	4.316E-04	mean	-3.3649
-0.1785	0.663	5.017E-01	mean	-0.2995
-1.8239	0.015	9.573E-05	mean - 3 std dev	-4.0189
-0.1785	0.663	1.113E-01	mean - 3 std dev	-0.9535

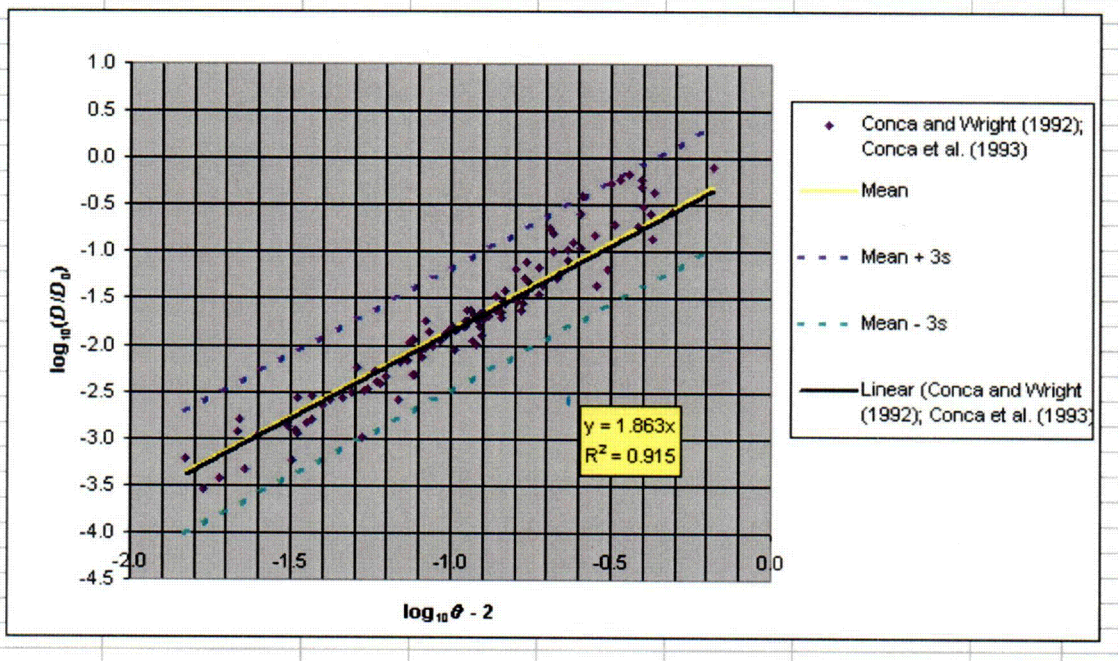

Model / Validation / Sheet3

Source: Conca and Wright 1992 [DIRS 100436]; Conca et al. 1993 [DIRS 170709].

Figure G-6. Spreadsheet "Invert Diffusion Coefficient," Worksheet "Model;" Plotted Results of Invert Diffusion Coefficient Data, Showing Uncertainty Range as Mean ±3 Standard Deviations

The data are further analyzed in Figure G-7 to demonstrate that the deviations approximately follow a normal distribution. Under the Microsoft Excel menu item Tools, Data Analysis… is clicked, and Histogram is selected under Analysis Tools. In the Histogram window, the error data (Column G, Rows 3 to 127) are entered for the Input Range. For the Bin Range, Column I, Rows 3 to 22, is entered. The frequency distribution is output in Column J, Rows 3 to 22. For comparison, a theoretical normal distribution is computed over the same range in Column M:

$$f(x;\mu,\sigma)=\frac{1}{\sigma\sqrt{2\pi}}e^{-(x-\mu)^2/2\sigma^2}, \qquad \text{(Eq. G-5)}$$

where x is the bin value, the mean $\mu \approx 0.033$, and the standard deviation $\sigma \approx 0.218$.

The Microsoft Excel formula is (for Cell M3, for example):

```
M3=EXP(-((I3-0.0329438386573088)^2)/(2*0.218121819319092^2))/
(0.218121819319092*(2*PI())^0.5)
```

	G	H	I	J	K	L	M	N	O	P
1	Error = [$\log_{10}(D_1/D_2)$									
2	- 1.863 ($\log_{10}\theta$ - 2)]		Bin	Frequency	Bin	Frequency	Normal Distribution			
3	0.1792		-1	0	0	34	0.000025			
4	-0.2455		-0.9	0	0.1	24	0.000195			
5	-0.2205		-0.8	0	0.2	18	0.001246			
6	0.1799		-0.7	0	-0.1	14	0.006462			
7	0.2863		-0.6	1	-0.2	10	0.027149			
8	-0.2687		-0.5	0	0.3	10	0.092442			
9	0.0209		-0.4	2	0.6	3	0.255101			
10	-0.0326		-0.3	1	0.7	3	0.570522			
11	-0.0757		-0.2	10	-0.4	2	1.034069			
12	-0.4465		-0.1	14	0.4	2	1.518954			
13	-0.1487		0	34	0.5	2	1.808246			
14	0.1938		0.1	24	-0.6	1	1.744570			
15	-0.1965		0.2	18	-0.3	1	1.364071			
16	-0.1377		0.3	10	0.8	1	0.864377			
17	-0.1260		0.4	2	-1	0	0.443902			
18	0.1253		0.5	2	-0.9	0	0.184752			
19	-0.0396		0.6	3	-0.8	0	0.062317			
20	-0.0230		0.7	3	-0.7	0	0.017035			
21	-0.0773		0.8	1	-0.5	0	0.003774			
22	-0.0642		0.9	0	0.9	0	0.000678			
23	0.1667		1	0	1	0	0.000099			
24	-0.6048		More	0	More	0				
25	-0.1193									
26	-0.1311									
27	0.0278									
28	-0.1033									
29	-0.1350									
30	-0.0995									
31	-0.4203									
32	-0.0259									
33	-0.0399									
34	0.1429									
35	0.1384									
36	-0.2352									
37	0.1531									
38	-0.2458									
39	-0.0214									
40	-0.0977									
41	0.2629									
42	-0.0203									
43	0.1285									
44	-0.0335									
45	-0.0282									
46	-0.0282									

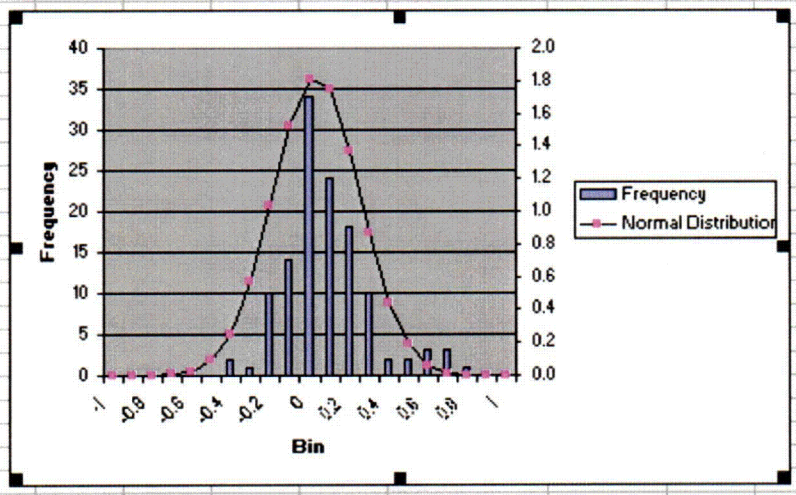

Model / Validation / Sheet3

Figure G-7. Spreadsheet "Invert Diffusion Coefficient," Worksheet "Model;" Further Analysis of Invert Diffusion Coefficient Data

SPREADSHEET "INVERT DIFFUSION COEFFICIENT" WORKSHEET "VALIDATION"

In this worksheet (Figure G-8), diffusion coefficient data (Column B) from Tables A-1 and A-2 of *The Determination of Diffusion Coefficient of Invert Materials* (CRWMS M&O 2000 [DIRS 156680]) are plotted against water content (Column A), along with the results of the analysis in Worksheet "Model." The purpose of this worksheet is partially to validate the diffusion coefficient submodel by showing that the model overestimates the value of the invert diffusion coefficient, thereby overestimating diffusive releases of radionuclides through the invert. The model curve fit (Equation 6.3.4.1.1-22), also shown on p. G-7 and in Figure 6.3-4 in Section 6.3.4.1.1, is reproduced in Columns D-G, Rows 3 and 4, and plotted in the figure below.

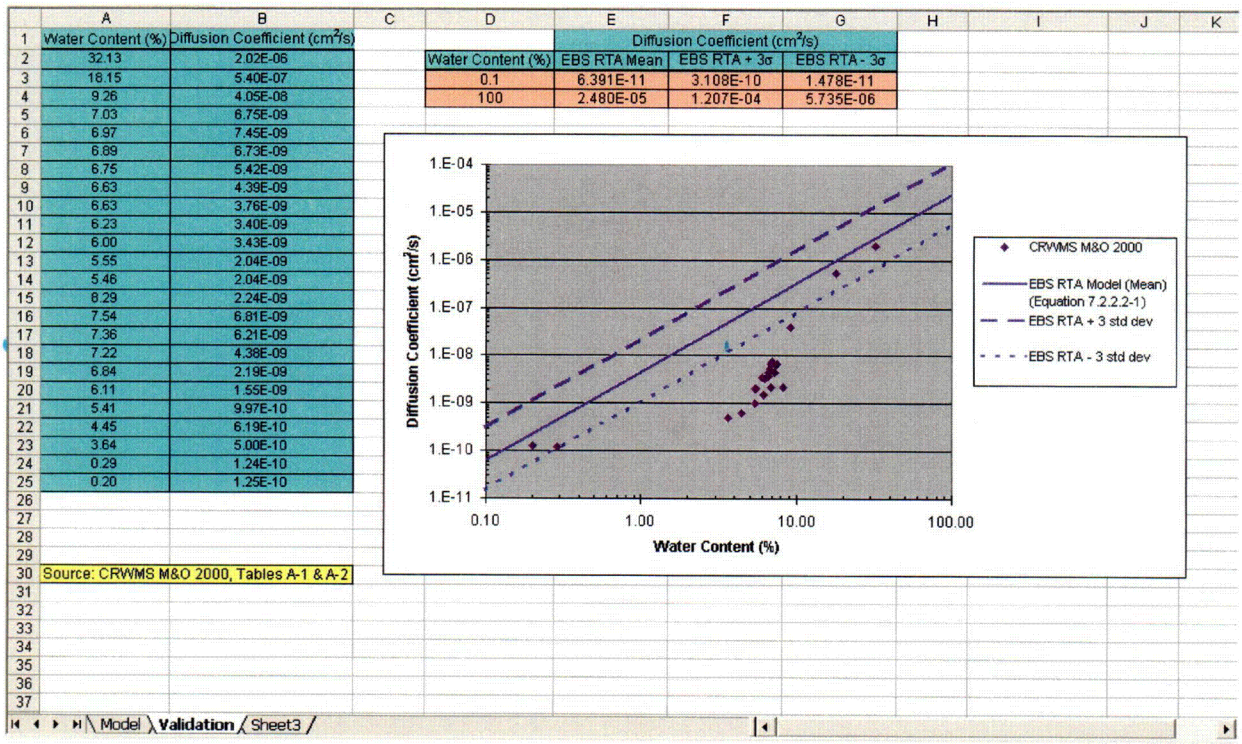

Water Content (%)	Diffusion Coefficient (cm^2/s)
32.13	2.02E-06
18.15	5.40E-07
9.26	4.05E-08
7.03	6.75E-09
6.97	7.45E-09
6.89	6.73E-09
6.75	5.42E-09
6.63	4.39E-09
6.63	3.76E-09
6.23	3.40E-09
6.00	3.43E-09
5.55	2.04E-09
5.46	2.04E-09
8.29	2.24E-09
7.54	6.81E-09
7.36	6.21E-09
7.22	4.38E-09
6.84	2.19E-09
6.11	1.55E-09
5.41	9.97E-10
4.45	6.19E-10
3.64	5.00E-10
0.29	1.24E-10
0.20	1.25E-10

Source: CRWMS M&O 2000, Tables A-1 & A-2

Water Content (%)	Diffusion Coefficient (cm^2/s)		
	EBS RTA Mean	EBS RTA + 3σ	EBS RTA - 3σ
0.1	6.391E-11	3.108E-10	1.478E-11
100	2.480E-05	1.207E-04	5.735E-06

Source: CRWMS M&O 2000 [DIRS 156680], Tables A-1 and A-2.

Figure G-8. Spreadsheet "Invert Diffusion Coefficient," Worksheet "Validation;" Validation of Invert Diffusion Coefficient Data

INTENTIONALLY LEFT BLANK

APPENDIX H

QUALIFICATION OF DIFFUSION COEFFICIENT DATA

QUALIFICATION OF DIFFUSION COEFFICIENT DATA

DESCRIPTION OF DATA TO BE QUALIFIED

The data reported in Conca and Wright (1992 [DIRS 100436]) and Conca et al. (1993 [DIRS 170709]) consist of measured diffusion coefficients of unsaturated soil, gravel, bentonite, rock, and crushed tuff from Yucca Mountain, over a broad range of water contents. These data have been collected and analyzed using standard scientific practices. The diffusivity data for various granular media at volumetric moisture contents ranging between 1.5% and 66.3% are given in Section 4.1.2, Table 4.1-17. These measured data have been used to analyze the dependence of the diffusion coefficient on volumetric moisture content for a variety of granular materials (Section 6.3.4.1.1). These data are qualified in accordance with the data qualification plan included in this appendix.

CORROBORATING DATA

The diffusion coefficient data for crushed tuff materials from *The Determination of Diffusion Coefficient of Invert Materials* (CRWMS M&O 2000 [DIRS 156680]) are used to qualify the data reported by Conca and Wright (1992 [DIRS 100436]) and Conca et al. (1993 [DIRS 170709]). The diffusion coefficient data found in *The Determination of Diffusion Coefficient of Invert Materials* (CRWMS M&O 2000 [DIRS 156680]) were collected in the DOE Atlas Facility. The tests were performed by the EBS Testing Department under YMP-approved procedures using the Unsaturated Flow Apparatus. The Unsaturated Flow Apparatus method is reported to be an accurate and fast indirect method of determining diffusion coefficients in porous media (Conca and Wright 1992 [DIRS 100436], p. 7). The method uses measurements of electrical conductivity, at specified volumetric moisture content, which is converted to diffusion coefficient. *The Determination of Diffusion Coefficient of Invert Materials* (CRWMS M&O 2000 [DIRS 156680]) reports that the error on the reported data is within ±7%. The reported data are shown in Table H-1.

DATA EVALUATION CRITERIA

The diffusion coefficient data from Conca and Wright (1992 [DIRS 100436]) and Conca et al. (1993 [DIRS 170709]) will be considered qualified if they are within one order of magnitude of the values reported in *The Determination of Diffusion Coefficient of Invert Materials* (CRWMS M&O 2000 [DIRS 156680]); or if greater differences are observed, they result in more conservative results with regard to radionuclide releases.

COMPARISON OF THE DIFFUSION COEFFICIENT DATA IN CONCA AND WRIGHT (1992 [DIRS 100436]) AND CONCA ET AL. (1993 [DIRS 170709]) TO CRWMS M&O (2000 [DIRS 156680])

The data reported by Conca and Wright (1992 [DIRS 100436]) and Conca et al. (1993 [DIRS 170709]) (shown in Section 4.1.2, Table 4.1-17) consist of diffusion coefficient data for the range of 1.5% to 66.3% volumetric moisture content. The data from *The Determination of Diffusion Coefficient of Invert Materials* (CRWMS M&O 2000 [DIRS 156680]) ranges between 0.2% and 32.13%. Figure H-1 shows a plot of moisture content versus diffusion coefficient for data from both sources. The figure shows that overall the Conca and Wright

(1992 [DIRS 100436]) and Conca et al. (1993 [DIRS 170709]) data have higher diffusion coefficient values over the measured range of water content. The differences are highest at low water content. At water content values below 10%, the Conca and Wright (1992 [DIRS 100436]) and Conca et al. (1993 [DIRS 170709]) diffusion coefficient values are higher by as much as two orders of magnitude. For water content values above 10%, the Conca and Wright (1992 [DIRS 100436]) and Conca et al. (1993 [DIRS 170709]) diffusion coefficient data show higher but comparable values.

The differences in diffusion coefficient at low water content values can be partly attributed to the measurement technique. As discussed in Section 6 of *The Determination of Diffusion Coefficient of Invert Materials* (CRWMS M&O 2000 [DIRS 156680]), errors in measurement are higher at low diffusion coefficient values. Conca and Wright (1992 [DIRS 100436], p. 10) also reported that, at low water content, reductions in water content result in sharp declines in the measured diffusion coefficient as surface films become thin and discontinuous, and pendular water elements become small. Measurement differences could also be attributed to the different porous medium samples used. The Conca and Wright (1992 [DIRS 100436]) and Conca et al. (1993 [DIRS 170709]) data include various material samples whereas the determination report (CRWMS M&O 2000 [DIRS 156680]) data are for crushed tuff only. The data from both sources show some scatter. The diffusion coefficient data of Conca and Wright (1992 [DIRS 100436]) and Conca et al. (1993 [DIRS 170709]) are thus comparable to those of the determination report (CRWMS M&O 2000 [DIRS 156680]) for volumetric water content values above 10%. For low volumetric water content values, the differences are greater. However, the higher diffusion coefficient values of Conca and Wright (1992 [DIRS 100436]) and Conca et al. (1993 [DIRS 170709]) will result in predicted radionuclide releases being higher.

The Conca and Wright (1992 [DIRS 100436]) data have been published in a peer-reviewed journal (*Applied Hydrology*), and thus have undergone strict review. The data are shown plotted in Figure 2 of Conca and Wright (1992 [DIRS 100436]).

The Conca et al. (1993 [DIRS 170709]) data have been published in the proceedings of the *Scientific Basis for Nuclear Waste Management XVI Symposium* held November 30 to December 4, 1992. This symposium was organized by the Materials Research Society, which was formed in 1973. The most recent *Scientific Basis for Nuclear Waste Management XVI Symposium* is XXVII, the proceedings of which were published in 2004. Papers published in the proceedings undergo peer review prior to publication and must be presented at the meeting in order to be published.

SUMMARY OF QUALIFICATION

The diffusion coefficient data of Conca and Wright (1992 [DIRS 100436]) and Conca et al. (1993 [DIRS 170709]) have been evaluated in the context of their use in radionuclide transport modeling, and are considered qualified for use within this report per LP-SIII.2Q-BSC, *Qualification of Unqualified Data,* Attachment 3, on the basis of:

- Availability of corroborating data–The corroborating data are YMP-generated data using the same measurement technique.

- Reliability of data sources–The data are published in a peer-reviewed journal and in a peer-reviewed symposium proceedings.

- Data demonstrate properties of interest–The published data, diffusion coefficients in crushed rock, are the data required for the model of transport in the invert.

The above comparison of the diffusion coefficient data of Conca and Wright (1992 [DIRS 100436]) and Conca et al. (1993 [DIRS 170709]) with the corroborating data from CRWMS M&O 2000 [DIRS 156680] shows that the data evaluation criteria have been met. The data to be qualified are within one order of magnitude of the values in the corroborating source for volumetric water content values above 10% (Figure H-1). The differences between the two data sets are greater than one order of magnitude below 10%; however, the higher diffusion coefficient values of Conca and Wright (1992 [DIRS 100436]) and Conca et al. (1993 [DIRS 170709]) will result in predicted radionuclide releases being higher. Therefore, the Conca and Wright (1992 [DIRS 100436]) and Conca et al. (1993 [DIRS 170709]) diffusion coefficient data shown on Table 4.1-17 are judged to be qualified for use in this report. Use of these data in other applications would require a comparable evaluation for that specific use.

Table H-1. Diffusion Coefficient of Crushed Tuff Invert Materials

Sample	Volumetric Moisture Content (%)	Diffusion Coefficient ($cm^2 s^{-1}$)
1	32.13	2.02×10^{-6}
2	18.15	5.40×10^{-7}
3	9.26	4.05×10^{-8}
4	7.03	6.75×10^{-9}
5	6.97	7.45×10^{-9}
6	6.89	6.73×10^{-9}
7	6.75	5.42×10^{-9}
8	6.63	4.39×10^{-9}
9	6.63	3.76×10^{-9}
10	6.23	3.40×10^{-9}
11	6.00	3.43×10^{-9}
12	5.55	2.04×10^{-9}
13	5.46	2.04×10^{-9}
14	8.29	2.24×10^{-9}
15	7.54	6.81×10^{-9}
16	7.36	6.21×10^{-9}
17	7.22	4.38×10^{-9}
18	6.84	2.19×10^{-9}
19	6.11	1.55×10^{-9}
20	5.41	9.97×10^{-10}
21	4.45	6.19×10^{-10}
22	3.64	5.00×10^{-10}
23	0.29	1.24×10^{-10}
24	0.20	1.25×10^{-10}

Source: CRWMS M&O 2000 [DIRS 156680].

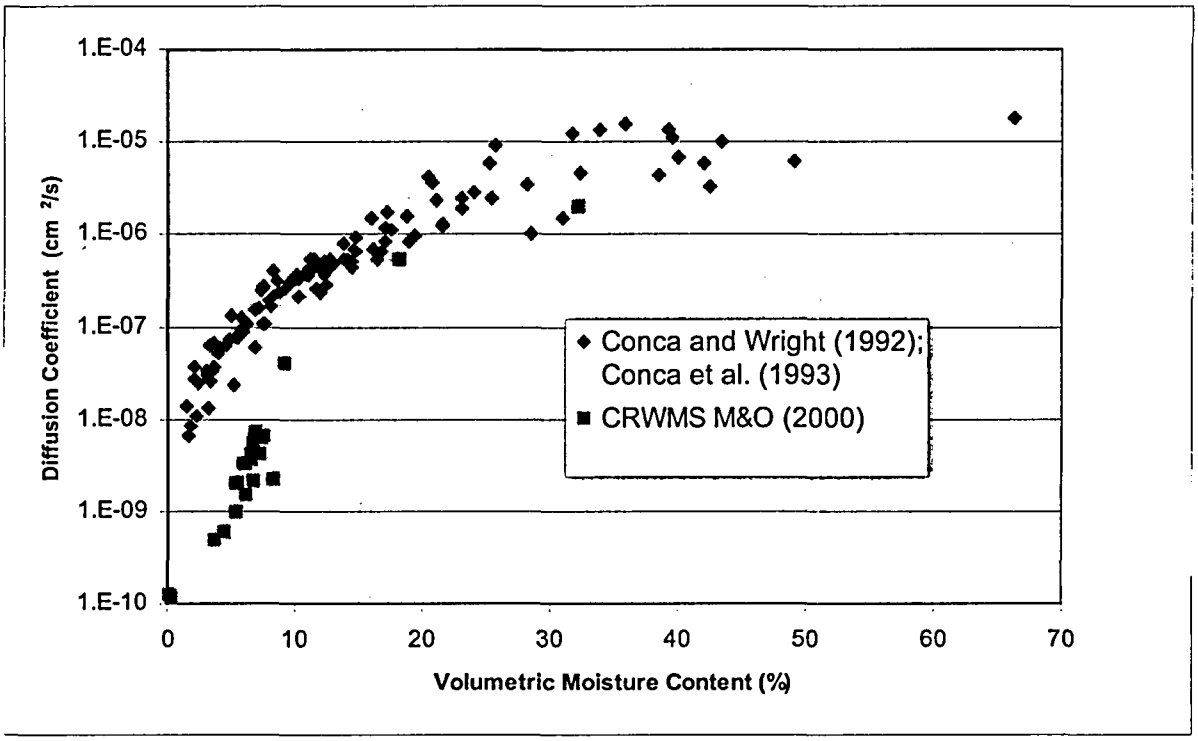

Source: Conca and Wright 1992 [DIRS 100436]; Conca et al. 1993 [DIRS 170709]; CRWMS M&O 2000 [DIRS 156680].

Figure H-1. Comparison of Diffusion Coefficients

DATA QUALIFICATION PLAN

A facsimile of the data qualification plan developed for the above qualification effort is provided in Figure H-2. The original is included in the records package for this model report.

BSC	Data Qualification Plan *Complete only applicable items.*	QA: QA Page 1 of 1

Section I. Organizational Information

Qualification Title

QUALIFICATION OF DIFFUSION COEFFICIENT DATA

Requesting Organization

Near-Field Environment and Transport

Section II. Process Planning Requirements

1. List of Unqualified Data to be Evaluated

Diffusion coefficient data reported in Conca and Wright (1992 [DIRS 100436]) and Conca et al. (1993 [DIRS 170709]). These data are shown on Table 4.1-17 of this report.

2. Type of Data Qualification Method(s) [Including rationale for selection of method(s) (Attachment 3) and qualification attributes (Attachment 4)]

Qualification method, from Attachment 3 of LP-SIII.2Q-BSC, REV 0 ICN 0: Corroborating Data. The diffusion coefficient data for crushed tuff materials from the Determination of Diffusion Coefficient of Invert Materials (CRWMS M&O 2000 [DIRS 156680]) are used to qualify the data reported by Conca and Wright (1992 [DIRS 100436]) and Conca et al. (1993 [DIRS 170709]).

Attributes used from Attachment 4: (3) The extent to which the data demonstrate the properties of interest, (8) Prior peer or other professional review of the data and their results; and (10) Extent and quality of corroborating data.

3. Data Qualification Team and Additional Support Staff Required

Chairperson: James Schreiber, Sandia National Laboratories
Technically competent individual: Teklu Hadgu, Sandia National Laboratories

4. Data Evaluation Criteria

The diffusion coefficient data from Conca and Wright (1992 [DIRS 100436]) and Conca et al. (1993 [DIRS 170709]) will be considered qualified if they are within one order of magnitude of the values reported in CRWMS M&O 2000 [DIRS 156680]; or if greater differences are observed, they result in more conservative results with regard to radionuclide releases.

5. Identification of Procedures Used

LP-SIII.2Q-BSC, Qualification of Unqualified Data
LP-SIII.10Q-BSC, Models

Section III. Approval

Qualification Chairperson Printed Name	Qualification Chairperson Signature	Date
James Schreiber	James D. Schreiber	8/24/05
Responsible Manager Printed Name	**Responsible Manager Signature**	**Date**
Ernest Hardin	Ehardin	8/24/05

LP-SIII.2Q-BSC FORM NO. LSIII2-1 (Rev. 01/19/2005)

Figure H-2. Data Qualification Plan

INTENTIONALLY LEFT BLANK

APPENDIX I

COMPARISON OF OUTPUT DTNS

COMPARISON OF OUTPUT DTNs

The output from this report consists of three preliminary output DTNs: SN0403T0507703.015, SN0409T0507703.017 and SN0503T0503305.001, and three final output DTNs: SN0410T0507703.018, SN0508T0503305.003, and MO0506SPAINPAR.000. In this appendix, the differences between two preliminary output DTNs (SN0403T0507703.015 and SN0409T0507703.017) are discussed. In addition, the final output DTN: SN0410T0507703.018 is compared with the second preliminary DTN: SN0409T0507703.017. These comparisons provide traceability for TSPA-LA applications that were initially developed based on the preliminary output DTNs.

The output in the three DTNs discussed in this appendix consists of tables from Section 8 (Conclusions) of the *EBS RT Abstraction*. Each of these tables is compared in this appendix. Numerous editorial revisions were made in converting the first preliminary version of the DTN to the second preliminary version; because these editorial revisions have no impact on TSPA-LA results, they are not discussed in this appendix.

TABLE 57 (DTN: SN0403T0507703.015) VS. TABLE 8.1-1 (DTN: SN0409T0507703.017)

Table 57 (Summary of EBS Flow Abstraction) in DTN: SN0403T0507703.015 corresponds to Table 8.1-1 in DTN: SN0409T0507703.017. The key differences in this table between the two DTN versions are the expressions for the flux through the drip shield, F_2, and the flux into the waste package, F_4. In preliminary DTN: SN0403T0507703.015, F_2 is expressed as:

$$F_2 = F_1 L_{DS_Patch} f'_{DS} / (2L_{DS}). \qquad \text{(Eq. I-1)}$$

The parameters are defined in the Table 57 in DTN: SN0403T0507703.015. This equation is technically correct, but it is expressed more completely in DTN: SN0409T0507703.017 as:

$$F_2 = \min[F_1 N_{bDS} L_{DS_Patch} f'_{DS} / (2L_{DS}), F_1]. \qquad \text{(Eq. I-2)}$$

The parameters are defined in the Table 8.1-1 in DTN: SN0409T0507703.017. Equation I-2 replicates Equation 6.5.1.1.2-37 in the *EBS RT Abstraction*. Equations I-1 and I-2 give the same result when the number of corrosion patches in the drip shield, N_{bDS}, is one, which is the case in the WAPDEG model of drip shield failure (BSC 2004 [DIRS 169996], Section 6.3). The min function in Equation I-2 provides a numerical check to prevent an unrealistic result of $F_2 > F_1$ from being obtained if the parameter values used in the equation were to give that result.

The same discussion applies to the flux into the waste package. In DTN: SN0403T0507703.015, F_4, is expressed as:

$$F_4 = F_2 L_{WP_Patch} f'_{WP} / (2L_{WP}). \qquad \text{(Eq. I-3)}$$

The parameters are defined in the Table 57 in DTN: SN0403T0507703.015.

This equation is technically correct, but it is expressed more completely in DTN: SN0409T0507703.017 as:

$$F_4 = \min[F_2 N_{bWP} L_{WP_Patch} f'_{WP} / (2L_{WP}), F_2]. \qquad \text{(Eq. I-4)}$$

The parameters are defined in the Table 8-1 in DTN: SN0409T0507703.017. Equation I-4 replicates Equation 6.5.1.1.3-1 in the *EBS RT Abstraction*. The difference between Equations I-3 and I-4 is the definition of L_{WP_Patch}. In Equation I-3, L_{WP_Patch}, is the length of *all* corrosion patches in the waste package, whereas in Equation I-4, L_{WP_Patch} is the length of *each* corrosion patch; thus, the product $N_{bWP}L_{WP_Patch}$ in Equation I-4 is equal to L_{WP_Patch} in Equation I-3. The min function in Equation I-4 provides a numerical check to prevent an unrealistic result of $F_4 > F_2$ from being obtained if the parameter values used in the equation were to give that result.

In the Flow Parameter column for Flow Pathway 8 in Table 57 in DTN: SN0403T0507703.015, a flux F_9 is erroneously included in the equation and is deleted in the final DTN. Since this flux does not exist, its inclusion in the preliminary DTN has no impact on the TSPA-LA calculation.

The references and comments in the Data Sources & Notes column in Table 8.1-1 in DTN: SN0409T0507703.017 are updated from Table 57 in DTN: SN0403T0507703.015; these updates have no impact on TSPA-LA calculations.

TABLE 58 (DTN: SN0403T0507703.015) VS. TABLE 8.1-2 (DTN: SN0409T0507703.017)

In DTN: SN0409T0507703.017, the cross-sectional area for radionuclide transport is clarified in Table 8.1-2, with references to sections in the report. In DTN: SN0403T0507703.015, the same parameter is referred to as the flow cross-sectional area in Table 58 and described in vague terms that prompted a revised description in the final DTN. References are updated in DTN: SN0409T0507703.017, Table 8.1-2. None of these changes has any impact on TSPA-LA calculations.

TABLE 59 (DTN: SN0403T0507703.015) VS. TABLE 8.2-1 (DTN: SN0409T0507703.017)

In Table 57 in DTN: SN0403T0507703.015, the lower end of the range on sampled parameter Diff_Path_Length_CP_CDSP is erroneously shown as 0.02 m; this error is also found in Table 63 in DTN: SN0403T0507703.015. Because the correct value, 0.025 m, is included in the database used for TSPA-LA, this error has no impact on TSPA-LA. In the corresponding table in DTN: SN0409T0507703.017, Table 8.2-1, the range for this parameter is not shown, since it is given correctly in Table 8.2-3.

References to parameter sources and sections in the *EBS RT Abstraction* are updated in DTN: SN0409T0507703.017. These changes have no impact on TSPA-LA calculations.

TABLE 60 (DTN: SN0403T0507703.015) VS. TABLE 8.2-2 (DTN: SN0409T0507703.017)

Table 8.2-2 in DTN: SN0409T0507703.017 (K_d values for corrosion products) is identical to Table 60 in DTN: SN0403T0507703.015. Therefore, there is no impact on TSPA-LA calculations.

TABLES 61 & 62 (DTN: SN0403T0507703.015) VS. TEXT (DTN: SN0409T0507703.017)

Tables 61 and 62 in DTN: SN0403T0507703.015 (K_d values and correlations for the invert) are replaced in DTN: SN0409T0507703.017 with text clarifying that TSPA-LA is to use UZ K_d values for the invert. This change has no impact on TSPA-LA calculations.

TABLE 63 (DTN: SN0403T0507703.015) VS. TABLE 8.2-3 (DTN: SN0409T0507703.017)

In Table 63 in DTN: SN0403T0507703.015, sampled parameter Diff_Path_Length_CP_CDSP is erroneously shown as having a lower end of the range of 0.02 m. Because the correct value, 0.025 m, is included in the database used for TSPA-LA, this error has no impact on TSPA-LA. The correct range is shown in Table 8.2-3 in DTN: SN0409T0507703.017. References are updated in Table 8.2-3 in DTN: SN0409T0507703.017. These changes have no impact on TSPA-LA calculations.

TABLE 64 (DTN: SN0403T0507703.015) VS. TABLE 8.2-4 (DTN: SN0409T0507703.017)

References are updated in Table 8.2-4 in DTN: SN0409T0507703.017. Three parameters were added to this table to provide a source for the values used in TSPA-LA: DS_Total_Length (5805 mm), Invert_Viscosity_Ref_Temp (298.15 K), and Interface_Scale_Factor (1×10^{-6}). These changes have no impact on TSPA-LA calculations. No other changes were made in converting Table 64 to Table 8.2-4.

TABLE 65 (DTN: SN0403T0507703.015) VS. TABLE 8.2-5 (DTN: SN0409T0507703.017)

The following changes were made to convert Table 65 to Table 8.2-5. References to the equations in the *EBS RT Abstraction* were added to the Input Description column. In the Parameter Description for Equation 8-1, clarification of the definition of *ND*, the truncated normal distribution, was added. In Equation 8-2, the range of validity was added to the definition of temperature. In Equation 8-3, the definition of θ_m was changed from fraction to percent, and the equation was modified accordingly by changing the term $0.138\theta_m$ to $0.00138\theta_m$. Equation 8-7 was completely revised in order to clarify the calculation of corrosion product mass as computed in TSPA-LA over each time interval, from t_0, when breach occurs, to t_{f1} and t_{f2}, the lifetimes of each type of steel. These changes have no impact on TSPA-LA calculations.

TABLE 66 (DTN: SN0403T0507703.015) VS. TABLE 8.2-6 (DTN: SN0409T0507703.017)

Table 8.2-6 DTN: SN0409T0507703.017 (Invert Diffusion Coefficient Alternative conceptual Model Parameters) is identical to Table 66 in DTN: SN0403T0507703.015. Therefore, there is no impact on TSPA-LA calculations.

TABLE 67 (DTN: SN0403T0507703.015) VS. TABLE 8.2-7 (DTN: SN0409T0507703.017)

Equation 8-8 was reformulated in the *EBS RT Abstraction* and revised accordingly in Table 8.2-7. Because this is an alternative conceptual model, this change has no impact on TSPA-LA calculations. Equation 8-9, the definitions of θ_{intra} and θ_{min} were changed from fractions to percent. This change has no impact on the results.

TABLE 8.1-1 (DTN: SN0410T0507703.018)VS. TABLE 8.1-1 (DTN: SN0409T0507703.017)

The differences in this table (Summary of EBS Flow Abstraction) between the two DTN versions are the expressions for the flux through the drip shield, F_2, and the flux into the waste package, F_4. In DTN: SN0409T0507703.017, F_2 is expressed as:

$$F_2 = \min\left[F_1 N_{bDS} L_{DS_Patch} f'_{DS} / (2L_{DS}), F_1\right]. \qquad \text{(Eq. I-5)}$$

The parameters are defined in Table 8.1-1 in both DTNs. Because L_{DS_Patch} is defined as the axial *half*-length of each corrosion patch, the factor of 2 should not appear in the denominator. This equation is presented correctly in DTN: SN0410T0507703.018 as:

$$F_2 = \min\left[F_1 N_{bDS} L_{DS_Patch} f'_{DS} / L_{DS}, F_1\right]. \qquad \text{(Eq. I-6)}$$

Similarly, in DTN: SN0409T0507703.017, F_4 is expressed in Table 8.1-1 as:

$$F_4 = \min\left[F_2 N_{bWP} L_{WP_Patch} f'_{WP} / (2L_{WP}), F_2\right]. \qquad \text{(Eq. I-7)}$$

This equation is presented correctly in Table 8.1-1 in DTN: SN0410T0507703.018 as:

$$F_4 = \min\left[F_2 N_{bWP} L_{WP_Patch} f'_{WP} / L_{WP}, F_2\right]. \qquad \text{(Eq. I-8)}$$

These differences have no impact because the correct equations (Equations I-6 and I-8) have been implemented in the TSPA.

TABLE 8.2-4 (DTN: SN0410T0507703.018)VS. TABLE 8.2-5 (DTN: SN0409T0507703.017)

The differences in this table (Calculated Model Inputs Used in the EBS Radionuclide Transport Abstraction) between the two DTN versions include Equation 8-5 for the effective water saturation of corrosion products. In DTN: SN0409T0507703.017, this equation is:

$$S_{we,CP} = 1.312 \times 10^{-6} \bar{s}_{CP} (-\ln RH)^{-1/2.45}. \qquad \text{(Eq. I-9)}$$

This equation, developed in an earlier draft of Section 6.5.1.2.1.4.2 as Equation 6.5.1.2.1-27, is incorrect. The correct equation (as shown in Section 6.3.4.3.5, Equation 6.3.4.3.5-5 of this report), is given in DTN: SN0410T0507703.018 as:

$$S_{we,CP} = 3.28 \times 10^{-6} \bar{s}_{CP} (-\ln RH)^{-1/2.45}. \qquad \text{(Eq. I-10)}$$

In addition, in DTN: SN0409T0507703.017, parameter $\bar{s}_{CP}$ is defined in Table 8.2-5 as having units of ($m^2\ g^{-1}$). The correct units for use in this parameter are given in DTN: SN0410T0507703.018 as ($m^2\ kg^{-1}$).

The impact of this correction has been assessed in a *Technical Management Review Board (TMRB) Decision Proposal* (BSC 2004 [DIRS 172219]). Because the water saturation in the waste package corrosion products is used to calculate the diffusion coefficient, this correction has a direct impact on dose estimates. In the preliminary assessment, using Equation I-10 instead of Equation I-9 increases the total peak mean annual dose from all scenario classes by 10% (BSC 2004 [DIRS 172219]).

INTENTIONALLY LEFT BLANK

APPENDIX J

SORPTION DATA USED IN TSPA-LA

SORPTION DATA USED IN TSPA-LA

The data used in TSPA-LA for the irreversible sorption submodel is contained in a preliminary output DTN: SN0503T0503305.001. Four of the data points in the preliminary DTN have been found to be incorrect. The correct data values are listed in Table 4.1-10, and included in the discrete distributions presented in Table 6.3-6. The data values and discrete distributions are also included in final output DTN: SN0508T0503305.003. This appendix describes the erroneous data and the sorption parameter distributions that are used in TSPA-LA.

The first erroneous data value in preliminary DTN: SN0503T0503305.001 is a sorption site density for goethite of 1.00 sites nm^{-2} attributed to Kooner (1993 [DIRS 173819]). This value is not given in Kooner (1993 [DIRS 173819]) and has been deleted from the discrete distribution for goethite site density shown in Table 6.3-6. This deletion has two effects. First, the lower end of the distribution increases from 1.00 sites nm^{-2} to 1.02 sites nm^{-2}. Since the upper end of the distribution is 8.38 sites nm^{-2}, this change results in a reduction of the range of less than 0.3 percent and is expected to have negligible impact on dose calculations in TSPA-LA. The second effect is to increase the probability of each entry in the distribution, since there are now 56 points instead of 57. Therefore, each data point now has a probability of 1/56 = 0.01786 instead of 1/57 = 0.01754. This change in the probability of each entry in the distribution should also have a negligible effect on TSPA-LA dose calculations.

The second data error in preliminary DTN: SN0503T0503305.001 is a total sorption site density for goethite of 5.92 sites nm^{-2}. The correct value, as given by Hiemstra and Van Riemsdijk (1996 [DIRS 173023], p. 498), is 6.15 sites nm^{-2} (DTN: SN0508T0503305.003).

The third data error in preliminary DTN: SN0503T0503305.001 is a sorption site density for goethite of 8.83 sites nm^{-2}. The correct value, as given by Robertson and Leckie (1997 [DIRS 173763], Table 4), is 8.38 sites nm^{-2} (DTN: SN0508T0503305.003).

These second and third data values have a minor impact on the discrete distribution for goethite site density in preliminary DTN: SN0503T0503305.001, shown in Table J-1, that is sampled in TSPA-LA. Comparing this with the correct distribution in Table 6.3-6 shows a negligible difference (see Figure J-1, where the cumulative distribution for goethite site density used in TSPA-LA, computed in Table J-2, is compared in with the distribution developed in the *EBS RT Abstraction*). The maximum value in the range of site densities is larger in Table J-1 due to the erroneous data point 8.83 sites nm^{-2}. This point expands the range by about 3%, from a range of 1.02 to 8.59 sites/nm^2 to a range of 1.02 to 8.83 sites nm^{-2}. The value being used in TSPA-LA (8.83) is about 5% greater than the correct value. Since it represents one of 57 data points in the distribution, the probability that it will be sampled is low (1/57 = 0.01754). Therefore, this error is expected to have negligible impact on dose calculations in TSPA-LA. The second error, where the value used in TSPA-LA is 5.92 sites nm^{-2} and the correct value is 6.15 sites nm^{-2}, will also have a negligible effect. The value used in TSPA-LA is smaller than the correct value by about 4%, and thus partially offsets the error in the maximum site density. The correct value and the erroneous value occupy the same position in the distribution, so this error does not alter the shape or range of the distribution. The net effect of these two small errors on dose calculations in TSPA-LA should be negligible.

The fourth data error in preliminary DTN: SN0503T0503305.001 is in a value for the percentage of high-affinity sorption sites for goethite. Instead of the correct value of 2.7 sites nm^{-2} (Hiemstra and Van Riemsdijk 1996 [DIRS 173023], p. 498), an incorrect value of 2.47 sites nm^{-2} was used. This value is used to obtain a value for the percentage of high-affinity sorption sites for goethite in Table 6.3-4b. The incorrect site density value resulted in a value for the percentage of high-affinity sorption sites for goethite of 41.67 percent, whereas the correct value is 43.90 percent (see Table 6.3-4b). The effect of this error on dose calculations in TSPA-LA should be negligible, as indicated by Figure J-2, where the cumulative distribution for the percentage of high-affinity sorption sites for goethite used in TSPA-LA, computed in Table J-2, is compared in with the distribution developed in the *EBS RT Abstraction.*

Table J-1 shows discrete probabilities for various values of several parameters. The sum of these parameters is 1.0, and the cumulative sum at any parameter value is the cumulative (probability) distribution function, CDF.

One additional deviation from the discrete distributions shown in Table 6.3-6 as shown in preliminary DTN: SN0503T0503305.001 involves the number of digits of precision used for the parameters. As discussed in Section 6.3.4.2.3.2, specific surface areas and site density data are accurate to at most three significant digits due to the difficulty in measuring these parameters and variability in samples. The high-affinity site percentages are even less precise. The parameters comprising the discrete distributions in Table 6.3-6 are presented to three significant digits. However, in the Excel file contained in preliminary DTN: SN0503T0503305.001, the data are available to 15 digits of precision. These are shown rounded to 9 digits in Table J-1 (goethite high-affinity site percentages are shown to 11 digits). The differences in precision between the data in Table 6.3-6 and the parameters used in preliminary DTN: SN0503T0503305.001 will have a negligible effect on dose calculations and is discussed here solely to provide full traceability of the data.

Table J-1. Sample Ranges and Distributions Used for Irreversible Sorption on Stationary Corrosion Products in TSPA-LA

Input Name	Input Description	Range	Distribution
Relative_Abundance_Goethite_a	Fraction of total iron oxide that is goethite	0.45 – 0.8	Uniform
Goethite_SA_a	Goethite surface area; discrete distribution	Specific Surface Area ($m^2\ g^{-1}$)	Probability Level
		14.7	0.018867925
		20.0	0.056603774
		21.0	0.037735849
		21.4	0.018867925
		27.7	0.018867925
		28.5	0.037735849
		30.8	0.018867925
		32.0	0.037735849
		33.0	0.056603774
		35.0	0.018867925
		37.0	0.018867925
		38.0	0.018867925
		39.9	0.018867925
		43.0	0.018867925

Table J-1. Sample Ranges and Distributions Used for Irreversible Sorption on Stationary Corrosion Products in TSPA-LA (Continued)

Input Name	Input Description	Range	Distribution
Goethite_SA_a (continued)		45.0	0.037735849
		47.5	0.018867925
		49.0	0.075471698
		50.0	0.018867925
		52.0	0.037735849
		54.0	0.018867925
		55.0	0.056603774
		55.4	0.018867925
		64.3	0.018867925
		66.0	0.037735849
		70.0	0.037735849
		80.0	0.037735849
		80.5	0.018867925
		81.0	0.075471698
		85.0	0.018867925
		86.0	0.018867925
		105.0	0.037735849
		110.0	0.018867925
HFO_SA_a	HFO (hydrous ferric oxide) surface area; discrete distribution	Specific Surface Area (m^2 g^{-1})	Probability Level
		600.0	1.000
Goethite_Site_Density_a	Goethite site density; discrete distribution	Density (sites nm^{-2})	Probability Level
		1.00000000	0.01754386
		1.01513714	0.01754386
		1.21013524	0.01754386
		1.32484000	0.03508772
		1.46000000	0.01754386
		1.50000000	0.01754386
		1.65500000	0.01754386
		1.68000000	0.03508772
		1.70000000	0.01754386
		1.80000000	0.01754386
		1.87000000	0.01754386
		1.92704000	0.01754386
		1.94573646	0.01754386
		1.97220500	0.01754386
		2.20000000	0.01754386
		2.30000000	0.07017544
		2.31000000	0.01754386
		2.31903106	0.01754386
		2.55000000	0.01754386
		2.60000000	0.03508772
		2.70000000	0.01754386
		2.88600000	0.01754386
		2.90000000	0.03508772
		3.00000000	0.01754386
		3.12251852	0.01754386
		3.13144000	0.01754386
		3.30000000	0.03508772
		3.40000000	0.01754386
		4.00000000	0.01754386
		4.20000000	0.01754386

Table J-1. Sample Ranges and Distributions Used for Irreversible Sorption on Stationary Corrosion Products in TSPA-LA (Continued)

Input Name	Input Description	Range	Distribution
Goethite_Site_Density_a (continued)		4.60000000	0.01754386
		4.84195023	0.01754386
		4.90000000	0.01754386
		5.00000000	0.01754386
		5.52819600	0.01754386
		5.92000000	0.01754386
		6.30000000	0.01754386
		6.31000000	0.03508772
		6.60000000	0.01754386
		7.00000000	0.05263158
		7.20000000	0.01754386
		7.40000000	0.01754386
		8.00000000	0.01754386
		8.16000000	0.01754386
		8.58737200	0.01754386
		8.83000000	0.01754386
HFO_Site_Density_a	HFO (hydrous ferric oxide) site density; discrete distribution	Density (sites nm^{-2})	Probability Level
		0.56480960	0.05263158
		1.12961921	0.10526316
		1.46850497	0.05263158
		1.58146689	0.05263158
		1.69442881	0.10526316
		1.80739073	0.05263158
		2.03331458	0.10526316
		2.25923842	0.26315789
		2.59812418	0.05263158
		2.71108610	0.05263158
		4.00000000	0.05263158
		5.64809604	0.05263158
HFO_Strong_Sites_a	Percentage of high affinity HFO (hydrous ferric oxide) sites; discrete distribution	Percentage	Probability Level
		0.20000000	0.01262626
		0.40000000	0.01010101
		0.41666667	0.01262626
		0.43478261	0.01262626
		0.50000000	0.06313131
		0.55555556	0.02525253
		0.60000000	0.00757576
		0.62500000	0.01262626
		0.66666667	0.02525253
		0.71428571	0.01262626
		0.76923077	0.01262626
		0.83333333	0.01010101
		0.86956522	0.01010101
		1.00000000	0.09343434
		1.11111111	0.02020202
		1.25000000	0.01767677
		1.30434783	0.00757576
		1.33333333	0.02020202

Table J-1. Sample Ranges and Distributions Used for Irreversible Sorption on Stationary Corrosion Products in TSPA-LA (Continued)

Input Name	Input Description	Range	Distribution
HFO_Strong_Sites_a (continued)		1.40000000	0.00252525
		1.42857143	0.01010101
		1.50000000	0.03787879
		1.53846154	0.01010101
		1.66666667	0.01515152
		1.87500000	0.00757576
		2.00000000	0.05303030
		2.08333333	0.01767677
		2.14285714	0.00757576
		2.17391304	0.01767677
		2.30769231	0.00757576
		2.50000000	0.08838384
		2.77777778	0.03535354
		2.91666667	0.00252525
		3.00000000	0.01515152
		3.04347826	0.00252525
		3.12500000	0.01767677
		3.33333333	0.03535354
		3.50000000	0.01262626
		3.57142857	0.01767677
		3.84615385	0.01767677
		3.88888889	0.00505051
		4.00000000	0.01010101
		4.16666667	0.00505051
		4.34782609	0.00505051
		4.37500000	0.00252525
		4.66666667	0.00505051
		5.00000000	0.06313131
		5.38461538	0.00252525
		5.55555556	0.01010101
		6.00000000	0.00757576
		6.25000000	0.00505051
		6.66666667	0.01010101
		7.00000000	0.00505051
		7.14285714	0.00505051
		7.69230769	0.00505051
		10.00000000	0.02777778
		14.00000000	0.00252525
		20.00000000	0.00505051
Goethite_Strong_Sites_a	Percentage of high affinity goethite sites; discrete distribution	Percentage	Probability Level
		8.835904628	0.1
		11.450381679	0.1
		12.357581069	0.1
		22.709163347	0.1
		23.059866962	0.1

Table J-1. Sample Ranges and Distributions Used for Irreversible Sorption on Stationary Corrosion Products in TSPA-LA (Continued)

Input Name	Input Description	Range	Distribution
Goethite_Strong_Sites_a (continued)		24.657534247	0.1
		26.829268293	0.1
		41.666666667	0.1
		49.664429530	0.1
		73.913043478	0.1

Source: Preliminary DTN: SN0503T0503305.001.

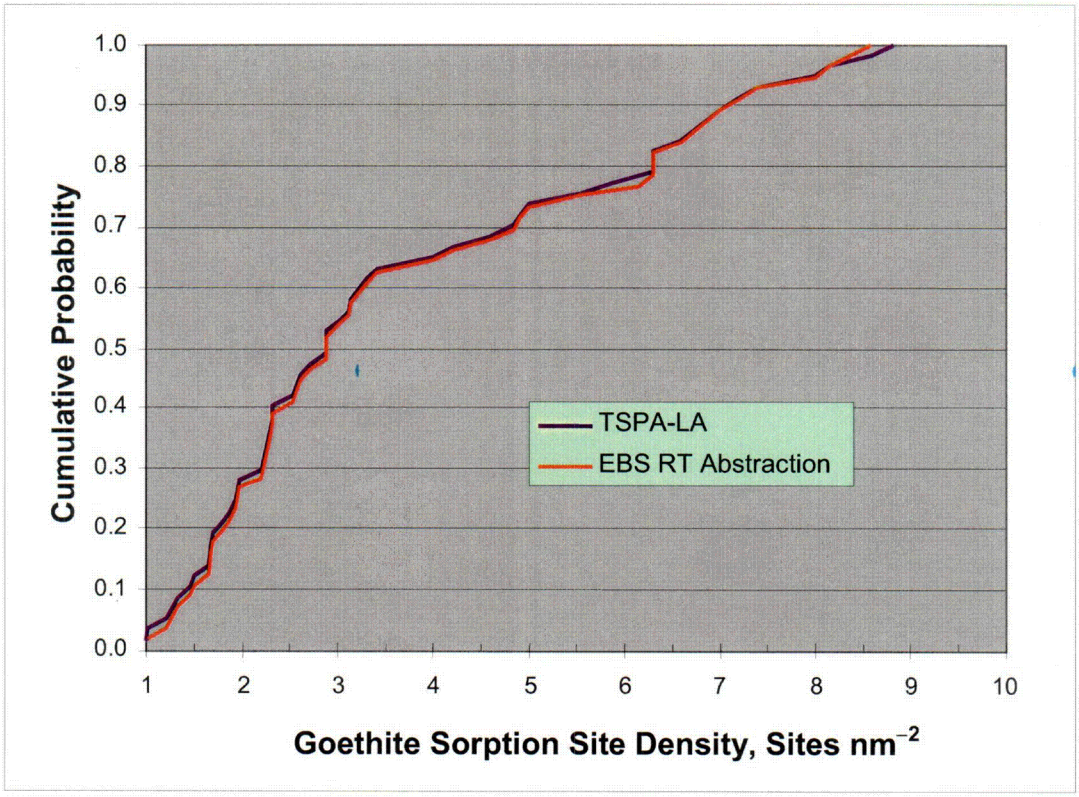

Sources: TSPA-LA: Table J-2.
EBS RT Abstraction: Output DTN: SN0508T0503305.003.

Figure J-1. Comparison of Cumulative Probabilities in Goethite Sorption Site Density Discrete Distributions Used in TSPA-LA and Developed in *EBS RT Abstraction*

Table J-2. Cumulative Probability Distributions for Goethite Site Density and Percentage of High-Affinity Goethite Sites Used in TSPA-LA

Input Description	Values	Probability Level	Cumulative Probability
Goethite site density (sites nm^{-2})	1.00000000	0.01754386	0.01754386
	1.01513714	0.01754386	0.03508772
	1.21013524	0.01754386	0.05263158
	1.32484000	0.03508772	0.08771930
	1.46000000	0.01754386	0.10526316
	1.50000000	0.01754386	0.12280702
	1.65500000	0.01754386	0.14035088
	1.68000000	0.03508772	0.17543860
	1.70000000	0.01754386	0.19298246
	1.80000000	0.01754386	0.21052632
	1.87000000	0.01754386	0.22807018
	1.92704000	0.01754386	0.24561404
	1.94573646	0.01754386	0.26315790
	1.97220500	0.01754386	0.28070176
	2.20000000	0.01754386	0.29824562
	2.30000000	0.07017544	0.36842106
	2.31000000	0.01754386	0.38596492
	2.31903106	0.01754386	0.40350878
	2.55000000	0.01754386	0.42105264
	2.60000000	0.03508772	0.45614036
	2.70000000	0.01754386	0.47368422
	2.88600000	0.01754386	0.49122808
	2.90000000	0.03508772	0.52631580
	3.00000000	0.01754386	0.54385966
	3.12251852	0.01754386	0.56140352
	3.13144000	0.01754386	0.57894738
	3.30000000	0.03508772	0.61403510
	3.40000000	0.01754386	0.63157896
	4.00000000	0.01754386	0.64912282
	4.20000000	0.01754386	0.66666668
	4.60000000	0.01754386	0.68421054
	4.84195023	0.01754386	0.70175440
	4.90000000	0.01754386	0.71929826
	5.00000000	0.01754386	0.73684212
	5.52819600	0.01754386	0.75438598
	5.92000000	0.01754386	0.77192984
	6.30000000	0.01754386	0.78947370
	6.31000000	0.03508772	0.82456142
	6.60000000	0.01754386	0.84210528
	7.00000000	0.05263158	0.89473686

Table J-2. Cumulative Probability Distributions for Goethite Site Density and Percentage of High-Affinity Goethite Sites Used in TSPA-LA (Continued)

Input Description	Values	Probability Level	Cumulative Probability
Goethite site density (sites nm^{-2}) (continued)	7.20000000	0.01754386	0.91228072
	7.40000000	0.01754386	0.92982458
	8.00000000	0.01754386	0.94736844
	8.16000000	0.01754386	0.96491230
	8.58737200	0.01754386	0.98245616
	8.83000000	0.01754386	1.00000002
Percentage of high-affinity goethite sites	8.835904628	0.1	0.1
	11.450381679	0.1	0.2
	12.357581069	0.1	0.3
	22.709163347	0.1	0.4
	23.059866962	0.1	0.5
	24.657534247	0.1	0.6
	26.829268293	0.1	0.7
	41.666666667	0.1	0.8
	49.664429530	0.1	0.9
	73.913043478	0.1	1

Source (Values and Probability Levels): Preliminary DTN: SN0503T0503305.001.

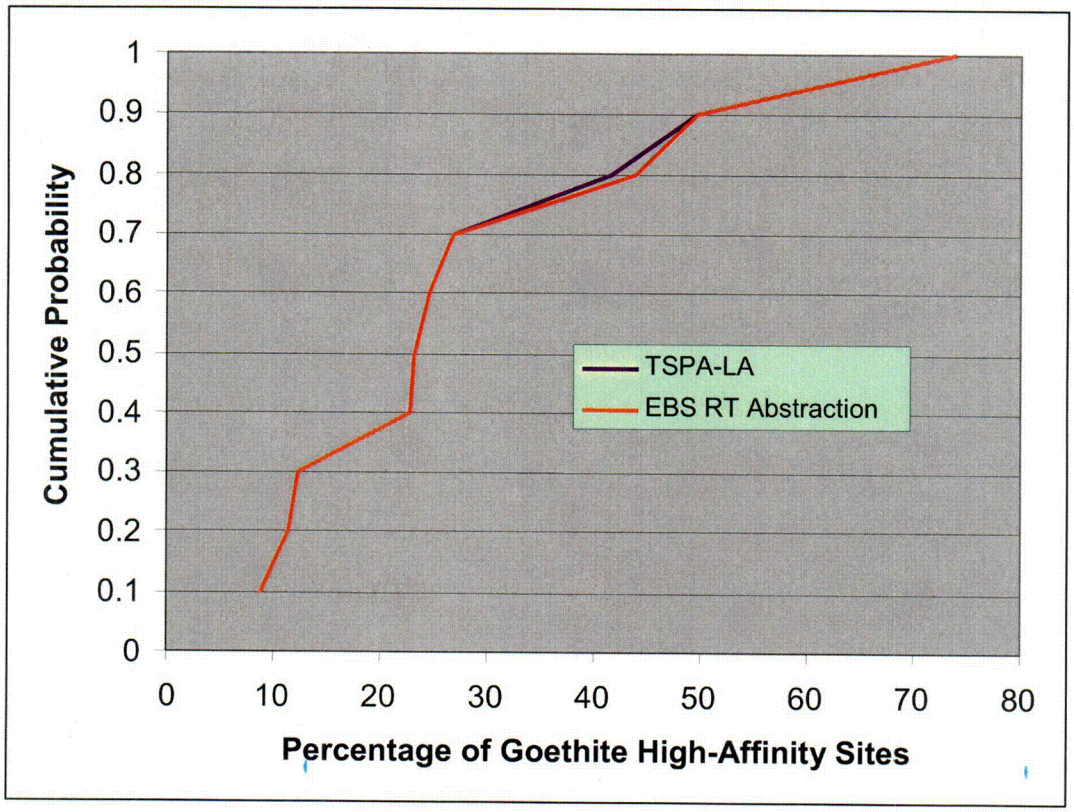

Sources: TSPA-LA: Table J-2.
EBS RT Abstraction: Output DTN: SN0508T0503305.003.

Figure J-2. Comparison of Cumulative Probabilities in Goethite Percentage of High-Affinity Sites Discrete Distributions Used in TSPA-LA and Developed in *EBS RT Abstraction*

INTENTIONALLY LEFT BLANK